IAEA-TECDOC-1889

IAEA TECDOC SERIES

IAEA-TECDOC-1889

Fuel Modelling in Accident Conditions (FUMAC)

Final Report of a Coordinated Research Project

IAEA
International Atomic Energy Agency

FUEL MODELLING IN ACCIDENT CONDITIONS (FUMAC)

The following States are Members of the International Atomic Energy Agency:

AFGHANISTAN
ALBANIA
ALGERIA
ANGOLA
ANTIGUA AND BARBUDA
ARGENTINA
ARMENIA
AUSTRALIA
AUSTRIA
AZERBAIJAN
BAHAMAS
BAHRAIN
BANGLADESH
BARBADOS
BELARUS
BELGIUM
BELIZE
BENIN
BOLIVIA, PLURINATIONAL STATE OF
BOSNIA AND HERZEGOVINA
BOTSWANA
BRAZIL
BRUNEI DARUSSALAM
BULGARIA
BURKINA FASO
BURUNDI
CAMBODIA
CAMEROON
CANADA
CENTRAL AFRICAN REPUBLIC
CHAD
CHILE
CHINA
COLOMBIA
CONGO
COSTA RICA
CÔTE D'IVOIRE
CROATIA
CUBA
CYPRUS
CZECH REPUBLIC
DEMOCRATIC REPUBLIC OF THE CONGO
DENMARK
DJIBOUTI
DOMINICA
DOMINICAN REPUBLIC
ECUADOR
EGYPT
EL SALVADOR
ERITREA
ESTONIA
ESWATINI
ETHIOPIA
FIJI
FINLAND
FRANCE
GABON
GEORGIA
GERMANY
GHANA
GREECE
GRENADA
GUATEMALA
GUYANA
HAITI
HOLY SEE
HONDURAS
HUNGARY
ICELAND
INDIA
INDONESIA
IRAN, ISLAMIC REPUBLIC OF
IRAQ
IRELAND
ISRAEL
ITALY
JAMAICA
JAPAN
JORDAN
KAZAKHSTAN
KENYA
KOREA, REPUBLIC OF
KUWAIT
KYRGYZSTAN
LAO PEOPLE'S DEMOCRATIC REPUBLIC
LATVIA
LEBANON
LESOTHO
LIBERIA
LIBYA
LIECHTENSTEIN
LITHUANIA
LUXEMBOURG
MADAGASCAR
MALAWI
MALAYSIA
MALI
MALTA
MARSHALL ISLANDS
MAURITANIA
MAURITIUS
MEXICO
MONACO
MONGOLIA
MONTENEGRO
MOROCCO
MOZAMBIQUE
MYANMAR
NAMIBIA
NEPAL
NETHERLANDS
NEW ZEALAND
NICARAGUA
NIGER
NIGERIA
NORTH MACEDONIA
NORWAY
OMAN
PAKISTAN
PALAU
PANAMA
PAPUA NEW GUINEA
PARAGUAY
PERU
PHILIPPINES
POLAND
PORTUGAL
QATAR
REPUBLIC OF MOLDOVA
ROMANIA
RUSSIAN FEDERATION
RWANDA
SAINT LUCIA
SAINT VINCENT AND THE GRENADINES
SAN MARINO
SAUDI ARABIA
SENEGAL
SERBIA
SEYCHELLES
SIERRA LEONE
SINGAPORE
SLOVAKIA
SLOVENIA
SOUTH AFRICA
SPAIN
SRI LANKA
SUDAN
SWEDEN
SWITZERLAND
SYRIAN ARAB REPUBLIC
TAJIKISTAN
THAILAND
TOGO
TRINIDAD AND TOBAGO
TUNISIA
TURKEY
TURKMENISTAN
UGANDA
UKRAINE
UNITED ARAB EMIRATES
UNITED KINGDOM OF GREAT BRITAIN AND NORTHERN IRELAND
UNITED REPUBLIC OF TANZANIA
UNITED STATES OF AMERICA
URUGUAY
UZBEKISTAN
VANUATU
VENEZUELA, BOLIVARIAN REPUBLIC OF
VIET NAM
YEMEN
ZAMBIA
ZIMBABWE

The Agency's Statute was approved on 23 October 1956 by the Conference on the Statute of the IAEA held at United Nations Headquarters, New York; it entered into force on 29 July 1957. The Headquarters of the Agency are situated in Vienna. Its principal objective is "to accelerate and enlarge the contribution of atomic energy to peace, health and prosperity throughout the world".

IAEA-TECDOC-1889

FUEL MODELLING IN ACCIDENT CONDITIONS (FUMAC)

FINAL REPORT OF A COORDINATED RESEARCH PROJECT

INTERNATIONAL ATOMIC ENERGY AGENCY
VIENNA, 2019

For further information on this publication, please contact:

Nuclear Fuel Cycle and Materials Section
International Atomic Energy Agency
Vienna International Centre
PO Box 100
1400 Vienna, Austria
Email: Official.Mail@iaea.org

Printed by the IAEA in Austria
December 2019

IAEA Library Cataloguing in Publication Data

Names: International Atomic Energy Agency.
Title: Fuel modelling in accident conditions (FUMAC) / International Atomic Energy Agency.
Description: Vienna : International Atomic Energy Agency, 2019. | Series: IAEA TECDOC series, ISSN 1011–4289 ; no. 1889 | Includes bibliographical references.
Identifiers: IAEAL 19-01281 | ISBN 978–92–0–163919–6 (paperback : alk. paper) | ISBN 978–92–0–164019–2 (pdf)
Subjects: LCSH: Nuclear fuels. | Computer simulation. | Nuclear reactors — Safety measures. | Nuclear reactors — Computer programs.

FOREWORD

Improved understanding of fuel performance can lead to a reduction in operating margins, increased flexibility in fuel management and improved operating economics. To better understand fuel performance, the IAEA has addressed different aspects of fuel behaviour modelling in a series of coordinated research projects aimed at assessing fuel performance codes and supporting countries with code development and application needs (FUMEX series); building a database of well defined experiments suitable for code validation, in association with the OECD Nuclear Energy Agency (OECD/NEA); transferring a mature fuel modelling code to developing countries and supporting its adaptation to the requirements of particular reactors; providing guidance on applying that code to reactor operation and safety assessments; and providing guidelines for code quality assurance, code licensing and code application to fuel licensing.

The present publication describes the results of the coordinated research project on Fuel Modelling in Accident Conditions (FUMAC), initiated under the IAEA Action Plan on Nuclear Safety implemented after the accident at the Fukushima Daiichi nuclear power plant. The project, which ran from 2014 to 2018, followed previous projects on fuel modelling: D-COM 1982–1984, FUMEX 1993–1996, FUMEX-II 2002–2006 and FUMEX-III 2008–2012.

The project participants used data derived from accident simulation experiments, in particular data designed to investigate the fuel behaviour during design basis accident and design extension conditions, to carry out calculations on selected priority cases identified at the first research coordination meeting. These priority cases were designed to support the participants' individual priorities and were chosen as the best available to help determine which of the many models used in the codes most closely reflect reality. The cases were also used for verification and validation purposes, and for inter-code comparisons.

The IAEA would like to thank all the organizations and individuals who contributed to the FUMAC project, in particular the Technical Working Group on Fuel Performance and Technology for suggesting and supporting the project; the OECD/NEA Halden Reactor Project, the United States Nuclear Regulatory Commission, the Hungarian Academy of Sciences Centre for Energy Research (MTA EK) and the Karlsruhe Institute of Technology (KIT) for providing experimental data; the OECD/NEA for supporting the International Fuel Performance Experiments Database; and the project participants for performing the calculations and submitting summaries and meeting contributions. The IAEA would also like to thank all those who prepared the intermediate working material and the final report. The IAEA officer responsible for this publication was M. Veshchunov of the Division of Nuclear Fuel Cycle and Waste Technology.

CONTENTS

ANNEX II (CAN BE FOUND IN THE ATTACHED CD)

1. INTRODUCTION

BACKGROUND

Fuel modelling is a priority within the IAEA sub-programme “Nuclear Power Reactor Fuel Engineering”. Development and verification of computer codes are possible based on good experiments that requires very expensive and carefully executed in-reactor tests and post-irradiation studies. That is why international cooperation in this area is highly desirable. IAEA supports interested Member States in their efforts to enhance the capacities of their computer codes used for predicting fuel behaviour.

Since the 1980’s, a series of four Coordinated Research Projects (CRPs): D-COM (1982–1984) [1], FUMEX (1993–1996) [2], FUMEX-II (2002–2007) [3] and FUMEX-III (2008–2012) [4], were carried out that targeted nuclear fuel modelling under normal operating conditions. Those projects were highly appreciated (and valued) by Member States. The proposed CRP T12028 on Fuel Modelling in Accident Conditions (FUMAC) is to continue the series with the focus on fuel behaviour under Design Basis Accident (DBA) and Design Extension Conditions (DEC).

The current CRP on Fuel Modelling in Accident Conditions (FUMAC) was initiated because of the Fukushima accident under the IAEA Action Plan on Nuclear Safety, following a recommendation from the IAEA Technical Working Group on Fuel Performance and Technology (TWGFPT, in 2012) to launch a new fuel modelling CRP focusing on accident conditions. Preliminary ideas were brainstormed during the Technical Meeting on Fuel Behaviour and Modelling under Severe Transient and Loss of Coolant Accident (LOCA) conditions that took place in Japan in October 2011, agreed with NEA/OECD in 2012 and finalized through more detailed discussions during another Technical Meeting on Modelling of Water-Cooled Fuel Including Design Basis and Severe Accidents, in China in 2013 and finally at the International QUENCH Workshop in Germany the same year. The CRP FUMAC has been launched by the IAEA since 2014, with the end-date in 2018.

OBJECTIVES

The objectives of the CRP FUMAC are to:

— Analyse and better understand fuel behaviour in accident conditions, with a focus on LOCA (DBA), in line with the early phase of the Fukushima accident (DEC);
— Assemble quality results from accident simulation experiments, and disseminate experience from Member States;
— Identify best practices in the application of physical models and computer codes used in different Member States for modelling fuel in accident conditions, and enhance the predictive capacities of these models and codes.

SCOPE

The CRP FUMAC was planned with the well proven organizational approach used in FUMEX-III [4], which presumed cross-comparisons of computer codes used in different Member States. Selected simulations from experimental results, provided by the CRP participants, will be integrated into the International Fuel Performance Experiments (IFPE) Database (developed in cooperation and coordination between OECD/NEA, IAEA and IFE/OECD/Halden Reactor Project) and used for codes verification. The codes involved ranged from fuel performance codes (DIONISIO, FRAPTRAN, FTPAC, RAPTA, SFPR, TRANSURANUS) to system or severe accident codes (ATHLET-CD, MELCOR, SOCRAT) as well as multi-dimensional fuel performance codes (ALCYONE, BISON).

The fuel behaviour during LOCAs was extensively studied during the last decades. Recent LOCA tests, performed in Halden, Norway, and Studsvik, Sweden, revived the interest in the fuel relocation and dispersion phenomena. Indeed, test results suggest that high burnup fuel pellets might pulverize into very fine fragments, with a higher potential for axial relocation and subsequent dispersal than observed for low to medium burnup fuel in early tests. This research area is also being addressed by the Working Group on Fuel Safety (WGFS) of the Nuclear Energy Agency (NEA), under the Committee on the Safety of Nuclear Installations (CSNI), and is identified as one of key issues in the IAEA coordinated research project FUMAC.

The preparatory Consultancy Meeting was held in March 2014 in Vienna, the outcomes of the consultancy group along with the survey of potential participants by means of a questionnaire were presented and discussed to structure and define the scope of the CRP. A preliminary list of available experiments for the benchmark were proposed for consideration

The first Research Coordination Meeting (RCM) of the CRP was held from November 11–14, 2014 in KIT (Karlsruhe, Germany) in conjunction with the 20th QUENCH Workshop. 27 participants from 21 organizations representing 18 Member States attended the meeting.

The 2nd Research Coordination Meeting took place in Vienna International Centre from May 30 to June 3, 2016. 27 participants from 21 organizations represented 18 Member States attended the Meeting.

The 3rd Research Coordination Meeting took place in Vienna International Centre on 13–17 November 2017. 24 participants from 22 organizations and 3 observers from 2 organizations represented 18 Member States attended the Meeting.

The final Consultancy Meeting to Finalize the Final Report of the CRP on Fuel Modelling in Accident Conditions was held on 21–23 February 2018 in Vienna.

STRUCTURE

This publication summarizes the finding and conclusions of the CRP FUMAC within a work plan jointly agreed on by twenty-six organizations from 18 Member States. A list of the participating organizations submitted Individual Contributions to this TECDOC (as Annex II) and their used codes (presented in more details in Section 3) are given in Table 1.

A list of chief scientific investigators who represented these organizations within the CRP is given at the end of this report. Well checked experimental datasets from separate-effect tests: clad ballooning tests (PUZRY from MTA EK); out-of-pile single rod LOCA tests (Studsvik 192, 198); in-reactor LOCA tests with single rods (IFA 650.9–11 from the Halden Project); KIT out-of-pile bundle LOCA test (QUENCH-L1) and bundle under severe accident test (CORA 15) were chosen for benchmark exercises, as outlined in Table 2 and presented in more details in Section 2.

Discussions related to the thermal hydraulic (T/H) boundary conditions (BC), new test cases were carried out during the CRP. It was agreed to apply a common BC to IFA650.9, 10 and 11 to be calculated by the integral severe accident code SOCRAT (from IBRAE, Russian Federation). In addition, the IFA-650.2 test with new PIE data on hydrogen uptake was analysed in view of the preparation of new licensing criteria in various Member States.

It has been also proposed that the available severe accident codes would be compared with experimental data for CORA 15 test. The IFA-650 cases and the QUENCH-LOCA1 test were to provide a common basis (the benchmark cases) for the different types of codes involved in the CRP.

TABLE 1. PARTICIPANTS OF THE CRP FUMAC

Country	Organization	Individual Contribution	Code	Experiment
Argentina	CNEA	Annex II	DIONISIO-2.0	–
Belgium	Tractebel	Annex II	FRAPTRAN-TE-1.5	–
Brazil	IPEN-CNEN	Annex II	FRAPTRAN	–
Bulgaria	INRNE	Annex II	TRANSURANUS	–
China	CIAE	Annex II	FTPAC	–
China	CNPRI	Annex II	FRAPTRAN-1.5	–
Germany	JRC	Annex II	TRANSURANUS	–
Germany	KIT	Data provided (Sections 2.4, 2.5) Annex II	–	QUENCH-LOCA1, CORA-15
Finland	VTT	Annex II	FRAPTRAN-1.5, 2.0	–
France	CEA	Annex II	ALCYONE-1D	–
Hungary	MTA EK	Data provided (Section 2.1) Annex II	FRAPTRAN-2.0	PUZRY
Italy	POLIMI	Annex II	Modelling	–
Japan	NSR	–	–	–
Republic of Korea	KAERI	Annex II	FRAPTRAN-1.5/ S-FRAPTRAN	–
Norway	IFE	Data provided (Section 2.2)	–	IFA-650.9/10/11 and 650.2
Russian Federation	Bochvar Institute	Annex II	RAPTA-5.2	
Russian Federation	IBRAE	Annex II	SOCRAT, SFPR	Boundary conditions for IFA-650.9/10/11
Spain	CIEMAT	Annex II	FRAPTRAN-1.5	–
Sweden	Swedish Radiation Safety Authority (SSA)	Annex II	FRAPTRAN-QT-1.5	–
Ukraine	Energorisk	–	MELCOR	–
Ukraine	SSTC NRS	Annex II	TRANSURANUS	–
USA	Battelle INL	Annex II	BISON-2D	–
USA	Westinghouse	Annex II	MAAP	–
USA	US NRC	Data provided (Section 2.3)	–	Studsvik 192, 198
Germany	GRS (Active observer)	Annex II	ATHLET-CD	–
International	OECD/NEA		Observer	–

TABLE 2. TEST MATRIX FOR BENCHMARK EXERCISES

IFA-650.9	IFA-650.10	IFA-650.11	Studsvik 192, 198	MTA-EK	QUENCH LOCA1	CORA 15	Uncertainty analysis
With UO_2 dispersal	PWR	VVER	Out-of-pile single fuel rod	Fuel rod segments	Out-of-pile bundle	Out-of-pile bundle	DAKOTA, URANIE, etc.

Many of the participants used the CRP to develop and provide (or extend) a validation database for their codes. Some were using commercial codes and used the CRP to help develop an understanding of their codes and to train young professionals. The wide range of participants and their needs contributed to valuable informative discussions and widespread cooperation between the participants. Comparison of simulation results were carried within the CRP, as presented in Section 4.

Finally, the participants also agreed to extend the analysis by means of an uncertainty and sensitivity analysis, as presented in Section 5 for IFA-650.10 test. Uncertainty analysis and its detailed specification prepared by Tractebel is summarized in Annex I. Final reports submitted by the participants are compiled as Annex II.

2. DESCRIPTION OF CASES

2.1. SEPARATE EFFECT TESTS (MTA-EK BURST TESTS)

The separate effect ballooning and burst tests provided to FUMAC were performed at the predecessor of MTA EK (KFKI AEKI).

The experiments proposed for benchmarking were ballooning and burst tests using unirradiated, unoxidized Zircaloy-4 tubing. The tubing was 50 mm long with inner/outer diameters of 9.3/10.75 mm. The specimens were heated in an induction furnace and held at constant temperature while the inner pressure was increased at a constant rate until burst occurred.

A detailed description of these tests and the test apparatus could be found in Refs [5, 6].

Six cases were selected as closest to real large-break LOCA scenarios:

— PUZRY-26 (700 °C, 0.119 bar/s);
— PUZRY-30 (800 °C, 0.263 bar/s);
— PUZRY-18 (900 °C, 0.115 bar/s);
— PUZRY-8 (1000 °C, 0.076 bar/s);
— PUZRY-10 (1100 °C, 0.071 bar/s);
— PUZRY-12 (1200 °C, 0.072 bar/s).

The results of these tests are illustrated in Figs 1 and 2.

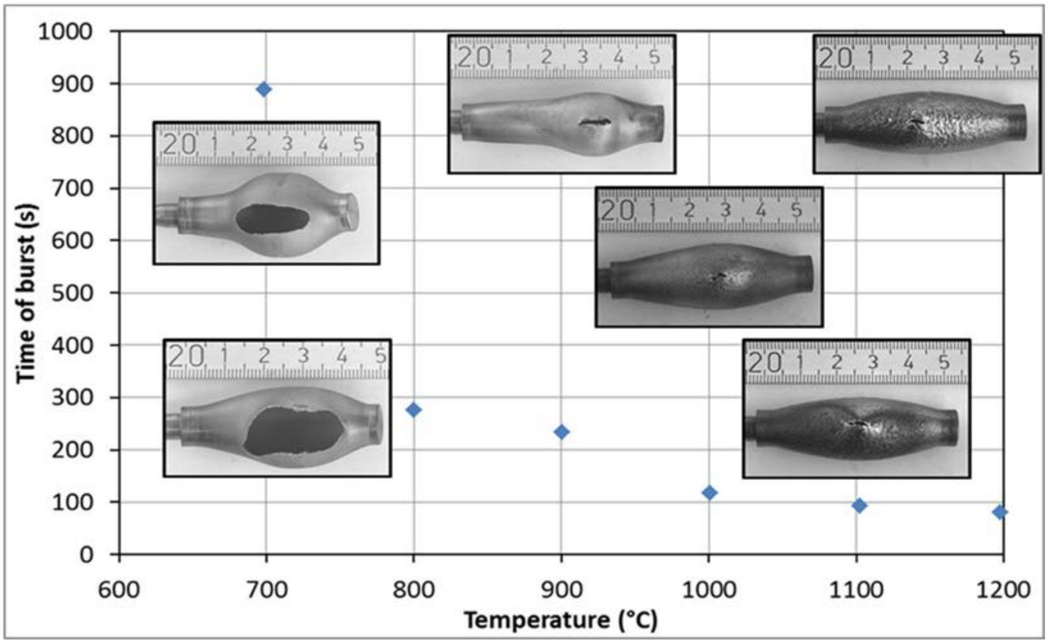

FIG. 1. Time of burst vs. temperature for the 6 PUZRY tests.

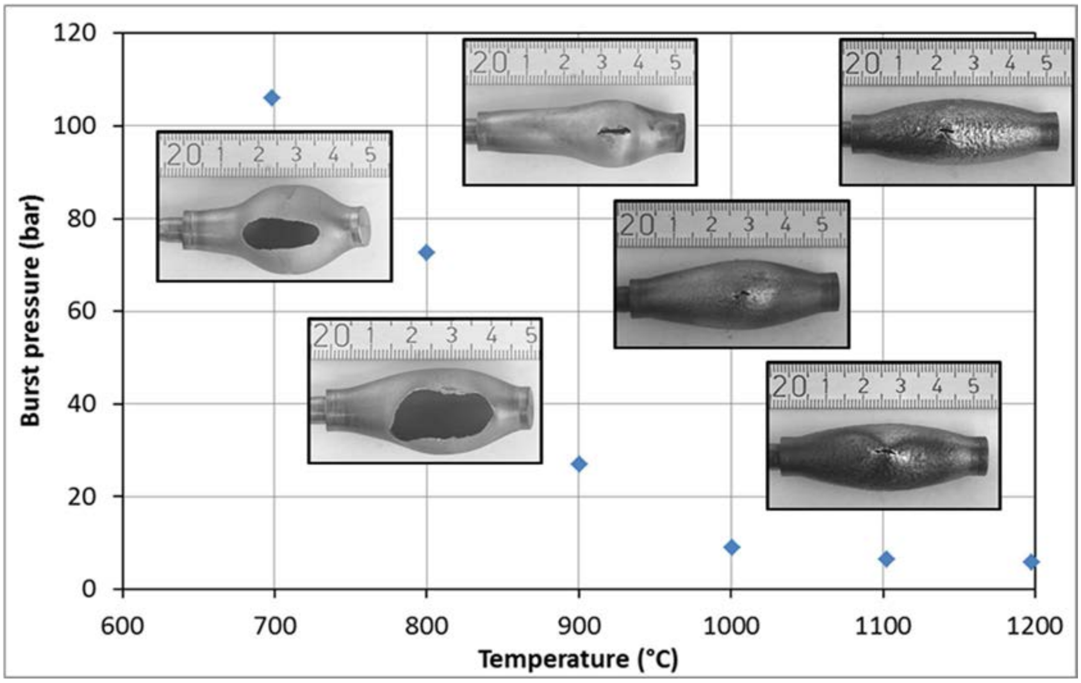

FIG. 2. Burst pressure vs. temperature for the 6 PUZRY tests.

2.2. HALDEN LOCA TESTS (IFA-650.2, 9, 10 AND 11)

The Halden Reactor test series IFA-650 was part of the joint international programme of the Halden Reactor Project. These tests addressed the LOCA performance of high burnup fuel irradiated in commercial nuclear power plants. The three experiments selected for FUMAC were:

— IFA-650.9 (PWR fuel): considerable ballooning, fuel fragmentation and relocation, when subjected to LOCA were indicated;
— IFA-650.10 (PWR fuel): moderate ballooning, fuel fragmentation and dispersal were indicated;
— IFA-650.11 (VVER fuel): little ballooning and fuel fragmentation were indicated.

IFA-650.2, a commissioning test with fresh fuel, was also evaluated by some participants and discussed during the research coordination meetings. Considering the complexity of IFA-650.9 (very high burnup, complicated T/H conditions, an axial relocation model is also required), participants agreed to use IFA-650.10 as the case for the uncertainty and sensitivity analysis (UASA), see Annex I.

Results obtained from various codes, as reported from participants, were in general having the same trends for both the IFA-650.10 and 11 tests.

2.2.1. Test design end execution

A schematic drawing of the test rig with its instrumentation is shown in Fig. 3. Most of the energy to drive the LOCA heat-up came from a low level of fission power in the fuel rod. An electrical heater surrounding the rod, served as a flow path divider, was installed to simulate some of the energies coming from neighbouring rods.

The instrumentation consisted of three cladding surface thermocouples (TCC), a cladding extensometer (EC), a fuel pressure sensor (PF), three vanadium neutron flux detectors, two heater surface thermocouples (TCH) and thermocouples at the inlet (TI) and outlet (TO) of the rig. The temperature of the heater was measured by two embedded thermocouples. The axial power distribution was determined with three self-powered vanadium neutron detectors (SPND).

A schematic sketch of the loop for the LOCA experiments in the Halden reactor is shown in Fig. 4. Initially, forced circulation was maintained through the in-core part (pressure flask, designated 'IFA-650' in Fig. 4) and the entire loop indicated by the flow path was marked as blue. Prior to blow-down, the pressure flask was isolated from the rest of the loop where circulation was maintained and marked as red, while the fuel rod was cooled by natural circulation in the pressure flask. To start the LOCA, valves in the green line to the blow-down tank were opened.

The blow-down tank had a volume of 100 L and initially contained 15–20 L of water. The water was cooled, and the steam from the in-core flask was condensed. At the end of blow-down, the pressure in the system was typically 2–3 bar due to non-condensable gases.

The LOCA test was performed at a rod power of 10–30 W/cm depending on target peak clad temperature. After a few minutes at maximum temperature, the experiment was terminated by switching off the electrical heating and scramming the reactor which caused the fission heat generation in the fuel rod to cease. The test rods were cooled down relatively slowly with the reactor to avoid disturbances, e.g. vibrations, which might possibly cause an unintentional fuel relocation.

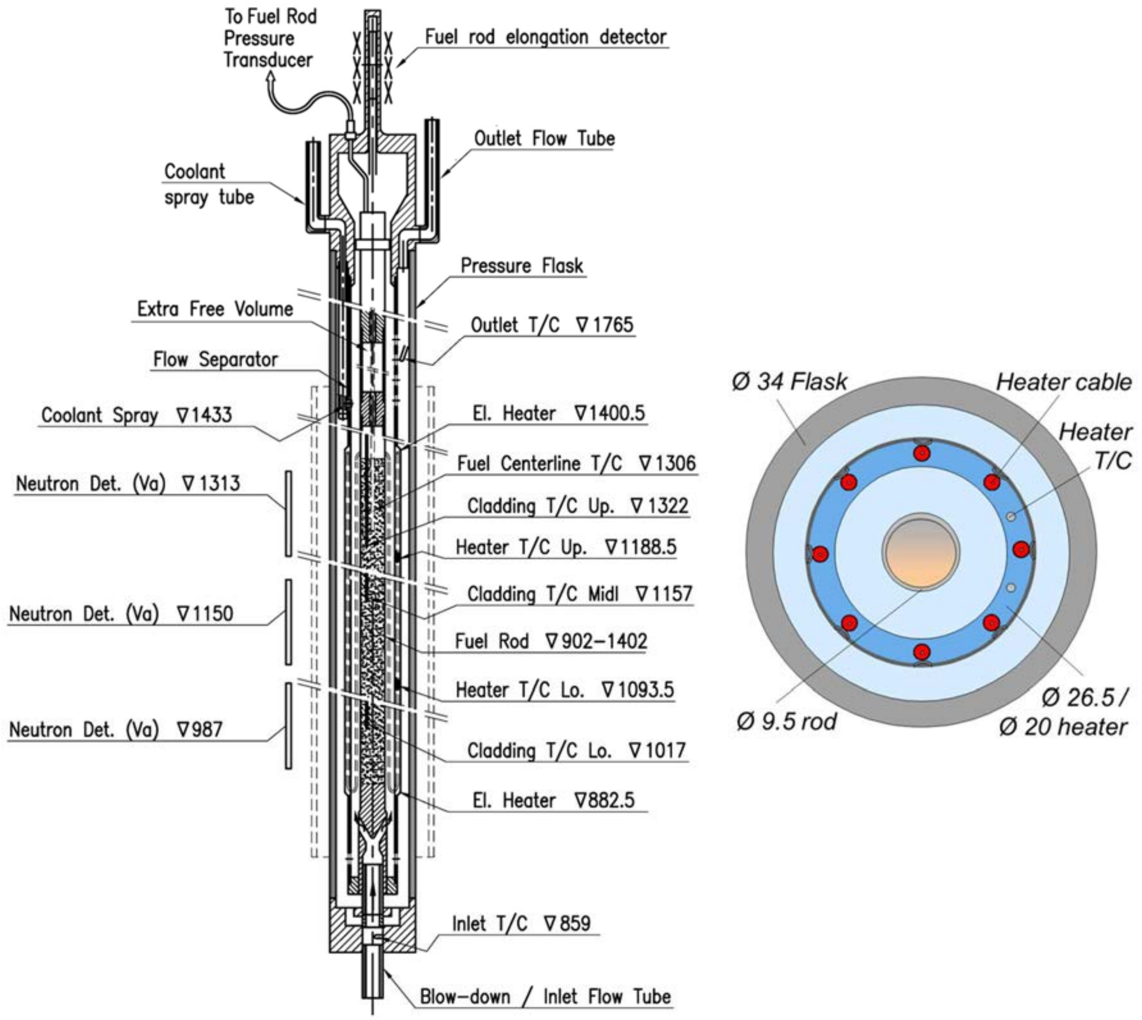

FIG. 3. Test rig used in IFA-650 tests (left) and a schematic cross section of the rig (right).

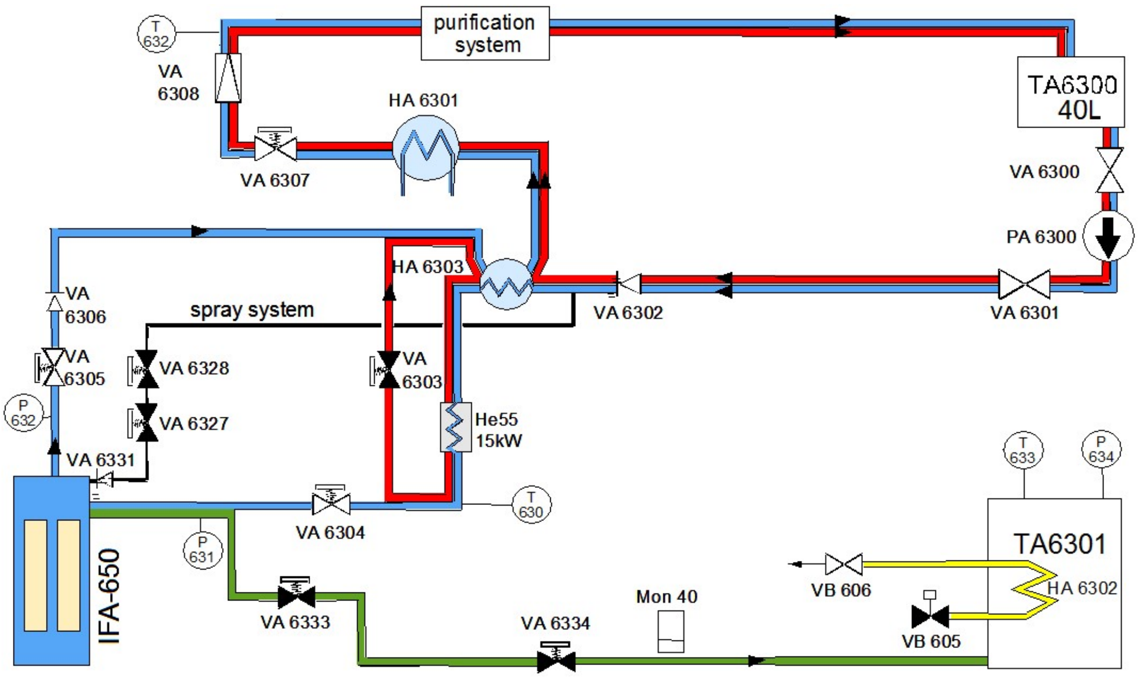

FIG. 4. Simplified drawing of the loop used for the IFA-650 experiments.

2.2.2. Data accuracy and data acquisition

Before test execution, the reactor was operated for 7–8 hours at about 15 MW to accumulate fresh fission products for the gamma scanning after unloading. The power was calibrated during this period. The calibration was to establish the relation between average neutron detector signal and total power.

The neutron detectors were, outside the pressure flask, in the moderator and would not be affected by temperature change during a transient. The relation between neutron flux and power found during calibration was therefore also valid for the transient. The power uncertainty was approximately ±5 % for the total power or the average linear heat rating. The uncertainty of the local power, which was derived from the neutron flux distribution, was slightly higher. There were additional uncertainties coming from the axial flux distribution that was based on: measurements at three points, the nature of the SPNDs that measured the average flux over a 10 cm length of their emitters, and the assumption that the fissile content was constant over the length of the test rod. The thermocouples for measuring the cladding surface temperature were standard industry type K-type thermocouple (Nickel-Chromium / Nickel-Alumel). The accuracy was ±2.2°C or ±0.75 %, whichever was greater. The thermocouple diameter at the tip was 0.5 mm. It was attached in contact with the cladding. The measured temperature was practically the same as the cladding surface temperature according to Quickfield temperature calculations.

Data logging and permanent storage were done with a frequency of two measurements per second.

2.2.3. Description of the tests

IFA-650.2 (fresh fuel)

The LOCA loop system was checked out with two trial runs using fresh fuel. The measurements from these runs could be used to calibrate codes to the geometry and dynamics of the Halden LOCA system before analyzing the outcome of tests with pre-irradiated fuels.

The main rod data of trial run IFA-650.2, which was used by some participants, are summarized in Table 3.

TABLE 3. MAIN DESIGN DATA OF IFA-650.2

Item	650.2
Active length (mm)	500
Burnup, (MWd/kgU)	0 (fresh)
Enrichment (%)	2
Pellet Diameter (mm)	8.29
Diam. Clearance (mm)	0.070
Pellet length (mm)	8
Dishing (both ends) (mm)	0.20
Land width (mm)	1.15
Cladding material	Zry-4 low tin
Cladding outer diam., (mm)	9.50
Cladding thickness (mm)	0.57
Fill gas/ rt pressure (bar)	Helium / 40
Plenum volume (cm^3)	15

The rod power was set to 23 W/cm and kept constant during the test. When the target peak cladding temperature of 1100°C was reached, the rod ballooned and failed as expected. The main measurements are shown in Figs 5 and 6.

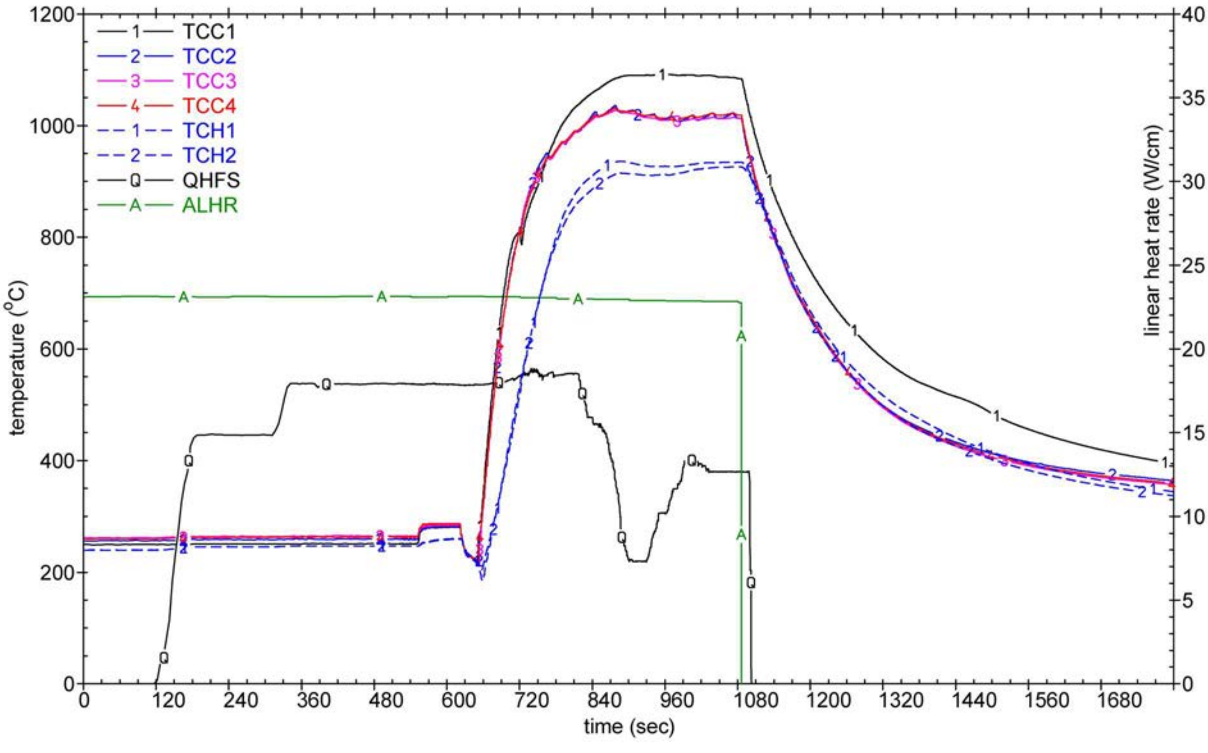

FIG. 5. Temperature in cladding (TCC1-4) and heater (TCH1,2).

The test run showed that the target temperature, which mainly depended on the rod power, could be achieved with a sufficient accuracy. The volume change due to ballooning was clearly reflected in the rod pressure data. It also manifested itself in the cladding elongation data (see Fig. 6).

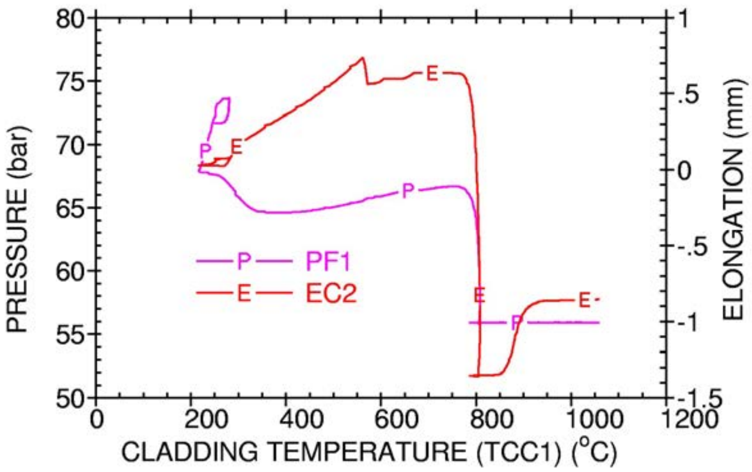

FIG. 6. Rod pressure and cladding elongation response to transient.

The test rod was equipped with three cladding thermocouples (TCC 2, 3, 4) attached 10 cm below the upper end of the fuel stack, 120 degrees apart from each other, to check the circumferential temperature distribution. Fig. 7 shows the respective temperature deviations from their average. The deviations were approximately ±3 K until the point of ballooning and rupture was reached at about 800°C. A uniform circumferential temperature distribution was intended in the Halden reactor LOCA tests to maximize ballooning.

In other tests selected for FUMAC, only two thermocouples were attached at the same axial elevation. A similarly uniform circumferential temperature distribution was observed.

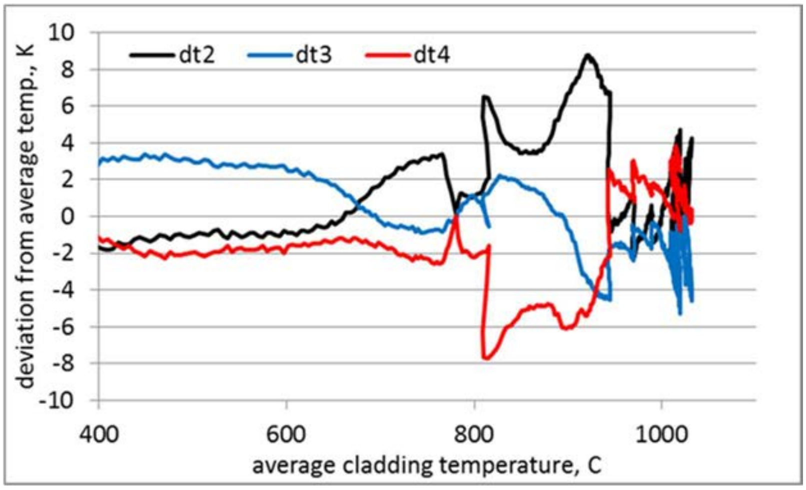

FIG. 7. Circumferential variation of cladding temperature at upper end.

Post-test examinations, IFA-650.2

The gamma scan (the left part of Fig. 8) indicated a ballooning and some fuel protruding into the opening. The scanning resolution was 5 mm vertically and 1 mm horizontally.

Visual inspection (the right part of Fig. 8) revealed a similar appearance. The opening was about 35 mm long and 20 mm wide. The pellets, which did not exceed 10 kW/m during their short irradiation, appeared to be broken into two equal pieces.

The rod developed a bow of about 7 mm, bending in the direction of the burst opening. Fig. 9 shows the cladding diameter measured at three orientations. The expansion increased gradually from both ends towards the burst region. The effects of secondary hydriding and oxide thickness, around the burst areas, are indicated in Fig. 10.

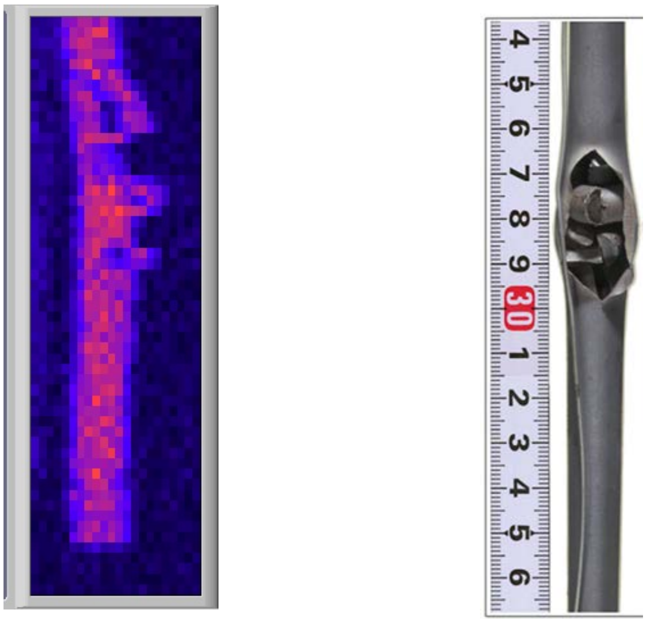

FIG. 8. Gamma scan and visual appearance, IFA-650.2

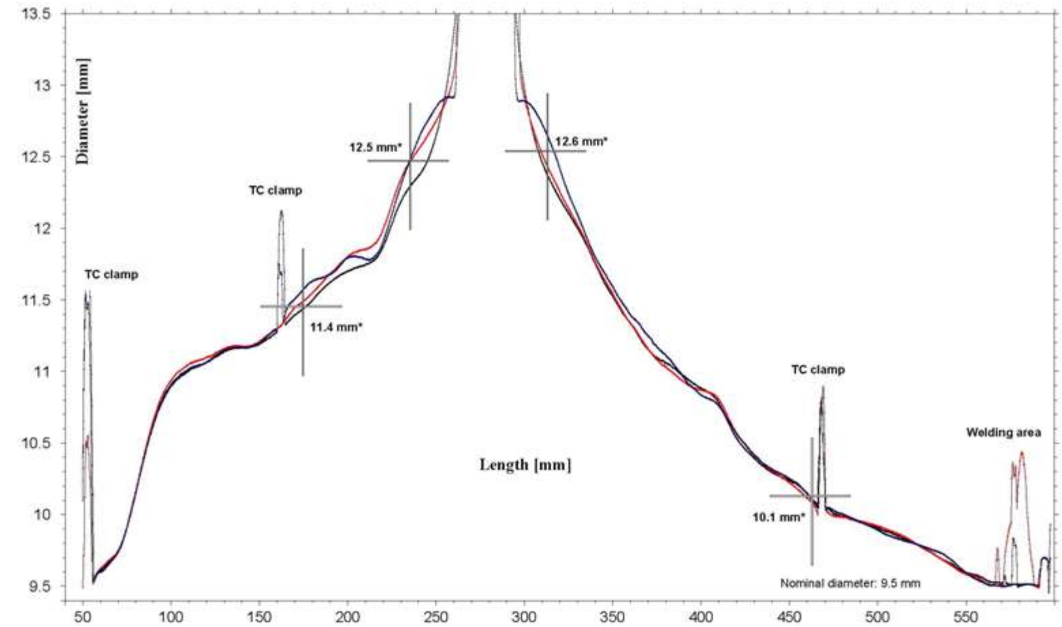

FIG. 9. Diameter measured at 0, 45 and 135 degrees orientation, IFA-650.2.

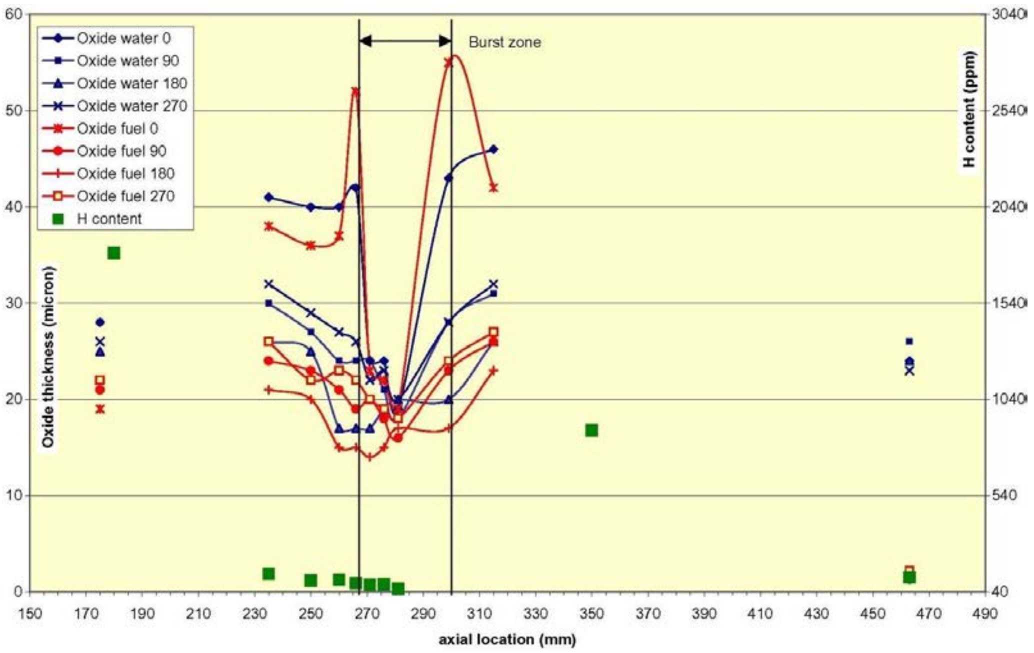

FIG. 10. Oxygen and hydrogen distribution after LOCA, IFA-650.2.

IFA-650.9 (PWR)

The fuel was provided by Framatome ANP and had been irradiated in the Swiss NPP Gösgen to 89.9 MWd/kgU. The rod power was set to 25 kW/m to achieve a target peak cladding temperature of 1100°C. Due to fuel relocation, the temperature measured with the lower cladding thermocouple approached 1200°C, and the test was terminated to avoid even higher temperatures. Cladding failure occurred at about 800°C, which was 130 s after the start of blow-down.

A special feature of this experiment is the strong fuel fragmentation, relocation and dispersal.

Rod characteristics and pre-test irradiation data

TABLE 4. ROD CHARACTERISTICS FOR IFA-650.9

Items	Properties	Value
Fuel - as fabricated and irradiated	Initial enrichment (wt%U^{235})	3.5
	UO_2 density (g/cm^3)	10.43
	Pellet diameter (mm)	9.131
	Dishing volume (total of both sides) (mm^3)	16
	Burnup (MWd/kgU)	89.9
Cladding - as fabricated and irradiated	Type	DX Zr2.5Nb (duplex)
	Outer diameter (mm)	10.75
	Thickness (mm)	0.725
	Outer liner (mm)	0.100
	Oxide thickness, irradiated, mean (µm)	7
	Hydrogen content, irradiated, ppm	30
Free volume - as fabricated	Fill gas / pressure (bar)	95% Ar + 5% He / 40
	Free volume (cm^3)	19

The pre-test irradiation history for the tested fuel rod in the PWR unit is shown in Fig. 11.

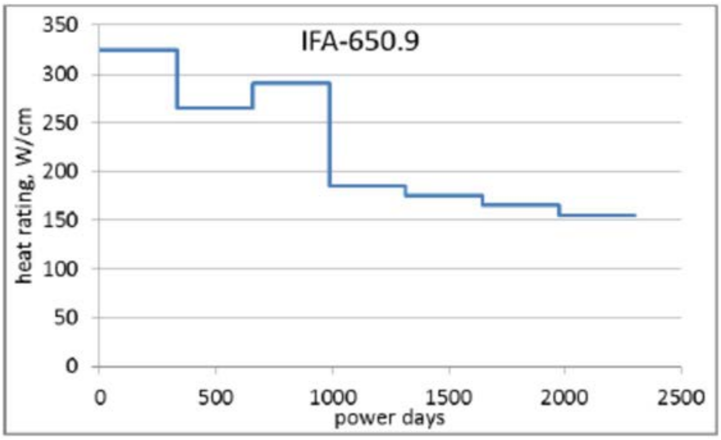

day	W/cm
0	325
330	325
330	265
659	265
659	290
988	290
988	185
1317	185
1317	175
1646	175
1646	165
1976	165
1976	155

FIG. 11. Pre-irradiation history for the IFA-650.9 test fuel rod.

In-core measurements

The transient was executed according to the general procedure described in Section 2.2.1 and terminated by a reactor scram and gradual cool-down without reflood. Rod burst occurred 130 s after the start of blow-down.

The principal measurements, i.e., cladding and heater temperatures, rod pressure and cladding elongation, are shown in Figs 12 and 13, respectively. Cladding thermocouples were attached 100 mm above the lower end (TCC1) and 80 mm below the upper end (TCC2, TCC3).

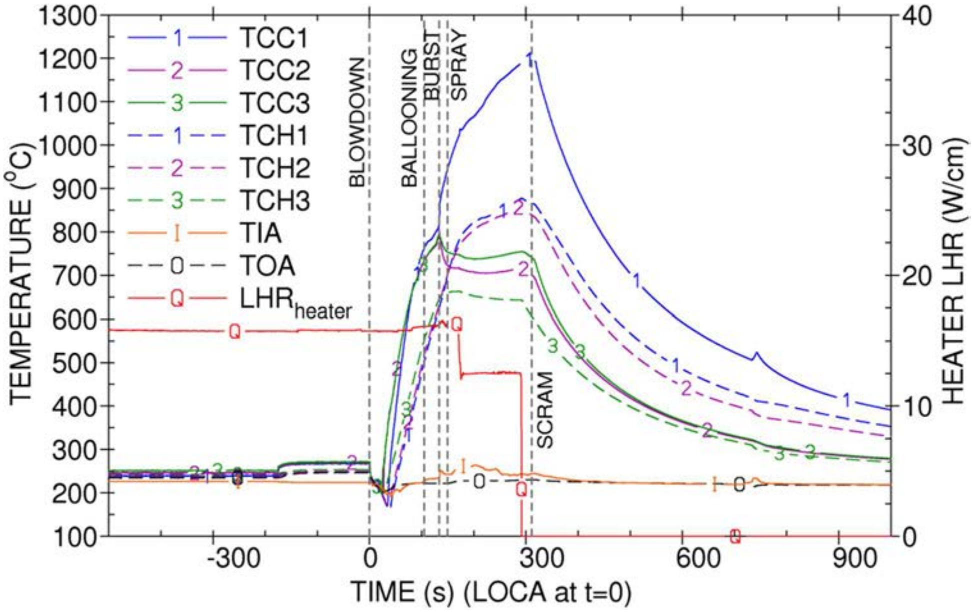

FIG. 12. Cladding and heater temperatures, IFA-650.9.

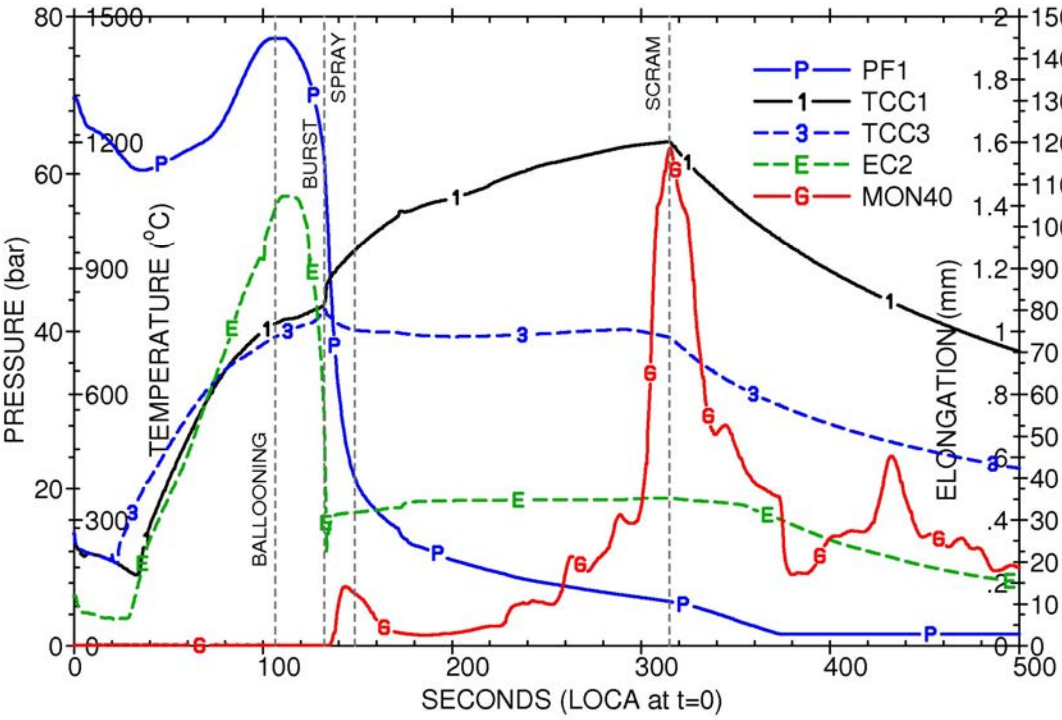

FIG. 13. Rod pressure and cladding elongation, IFA-650.9.

The temperatures at the upper end, as measured by TCC3 (similar to TTC2), started to increase at about the same time and changed with the same rate as measured by TCC1 at the lower end. At the time of ballooning and burst, the temperature difference between the lower and upper end was about 35°C. However, when burst occurred, the cladding temperatures at the two ends started to take completely different courses which was attributed to fuel relocation.

Cladding elongation (EC2) and rod pressure (PF1) showed a strong response to the rod burst about 130 s after the start of blow-down, see Fig. 13. The rod pressure did not drop instantaneously, but required about 200 s to reach equilibrium with the loop pressure.

The gamma monitor (MON40) on the blow-down line registered the failure as shown in Fig. 13. The maximum activity of about 120 mSv/h was reached when the experiment was terminated with a reactor scram.

Post-irradiation examination results

The gamma scan taken after the LOCA test (Fig. 14) showed that the rod was considerably ballooned at the lower end. A ‘hot spot’ at half height is associated with a secondary ballooning.

At the upper end, a plug of two pellets remained while 12.5 cm below contained no fuel. The balloon, which expanded to the heater limit, was filled with relocated fuel. Fuel had been ejected and was found at the bottom of the pressure flask and in the blow-down line.

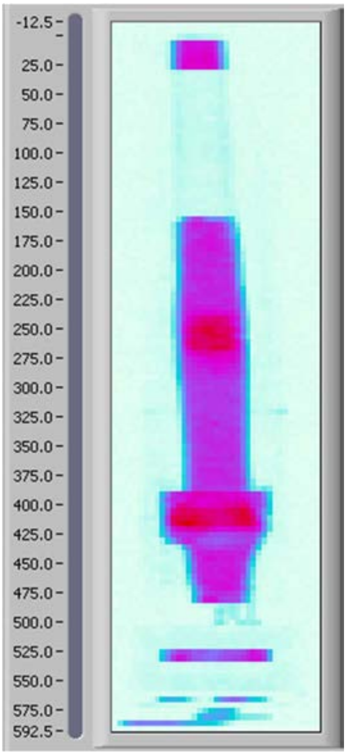

FIG. 14. Gamma scan IFA-650.9.

Figure 15 shows the profile of the rod diameter determined by visual inspection. The expansion of the cladding increased gradually until reached about half-height where a secondary ballooning (no failure) could be seen. Ballooning was indicated continuously to the heater wall of the lower half.

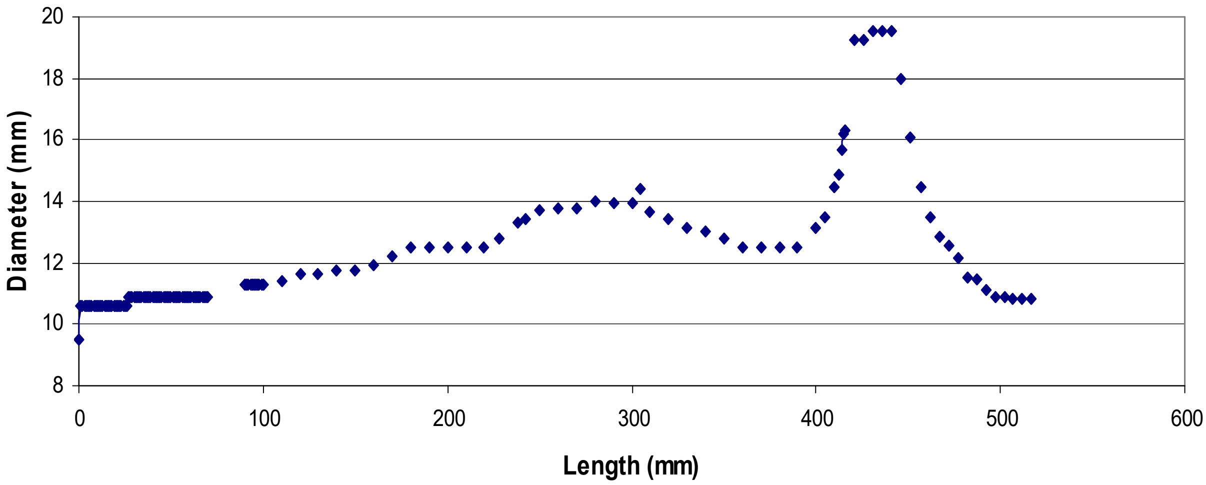

FIG. 15. Diameter profile of IFA-650.9.

The neutron radiography picture is shown in Fig. 16. The rod was broken into two pieces at the location of the primary balloon. Due to transportation and handling after gamma scanning, fuel fragments moved back to what was used to be the upper part where gamma scanning showed a gap in the fuel stack. Where the fuel stayed in place, the dishing had disappeared except for a few pellets at the upper and lower ends. In general, the fuel appeared to be extremely fragmented and could easily be relocated.

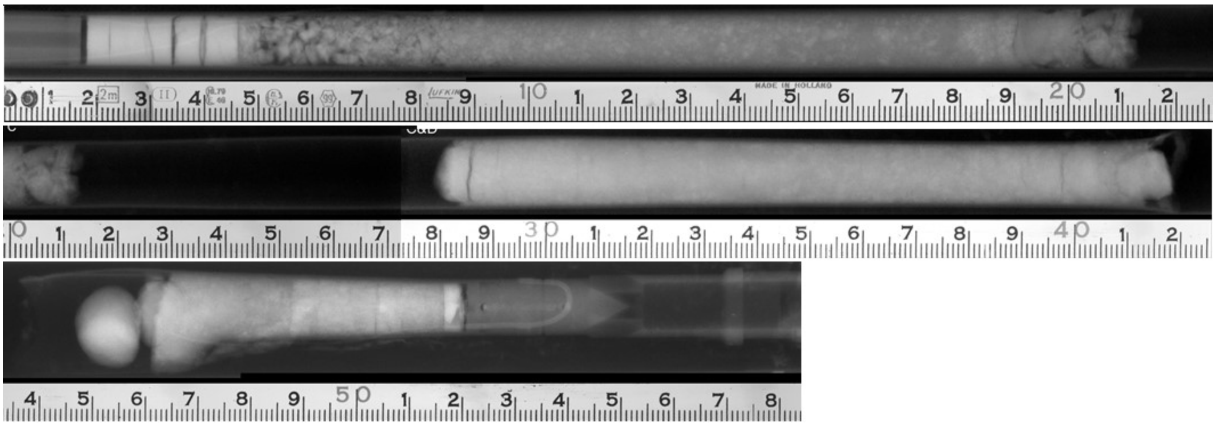

FIG. 16. Neutron radiography, IFA-650.9.

The burst opening (see Fig. 17) was about 40 mm long and 7 mm wide (maximum). Two fuel ceramography pictures are shown in Fig. 18; fine and often oblong fragments have formed.

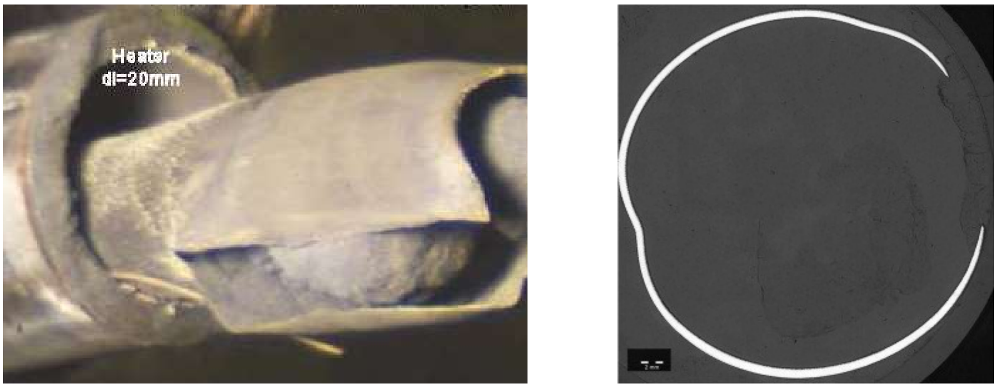

FIG. 17. Burst opening, IFA-650.9.

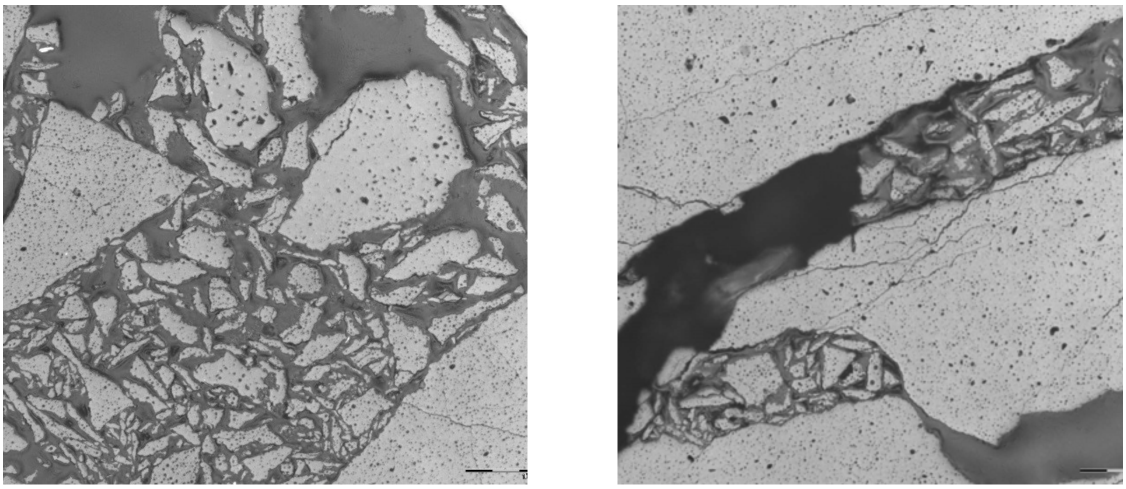

FIG. 18. Ceramography showing fuel fragmentation, IFA-650.9.

IFA-650.10 (PWR)

The fuel was supplied by EDF/FRAMATOME and had been irradiated in the French Graveline 5 PWR to 61 MWd/kgU. The target peak cladding temperature (PCT) was 850°C.

Rod burst was detected 249 s after the start of blow-down. Minor fuel relocation was confirmed by gamma scanning and PIE.

Rod characteristics and pre-test irradiation data

TABLE 5. ROD CHARACTERISTICS FOR IFA-650.10

Items	Properties	Value
Fuel - as fabricated and irradiated	Initial enrichment (wt%U^{235})	4.49
	UO_2 density (g/cm^3)	95.32
	Pellet diameter (mm)	8.21
	Dishing volume (total of both sides) (mm^3)	n/a (dished)
	Burnup (MWd/kgU)	61
Cladding - as fabricated and irradiated	Type	Zry-4
	Outer diameter (mm)	9.50
	Thickness (mm)	0.57
	Oxide thickness, irradiated, mean (µm)	20–30
	Hydrogen content, irradiated, ppm	150–220
Free volume - as fabricated	Fill gas / pressure (bar)	95% Ar + 5% He / 40
	Free volume (cm^3)	17

The pre-test irradiation history for the tested fuel rod in the PWR unit is shown in Fig. 19.

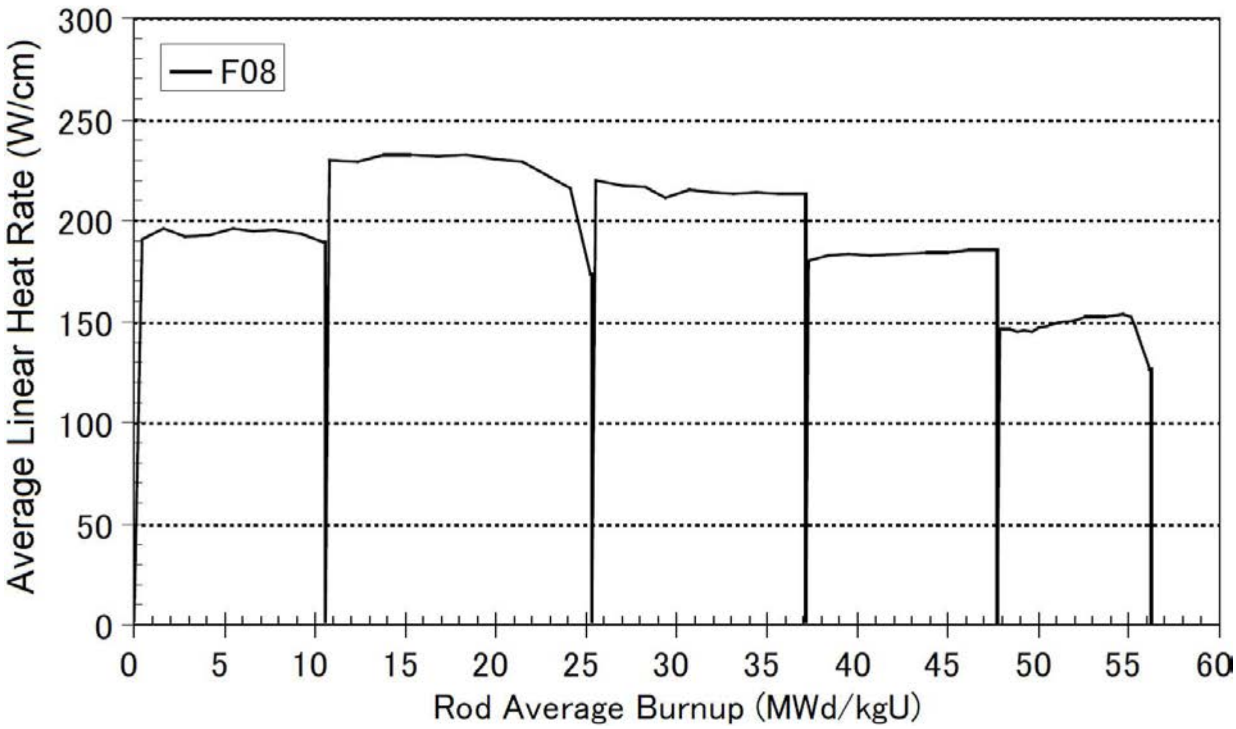

FIG. 19. Pre-irradiation history for the IFA-650.10 test fuel rod.

In-core measurements

The transient was executed according to the general procedure described in Section 2.2.1 and terminated by a reactor scram and gradual cool-down without reflood.

The principal measurements, i.e., cladding and heater temperatures, rod pressure and cladding elongation, are shown in Figs 20 and 21, respectively.

After the burst, the cladding and heater temperatures continued to increase at similar rates. Extensive fuel relocation was not observed from this experiment. PIE revealed that the ballooning and the burst opening were moderate.

Burst was detected 249 s after the start of blow-down. The rod pressure dropped instantaneously.

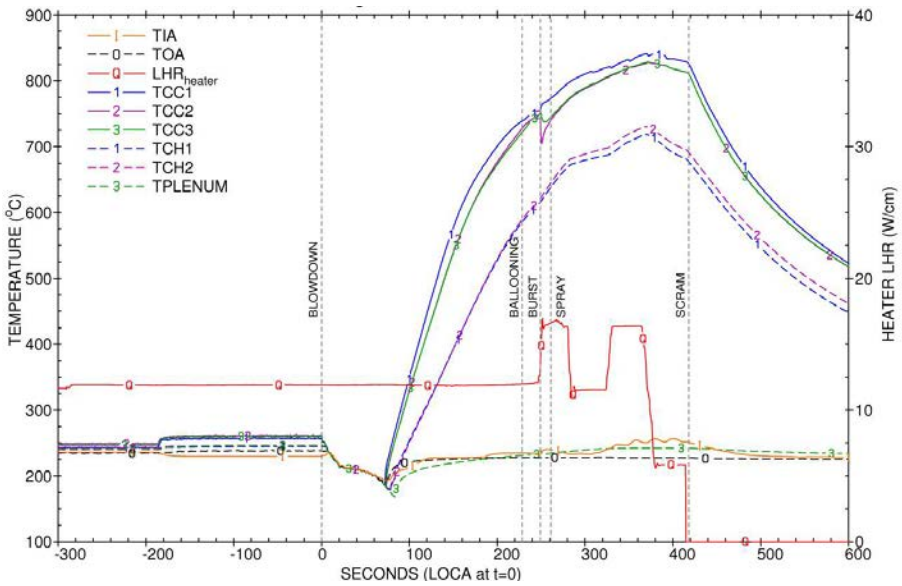

FIG. 20. Cladding and heater temperatures, IFA-650.10.

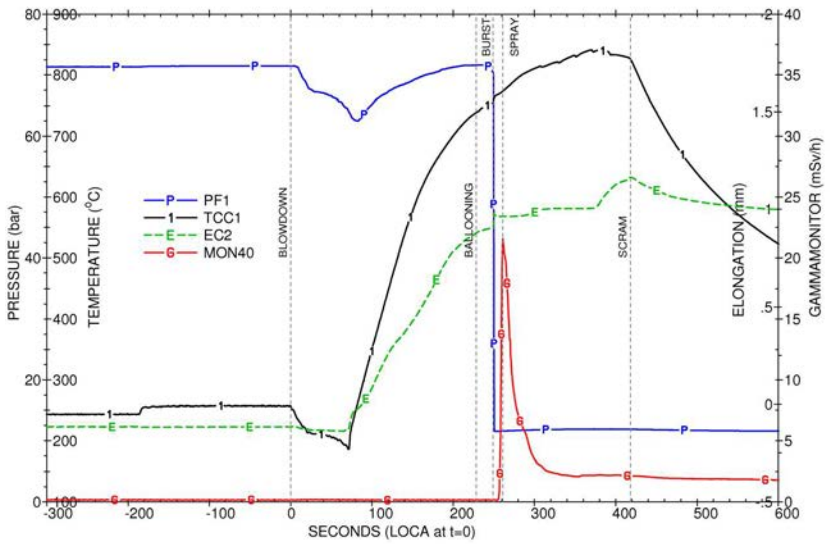

FIG. 21. Rod pressure and cladding elongation, IFA-650.10.

The gamma monitor (MON 40) installed on the blow-down line registered the failure as shown in Fig. 21. The maximum equivalent dose rate of 22 mSv/h was reached shortly after the burst and decayed rapidly.

Post irradiation examination

The gamma scan taken after the LOCA test is shown in Fig. 22. The rod was slightly bowed, with ballooning and a burst opening indicated at an elevation of 200. There was no indication of fuel relocation in the fuel stack itself, but some fuel had fallen to the bottom of the pressure flask (at elevation 500). The faint gamma signal at elevation 525 and below (the horizontal lines) stemmed from fuel in the blow-down line.

The neutron radiography picture is shown in Fig. 23. The burst location was covered by some materials. The dishing and pellet-pellet interfaces were preserved and not smeared out as in IFA-650.9. Fuel cracks were visible, but not strongly correlated with the burst location.

Fig. 24 indicated the diameter profile determined from visual inspection and neutron radiography. The cladding expansion increased from the both ends towards the ballooning location.

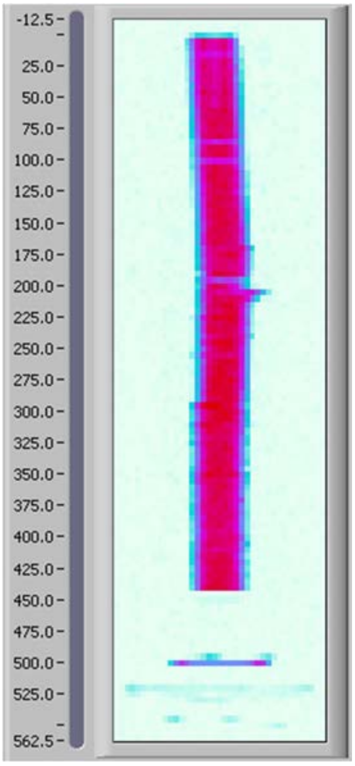

FIG. 22. Gamma scan IFA-650.10.

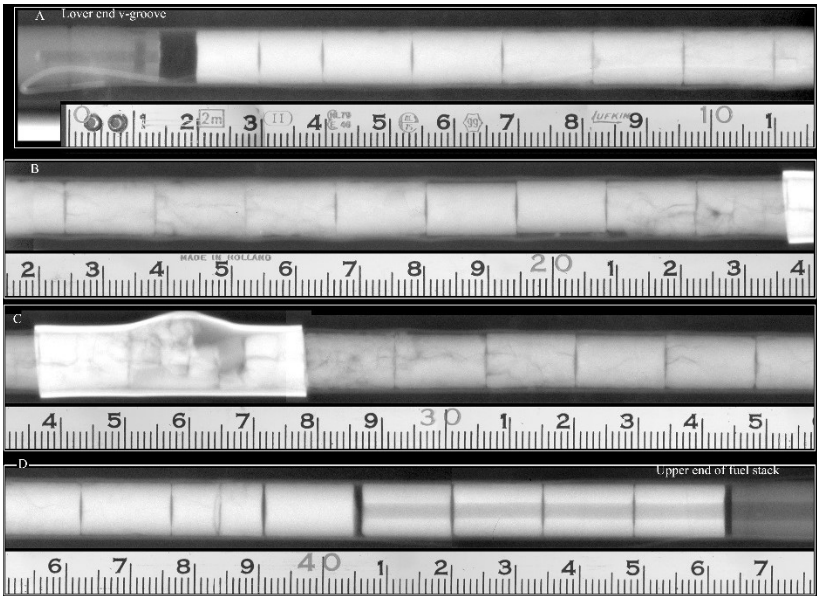

FIG. 23. Neutron radiography, IFA-650.10.

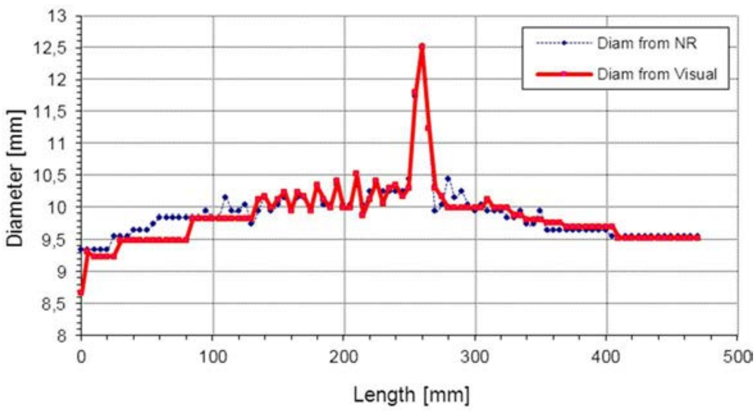

FIG. 24. Diameter profile of IFA-650.10.

The burst opening (Fig. 25) had an axial length of about 15 mm and a maximum width of about 5 mm. Fuel fragments were visible through the opening.

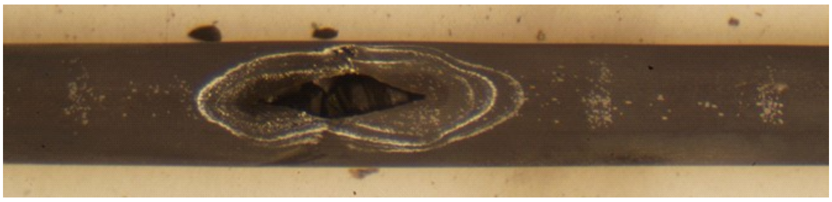

FIG. 25. Burst opening, IFA-650.10.

Some cross-section ceramography pictures are presented in Fig. 26. The elevations as indicated were corresponded to the scale displayed in Fig. 24. Ceramography revealed pellet fragmentation where the larger fragments seemed to have separated mainly along cracks stemming from the base irradiation. Fine fragments seemed to be originated from the high burnup structure from the pellet periphery (micrometre size pores within the fragments were indicated in the bottom left of Fig. 26).

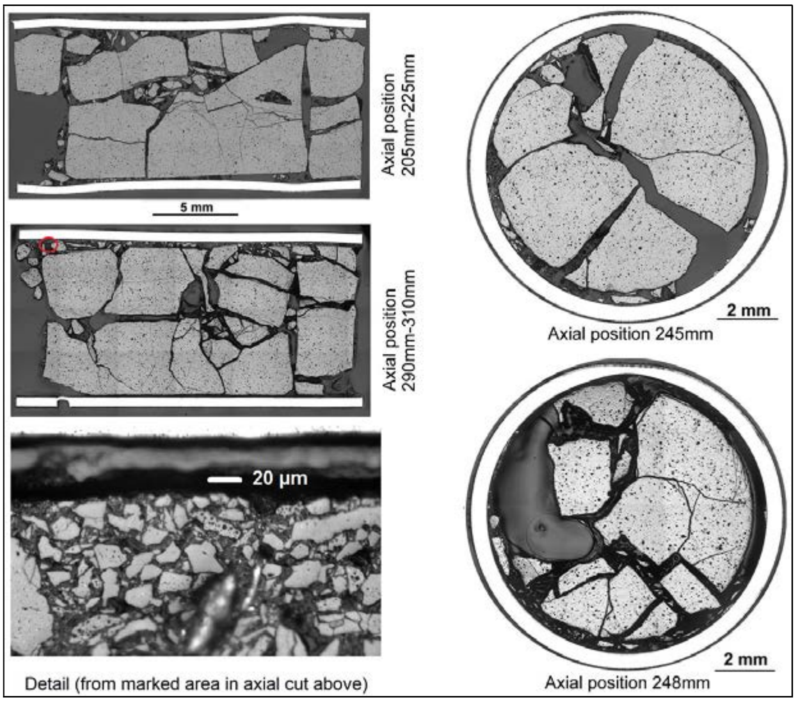

FIG. 26. Ceramography showing fuel fragmentation, IFA-650.10.

IFA-650.11 (VVER)

The fuel, manufactured by JSC TVEL, was supplied by Fortum Nuclear Services Ltd (Finland). The VVER-440 fuel segment had been irradiated in the Finnish Loviisa NPP to a burnup of 56.0 MWd/kgU. The LOCA test was performed at a rod heat rating of 24 W/cm for a target peak cladding temperature (PCT) of 1273 K. The rod failed in 207 s after the start of blow-down.

Tested fuel rod characteristics are shown in Table 6. The pre-test irradiation history for the tested fuel rod in the VVER unit is shown in Fig. 27.

Analysis of the IFA-650.9–11 tests by an integral code SOCRAT/V3 (presented in Annex II) that was nominated to provide T/H boundary conditions for fuel performance codes (see Section 4.2) has revealed quite a good agreement between the measured and calculated data for IFA-650.9 and 650.10 tests, However, the cladding and heater temperatures in the IFA-650.11 test were apparently overestimated. Basing on additional parametric calculations to understand the possible reasons of observed differences in the IFA-650.11 test (see Annex II), a reduction of the rod power to 71% was substantiated and agreed with the CRP participants from Halden Project.

TABLE 6. ROD CHARACTERISTICS FOR IFA-650.11

Items	Properties	Value
Fuel - as fabricated and irradiated	Initial enrichment (wt%U^{235})	3.6
	UO_2 density (g/cm^3)	10.64
	Pellet diameter (mm)	7.55
	Pellet centre hole (mm)	1.484
	Dishing volume (total of both sides) (mm^3)	No dishing
	Burnup (MWd/kgU)	56.0
Cladding - as fabricated and irradiated	Type	E110
	Outer diameter (mm)	9.13
	Thickness (mm)	0.679
	Oxide thickness, irradiated mean (µm)	5
	Hydrogen content, irradiated, ppm	100
Free volume - as fabricated	Fill gas / pressure (bar)	95% Ar + 5% He / 30
	Free volume (cm^3)	16

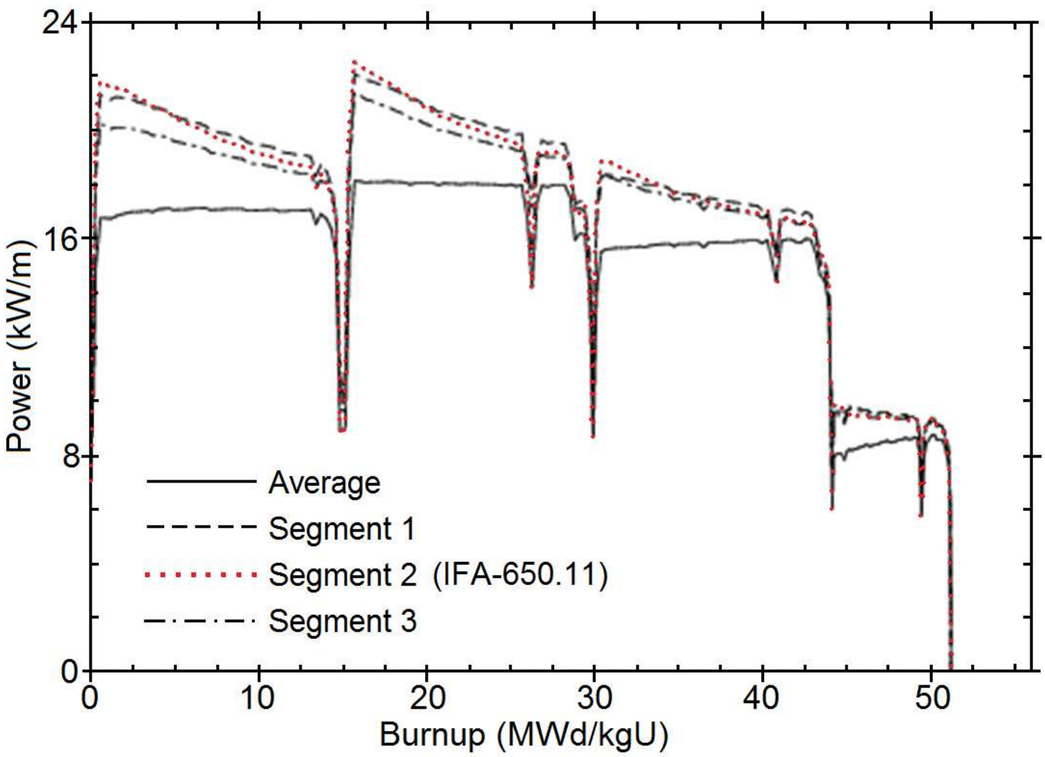

FIG. 27. Pre-irradiation history for the IFA-650.11 test fuel rod.

In-core measurements

The transient was executed according to the general procedure described in Section 2.2.1 and terminated by a reactor scram and gradual cool-down without reflood.

The heater power was increased from 16 to 20 W/cm after the burst to obtain the desired peak clad temperature.

The principal measurements, i.e., cladding and heater temperatures, and rod pressure are shown in Figs 28 and 29, respectively. The heater had only two TCs, one at the bottom and one in the middle. The third TC was mounted on the outside surface at the axial mid-plane of the plenum.

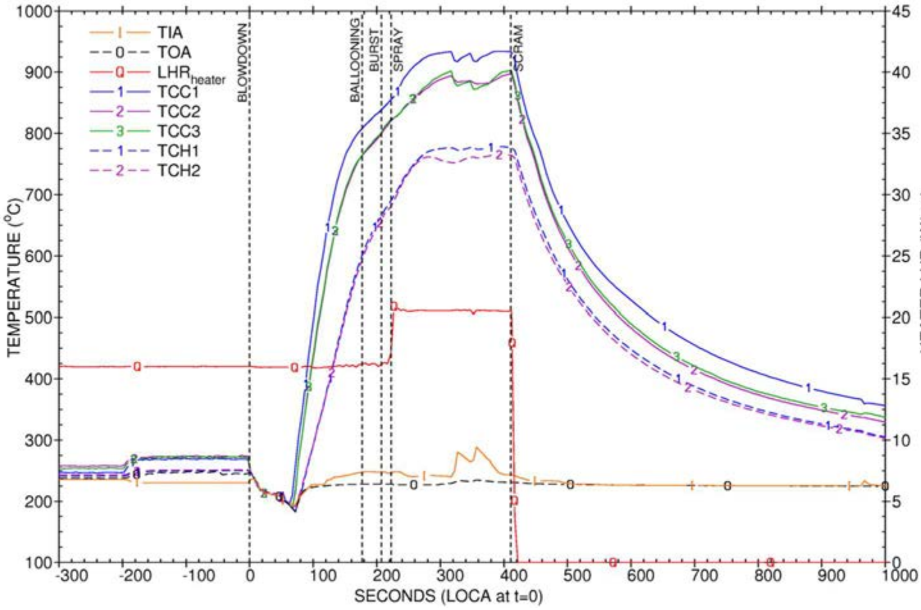

FIG. 28. Cladding and heater temperatures, IFA-650.11.

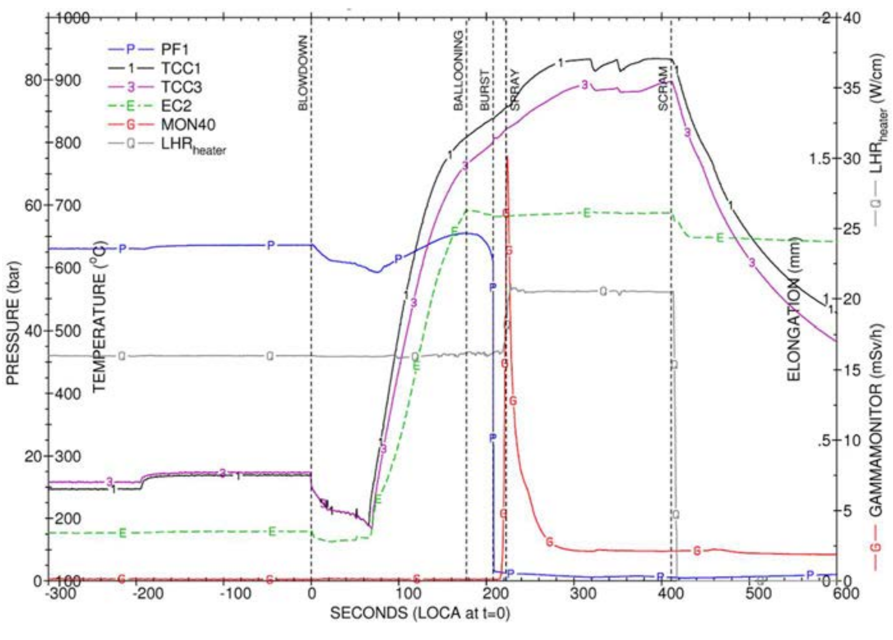

FIG. 29. Rod pressure and cladding elongation, IFA-650.11.

Burst was detected at about 207 s after the start of the blow-down. The rod pressure dropped instantaneously after the burst. The gamma monitor installed on the blow-down line responded to the failure as shown in Fig. 29. The activity peaked at ~30 mSv/h at about 20 s after the burst and decayed rapidly thereafter.

Post irradiation examination

The gamma scan taken after the LOCA test is shown in Fig. 30. The rod was bent. There were signs of ballooning in the lower half. This ballooning region was filled with fuel, but there was no sign of fuel on the bottom of the flask. The axial gap at position 90 might have been caused by fuel relocation.

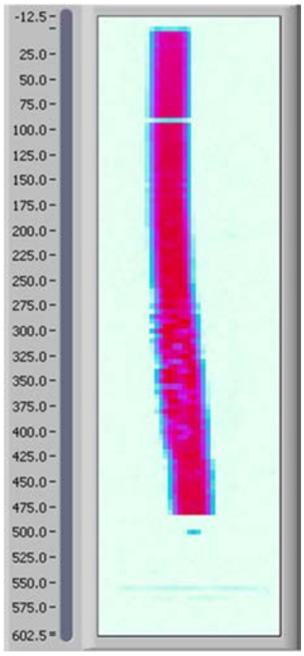

FIG. 30. Gamma scan IFA-650.11.

The diameter measurement results are shown in Fig. 31. The cladding expansion was more pronounced in the lower half and gradually decreased towards the upper end. The axial shape reflected the temperature distribution along the element where higher temperatures were measured at the bottom half. The maximum uniform diameter increase was about 20 %.

Neutron radiography, Fig. 32, revealed fuel broken into coarse pieces. The cracking was correlated with the radial expansion.

Ceramography revealed the fuel pellet fragmentation, Fig. 33. The pellets were broken into several large pieces. It could be assumed that the fragments were formed during the base irradiation in the Loviisa VVER. The fragmentation pattern together with a small burst opening (of about 3 mm long and max. 1 mm wide, Fig. 34) supported the fact that no fuel was detected at the bottom of the pressure flask.

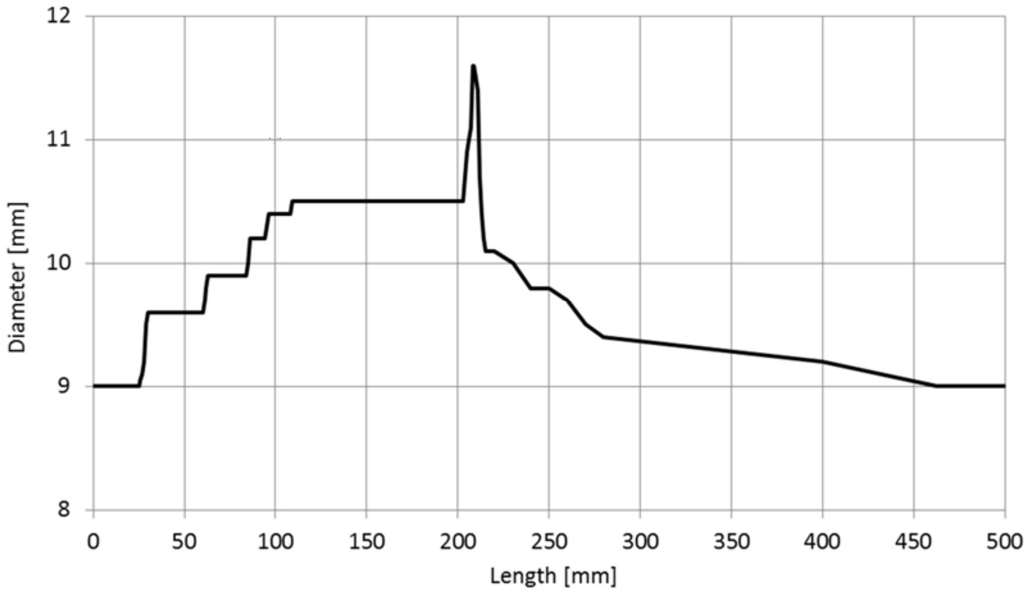

FIG. 31. Diameter profile of IFA-650.11 after the test.

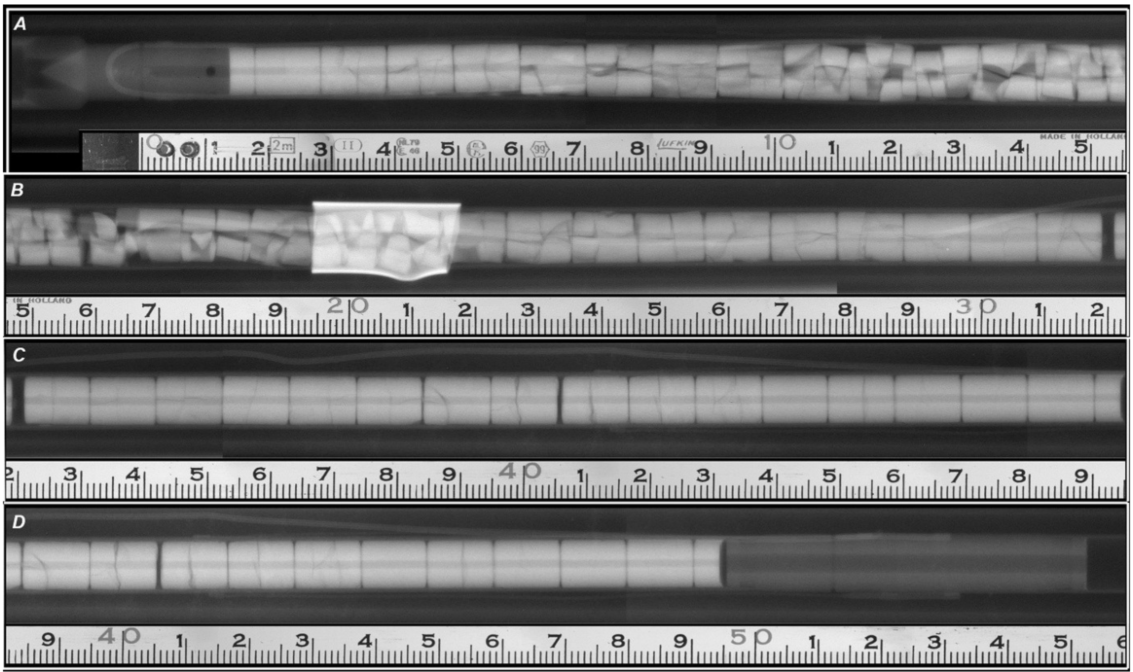

FIG. 32. Neutron radiography, IFA-650.11.

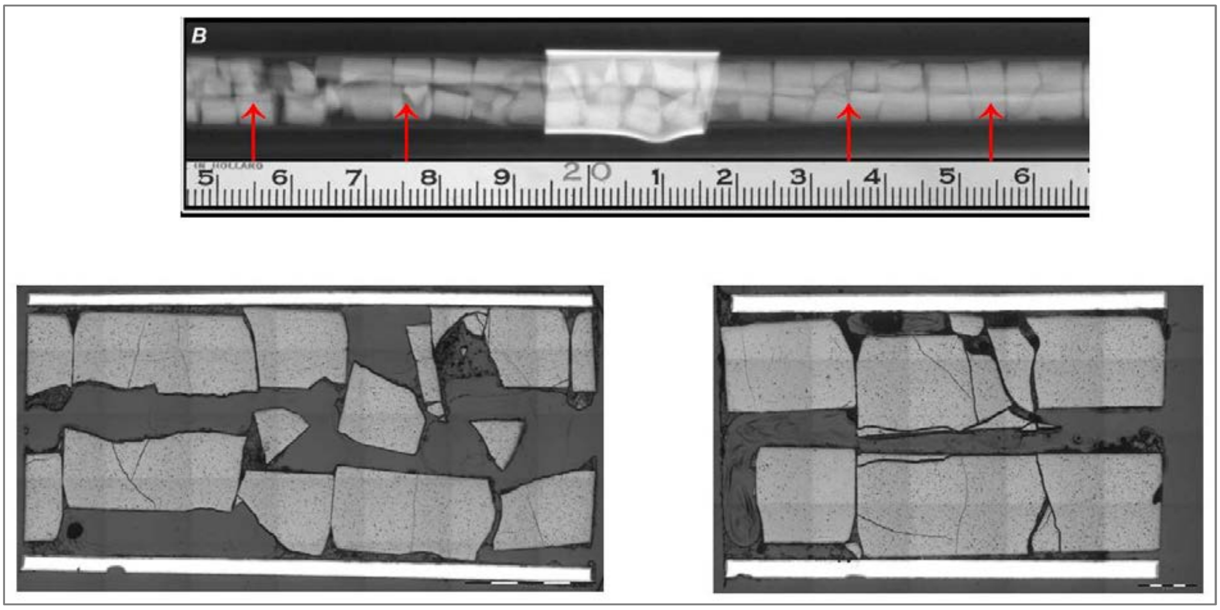

FIG. 33. Fuel fragmentation, IFA-650.11.

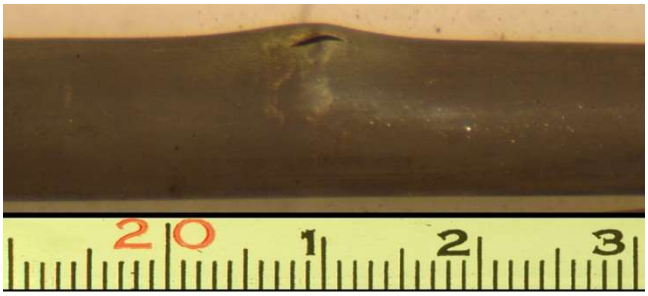

FIG. 34. Burst opening, IFA-650.11.

2.3. STUDSVIK LOCA TEST (NRC-192)

A series of six out-of-reactor LOCA simulation tests were performed from 2011 to 2012 by Studsvik Nuclear AB, Sweden, under contract with the U.S. Nuclear Regulatory Commission (U.S. NRC). The tests were done on fuel pellets that had been sampled from full-length elements with average burnups ranging from 55 to 72 MWd/kgU. All the fuel elements were of Westinghouse PWR design, with UO_2 fuel pellets and first generation ZIRLO (Zr-1.03Nb-0.98Sn by wt%) cladding. The tests were designed to assess the mechanical performance of ballooned and ruptured high burnup fuel rods under typical LWR LOCA conditions; useful information on fuel fragmentation, axial relocation and dispersal were achieved from these tests [7, 8].

2.3.1. Design and operation of the Studsvik LOCA test rig

The design of the Studsvik LOCA test rig is shown in Fig. 35. A single test element with an active length of about 0.30 m was centred inside a quartz tube and externally heated by infrared radiation from a clamshell furnace. There was no nuclear heating in the tests, and the rig was placed in a hot cell. The rodlet was heated with steam at atmospheric pressure, and the test could be terminated by quenching the rodlet with room temperature water.

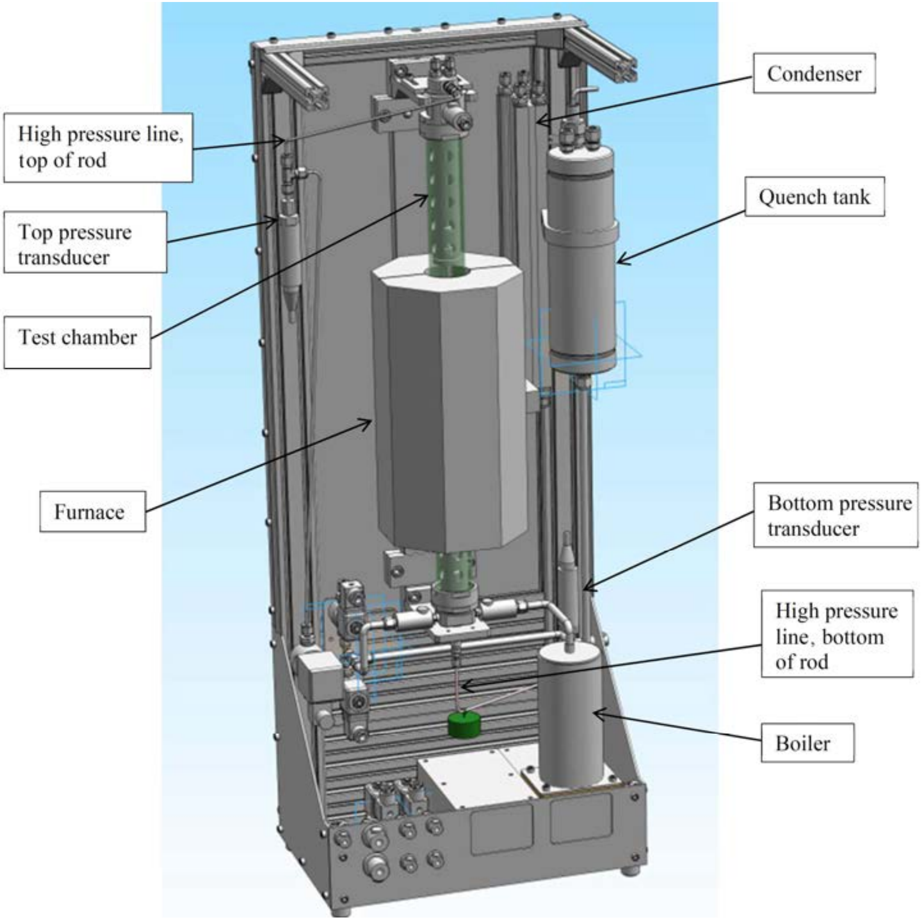

FIG. 35. Design of the Studsvik LOCA test rig [8] .

A typical test started at a temperature of 573 K, the rodlet was heated with a nearly constant heating rate of 5 Ks^{-1}. The cladding temperature was monitored by a single thermocouple, attached by a metal clamp and, located at about 50 mm above the axial midplane of the element. The peak cladding temperature ranged from about 1220 to 1430 K for the six tests, and the rodlets were held at the peak temperature for 0, 5, 25 or 85 s to achieve various degrees of oxidation. Following the high temperature hold, two of the tests (189 and 196) were terminated by switching off the furnace and letting the rodlets cool slowly. In the other four tests, the rodlets were first cooled with an average rate of 3 $K{\cdot}s^{-1}$ to 1073 K, after which they were quenched rapidly by filling the quartz tube with room temperature water [7, 8].

The test elements were initially filled with helium to pressures between 8.2 and 11.0 MPa at 573 K. These pressures corresponded to the of internal pressures in PWR fuel rods at the end-of-life and were chosen to induce cladding ballooning and rupture with hoop rupture strains in the range of 30–50%. Rupture typically occurred at cladding temperatures around 950–1000 K, i.e. significantly below the peak cladding temperatures targeted in these tests.

During the tests, the rod internal pressure was monitored by pressure transducers connected to the top and bottom ends of the element; see Fig. 35. The internal free volume of the pressure lines to the transducers was large: about 7.3 cm^3 in the upper end and 3.1 cm^3 in the lower end of the test element. Most of this gas volume remained near room temperature during the tests.

After each LOCA simulation test, the element was subjected to a four-point bend test at room temperature to measure the residual mechanical strength and ductility at the ballooned and ruptured regions. The two broken halves of the element were then inverted and gently shaken to dislodge loose fuel pellet fragments. Mass measurements were made before and after the LOCA simulation test, after the bend test and after the shake test to determine the fuel release at each stage. After the final stage, the size distribution of the dislodged fuel fragments was measured for five of those six elements [7–9].

2.3.2. Test rodlet NRC-Studsvik-192

The element used in the NRC-Studsvik LOCA Test # 192 was sampled from the middle section of a full-length Westinghouse 17×17 PWR UO_2 fuel rod with the first generation ZIRLO cladding, which had been operated to a rod average discharge burnup of 68.2 MWd/kgU during four reactor cycles at a twin-unit plant in the USA. The first three cycles took place in the first unit from 1987 to 1994 with a two-year interruption between the first and second cycle. After the first cycle, the fuel rod was removed from the discharged fuel assembly and re-inserted into a new assembly, which was operated for an additional reactor cycle in the second unit of the plant from 1999 to 2001. This procedure was applied for a total of ten elements in the original fuel assembly. Some of the other high burnup elements (from the same assembly) were refabricated into elements and used for other tests by Studsvik Nuclear [10, 11]. The design and pre-test material conditions for Test# 192 are summarized in Table 7.

The pre-irradiation history for the re-fabricated short length elements tested in the two PWR units is shown in Fig. 36.

TABLE 7. DESIGN DATA AND PRE-TEST CONDITIONS [7], [10]–[12]
(for the NRC-Studsvik-192 Test rodlet)

Parameter	Value
Rodlet active length (mm)	300
Cold free volume (cm^3)	10.4
Fill gas pressure at 573 K (MPa)	8.2
As fabricated enrichment of U^{235} (wt%)	3.99
As fabricated fuel pellet density ($kg{\cdot}m^{-3}$)	10440
As-fabricated fuel pellet diameter (mm)	8.192
As-fabricated fuel pellet height (mm)	9.830
As-fabricated dish volume per pellet (mm^3)	4.2
Pre-test average fuel burnup (MWd/kgU)	78
Cladding tube design	Monotube
Cladding tube material	ZIRLO
Heat Treatment	SRA
As-fabricated cladding outer diameter (mm)	9.500
As-fabricated cladding wall thickness (mm)	0.571
Pre-test oxide thickness (mean) (µm)	27
Pre-test oxide thickness (max) (µm)	30
Pre-test hydrogen concentration (wppm)	235
Pre-test fast neutron fluence (> 1 MeV) (m^{-2})	1.31×10^{26}

Note: The data for the rod design are taken from open literature reports on sibling fuel rods that have been used in earlier tests by Studsvik Nuclear AB.

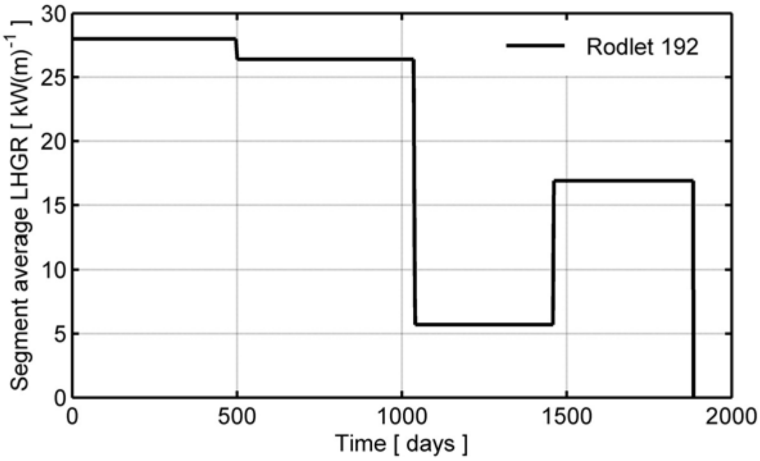

FIG. 36. Pre-irradiation history for the NRC-Studsvik-192 LOCA test rodlet [12].

2.3.3. Summary of test conditions and test results

The important test parameters for the NRC-Studsvik LOCA Test # 192 are summarized in Table 8. Further details on the test and the results of PIE were given in reference [13]. Temperature, pressure and diametral expansion are indicated in Figs 37 and 38.

TABLE 8. SUMMARY OF TEST PARAMETERS FOR THE [7] [12]
(for the NRC-Studsvik LOCA Test 192)

Parameter	Value
Initial temperature (K)	574
Initial rod pressure (at 574 K) (MPa)	8.21
Cladding temperature at failure (K)	981
Peak cladding temperature (PCT) (K)	1446
Hold time at PCT (s)	5
Steam mass flow ($kg\cdot s^{-1}$)	1.8×10-4
Timing of events (after start of heating):	
Cladding tube failure (s)	81
Hold at PCT (s)	173–178
Quenching (s)	297

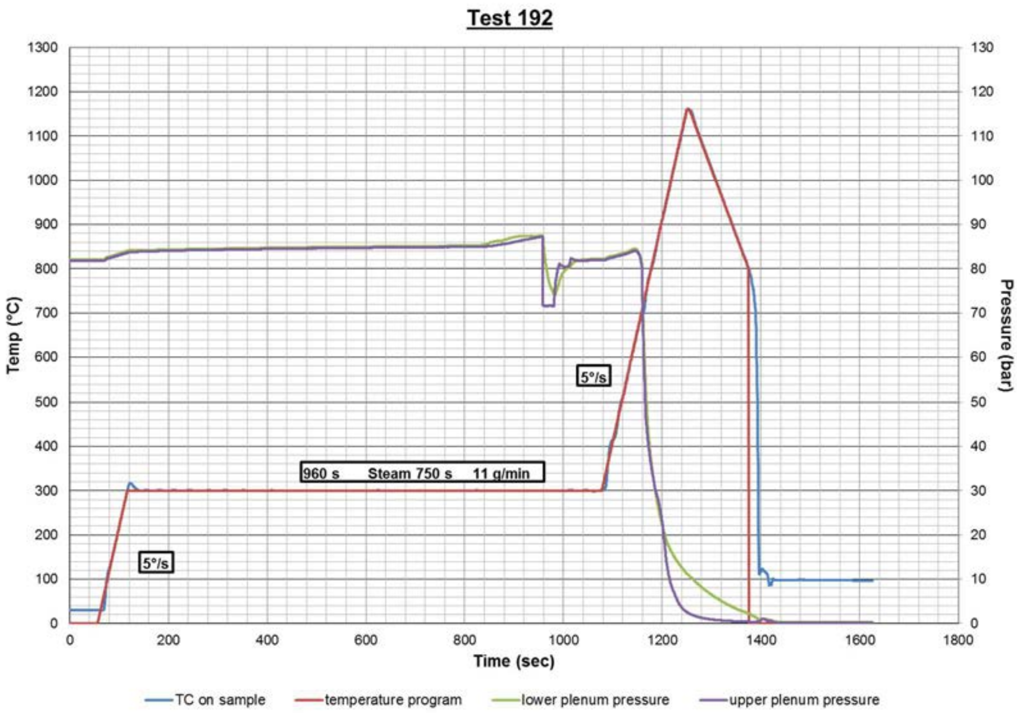

FIG. 37. Experimental data during test (pressure/temperature) for Studsvik Test # 192.

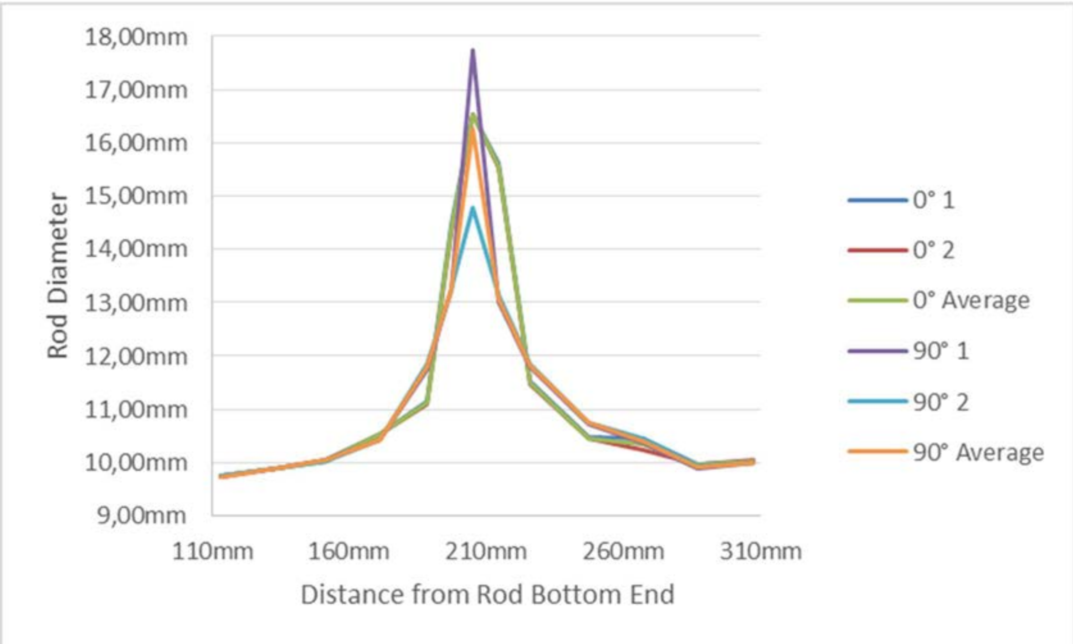

FIG. 38. Profilometry after test (Studsvik Test # 192).

2.4. KIT QUENCH-L1 BUNDLE TEST

Test QUENCH-LOCA-1 (QUENCH-L1) with electrically heated bundle (tantalum (Ta) heaters inside each 21 rods) was performed in accordance with a temperature/time-scenario that was typical for a LBLOCA in a German PWR with maximal heat-up rate of 7 K/s during a transient. During the transient, a gas mixture of steam (at 2 g/s) and argon (at 6 g/s) was injected from the bundle bottom. The cooling stage was performed in steam (20 g/s) and argon (6 g/s) during the lasted 120 s and terminated by flooding with 3.3 g/s of water per fuel element. The maximal temperature of 1373 K was reached at the end of the heat-up phase at an elevation of

850 mm. The details of the QUENCH facility and the test procedure could be found from the participant final report (see Annex II).

The test results were as follows: The decreased yield strength and increased ductility of the heated claddings with increasing temperature resulted in a progressive ballooning and consequent burst of all elements during the transient. Due to prototypical internal heating and enhanced heat transfer at the contact between pellet and cladding, the non-uniform heating had caused thinning on one-side of the cladding during ballooning. In accordance with the ultra-sound results, the cladding wall thickness was varied from 725 to 350 µm at about 50 mm below and above the burst opening.

The cladding burst occurred at temperatures between 801 and 896 °C, with an average value of 853 ± 30 °C. The inner rod pressure was relieved in less than 40 s. The average linear burst opening dimensions were 4.2 ± 2.6 mm in width and 15 ± 6 mm in length. These opening sizes were quite small for the release of pellet fragments.

Element bending of up to 23 mm was observed for several rods (as the axial expansion was restricted by the heaters). The average cladding strain at the burst opening location was about 30 ± 6% including the opening width (or about 20 ± 5% only for cladding perimeter without opening). At a cladding location of about 15 mm above and below the opening, the cladding diameter was minimal and the difference between maximal and minimal cladding diameters was up to 0.5 mm.

The maximum blockage of ~24% was observed for cooling channels at an elevation of 950 mm. If hypothetically all breaks were to locate at the same level, the blockage would be 46%. The 46% was still enough to maintain bundle coolability. According to the REBEKA tests [14], a flow blockage of up to 90% was still acceptable.

After the burst, the steam penetrated the gap (between cladding and pellet) and oxidized the inner surface of the cladding. The hydrogen diffused partially into the cladding (secondary hydriding) and built asymmetrical bands above and below the burst opening. Like the commissioning test QUENCH-L0 [15], the oxide layer thickness on the *inner* cladding surface was measured up to 25 µm at burst elevations and less than 2 µm at hydrogenated bands.

No hydrogen bands around the burst openings were observed by means of neutron radiography for outer elements. The maximum hydrogen content in cladding, with a cross-section area of about 25 × 25 µm^2, inside the hydrogen bands of inner elements varied between 700 and 1800 ppm. It is comparable with values predicted by the SVECHA/QUENCH mechanistic code [16]. Concentration of hydrogen dissolved in metallic matrix was estimated as < 300 ppm.

During quenching, following the high-temperature phase, no fragmentation of claddings was observed. This implies residual strengths or ductility was sufficient.

During tensile tests at room temperature, all thirteen tested claddings were fractured due to stress concentration at the burst position. This observation was similar to elements of the QUENCH-L0 bundle with maximum hydrogen concentrations of < 1500 ppm. For the central element (#1) with a maximum hydrogen concentrations of > 1500 ppm, the element was brittle at the hydrogen bands and was damaged when pulling it out of its heater.

2.5. CORA-15

The CORA-15 bundle test was performed under transient conditions typical for many CORA-PWR tests with bundle containing two Ag-In-Cd neutron absorber rods. Unlike other CORA bundles, all heated and unheated fuel rod simulators (16 + 7 correspondingly) were filled with helium and pressurized to 6.0 MPa before transient. During the transient, all rods underwent ballooning and burst. Ballooning progressed for about 100 s. Bursts occurred within 150 s (between 3500 and 3650 s) in the temperature bandwidth between about 700 and 800 °C.

The mostly probable burst elevation for the bundle was at 750 mm (which was the hottest elevation during the burst period).

During further heat-ups, temperature escalation due to the zirconium-steam reaction starts at elevations of 550 to 950 mm at temperature of about 1100 °C. In presence of PWR absorber rods, the sequence of failure starts with the release, relocation and re-solidification of the (Ag, In, Cd) melt. The melt release occurred between 1290 and 1350 °C at elevations between 750 and 800 mm. Most of the melt reacted with the cladding and guide tube by liquefying the zirconium components, forming a metallic melt of the type (Ag, In, Zr). This melt was capable of dissolving Zircaloy as low as 1250 °C, i.e. clearly below the melting point of Zircaloy (1760 °C).

During the temperature escalation above 1800 °C, Zr melt formed in the gap between ZrO_2 and UO_2 was relocated partially inside the gap to lower bundle elevations and partially penetrated through the failed ZrO_2 layer into the space between its neighbouring elements. The resulting melt of the fuel rod interaction, containing mainly U, Zr and O relocated downwards as a slug and solidified between 400 and 550 mm according to its solidus temperature as a large lump of porous structure. The maximum bundle blockage (almost 100%) was observed at the top of the Inconel grid spacer (at about 500 mm). The (Ag, In, Cd) absorber melt with the much lower solidus temperature solidified down at the lower elevation of about 150 mm.

Post-test investigations showed negligible oxidized cladding up to elevation of about 350 mm. The claddings were completely oxidized between elevations 480 and 1000 mm. The maximum hydrogen release rate of 210 mg/s was measured on the end of the transient (4800 s). The total hydrogen release was 145 ± 15 g.

Based on the CORA-15 experimental data, computer codes ATHLET-CD and SOCRAT were used for a benchmarking exercise. Corresponding descriptions of code applications are presented in Sections 3.3.1 and 3.3.3; the comparison of simulation results is given in Section 4.5.

In the framework of the FUMAC project, the implementation of a slug relocation/oxidation model in the single-rod SFPR code (IBRAE) demonstrated the possibility of extending the fuel performance codes to severe accidents (see Annex II).

3. DESCRIPTION OF CODES AND MODEL IMPROVEMENTS

3.1. SINGLE FUEL ROD CODES

3.1.1. FRAPTRAN

FRAPTRAN code is a fuel rod transient analysis code, designed to calculate the thermal and mechanical behaviour of a LWR single fuel rod during hypothetical accident and operation transients such as reactivity insertion accidents (RIA) or loss-of-coolant accidents (LOCA), and power oscillations without scram.

The latest version FRAPTRAN-1.5 was released in May 2014. The code was described in [17] and an integral assessment was performed in [18]. This standard version has been used by several participants. Several improvements have been made to FRAPTRAN code during the FUMAC project.

SSM/QT-version of the fuel rod analysis program FRAPTRAN-QT-1.5

In a recent project funded by the Swedish Radiation Safety Authority (SSM), Quantum Technologies AB developed a computational model for axial fuel relocation under LOCA [19]. The relocation model has been fully integrated with an in-house SSM/QT-version of the fuel rod analysis program FRAPTRAN 1.5. In contrast to earlier relocation models for fuel rod analysis programs (such as the one developed by SCK•CEN [20]), the model considered thermal feedback effects from the fuel relocation. It also uses sub-models to estimate the packing fraction and effective thermal conductivity of particle beds formed by crumbled fuel in ballooned regions of the fuel rod, based on the estimated state of fragmentation and pulverization of the fuel pellets. Models in the SSM/QT-version of FRAPTRAN 1.5, including the fuel relocation model, were validated against recent LOCA tests in Halden and Studsvik [20].

Tractebel-version of the fuel rod analysis program FRAPTRAN-TE-1.5

Tractebel requested the SSM/ Quantum Technologies to implement their model in the Tractebel version of FRAPTRAN-1.5 [22–24] and to perform further model validation and improvements. The extensions and adaptations in the FRAPTRAN-TE-1.5 code were documented in the SSM/ Quantum Technologies report [25].

The correctness of the code changes had been verified by comparing calculated results with simple analytical solutions. In addition, FRAPTRAN-TE-1.5 had also been validated against three LOCA simulation experiments in the Halden IFA-650 test series. The results of these tests are summarized, and recommendations for further testing and for using different modelling options in FRAPTRAN-TE-1.5 program are given in Ref. [25].

3.1.2. TRANSURANUS

TRANSURANUS is a computer programme written in FORTRAN95 for the thermal and mechanical analysis of fuel rods in nuclear reactors that is owned by the Joint Research Centre of the European Commission. TRANSURANUS has been used by research centres, nuclear safety authorities, universities and industrial partners, (see Refs [26–38]).

International benchmark exercises are of high importance for developing simulation systems of various nuclear reactor components. One of the main benefits of this CRP is the possibility for cross-comparison and complementary validation of many codes involved. Several exercises were organized during the last 3 decades: D-COM in the mid 80's, FUMEX-I from 1992 to 1996, FUMEX-II from 2002 to 2006 and FUMEX-III from 2008 to 2012.

TRANSURANUS is generally referred to as a fuel performance code meaning that it solves the equations for the radial heat transfer, the radial displacement along with the stress distribution in both the fuel and its surrounding cladding, and the release of fission product and its behaviour as a function of time. The equations, in general for fuel performance prediction, embody the following phenomena:

- Thermal performance: heat conduction, radiation and convection;
- Mechanical performance: creeps (radiation and high temperature), densification, thermal expansion, pellet cracking and relocation, solid and gaseous swelling;
- Actinide behaviour: depletion and build-up of main Th, U, Np, Pu, Am and Cm nuclides, impact on the radial power profile;
- Fuel restructuring: Pu and Am redistribution, grain growth (normal and columnar), central void formation;
- Fission product behaviour: creation in the fuel matrix, diffusion to grain boundaries, release to free rod volume after saturation of grain boundaries, athermal release, recoil, formation of High Burnup Structure (HBS, which is depleted and contain porosity).

The heat transfer in the fuel-to-cladding gap is simulated by means of a combination of heat conduction, radiation and convection (URGAP model [39]). Main assumptions and equations for mechanical performance are provided in Ref. [27].

Main assumptions and equations for actinide concentrations could be found in Refs [37, 38].

In the TUBRNP model the calculation of the radial power profiles is split into (a) the approximation of the neutron flux through thermal diffusion theory, and (b) the computation of the local concentrations of the relevant actinide isotopes with simplified depletion equations. The most recent extension covers the nuclides ^{232}Th, $^{233\text{-}236,238}$U, ^{237}Np, $^{238–242}$Pu, ^{241}Am, ^{243}Am, $^{242–245}$Cm. More details are given in Ref. [40].

The TRANSURANUS code consists of a well defined mechanical and mathematical framework, which additional physical models can easily be incorporated. The code has a comprehensive material data files for oxide, mixed oxide, carbide and nitride fuel types, Zircaloy and steel claddings and several different coolants (water, sodium, potassium, lead, bismuth). TRANSURANUS can be used as a single code system for simulating both long-term irradiations under normal operating conditions as well as transient tests. The 'restart' mode allows simulating re-fabricated (recycled) fuel rods, where the fill gas has been completely changed as an example.

The code can be employed in two different approaches: as a deterministic or a statistical code. Restart may be used to perform a statistical analysis employing the Monte Carlo technique. This option may be helpful for the analysis of a long base irradiation then followed by a transient. Fig. 39 gives an overview of these possibilities.

Besides its flexibility for fuel rod design, the TRANSURANUS code can deal with a wide range of different situations, as demonstrated in experiments, under normal, off-normal and accident conditions, although some models specific for RIA (e.g. plenum temperature) are still under development. Furthermore, the code is being used for BWRs, PWRs and VVERs. The time scale of the problems to be treated may range from milliseconds to years. Hence complex irradiation experiments can be simulated including re-fabricated instrumented fuel rods and changing operating conditions.

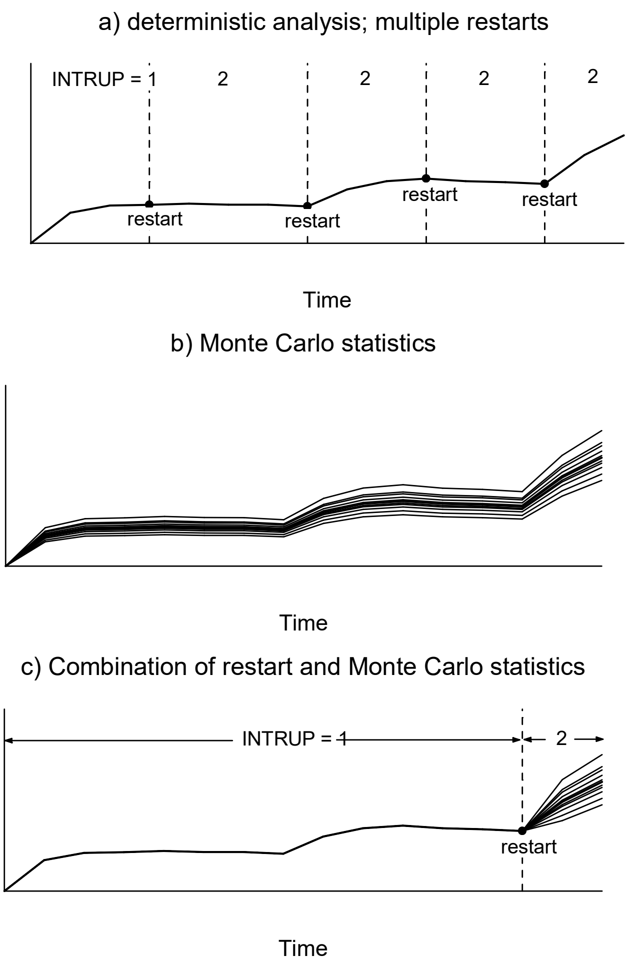

FIG. 39. An illustration of deterministic and probabilistic approaches with restarts.

3.1.3. ALCYONE

ALCYONE [41] is a multi-dimensional fuel performance code co-developed in the PLEIADES [42]platform by the CEA, EDF and AREVA. It is dedicated to the modelling of the in-reactor behaviour of PWR fuel rods during normal (the base irradiation) and off-normal (with power ramp and transient) operating conditions. ALCYONE has incorporated three calculation schemes. A one-dimensional reference scheme, based on a symmetric description of the fuel element with a discrete axial composition of the fuel rod in a stack (i.e. slumping), is used to study the behaviour of the complete fuel rod [43]. A two-dimensional scheme, which describes Pellet-Cladding Interaction (PCI), to assess stress concentration in the cladding near a pellet crack tip [44]. A three-dimensional model with a complete pellet fragment for a detail analysis of PCI at the pellet-cladding interfaces [45]. These schemes use the Finite Element (FE) code (Cast3M) to solve the thermo-mechanical problem and share the same physical material models at each node or integration points of the FE mesh. Fig. 40 presents the flows chart of ALCYONE 1D. This Fig. identifies difference convergence loops in blue, the thermal-physical models in beige and the other models are in green if they are calculated before the thermal physical loop or in grey pink if after.

ALCYONE has been extensively validated for PWR rods (UO_2 and MOX fuel up to 80 GWd/tM with Zry-4 or M5 cladding) under base-loaded irradiation during the French survey program. Power ramp tests performed in MTR are used to validate the behaviour of the fuel rod in case of power transients. Fuel temperature calculations are validated specifically by a MTR experiment, which has a representative thermocouple located at the fuel center [43].

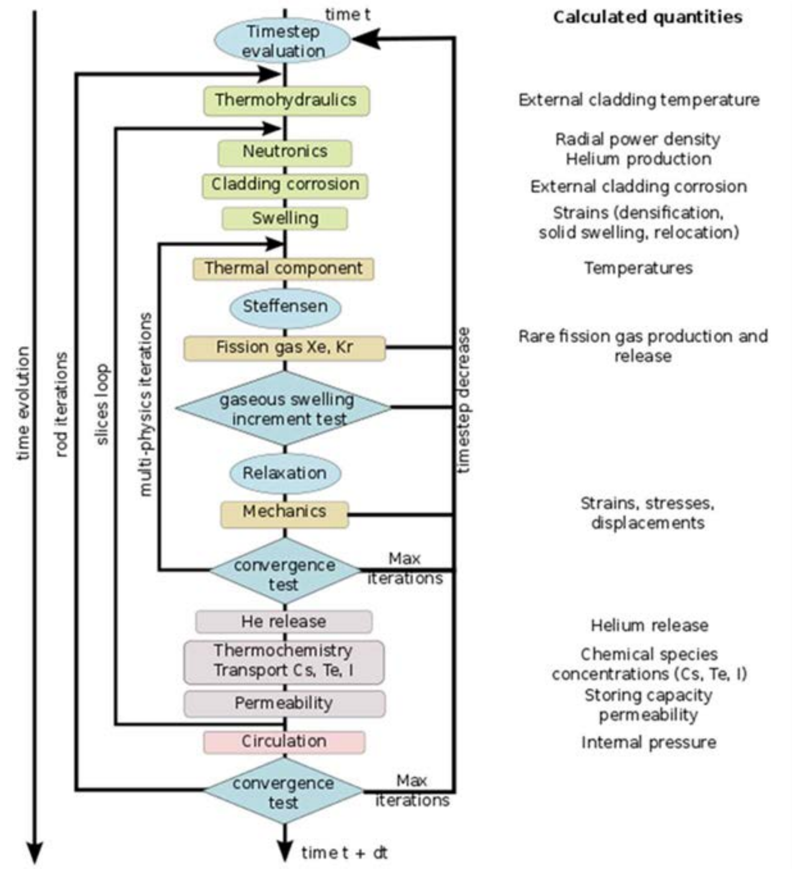

FIG. 40. ALCYONE flow chart.

The coupling of ALCYONE [46] with the system code CATHARE will be available soon. For LOCA analysis, the evaluation of the rod internal pressure is crucial. The evaluation of the quantity of fuel which could be fractured during the accident phase (i.e. at least the fuel zone which are restructured) is also important. These calculations are performed by two fission gas models CARACAS [47] or MARGARET [48].

The EDGAR model [41] describes the viscoplastic behaviour of a zirconium alloy tube under a pressure (an imposed loading) and at a high temperature (more than 950 K). This model also gives the phase fractions evolution (alpha, beta and a transition phase are considered).

The EDGAR model is established as a point model in a Finite Element 3D calculation tool. The mechanical analysis and definition of the mechanical constitutive equations are discussed in detail in Ref. [42].

The mechanical behaviour is expressed in the logarithmic strain framework proposed by Miehe et al [45]. The EDGAR experiments are being simulated using ALCYONE to validate this implementation.

The 1D code generally considers that for a solid pellet, the radial displacement of the central point is not permitted. In case of LOCA, the thermal gradient is significantly lower, the gap is considered as open. One may consider that the central point of the pellet is able to move radially.

Figure 41 presents stress distribution in the pellet when the gap is open under cold conditions at the end of a base irradiation. During a LOCA, stresses distribution is likely to be in the same shape, as the thermal gradient remains low in the fuel pellet. Nevertheless, the actual value of the stress level depends on the fission gas swelling contribution and the irradiation power history.

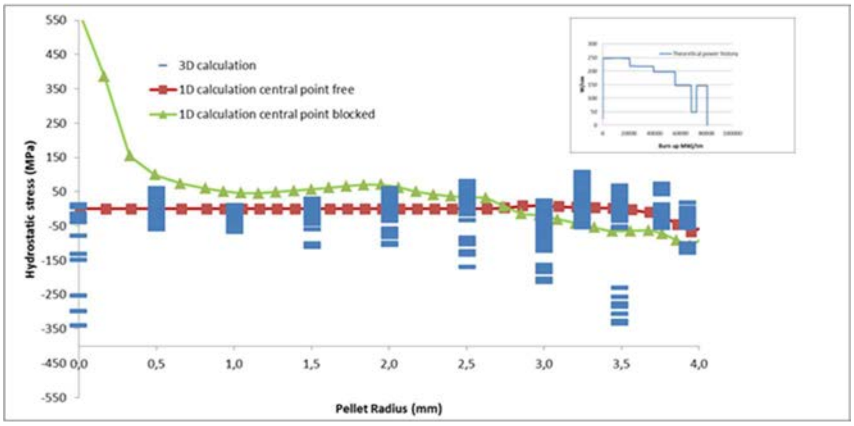

FIG. 41. Hydrostatic stresses distribution in the pellet at room temperature.

The fission gas model used in the ALCYONE calculations is CARACAS [47], which considers the following fission gas populations: nanometric intragranular bubbles, precipitated intragranular bubbles, intergranular bubbles, rim structure formation and rim bubbles evolution. This model is validated for base irradiation and power ramp conditions for UO_2 up to 70 GWd/tM.

During the first part of the LOCA transient, fuel temperature remains low enough to affect only the intergranular gas diffusion. A specific criterion for the initiation of intergranular fracture has been developed. It is based on the evaluation of stress applied to grain boundary resulting from macroscopic hydrostatic stress and from stress induced by over-pressurized intergranular bubbles (tensile stress). If the tensile stress on the grain boundary induced by intergranular bubbles is higher than the grain boundary yield stress, partial or total fracture of the grain boundaries is possible. This allows a connected path for fission gas release. One has also assumed that grain boundary yield stress is reduced by irradiation (fission gas atoms dissolved on the grain boundary).

3.1.4. BISON

The US Department of Energy (DOE) has been developing capabilities to simulate nuclear fuel behaviour within the Nuclear Energy Advanced Modelling and Simulation (NEAMS) and Consortium for Advanced Simulation of Light Water Reactors (CASL) programs. The result is the BISON code [49], a multidimensional, finite-element based fuel performance code developed at Idaho National Laboratory (INL).

BISON is built using the INL Multiphysics Object-Oriented Simulation Environment, or MOOSE [50]. MOOSE is a massively parallel, finite element-based framework to solve systems of coupled non-linear partial differential equations using the Jacobian-Free Newton Krylov (JFNK) method. BISON can use 1D, 2D or 3D geometric representation to analyze the global fuel element behaviour including local multidimensional effects. BISON's ability to use massively parallel computing allows for analyzing integral fuel rods in 2D for a detailed irradiation history as well as for large 3D problems. BISON has been applied to a variety of fuel types including LWR fuel rods, TRISO particle fuel, fast reactor oxide fuel, and metallic fuel in both rod and plate geometries. The code is applicable to both steady-state and transient conditions and is used for the analysis of fuel behaviour during both operational and design-basis accident conditions.

Most recent applications of BISON include 3D analysis of BWR fuel with missing pellet surface (MPS, as manufacturing defects), analysis of accident tolerant fuel (ATF concepts, such as FeCrAl cladding and U_3Si_2 fuel), and design calculations for a new Halden experiment (IFA-800) that investigates MPS effects. Details are given in separate publications.

The BISON governing equations consist of fully-coupled partial differential equations for energy, species, and momentum conservation. Nonlinear kinematics in BISON follows the approach described in [51].

Material models are included in BISON for UO_2 fuel to describe temperature and burnup dependent thermal properties, solid and gaseous fission product swelling, densification, cracking, pellet-fragment relocation, thermal and irradiation creep [50, 52]. Fission gas swelling and release are calculated using the model described in Reference [53]. For Zircaloy cladding, models are available for thermal physical properties, instantaneous plasticity, thermal and irradiation creep, irradiation growth, oxidation, as well as cladding phase transition, ballooning and burst failure during LOCAs. Gap heat transfer is modelled in the traditional manner with the total conductance across the gap computed as a sum of the gas conductance, the increased conductance due to solid-solid contact, and the conductance due to radiant heat transfer. Mechanical contact between materials is implemented using node/face constraints [49, 52].

A variety of other material models are available in BISON. These include fuel models for MOX, U_3Si_2, U-Pu-Zr and U-10Mo, and cladding models for HT9, 316 and FeCrAl claddings. The BISON models are described in more detail in Ref. [52].

For BISON an extensive set of code verification problems exists, from fundamental finite element solid mechanics and heat transfer tests, to problems specific to nuclear fuel models. In addition to code verification, the numerical accuracy of the solution is performed. For this purpose, simulations with representative validation-problem features were spatially and temporally resolved and the results compared.

Validation work for BISON has focused initially on LWR fuel during normal operating conditions and power ramps [54,55]. In recent years, significant work has also been performed on the analysis of design-basis accident scenarios (DBAs), including both LOCA [56, 57] and RIA [58, 59]. For TRISO particle fuel, several benchmark cases have been considered which compare BISON results to those from other fuel performance codes [55] [60].

BISON has incorporated a large-strain mechanics formulation, essential to correctly analyze cladding ballooning during LOCAs. In addition, specific material models for the high-temperature, transient phenomena involved in fuel rod behaviour during LOCAs.

Specifically, models are implemented in BISON for high temperature cladding oxidation, Zircaloy solid-solid phase transformation, Zircaloy high temperature creep, and cladding burst failure [56, 57]. In addition, BISON's model of fission gas swelling and release in UO_2 was extended to include a specific treatment of the burst release effect during transients [61, 62]. This capability can potentially be adapted and applied to the simulation of LOCA transients. Also, models for cladding oxidation energy deposition and axial fuel relocation have recently been implemented and will be applied in future LOCA simulations with BISON.

The extended BISON code has been applied to simulations of LOCA experiments, including many separate effects tests from the PUZRY, REBEKA and Hardy experiments as well as integral fuel rod experiments including QUENCH L1 rods 4 and 7, NRU-MT4 and MT6A tests, and Halden IFA-650.2 and IFA-650.10 tests. Details and simulation results can be found in [55].

BISON models for LOCA analysis and results for the simulations of the FUMAC cases are presented in detail in the final report on INL's contribution to FUMAC (see Annex II).

3.1.5. DIONISIO

DIONISIO 2.0 is a code able to simulate a fuel rod in extended burnup conditions. Particularly, in the high burnup range, when the inventory of the more relevant isotopes and the microstructure at the pellet periphery are described.

The code results have been compared with 34 experiments published in the IFPE data base, covering more than 380 fuel rods irradiated up to average burnup levels of 40-60

MWd/kgU. The results of these comparisons are satisfactory and reveal the good quality of the simulations. They were performed within the frame of the IAEA Research Project FUMEX III. The diverse models have been explained in detail in several papers [63–67].

In the framework of the Research Project FUMAC, the application range of the code is expanded to conditions typical for LOCA. To this end, a new module able to reproduce the thermal-hydraulic conditions in the coolant has been developed. This module is intended to account for numerous parameters that govern the heat exchange between the fuel rod and the coolant in accident situations, thus providing the boundary conditions necessary to simulate the fuel rod behaviour during a fast excursion.

3.1.6. FTPAC and FTPAC - ABAQUS

FTPAC consists of models calculating the behaviour of LWR fuel rods under transient conditions, which simulates the following processes [68]:

- Heat conduction from fuel pellet to coolant through gas gap-cladding and cladding-coolant;
- Fuel pellet cladding deformation;
- Fuel rod gas pressure history;
- and cladding oxidation evolution.

The fuel pellet deformation model is used to calculate the fuel stack length change and fuel radial displacement. If the fuel pellet and cladding is in contact, there will be pellet-cladding mechanical interaction (PCMI). The fuel deformation model will apply a driving force to the cladding deformation model. A slip coefficient is calculated to decide the extent of cladding elongation transmitted by axial expansion of fuel pellet stack. The larger the contact pressure is, the bigger the slip coefficient is. The slip coefficient is associated with friction factor and interface area between fuel pellet and cladding.

If the cladding effective plastic strain is greater than the cladding instability strain, the ballooning model is used to calculate the localized large deformation of cladding. Large deformation model calculates the extent and shape of the cladding ballooning node. Another ballooning model is added to FTPAC code recently by coupling ABAQUS [69]. The coupled code calculation framework is illustrated in Fig. 42.

Deformation and stresses under large deformation condition in the cladding are calculated using an ABAQUS model which considers the cladding to be a thick cylindrical shell loaded with specified internal and external pressures and a prescribed uniform temperature [70]. The deformation result from the ballooning model is fed back to the main program FTPAC used for subsequent calculation.

The cladding-steam reaction is modelled by means of kinetic correlations for both the oxygen mass gain and the ZrO_2 layer thickness growth. A few experiments were selected to demonstrate the specific models in FTPAC are working correctly. The selected tests were the IFA-432, FA-513, IFA-507, NSRR and CABRI experiments [71]. The experimental data were successfully used to compare against the FTPAC prediction as a function of time.

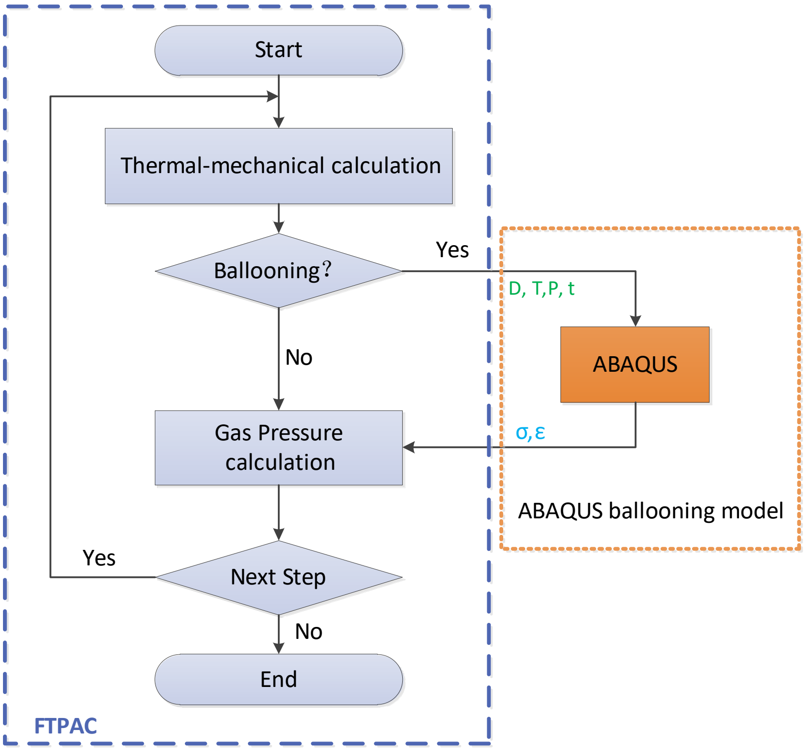

FIG. 42. The calculation framework of FTPAC coupled ABAQUS.

3.1.7. RAPTA-5.2

Organization-developer of the code RAPTA-5.2 is A.A. Bochvar High-Technology Research Institute of Inorganic Materials (JSC "VNIINM"). RAPTA-5.2 is a licensing code for VVER fuel rods used by JSC "VNIINM" to model fuel rods behaviour in design basis accidents. The code determines the fuel rod characteristics and verifies the fuel safety criteria such as: maximum fuel temperature, peak fuel enthalpy, peak cladding temperature, number of failed rods, cladding oxidation and hydrogen production.

The RAPTA-5.2 code was approved, and licensed by the Federal Environmental, Industrial and Nuclear Supervision Service of Russia, to extend its applicability up to a burnup of 75 MW·d/kgU [72].

The RAPTA-5.2 code solves the thermal-mechanical deformation of LWR fuel rods during fast transients such as LOCA and RIA accidents. The following physical phenomena are modelled:

a) Heat transfer in fuel rod by considering:

— Transient power generation in the fuel volume (input data) accounting for the radial power distribution at various burnups;
— Surface thermal effect due to zirconium oxidation in steam;
— Transient boundary conditions (time stepping) on the cladding surface (input data);
— Changes in the geometric cross-sectional area of the fuel rod;
— Material properties at high temperatures and burnups considering the radial power distribution;
— Change in the fission gases content, release and pressure in the fuel rods during a transient.

b) Geometry in fuel rod by considering:

— Boundary conditions before the initiation of an accident with accumulated burnup (input data);
— Thermomechanical deformations of fuel and cladding, considering fuel-cladding interaction, during steady and transient states;
— Fuel swelling and FGR during steady and transient states;
— Cladding rupture as the result of excessive strains;
— Zirconium oxide thickness on the cladding outer and inner (after rupture) surfaces.

c) Cladding oxidation under non-isothermal conditions, with feedback from heat release and hydrogen generation.

Temperature and irradiation will affect the material properties during normal operation prior to the initiation of an accident. For calculating the cladding deformation kinetics under non-steady state conditions, such as temperature and non-linear contact, the flow stress and strain of E110 alloy also considered is the effect of annealing on radiation damages [73–75]. To analyze the cladding depressurization under internal overpressure, the deformation criterion is used [4].

The steam-zirconium reaction is calculated using weight gain. Conservative and realistic dependencies derived for electrolytic and sponge based E110 alloy could be used. Cathcart-Pawel or Baker-Just correlations are considered as optional. The ECR and integral weight gain of oxygen are determined taking into the consideration cladding deformation. In case of cladding rupture, the oxidation of the cladding inner surface is also considered for determining the total amount of hydrogen gas being generated. The thermal effect due to the steam-zirconium exothermic reaction is also included when solving the heat transfer problem.

3.1.8. SFPR

The SFPR code [76] for mechanistic modelling of single fuel rod behaviour under various regimes of LWR reactor operation (normal and off-normal, including severe accidents) is under development at IBRAE (Moscow). The code is designed by coupling of the two stand-alone mechanistic codes MFPR (for mesoscale modelling of irradiated UO_2 fuel behaviour and fission products release, in collaboration with IRSN, Cadarache) [77, 78] and SVECHA/QUENCH, or S/Q (for modelling of fuel rod thermo-mechanical and physico-chemical behaviour, in collaboration with KIT (former FZK, Karlsruhe) experimentalists [79, 80], intensively developed during the last two decades. Coupling of the two codes allows mechanistic modelling of LWR fuel element behaviour in steady, transient and abnormal conditions.

The main physical models of the two codes were adapted and used in the Russian best-estimate integral code SOCRAT (see Section 3.3.2) designed for analysis of DBA and DEC at Nuclear Power Plants. For this reason, SOCRAT was used in FUMAC benchmark exercises on simulation of the reactor tests IFA-650.9–11 and integral bundle test CORA-15, whereas SFPR was applied to analysis of cladding oxidation and secondary hydriding measured in IFA-650.2 test (see Annex II). Besides, SFPR was further developed for description of corium melt relocation and oxidation during core degradation observed in CORA tests by implementation in the code of the molten corium slug relocation/oxidation model [81], demonstrating possibility of a fuel performance code extension to severe accident conditions (one of the goals of the FUMAC Project), as presented also in Annex II.

3.2. COUPLED THERMAL HYDRAULIC AND FUEL ROD CODES

3.2.1. MARS-KS

The MARS-KS (Multi-dimensional Analysis of Reactor Safety) code has been developed by KAERI for a multi-dimensional and multi-purpose realistic thermal-hydraulic system analysis of light water reactor transients. The backbone of the code has been built by unifying and restructuring the RELAP5/MOD3 and COBRA-TF1 codes. The MARS-KS code has the capability of analyzing a one-dimensional and three-dimensional thermal-hydraulic system as well as the fuel responses of light water reactor transients. Many improved models and capabilities were added to the code, and the latest version of the series is the MARS-KS 1.4. Notable upgrades include 3-dimensional simulation capabilities incorporated into the latest version with a turbulent mixing model and a conduction model. MARS-KS has been mainly used for regulatory activities by Korea Institute of Nuclear Safety (KINS) [82–84].

To develop the MARS-KS/FRAPTRAN code system, the coupling methodology should be developed, because each code system has already been used and validated with their own methodology (see details in Annex II). FRAPTRAN2.0 code was modified as S-fraptran module for implementation into MARS-KS. To couple the variables of two codes, a new module (MARSLINK) was created in S-FRAPTRAN.

As shown in Fig. 43, a coupling methodology for steady state and transient analyses by maintaining each calculation flow and I/O (Input/Output) system is developed.

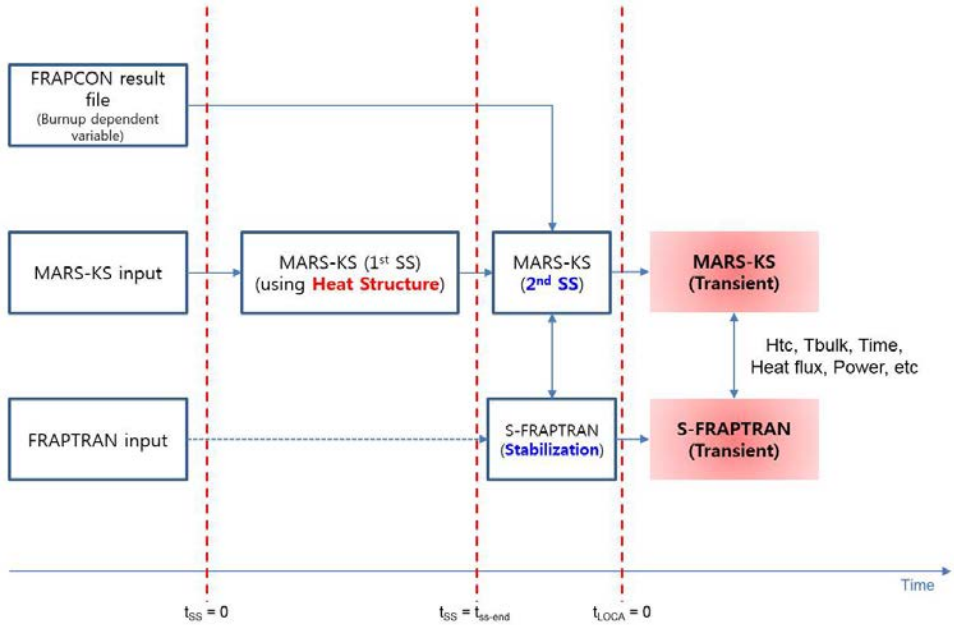

FIG. 43. Methodology of fully coupled MARS-KS/FRAPTRAN.

Coupling variables between MARS-KS and FRAPTRAN are shown in Table 9. For the current time step, MARS-KS calculates the time increment, LHGR, coolant pressure, heat transfer coefficient, and coolant temperature. All variables are stored for S-FRAPTRAN calculation. Subsequently, S-FRAPTRAN calculates the deformed cladding diameter, heat flux, and cladding surface temperature. Those variables are also stored for MARS-KS calculation for the next time step.

The fuel module requires power and thermal hydraulic boundary conditions at the surface of the outer cladding to calculate the thermo-mechanical behaviour of fuel during a LOCA. In addition, the coolant pressure affects the cladding deformation. The system code requires the outer diameter of the cladding and heat flux considering the radial burnup distribution, gap conductance, and metal water reaction energy. All variables are stored in the module and updated at each time step.

TABLE 9. COUPLED VARIABLES OF MARS-KS/FRAPTRAN CODE SYSTEM

Calling module	Variable name	Content
S-fraptran	Timeincrement	Size of Time step
	Power	Linear Heat Generation Rate (LHGR)
	CoolPress	Coolant pressure
	Htc	Heat transfer coefficient of cladding surface
	Tbulk	Coolant T
MARS-KS	Outdia	Cladding outer diameter (incl. oxide thickness)
	Heatflux	Cladding heat flux
	Tsurf	Cladding surface T

3.2.2. GENFLO-FRAPTRAN

The single-rod transient fuel performance code FRAPTRAN developed by PNNL for U.S.NRC [85], has been coupled with the thermal hydraulics code GENFLO, developed at VTT [86, 87].

GENFLO is a fast running program due to its non-iterative solution model of the thermal hydraulics equations. The coupled code has been verified against the experimental results from the Halden project IFA-650 LOCA tests [88]. The principles and models used during the LOCA are based on the SMABRE code developed at VTT [89]. The coupled code, FRAPTRAN-GENFLO, has been previously applied in [90, 91].

3.3. SEVERE ACCIDENT CODES

3.3.1. ATHLET-CD

The system code ATHLET-CD (Analysis of THermal-hydraulics of LEaks and Transients with Core Degradation) [92] describes the reactor coolant system thermal-hydraulic response during severe accidents, including core damage progression as well as fission product and aerosol behaviour, to calculate the source term for containment analyses and to evaluate accident management measures. It is developed by GRS in cooperation with IKE, University of Stuttgart. ATHLET-CD includes also the aerosol and fission product transport code SOPHAEROS, developed by IRSN, and is coupled with the GRS code COCOSYS for modelling thermal-hydraulics and iodine behaviour in the containment.

The code structure is highly modular to include a manifold spectrum of models and to offer an optimum basis for further development (see Fig. 44). The ATHLET code comprises a thermo-fluid-dynamic module, a heat transfer and heat conduction module, a neutron kinetics module, a general control simulation module, and a general-purpose solver of differential equation systems called FEBE. The thermo-fluid-dynamic module is based on a six-equation model, with fully separated balance equations for liquid and vapor, complemented by mass conservation equations for up to 5 different non-condensable gases and by a boron tracking model. Specific models for pumps, valves, separators, mixture level tracking, critical flow etc. are also included in ATHLET.

The rod module ECORE consists of models for fuel rods, absorber rods (AgInCd and B_4C) and for the fuel assemblies including BWR canisters and absorbers. It describes mechanical rod behaviour (ballooning), Zr-alloy and B_4C oxidation (Arrhenius-type rate equations), Zr-UO_2 dissolution and melting of metallic and ceramic components. Melt relocation (candling) is simulated by rivulets with constant velocity and cross-section, starting from the node of a rod failure. The models allow oxidation, freezing, re-melting, re-freezing and melt accumulation due to blockage formation. Feedback to the thermal-hydraulics considers steam starvation and blockage formation. Besides convective heat transfer, energy can be exchanged by radiation amongst fuel rods and to surrounding core structures.

The release of fission products is modelled by rate equations or by a diffusion model within the module FIPREM. The transport and retention of fission products and aerosols in the reactor coolant system are simulated by the module SOPHAEROS. For the simulation of debris bed, a specific model MEWA can be applied, with its own thermal-hydraulic equation system, coupled to the ATHLET fluid-dynamics on the outer boundaries of the debris bed. The transition of the simulation of the core zones from ECORE to MEWA depends on the degree of degradation in the zone. Finally, the code also comprises late phase models for core slumping, melt pool behaviour in the lower plenum and vessel failure within the module AIDA.

The code validation is based on integral- and separate-effect tests, as proposed by the CSNI validation matrices, and covers thermal hydraulics, bundle degradation as well as release and transport of fission products and aerosols. They include out-of-pile bundle experiments performed in the CORA and in the QUENCH facility as well as in-pile experiments performed in the PHÉBUS or in the LOFT facility. The TMI-2 accident is used to assess the code for reactor applications.

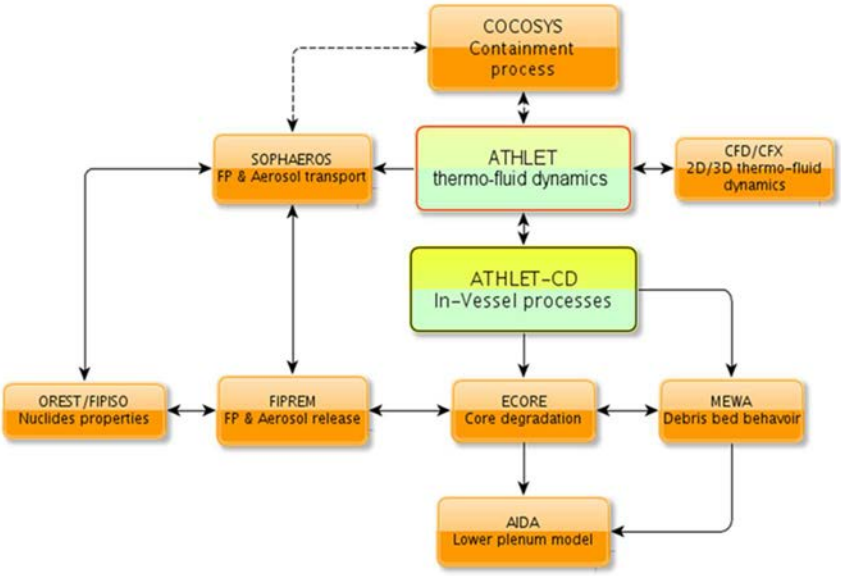

FIG. 44. Modular structure of the system code ATHLET-CD.

3.3.2. SOCRAT

Code SOCRAT is designed for safety assessment of NPP with LWR under severe accident conditions [93]. At in-vessel stage of severe accidents, the following general processes are considered (Fig. 45): core uncover and heat up; radiative and convective heat transfer inside the core and between the core and surrounding the in-vessel structures; deformation and burst (collapse) of fuel rod claddings; release of fission products from solid fuel into reactor coolant system (RCS); coagulation, transport and deposition/resuspension of fission products in RCS; oxidation of fuel rod claddings, absorbers and steel structures in steam or air; fuel degradation (dissolution of UO_2 and ZrO_2 by solid and molten Zr, failure of ZrO_2 protective layer; melting of oxides); fission product release from molten fuel; material relocation (formation of eutectics U-Zr-O, SS-Zr, SS-B_4C; candling down of liquid masses; collapse of fuel rods with formation of debris bed; formation and spreading of molten pools; relocation of corium to lower plenum); melt oxidation, especially containing liquid Zr; account for failure of RCS boundaries (hot leg nozzles, surge-line of pressurizer, SG tubes); fuel-coolant interaction in lower plenum;

behaviour of molten corium inside RPV (convection; crust formation, stratification into metallic and oxide layers); degradation of lower head by molten corium impact; release of molten materials into containment after to RPV breach.

At ex-vessel stage, the following processes are focused in models: hydrogen and steam-air mixture distribution in multicompartment containment by coupling with lumped parameter containment codes KUPOL-M or ANGAR; molten corium – concrete interaction (or retention in core catcher, for example in new designs of VVER); FP behaviour in containment (transport, deposition and resuspension, iodine chemistry, sump chemistry); FP leakage into environment following containment non-tightness; FP release into environment due to containment failure or bypass.

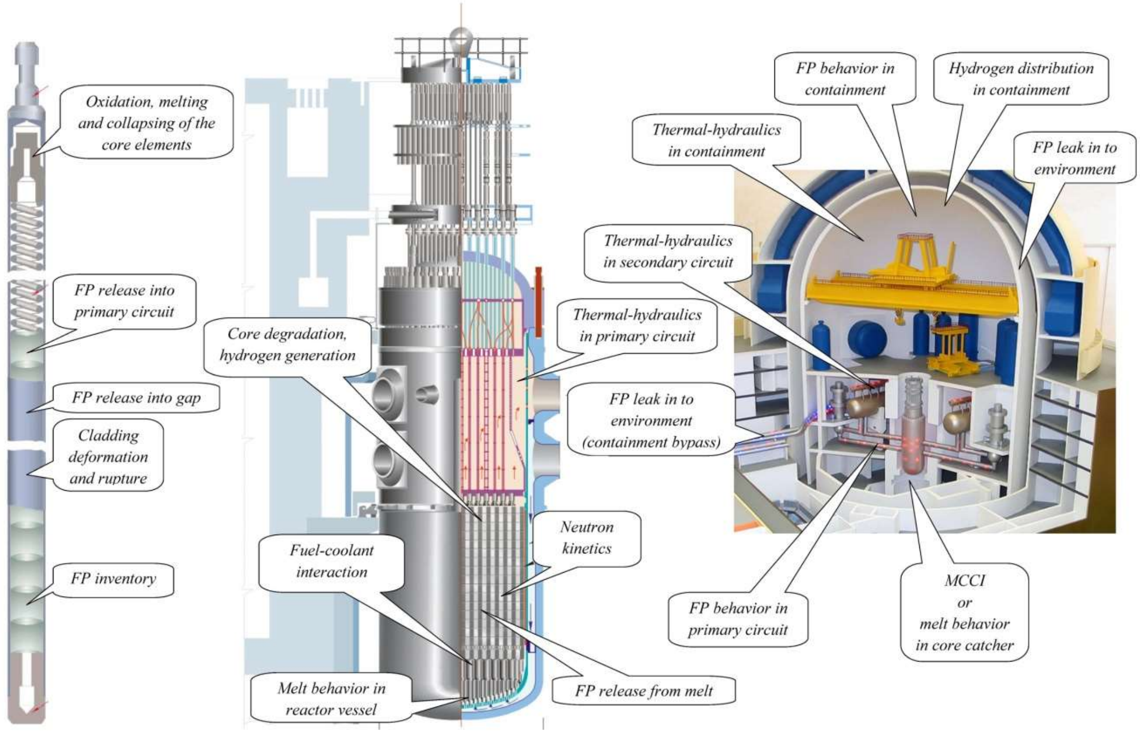

FIG. 45. Phenomena modelled in SOCRAT (reprinted from Ref. [93] *with permission from Elsevier).*

In the framework of FUMAC Project, the goal of the application of the SOCRAT code was twofold. The first one was to verify the code capability to model balloning and burst of irradiated claddings against the Halden IFA-650 tests as well as pressurised fuel bundle degradation in the high temperature CORA-15 test. The second goal was to provide the Project participants with common thermal hydraulic boundary conditions for the fuel performance codes in the benchmark exercise based on Halden IFA-650.9, 10 and 11 tests .

4. COMPARISON OF SIMULATION RESULTS

4.1. MTA EK BURST TESTS

Five organizations provided results for the MTA EK isothermal ballooning cases described in Section 2.1:

- MTA EK (Hungary), FRAPTRAN 2.0 code;
- JRC (European Commission), TRANSURANUS v1m2j17 code;
- INL (USA), BISON 1.4 code;
- CIEMAT (Spain), FRAPTRAN 1.5 code;
- SSTC (Ukraine), TRANSURANUS v1m1j11 code.

Participants were asked to provide results in terms of: 1) time to cladding burst failure, 2) cladding inner pressure at burst and 3) maximum cladding outer hoop strain at burst.

4.1.1. Results of time to burst failure

Result from participants in terms of time to burst for the six MTA EK cases are reported in histogram form in Fig. 46. Experimental data are also included. Test temperature is being arranged in the order of decreasing.

There was a general tendency of the codes to underpredict the time to burst. The TRANSURANUS code (both JRC and SSTC), however, compared very well to the experimental data. The BISON code also compared well, although it was moderately underpredicted the data. The FRAPTRAN code underpredicted the time to cladding burst more pronouncedly than other codes, as indicated from results obtained from both MTA EK and CIEMAT. CIEMAT conducted a parametric exercise to explore the sensitivity of the results to the internal thermal state of the tube. This sensitivity analysis was performed because the gas in the tube might not have reached a thermal equilibrium with the furnace in the FRAPTRAN heat transfer calculation. The study was limited to tests PUZRY-12 and 26 as the time to failure was sensitive to temperature, even doubles in one case (Test # 12), when considering a temperature of 60–80 K lower than the furnace temperature.

JRC commented that the accuracy of the TRANSURANUS predictions of time to burst was in line with previous simulations of similar ballooning tests [94]. Also, JRC tested two different criteria for rod failure (i.e., limiting hoops stress and limiting hoop strain) and noted that the cladding failure criterion had only a small influence on predicting the time to burst, because ballooning occurred very rapidly at its late stage.

Both JRC and INL analyzed the burst time results obtained with TRANSURANUIS and BISON, respectively, as a function of the test temperature. Both institutions noted that the reduction of the burst time as a function of the temperature was reproduced. Deviations of predictions from the experimental data appeared to increase at low temperatures. The latter circumstance was also confirmed by MTA EK in terms of their calculations with FRAPTRAN. Higher discrepancies between calculations and experiments at lower temperatures indicated that deviations might be partly due to a lack of properly modelling of anisotropic creep behaviour, which characterized the alpha-Zr [95].

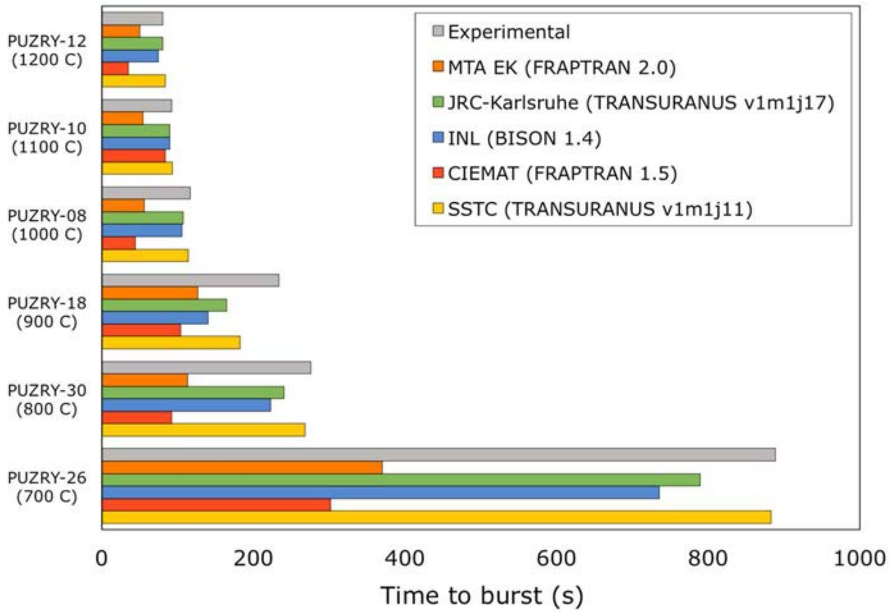

FIG. 46. Time to burst for the MTA-EK ballooning tests. Code-to-code comparisons and experimental data are illustrated.

The high-temperature creep correlations in the codes were generally based on the experimental work of Erbacher et al. [95]. Differences might exist in the chemical composition between the Zr-4 alloy used in the PUZRY experiment and those used in Ref. [95]. Consequently, the observed difference in creep behaviour.

Users effects observed for results obtained from TRANSURANUS and FRAPTRAN might be due to differences in the code versions, as well as a different selection of the modelling options available (such as the burst failure criterion).

4.1.2. Results of pressure at burst failure

Results from participants in terms of cladding inner pressure at the time of burst failure are reported in Fig. 47. Experimental data are also included.

Underpredicting the experimental values for the burst pressure was generally observed. The pressure increase rate was an experimental parameter and an input for the code calculations. An underprediction of the pressure reached at burst time corresponds to an underprediction of the burst time itself.

The calculations from both TRANSURANUS users appeared to be in good agreement with the data. Predictions with the BISON code were also reasonable. A significant underprediction was associated with the FRAPTRAN calculations.

4.1.3. Results of maximum hoop strain at burst failure

Results from participants in terms of hoop strain at the axial peak position (burst location) on the cladding outer surface, at the time of burst failure, are reported in Fig. 48. Experimental data are also included.

Large differences were observed between predictions from different codes and, in many cases, predictions were deviated markedly from the experimental data.

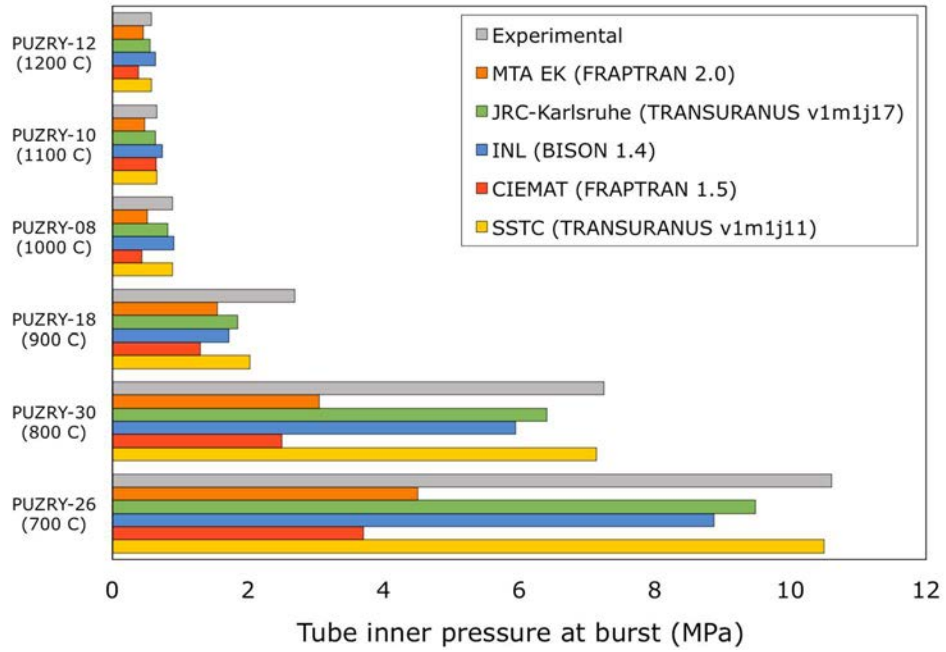

FIG. 47. Cladding inner pressure at burst for the MTA-EK ballooning tests. Code-to-code comparisons and experimental data are illustrated.

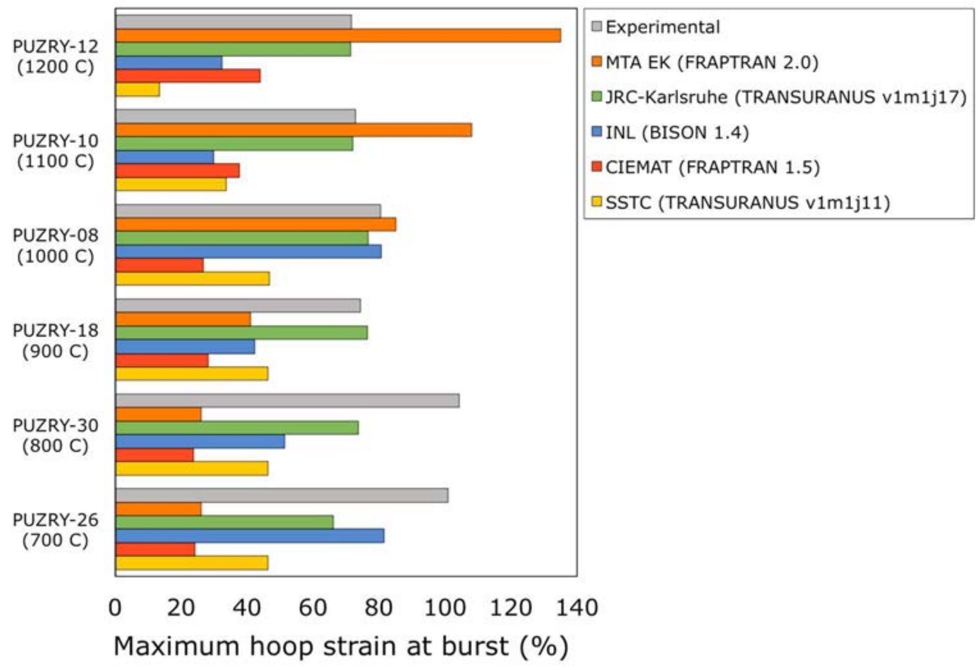

FIG. 48. Maximum cladding outer hoop strain at burst time for the MTA-EK ballooning tests. Code-to-code comparisons and experimental data are illustrated.

Prediction of cladding maximum strain was a difficult task for fuel performance codes, which relates to the number, complexity and mutual dependence of the involved phenomena. Uncertainties in cladding burst strain calculations could be large for LOCA analysis, as very high strain rates were reached when cladding burst was approached. This implied that the maximum strain was very sensitive to the specific criterion adopted to determine the time-of-failure, since a small difference in the failure time could correspond to a large difference in the maximum strain. This was demonstrated by JRC-Karlsruhe when different failure criteria were tested in cladding ballooning and burst simulations with the TRANSURANUS code [94].

INL, JRC and CIEMAT noted that the uncertainty in burst strain predictions was related to the burst criterion. The burst strain results obtained from TRANSURANUS should be considered carefully, since those values exceed the range of acceptability of the models. JRC further commented that the strains obtained from bundle tests (e.g. QUENCH) were typically smaller than those observed in single rod tests, which could be attributed in part due to the azimuthal temperature gradient along the cladding, as indicated by the available experimental evidence [96]. Taking this aspect into calculations would require a full 3D modelling[1], while calculations within FUMAC were performed using either 1.5D or 2D-rz geometrical representations.

Besides modelling uncertainties, measurement and instrument uncertainties could also be added to the expected discrepancies between calculations and experimental data. The interpretation of the burst opening (cladding flaps that protrude outwards following burst) might also introduce a bias in the measured strain relative to the strain due to ballooning only. This was evident in the post-test cladding diameter profile measured for the Halden IFA-650.10 experiment[2] [97]. Code predictions referred to the strain in the cladding just before burst, i.e., the maximum ballooning strain. For the MTA EK tests, the nature of the measurements could not be clarified.

4.2. HALDEN LOCA TESTS (IFA-650.9, 10, 11)

It was agreed at the 2nd Research Coordination Meeting to use common thermal hydraulic (T/H) boundary conditions (BCs) for all fuel performance codes in the benchmark exercise based on Halden IFA-650.9, 10 and 11 tests, which were provided by the integral code SOCRAT.

The developed Halden IFA-650 geometrical model of the test rig in SOCRAT allowed simulating the main phases of the test scenarios – natural circulation, blowdown, heat-up and spray operation, and cool-down phases. It comprised the test flask, blowdown system, and some part of high-pressure heavy water loop connected to the flask (both hot and cold legs). The nodalization of the test flask was furher completed for each test in order to account for some specific details of the test section (for example, fuel rod geometry).

The delivered information for the code benchmarking was: evolution of the cladding and coolant temperatures, heat transfer rates by convection and radiation (for the derivation of the heat transfer coefficient) in 26 nodes, coolant inlet/outlet pressure, temperatures of both phases, void fraction, and flowrates of the fluid and the gas mixture components (steam, hydrogen, argon and helium) at the time span from the end of phase 1 (forced circulation) to the end of the tests. Total rod and heater power evolutions were provided for information to obtain more consistent results. More details on the development of the T/H boundary conditions can be found in Annex II (paper entitled “Simulation of initial and boundary conditions with SOCRAT code for benchmarks based on IFA-650.10 AND IFA-650.11 tests”).

4.2.1. IFA-650.9

Results from code prediction for these Halden LOCA Tests (IFA-650.9, 10, 11), from the participants were similar, in terms of comparison with the experimental data. Ten organizations from different countries provided results for the IFA-650.9 test:

---

[1] Strictly speaking, azimuthal variations can be also captured with 2D-rz representations. However, 3D is needed to include also axial variations.

[2] During the FUMAC RCM 3, it was clarified that the peak observed in the measured cladding diameter profile for IFA-650.10 [97] is an effect of the burst opening and should not be considered when comparing to calculations.

— CIAE (China), FTPAC 1.0;
— CIEMAT (Spain), FRAPCON 3.5 and FRAPTRAN 1.5;
— CNPRI (China), FRAPCON 3.4 and FRAPTRAN 1.5;
— CNEA (Argentina), DIONISIO 2.0;
— KAERI (Republic of Korea), FRAPCON 3.4 and FRAPTRAN 2.0;
— IBRAE (Russia), SOCRAT/V3;
— IPEN (Brazil), FRAPCON 3.4 and FRAPTRAN 1.5;
— SSM/ Quantum Technologies AB (Sweden), FRAPCON 3.5 and FRAPTRAN-QT-1.5b;
— Tractebel (Belgium), FRAPCON 4.0 and FRAPTRAN-TE-1.5 (with axial fuel relocation and FEA models);
— VNIINM, Bochvar Institute (Russia), RAPTA 5.2.

4.2.1.1. Results at the end of the base irradiation

For all participants, the calculated burnup was close to the average measured discharge burnup for the fuel rod (Fig. 49). The predicted pellet to cladding gap at the end of the irradiation was more scattered (Fig. 50), with gap closure predicted by one participant. As a general trend, low values of residual gap were expected at this burnup, but no experimental data was available. The diametral clad strain was also scattered among various calculations (Fig. 51). On the other hand, a reasonable agreement was achieved for the clad elongation (Fig. 52). The calculated corrosion layer (Fig. 53) was in good agreement with the experimental data (7 µm) for most of the participants.

Only two participants provided results for the radial distribution of fission gas inventory before the transient (Fig. 54). A significant discrepancy between the calculated and measured values was evident.

Calculated data after the pre-test irradiation, presented in Figs 49–54, were used by some participants as the initial conditions for the IFA-650.9 transient calculations. For some codes such as SOCRAT, RAPTA 5.2 and FTPAC 1.0 that were used by IBRAE, Bochvar Institute and CIAE respectively, experimental data were used as the initial conditions for the benchmark exercise, for example a burnup of 89.9 MWd/kgU and a corrosion layer of 7 µm were used for IFA-650.9. Similar approaches were applied for the other IFA-650 transient simulations.

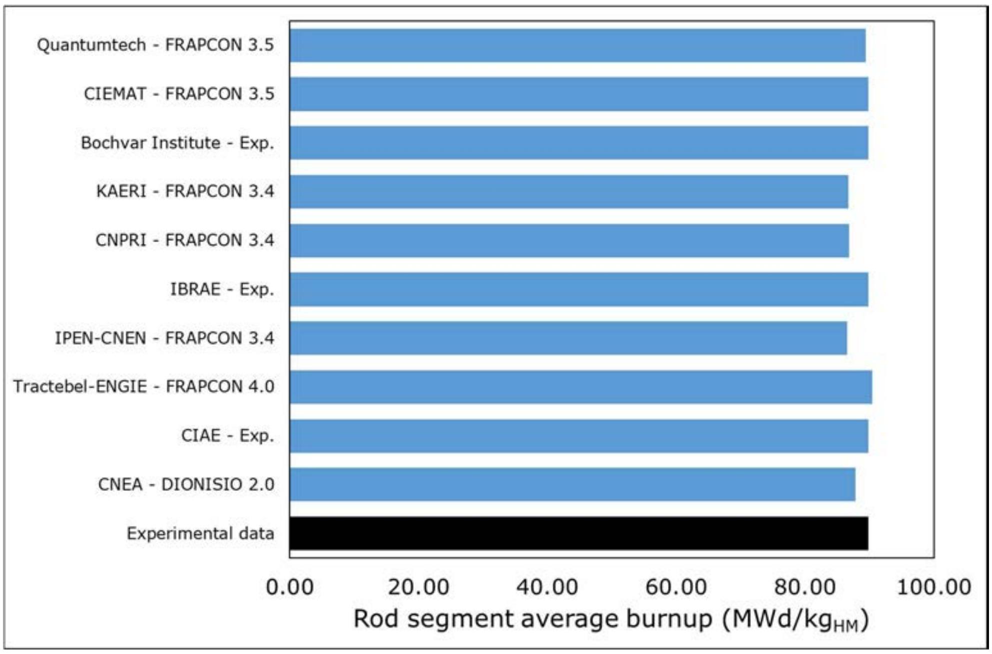

FIG. 49. Comparison of the rod segment average burnup for the IFA-650.9 test.

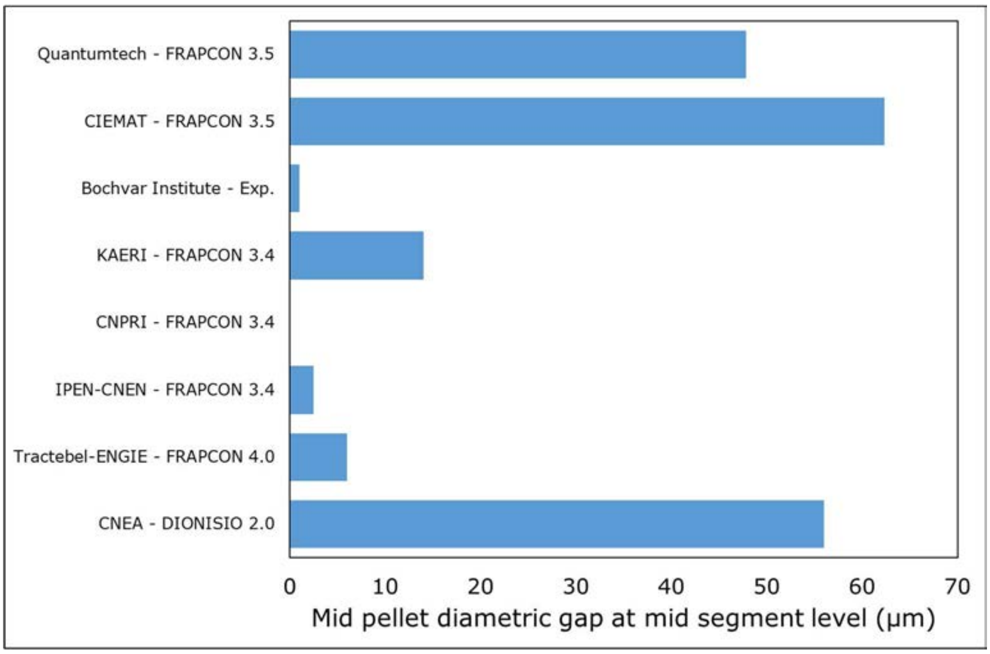

FIG. 50. Comparison of the diametral gap at the mid pellet region for the IFA-650.9 test.

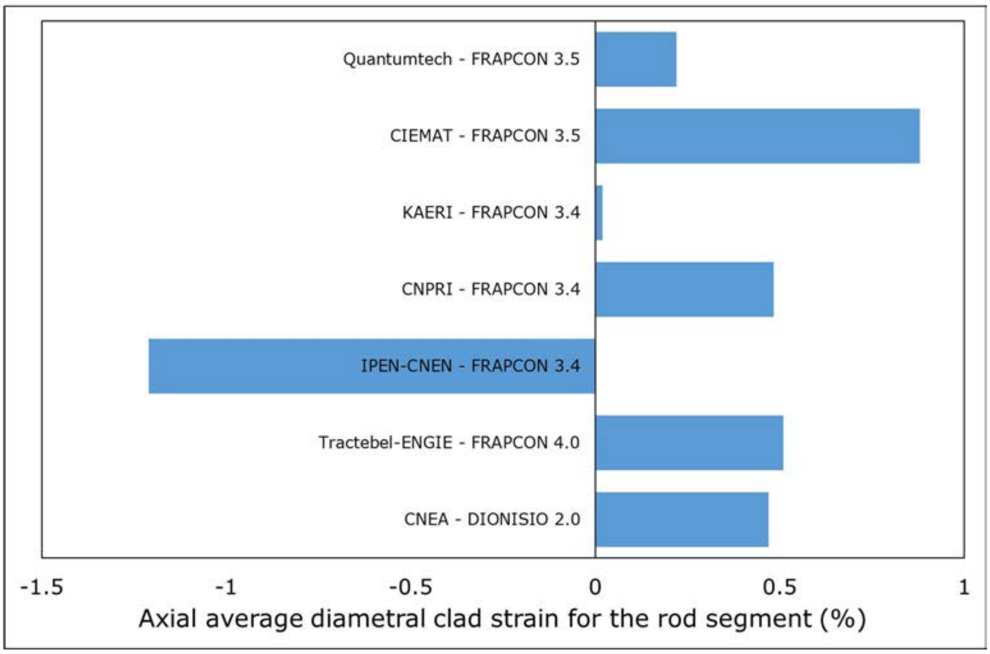

FIG. 51. Comparison of the average diametral clad strain for the IFA-650.9 test.

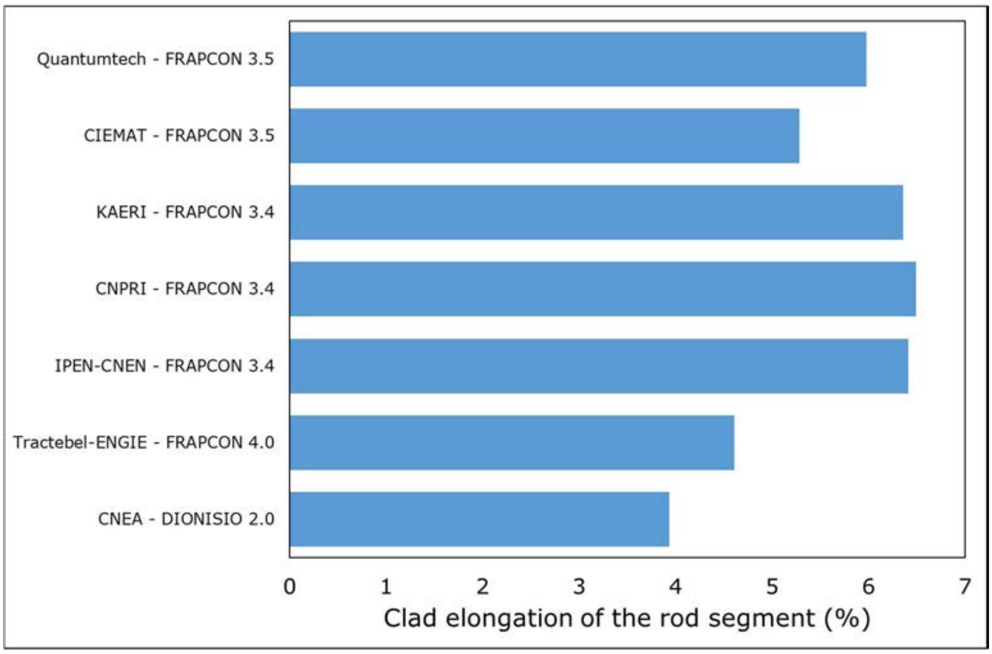

FIG. 52. Comparison of clad elongation for the IFA-650.9 test.

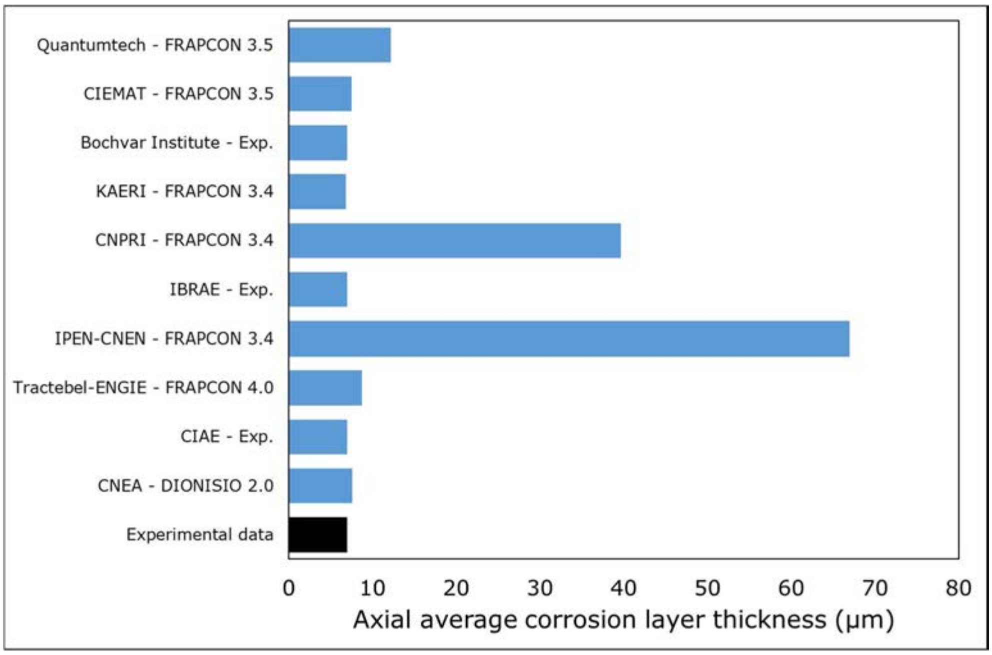

FIG. 53. Comparison of the average corrosion layer thickness for the IFA-650.9 test.

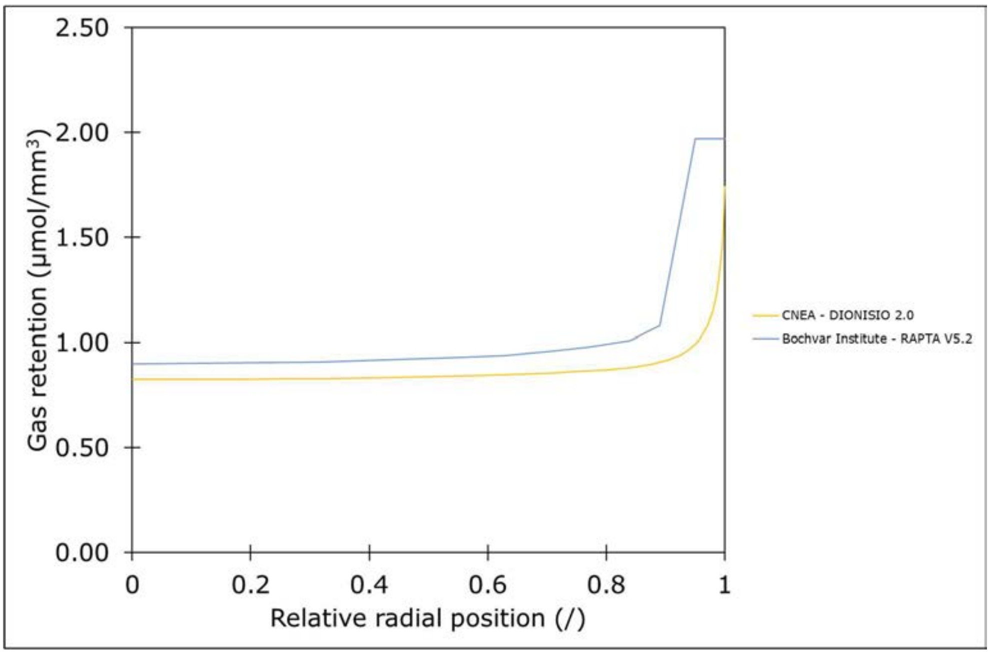

FIG. 54. Comparison of gas retention for the IFA-650.9 test.

4.2.1.2. Results during the LOCA transient

For this section, time reference was set at the beginning of the transient. Figure 55 indicated a comparison of the calculated plenum temperature. A clustering in two group of results was emerged. The difference was probably caused by the modelling assumptions selected by the participants for the calculation of the plenum temperature. The clustering did not depend on the code used for the simulation.

A comparison of the calculated total fission gas release is indicated in Fig. 56. The scattering of results among various participants was significant, as the kinetic evolution of the fission gas release along the transient was deviated significantly. The number of participants able to calculate this quantity was limited. This observation indicated the importance of further model development for the prediction of fission gas behaviour during the transients.

A comparison of the calculated internal pressure is indicated in Fig. 57. Instead of the ballooning phase (pressure decreased before burst), several participants predicted an increase in the pressure prior to the burst. As described by CIEMAT, a specific algorithm was used by FRAPTRAN to evaluate the inner pressure in the plenum. The qualitative agreement among the participants was reasonable.

A comparison of the cladding outer temperature (at the position of the burst) is indicated in Fig. 58. All results were reasonably close to each other, with a similar time evolution. These trends depended on the boundary conditions adopted by the participants.

A comparison of the cladding elongation is indicated in Fig. 59. The scattering of results among various participants was significant. This could be ascribed to the difference in material properties of the cladding used in different codes, since the thermal boundary conditions are similar among the partners.

A comparison of the cladding radial displacement (at the position of the burst) is indicated in Fig. 60. Similar observations and comments as for the elongation (in Fig. 59) could be made.

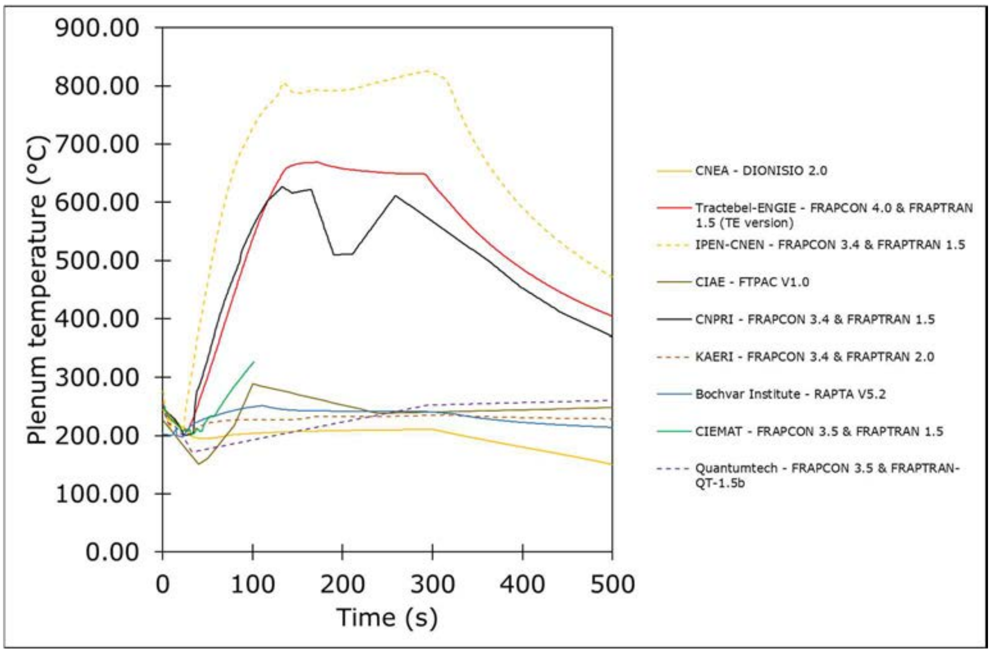

FIG. 55. Comparison of the plenum temperature during the LOCA transient of the IFA-650.9 test.

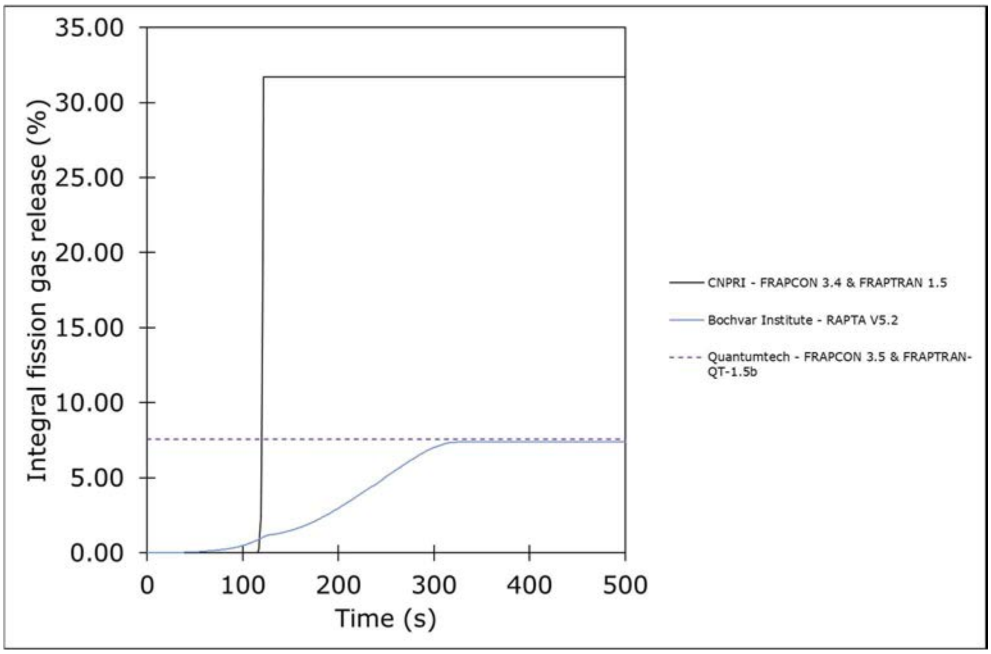

FIG. 56. Comparison of the integral fission gas release during the LOCA transient of the IFA-650.9 test.

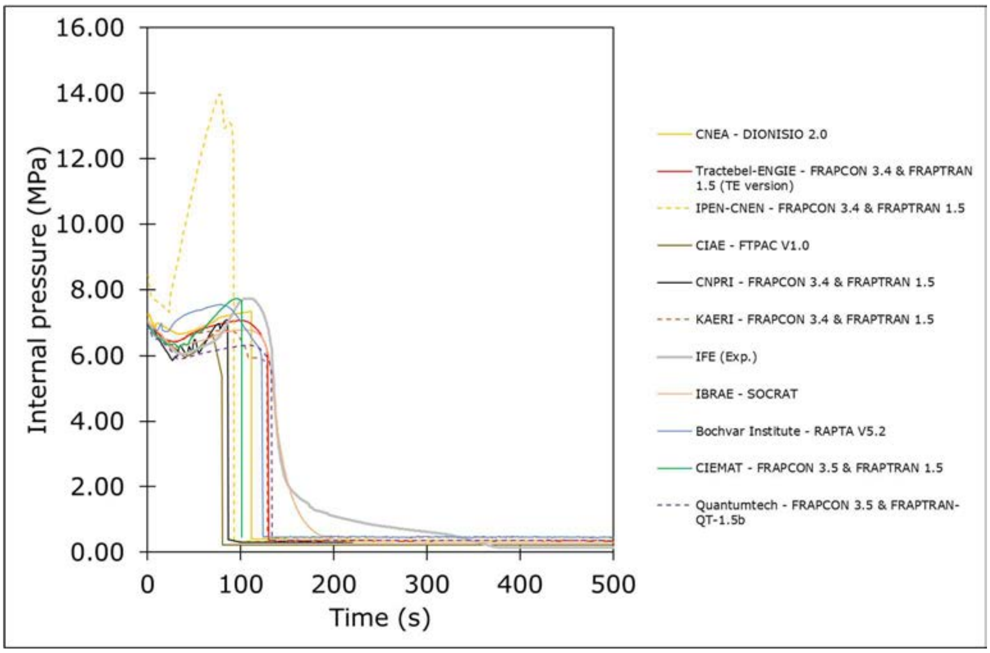

FIG. 57. Comparison of the internal pressure during the LOCA transient of the IFA-650.9 test.

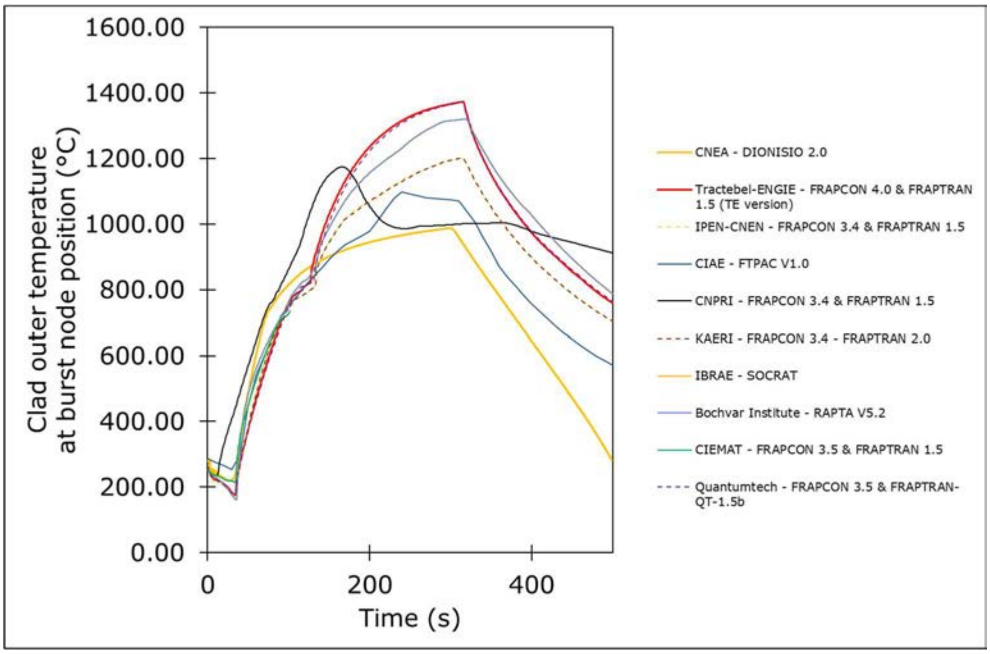

FIG. 58. Comparison of the clad outer temperature at burst position during the LOCA transient of the IFA-650.9 test.

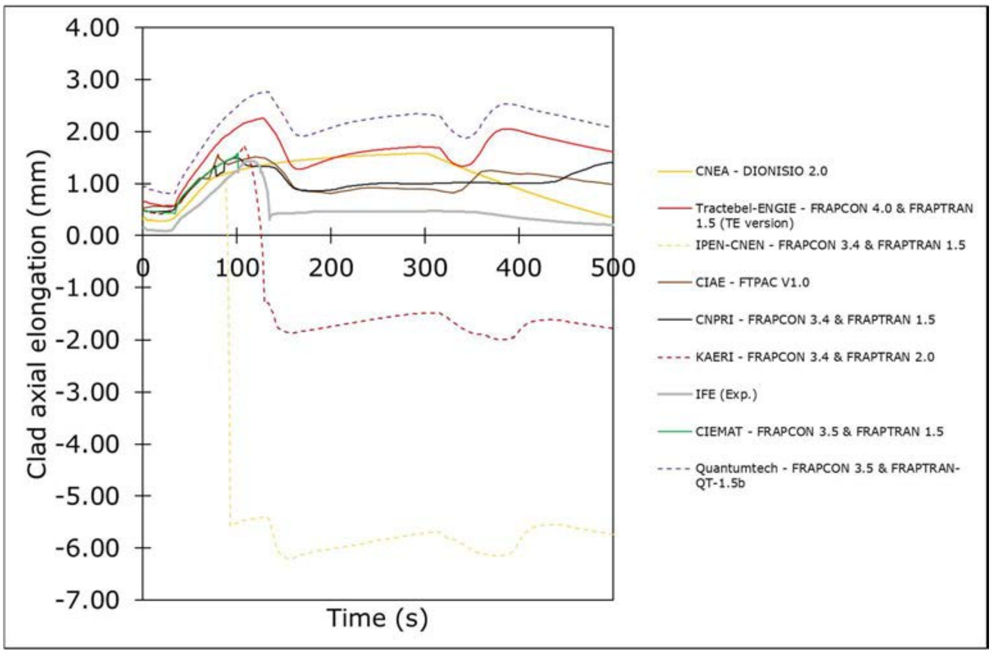

FIG. 59. Comparison of the clad axial elongation during the LOCA transient of the IFA-650.9 test.

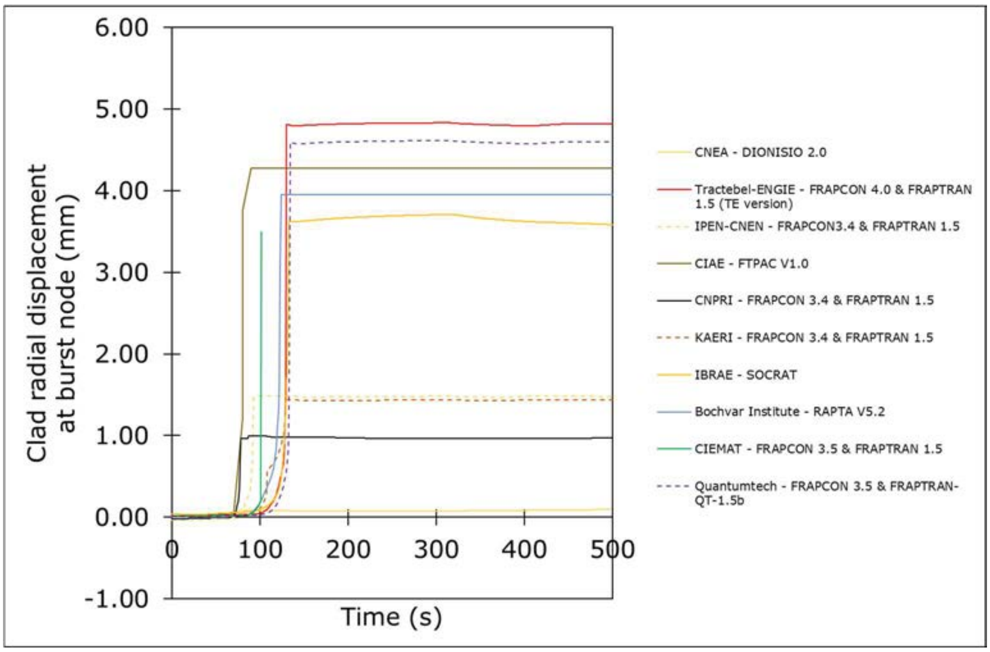

FIG. 60. Comparison of the clad radial displacement at burst position during the LOCA transient of the IFA-650.9 test.

4.2.1.3. Results at the end of the LOCA transient

The scattering in the predicted failure times among the different participant was significant (see Fig. 61).

The axial profile of the cladding diameter (and in general indicating the location of the burst) and the diametral gap are shown in Figs 62 and 65, respectively. The scattering of the calculated deformation was related to the burst criteria used in various codes. The experimental data (i.e. the maximum strain or stress criteria) were quite scattered that led to different results.

The cladding oxide thickness calculated by the participants was also scattered (Fig. 63), despite the cladding temperature used as an input for the code was similar for all participants. The same level of scattering was observed for the equivalent cladding reacted (Fig. 64). Potentially, different oxidation models were existed for different participants.

Some participants provided an assessment of fuel fragmentation volume fraction along the rod segment, as indicated in Fig. 66. A reasonable agreement was obtained considering the novelty of the models involved.

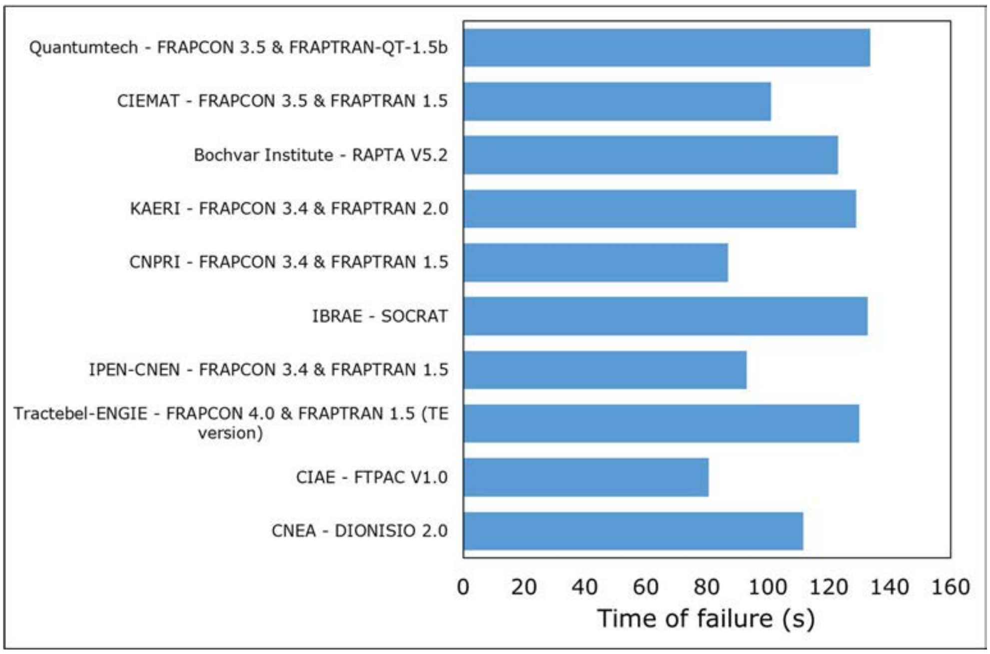

FIG. 61. Comparison of the time of failure of the IFA-650.9 test.

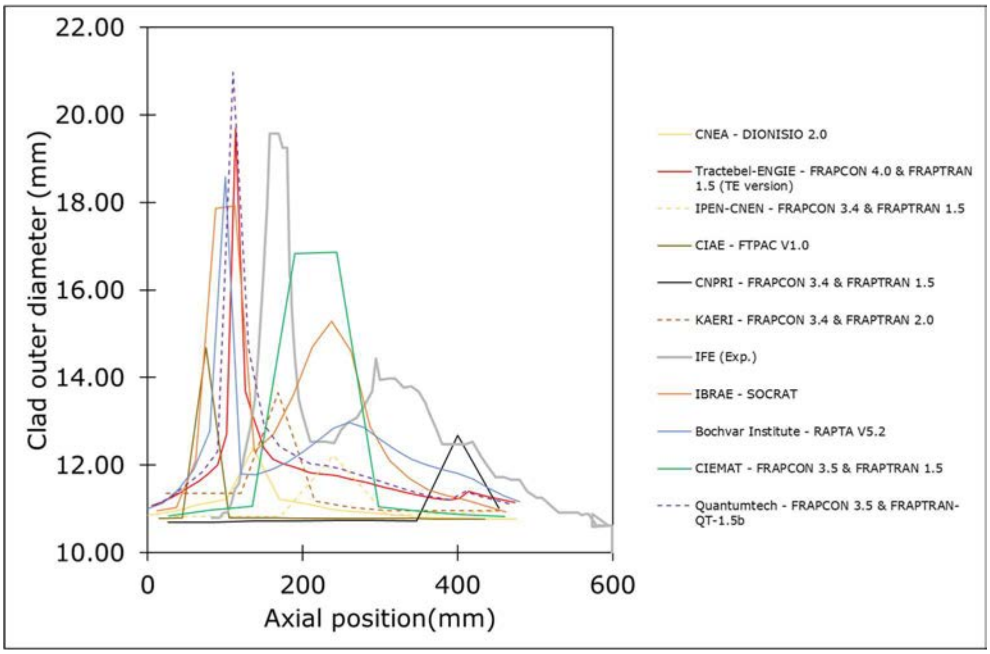

FIG. 62. Comparison of the cladding outer diameter after the IFA-650.9 test.

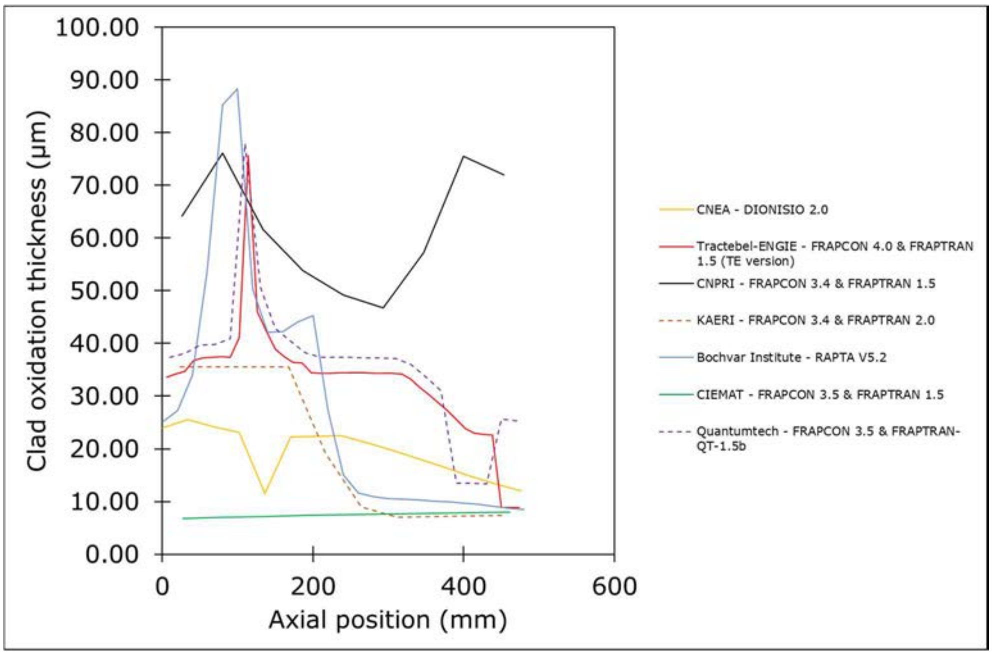

FIG. 63. Comparison of the cladding oxide thickness after the IFA-650.9 test.

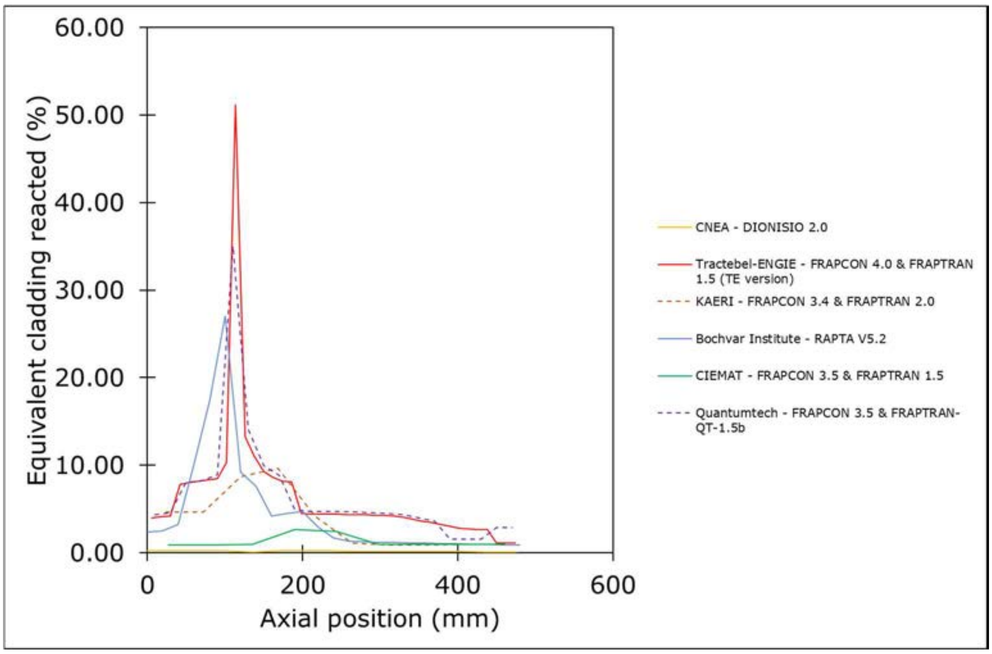

FIG. 64. Comparison of the equivalent cladding reacted after the IFA-650.9 test.

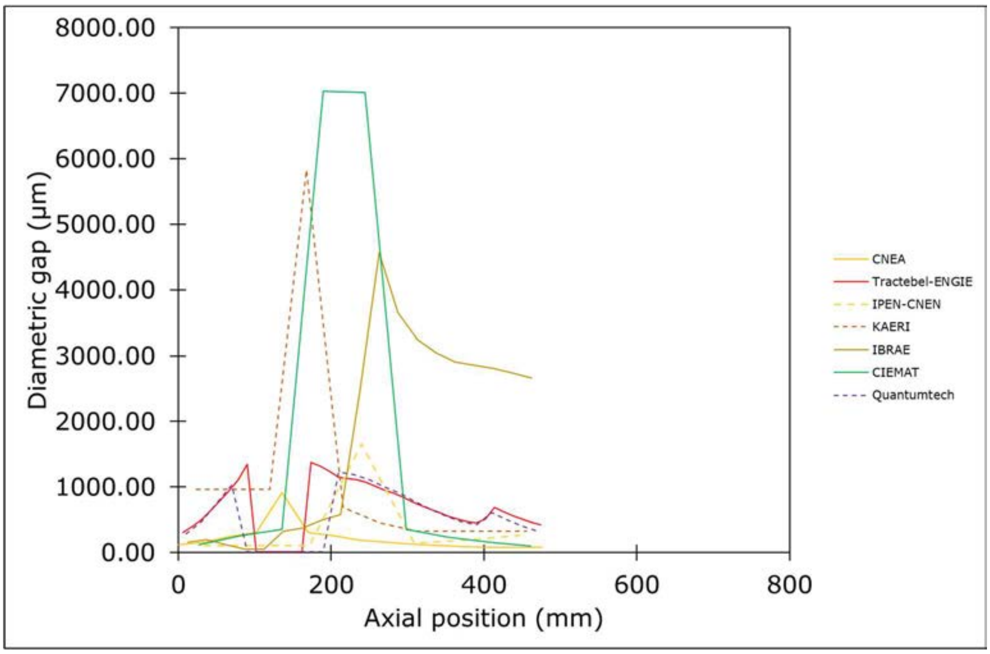

FIG. 65. Comparison of the diametral gap after the IFA-650.9 test.

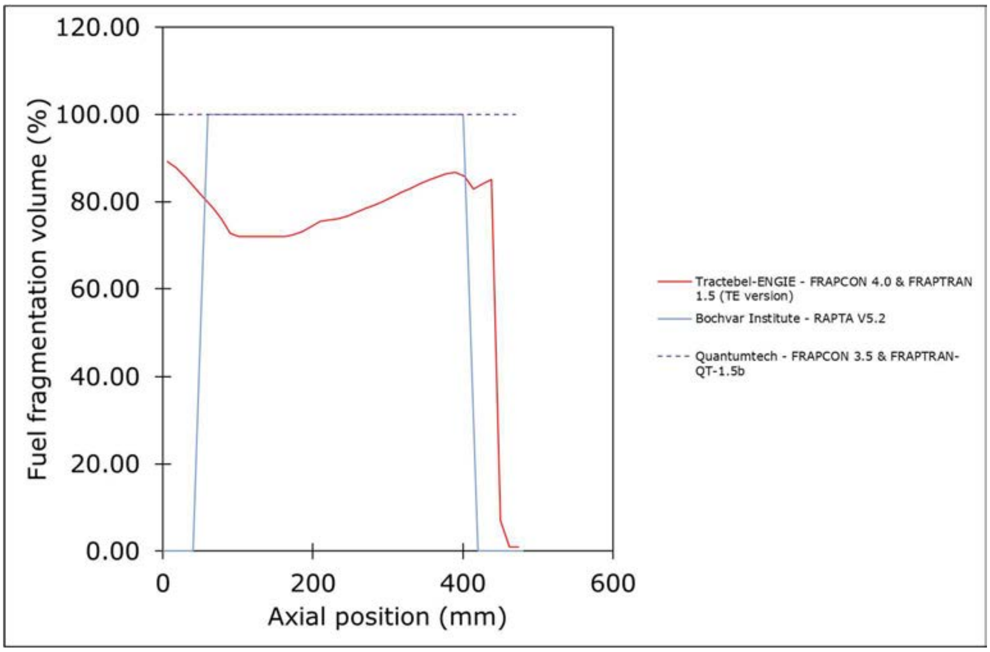

FIG. 66. Comparison of the fuel fragmentation volume after the IFA-650.9 test.

4.2.2. IFA-650.10

Sixteen organizations from different countries provided results for the IFA-650.10 test:

— CNPRI (China), FRAPCON 3.4 and FRAPTRAN 1.5;
— INRNE (Bulgaria), TRANSURANUS v1m1j17;
— CEA (France), ALCYONE v1.4;
— CIEMAT (Spain), FRAPCON 3.5 and FRAPTRAN 1.5;
— CNEA (Argentina), DIONISIO 2.0;
— IBRAE (Russia), SOCRAT/V3;

— JRC-Karlsruhe (European Union), TRANSURANUS;
— KAERI (Republic of Korea), FRAPCON 3.4 and FRAPTRAN 2.0;
— CIAE (China), FTPAC 1.0;
— IPEN (Brazil), FRAPCON 3.4 and FRAPTRAN 1.5;
— SSM/ Quantum Technologies AB (Sweden), FRAPCON 3.5 and FRAPTRAN-QT-1.5b;
— INL (United States), BISON 1.4;
— SSTC NRS (Ukraine), TRANSURANUS v1m1j17;
— Tractebel (Belgium), FRAPCON 4.0 and FRAPTRAN-TE-1.5 (with axial fuel relocation and FEA models);
— VTT (Finland), FRAPCON 4.0 and FRAPTRAN 2.;0
— VNIINM, Bochvar Institute (Russia), RAPTA 5.2.

4.2.2.1. Results at the end of the base irradiation

For all participants, the calculated burnup was quite close to the average measured discharge burnup of the fuel rod (Fig. 67). The residual pellet to cladding gap was scattered (Fig. 68). As a general trend, a low value of residual gap was expected at this burnup, but no experimental data was available for comparison. The diametral strain was rather scattered among different calculations (Fig. 69). On the other hand, a reasonable agreement was achieved for the clad elongation (Fig. 70). The corrosion layer calculated (Fig. 71) was in good agreement with the experimental data (of 25 µm) for most cases.

Some participants provided results for the distribution of the fission gas inventory before the transient (Fig. 72). However, a significant discrepancy was evident.

For SOCRAT calculation by IBRAE, the experimental data for a burnup of 61 MWd/kgU and a corrosion layer of 30 µm were used as the initial states for the benchmark exercise.

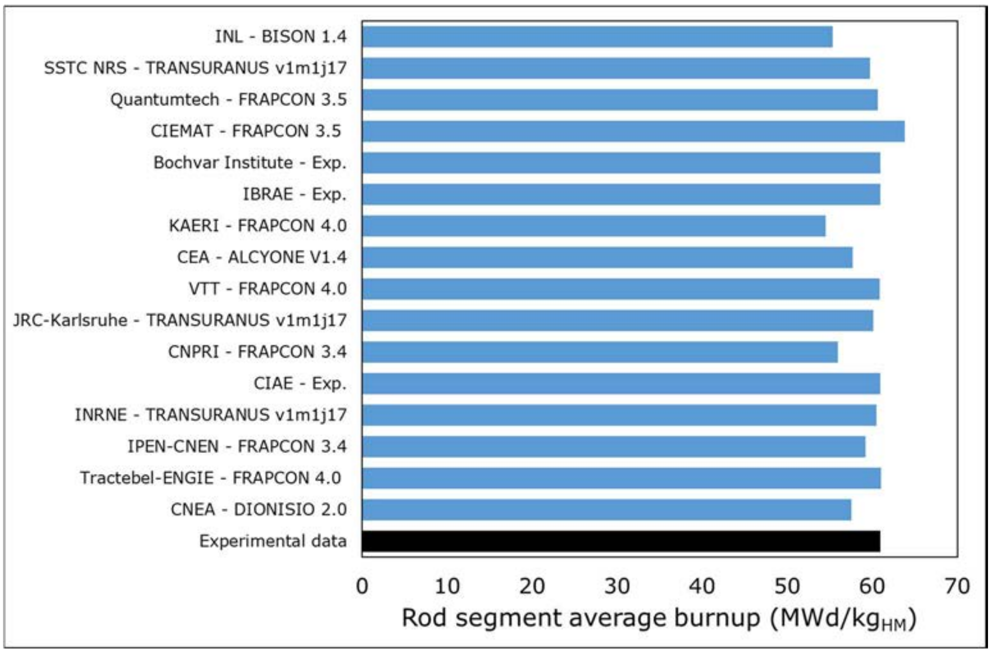

FIG. 67. Comparison of the rod segment average burnup for the base irradiation of the IFA-650.10 test.

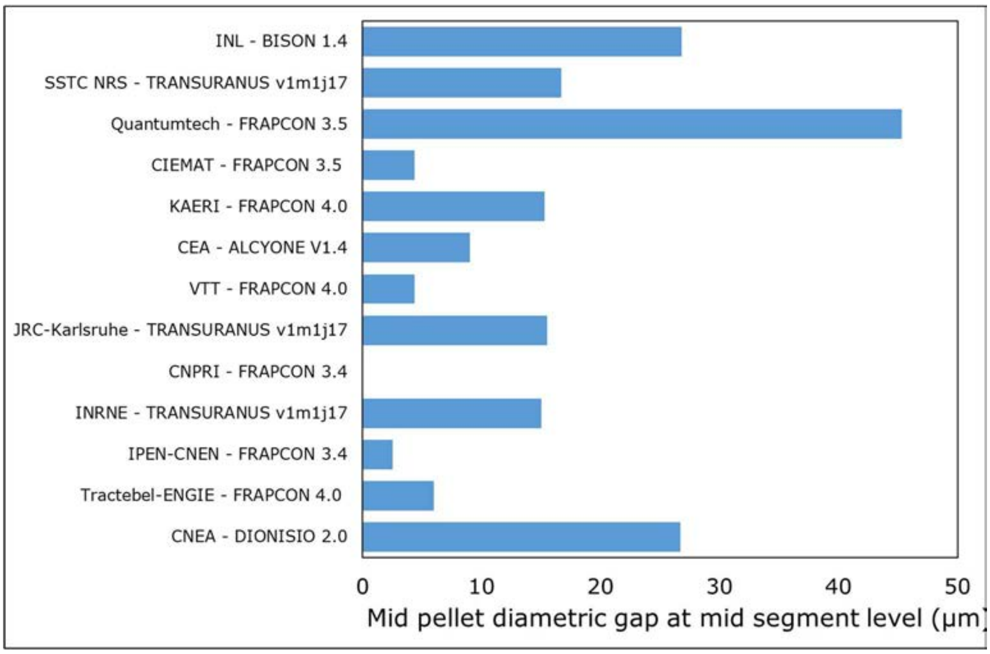

FIG. 68. Comparison of the diametral gap at the mid pellet at the end of the base irradiation of the IFA-650.10 test.

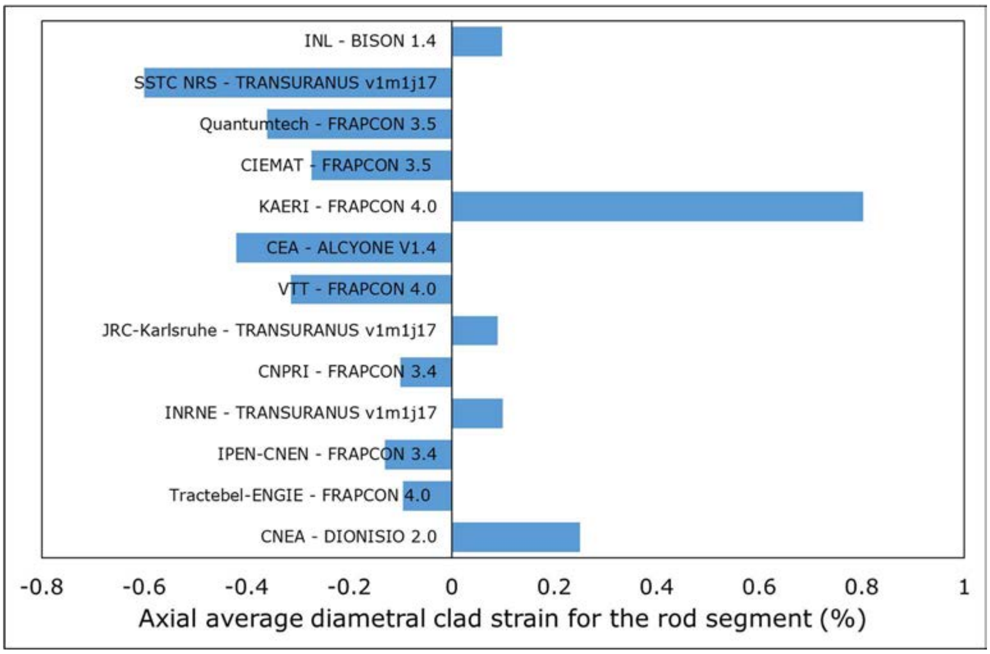

FIG. 69. Comparison of the axial average diametral clad strain at the end of the base irradiation of the IFA-650.10 test.

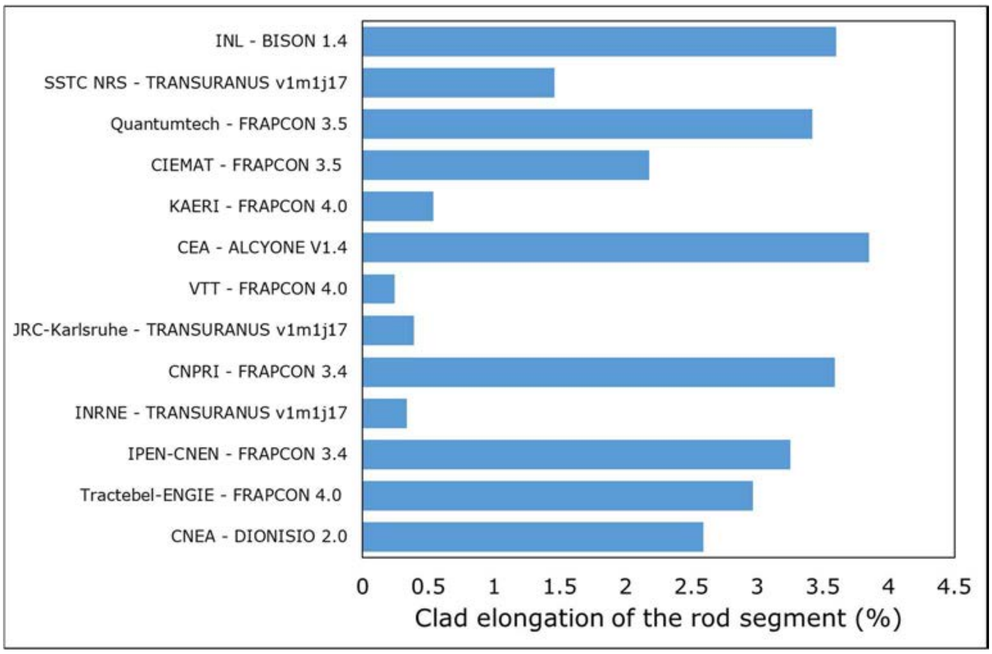

FIG. 70. Comparison of the clad elongation at the end of the base irradiation of the IFA-650.10 test.

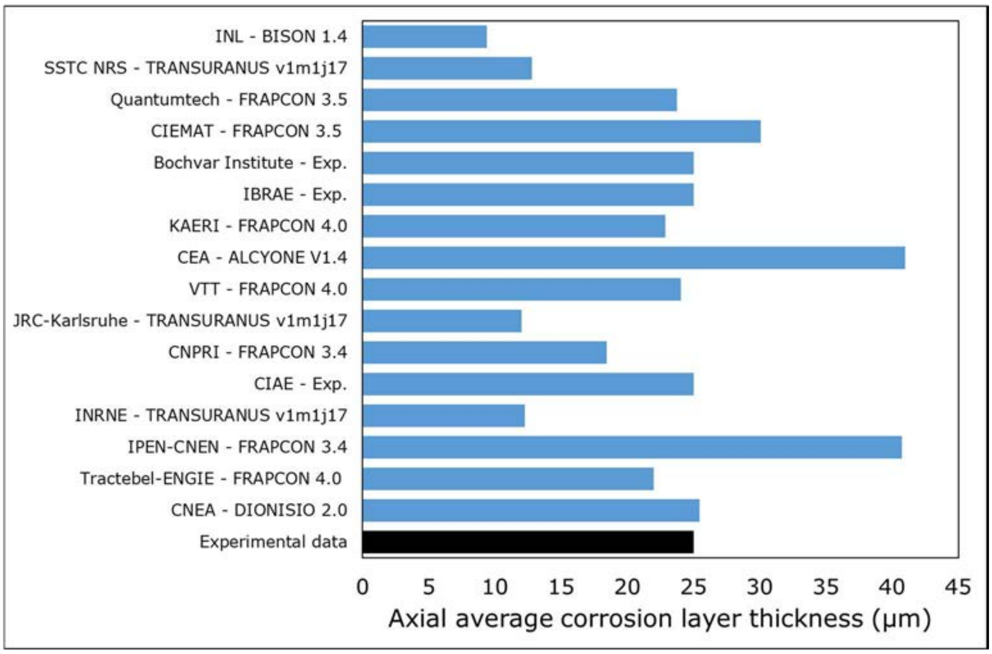

FIG. 71. Comparison of the axial average corrosion layer thickness at the end of the base irradiation of the IFA-650.10 test.

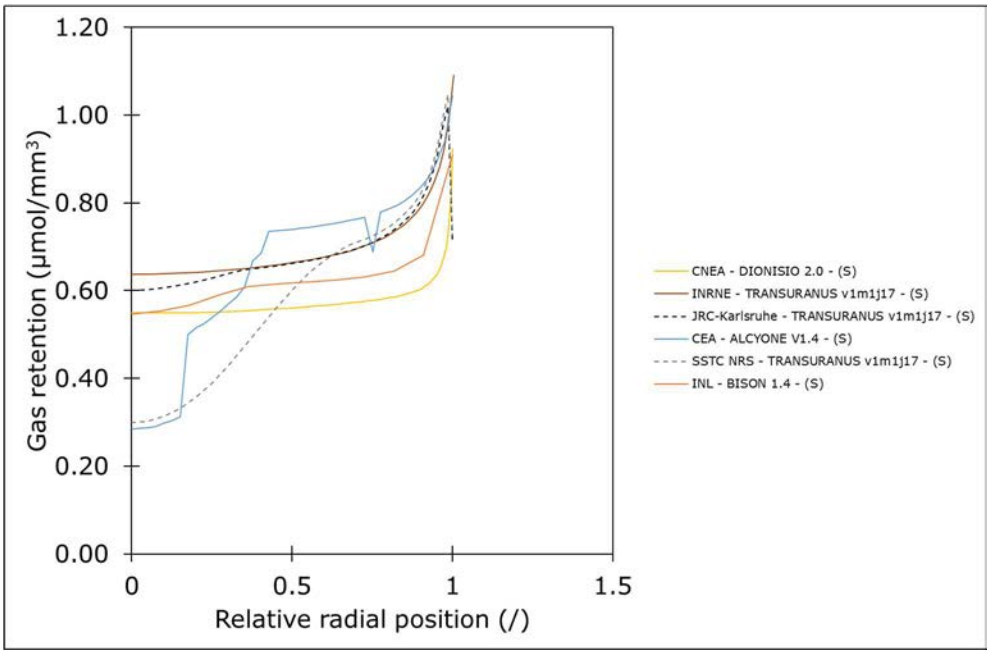

FIG. 72. Comparison of fission gas inventory at the end of base irradiation for the IFA-650.10 test. (S) stands for simulated boundary conditions, while (M) stands for measured boundary conditions.

4.2.2.2. Results during the LOCA transient

For the following Figs, time reference is set at the beginning of the transient. Results are similar to those obtained for the IFA-650.9 test.

A comparison of the calculated plenum temperature is indicated in Fig. 73. A clustering of two group of results was evident. The difference was probably caused by the modelling options selected by the participants for the calculation of the plenum temperature (the clustering did not depend on the code used for the simulation).

A comparison of the calculated total fission gas release is indicated in Fig. 74. The scattering among the predicted values was significant. The differences in the kinetic evolution of the fission gas release along the transient were also significant. The number of participants that could calculate this affect was limited. These observations suggested the importance of further model development for the prediction of fission gas release during a LOCA transient.

A comparison of the calculated internal pressure is indicated in Fig. 75. Instead of the ballooning phase (pressure decrease before burst), several participants predicted an increase in the pressure prior to the burst. As described by CIEMAT, a specific algorithm was used by FRAPTRAN to evaluate the inner pressure in the plenum. The qualitative agreement among the participants was reasonable.

A comparison of the cladding outer temperature (at the position of the burst) is indicated in Fig. 76. Results were reasonably close to each other, with a similar time evolution. The predicted cladding temperature would depend on the boundary conditions adopted by the participants.

A comparison of the cladding elongation is indicated in Fig. 77. The scattering of results among different participants was significant. This could be ascribed to the difference in material properties of the cladding used in different codes, since the thermal boundary conditions are similar among the partners.

A comparison of the cladding radial displacement (at the position of the burst) is indicated in Fig. 78. Similar explanations as those for the elongation could be made.

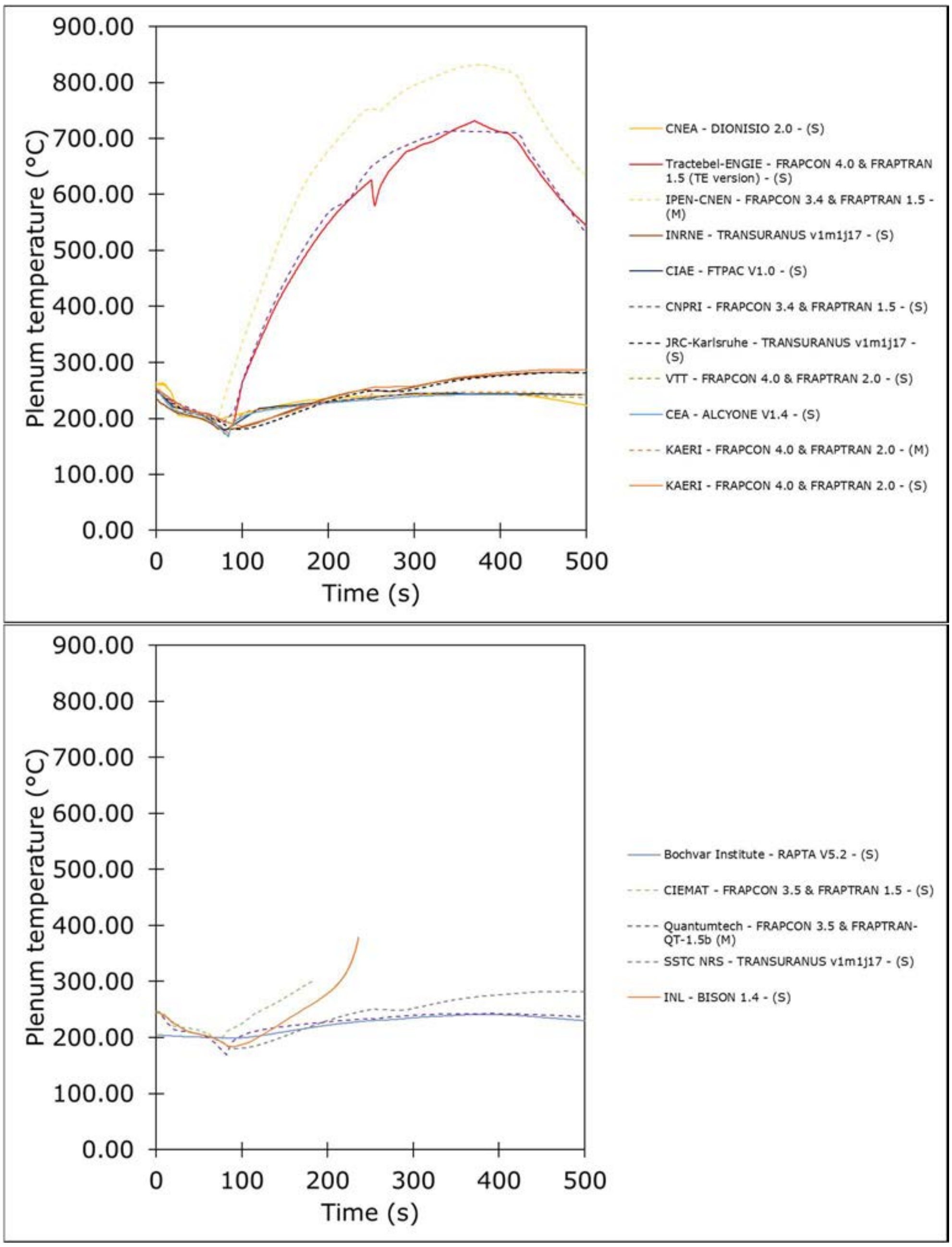

FIG. 73. Comparison of the plenum temperature during the LOCA transient of the IFA-650.10 test. (S) stands for simulated boundary conditions, while (M) stands for measured boundary conditions.

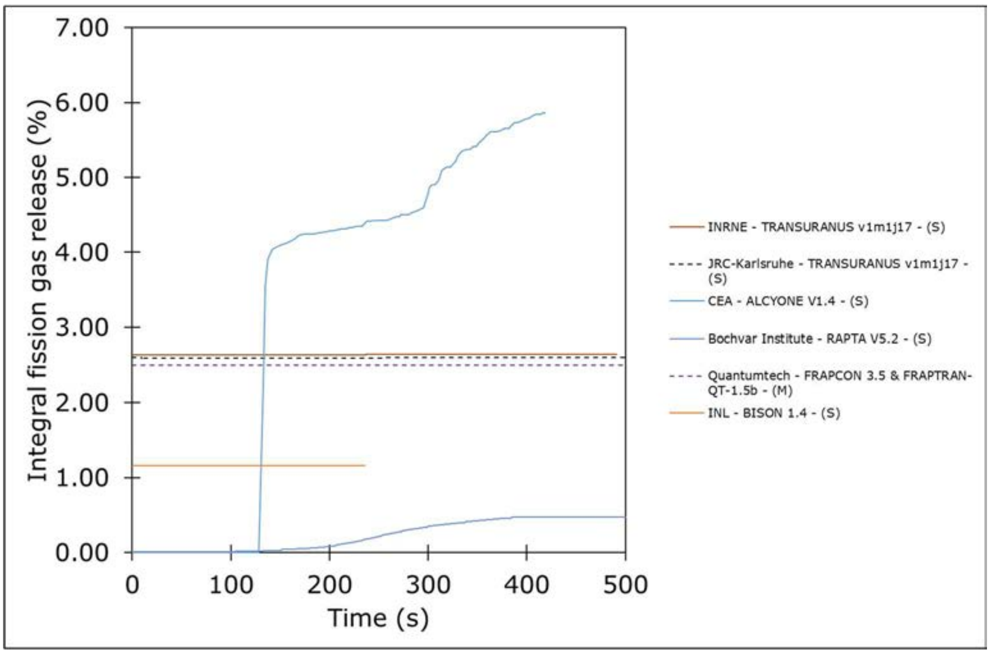

FIG. 74. Comparison of the total fission gas release during the LOCA transient of the IFA-650.10 test. (S) stands for simulated boundary conditions, while (M) stands for measured boundary conditions.

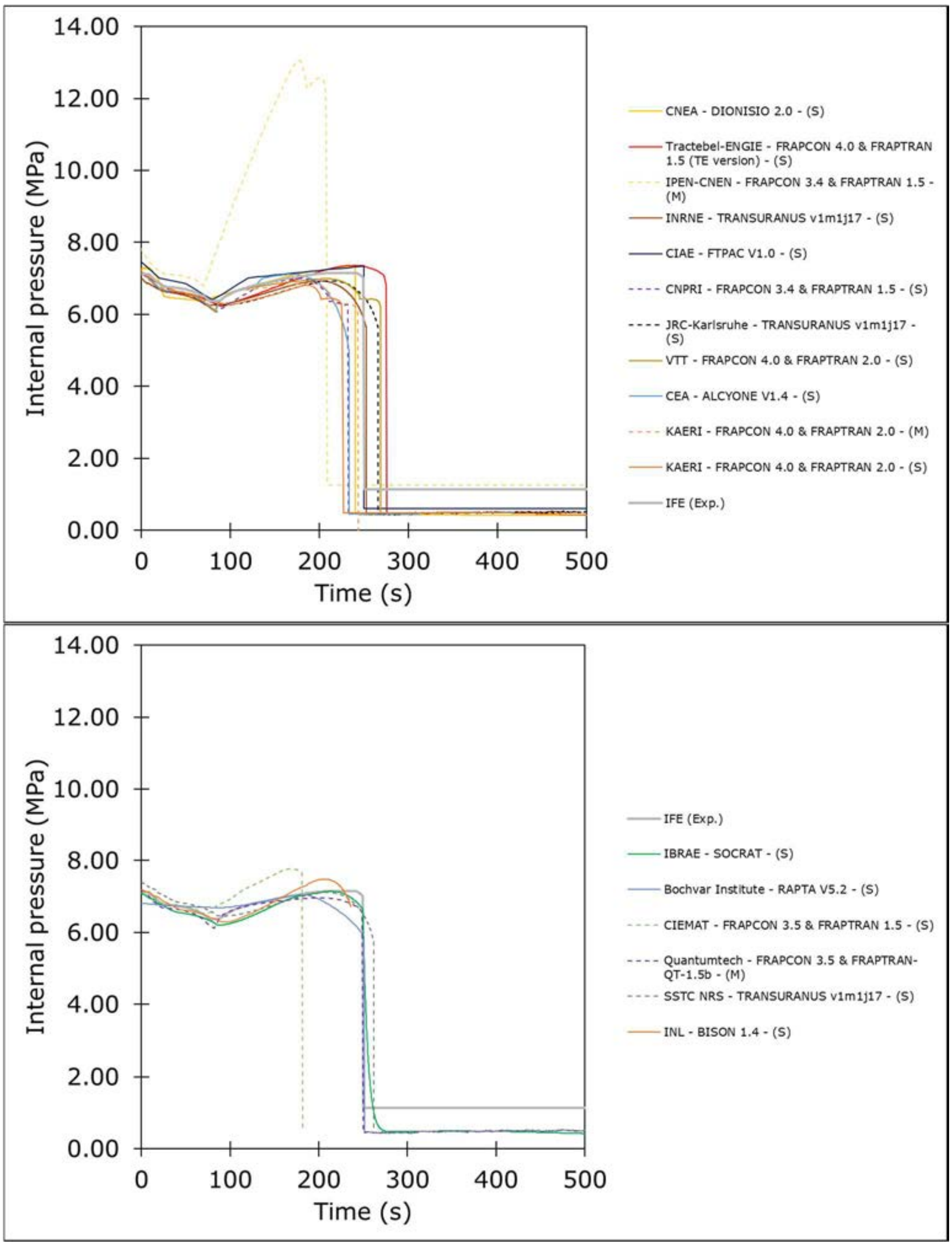

FIG. 75. Comparison of the internal pressure during the LOCA transient of the IFA-650.10 test. (S) stands for simulated boundary conditions, while (M) stands for measured boundary conditions.

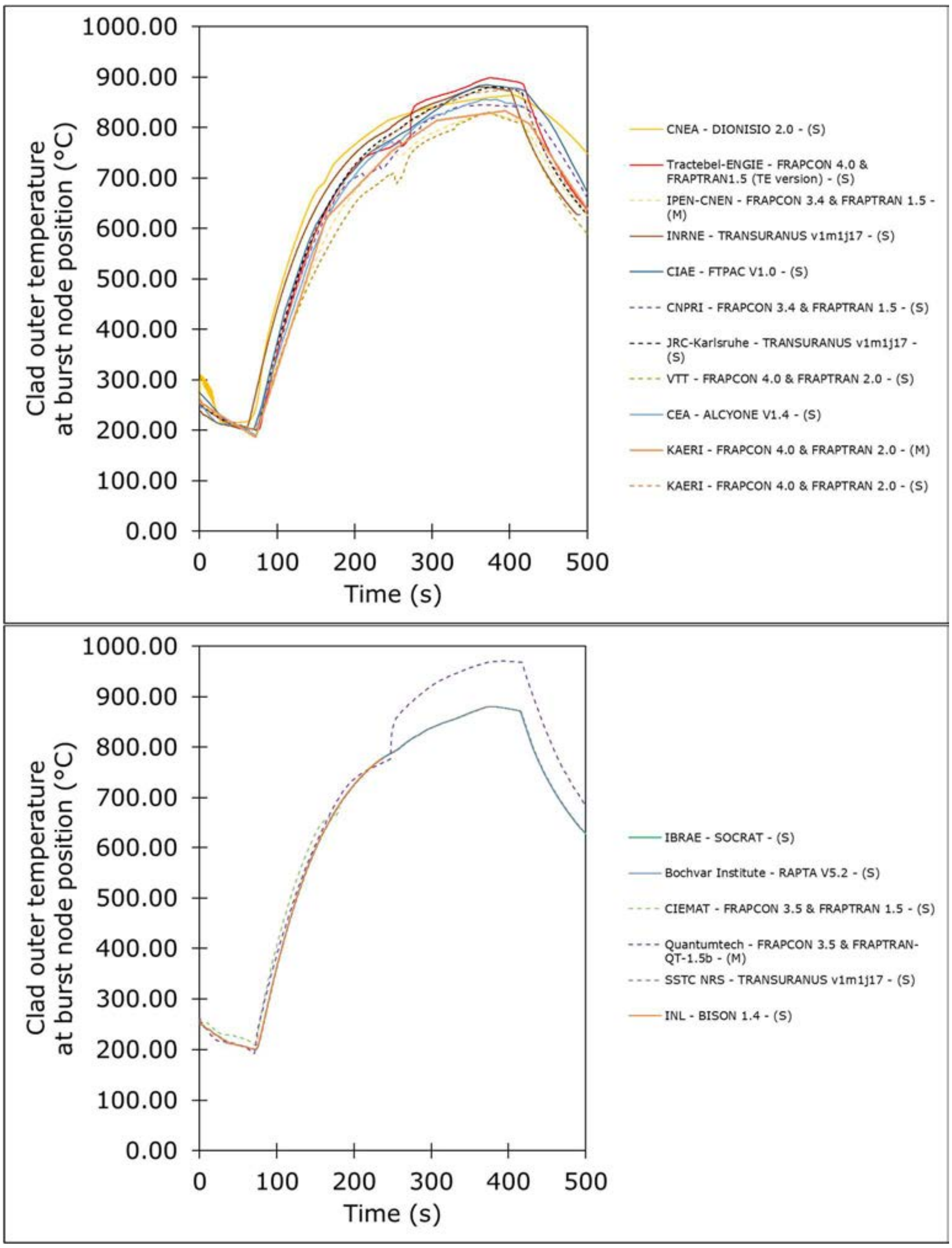

FIG. 76. Comparison of the clad outer temperature at burst position during the LOCA transient of the IFA-650.10 test. (S) stands for simulated boundary conditions, while (M) stands for measured boundary conditions.

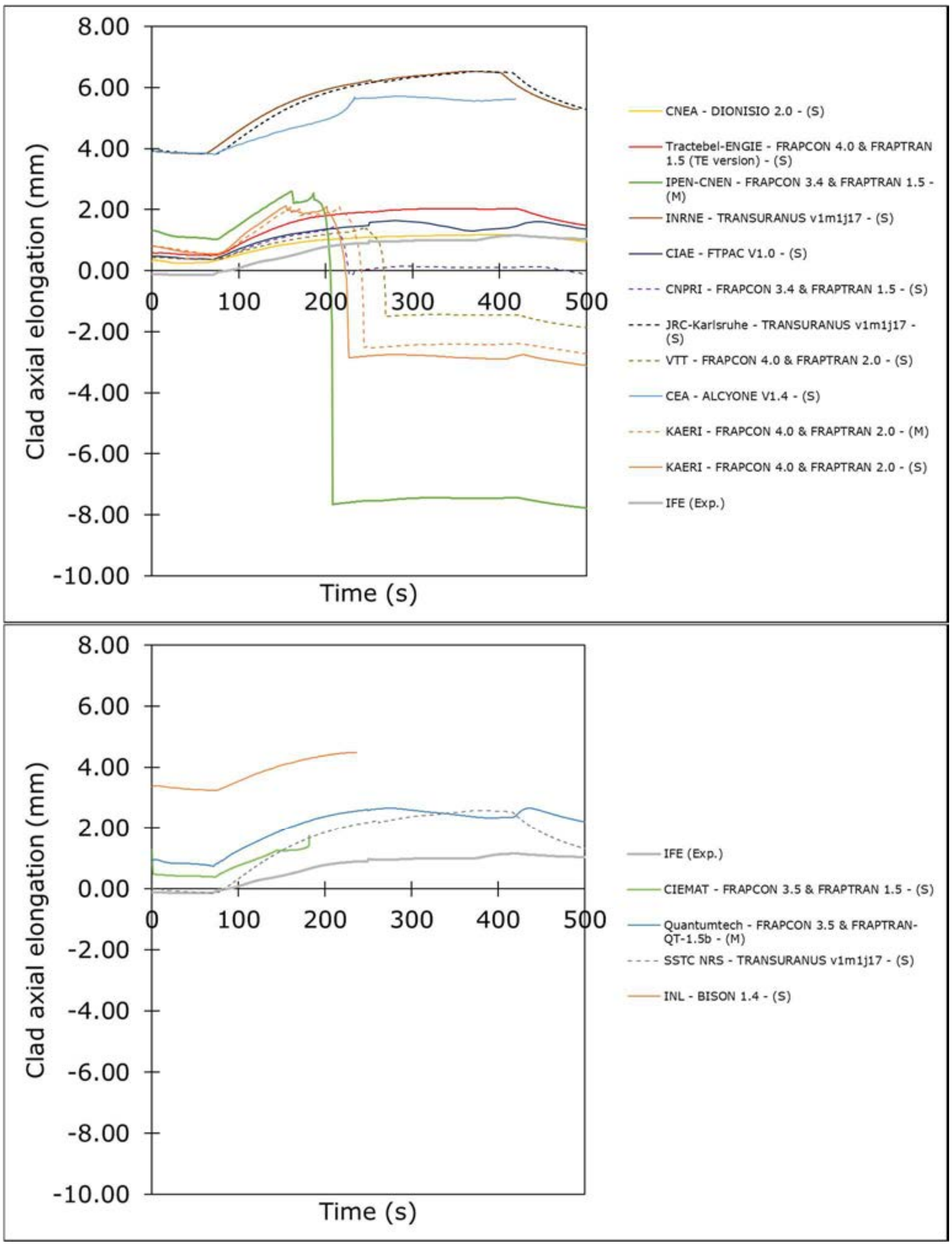

FIG. 77. Comparison of the clad axial elongation during the LOCA transient of the IFA-650.10 test. (S) stands for simulated boundary conditions, while (M) stands for measured boundary conditions.

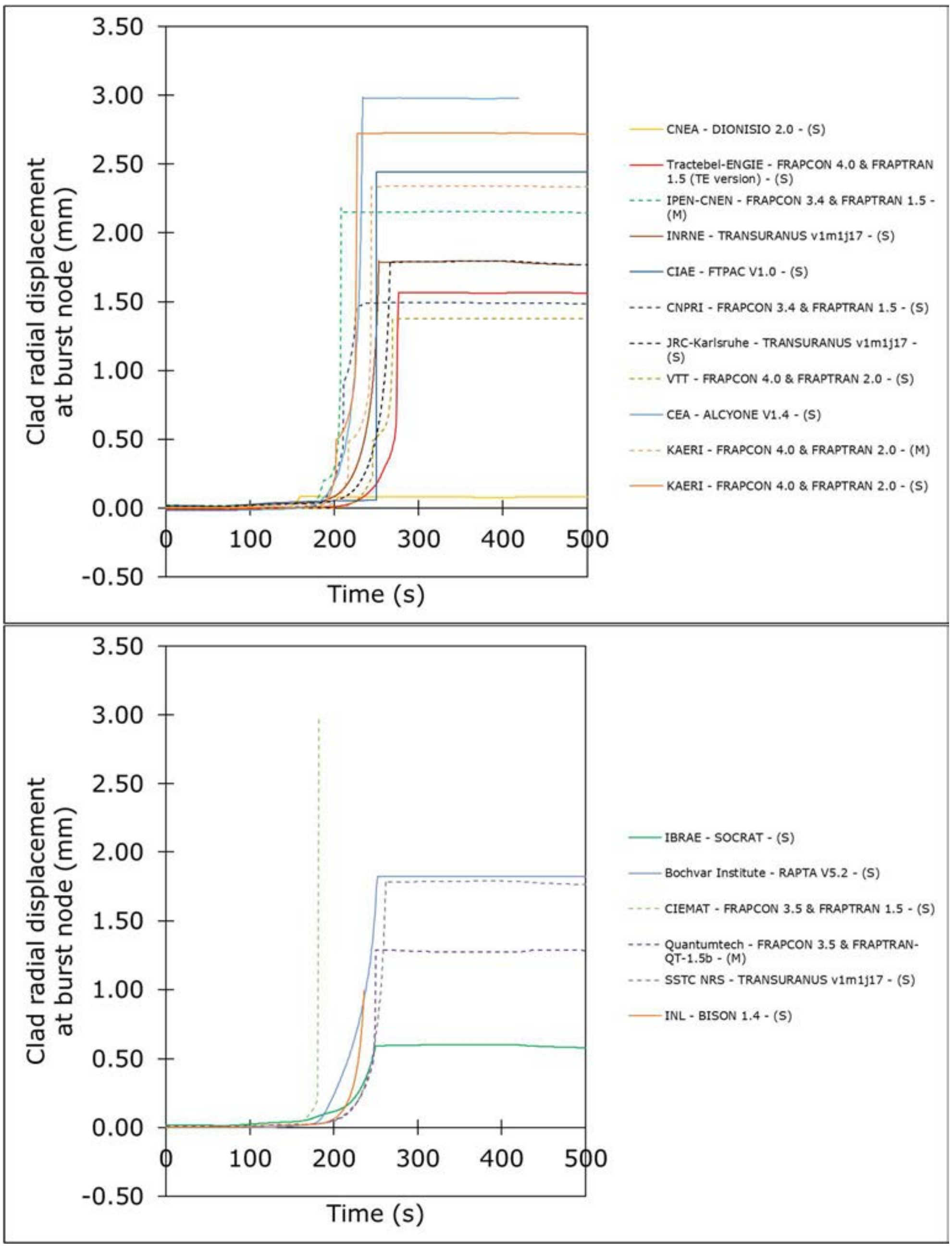

FIG. 78. Comparison of the clad radial displacement at burst position during the LOCA transient of the IFA-650.10 test. (S) stands for simulated boundary conditions, while (M) stands for measured boundary conditions.

4.2.2.3. Results at the end of the LOCA transient

The scatter in the predicted failure times among the different participant was significant (see Fig. 79). Results are similar to those obtained from the IFA-650.9 test.

The axial profile of the cladding diameter (and in general indicating the position of the burst) and the diametral gap are shown in Figs 80 and 83, respectively. The scattering of the calculated deformation was related to the burst criteria used in various codes. The experimental data (i.e. the maximum strain and stress criteria) were quite scattered that led different results.

The cladding oxide thickness calculated by the participants was also scattered (Fig. 81), despite the cladding temperature used as an input for the code was similar for all participants. The same level of scattering was observed for the equivalent cladding reacted (Fig. 82). Potentially different oxidation models were existed for different participants.

One participant provided an assessment of fuel fragmentation volume fraction along the rod segment (Fig. 84). The result was in good qualitative agreement with that of the IFA-650.9 test.

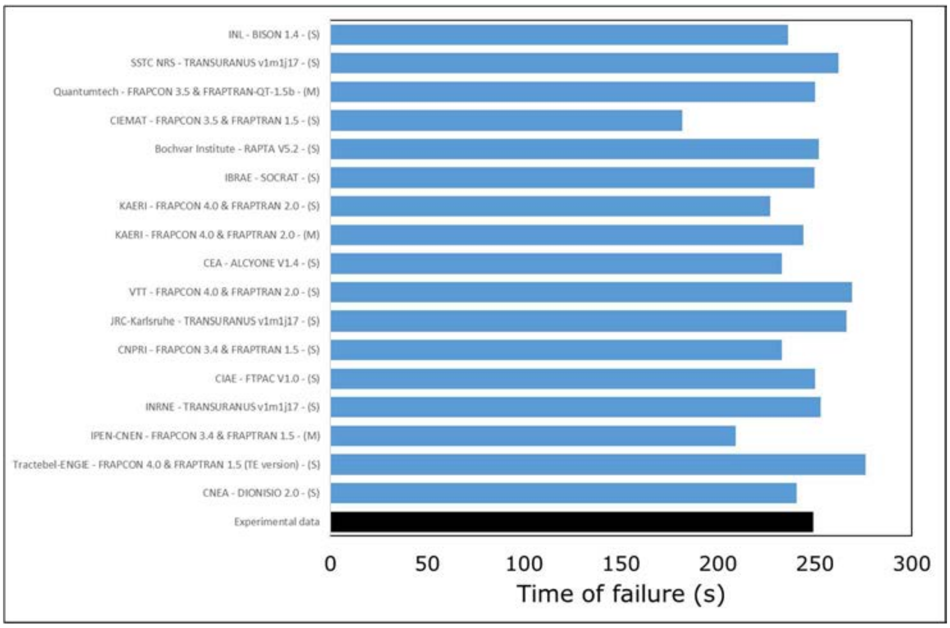

FIG. 79. Comparison of the time of failure of the IFA-650.10 test. (S) stands for simulated boundary conditions, while (M) stands for measured boundary conditions.

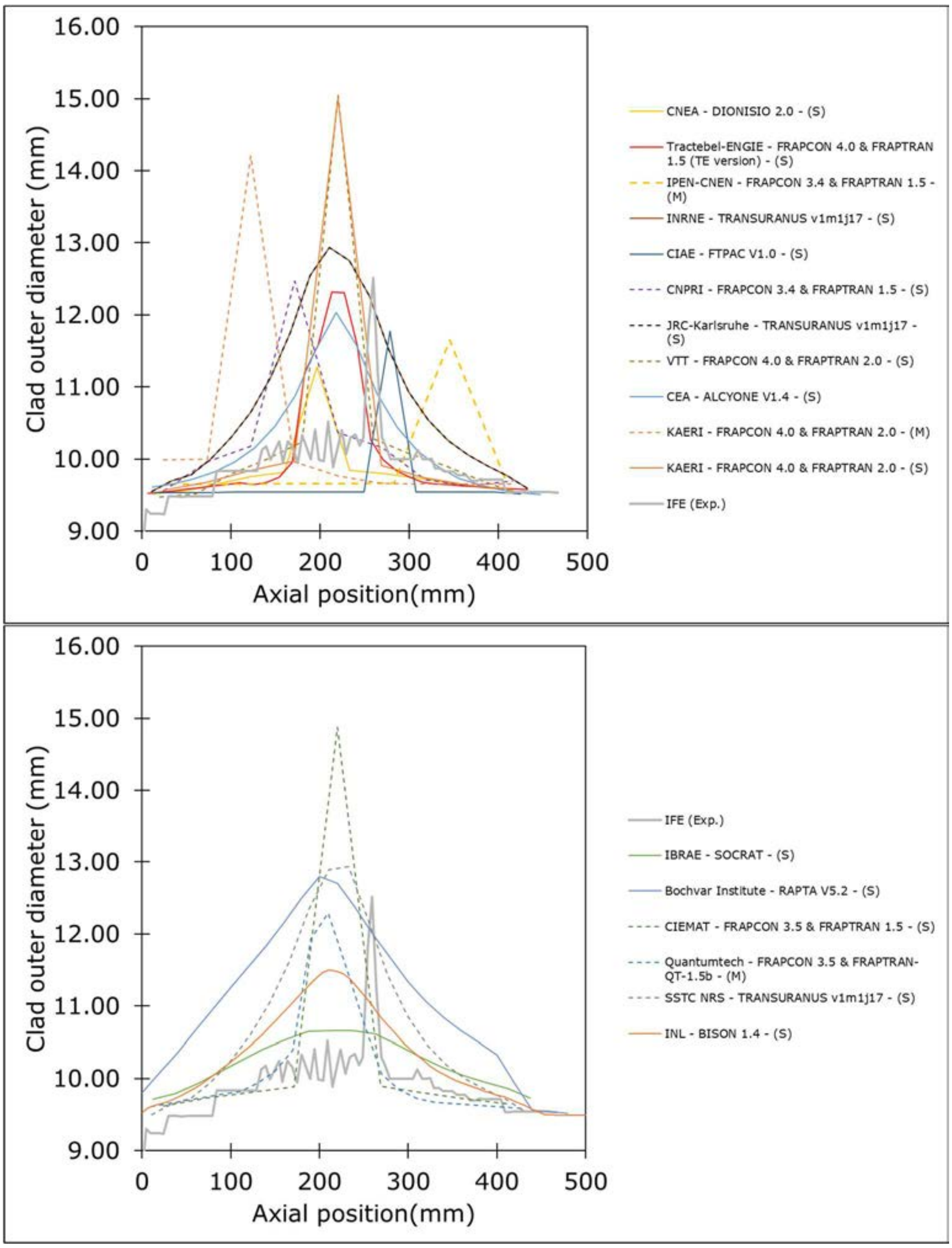

FIG. 80. Comparison of the cladding outer diameter after the IFA-650.10 test. (S) stands for simulated boundary conditions, while (M) stands for measured boundary conditions.

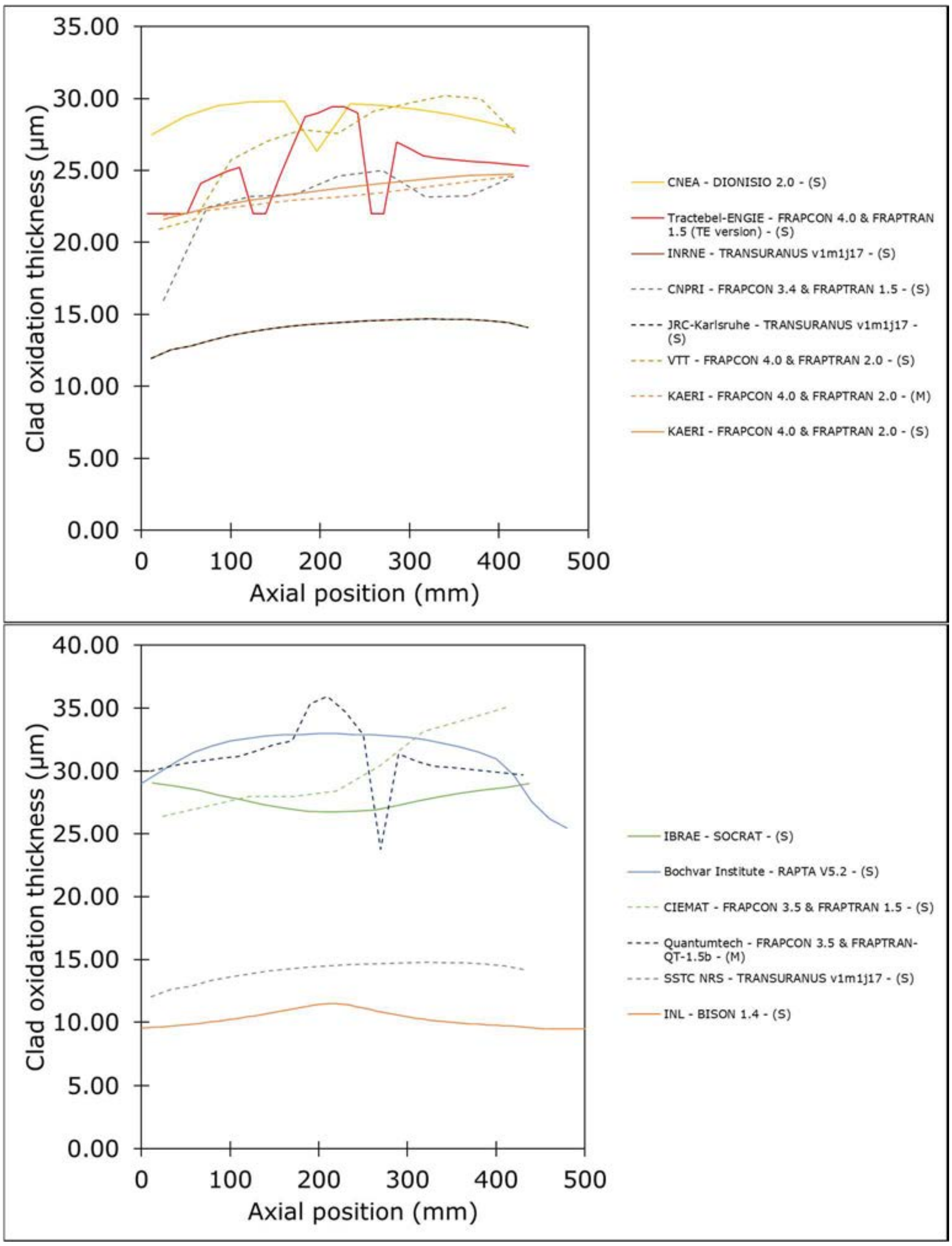

FIG. 81. Comparison of the cladding oxide thickness after the IFA-650.10 test. (S) stands for simulated boundary conditions, while (M) stands for measured boundary conditions.

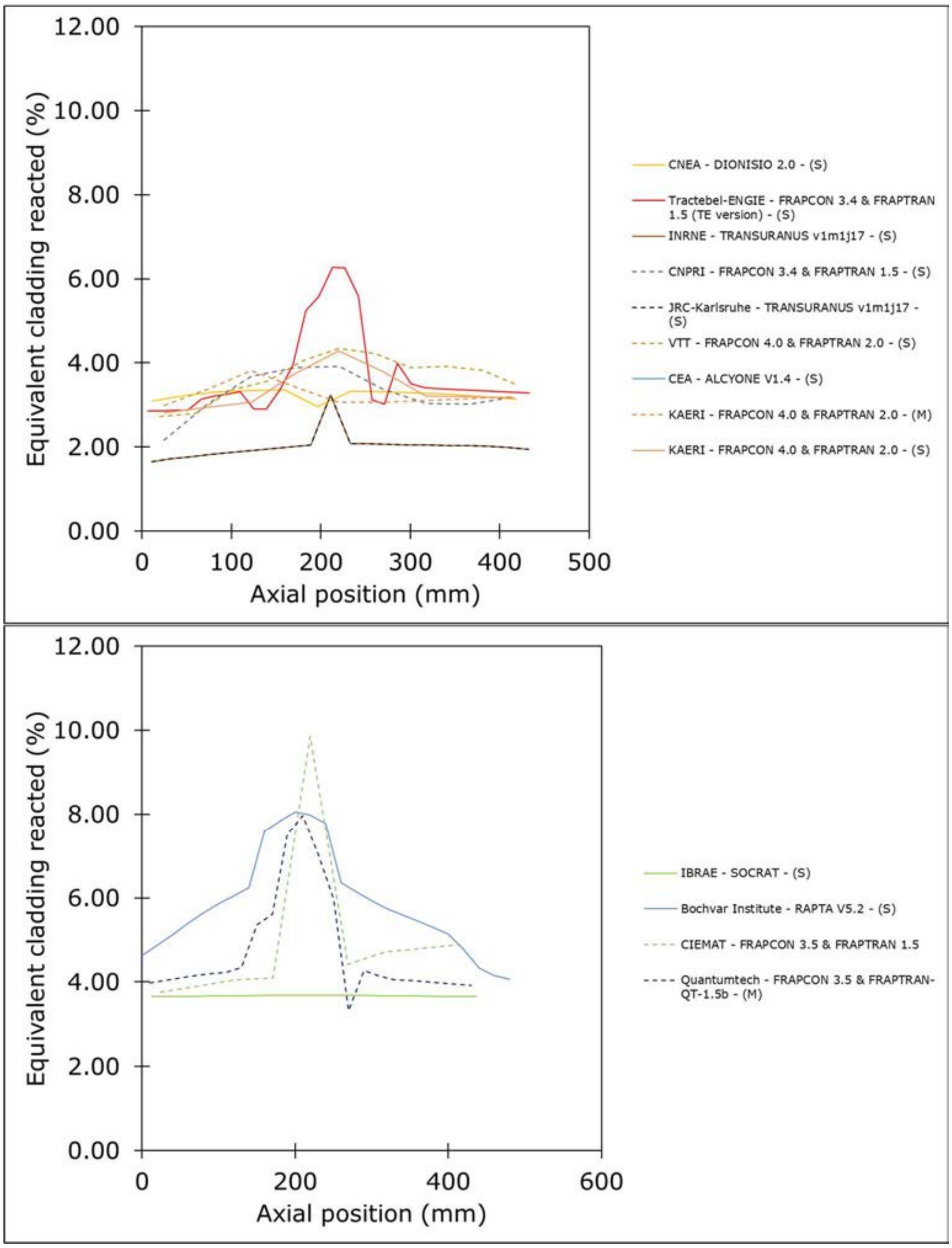

FIG. 82. Comparison of the equivalent cladding reacted after the IFA-650.10 test. (S) stands for simulated boundary conditions, while (M) stands for measured boundary conditions.

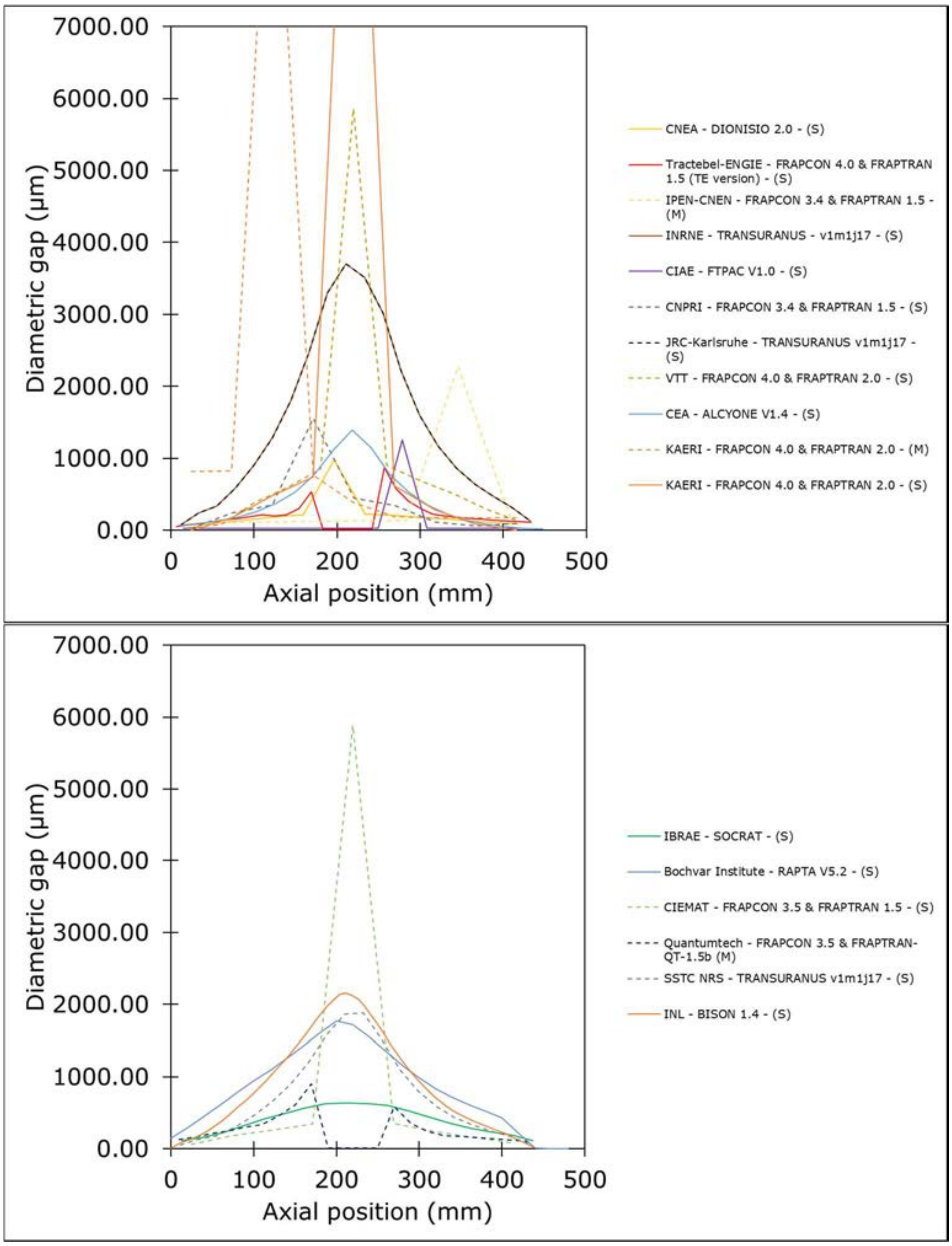

FIG. 83. Comparison of the diametral gap after the IFA-650.10 test. (S) stands for simulated boundary conditions, while (M) stands for measured boundary conditions.

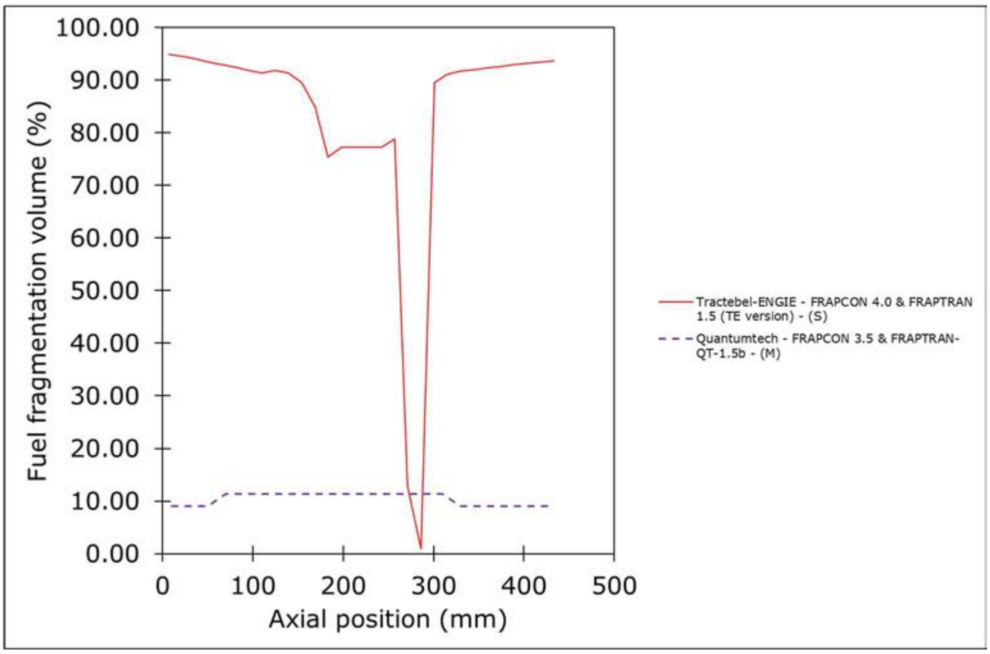

FIG. 84. Comparison of the fuel fragmentation volume after the IFA-650.10 test. (S) stands for simulated boundary conditions, while (M) stands for measured boundary conditions.

4.2.3. IFA-650.11

Nine organizations from different countries provided results for the IFA-650.11 test:

— CNPRI (China), FRAPCON 3.4 and FRAPTRAN 1.5;
— INRNE (Bulgaria), TRANSURANUS v1m1j17;
— CNEA (Argentina), DIONISIO 2.0;
— IBRAE (Russia), SOCRAT/V3;
— JRC-Karlsruhe (European Union), TRANSURANUS ;
— IPEN (Brazil), FRAPCON 3.4 and FRAPTRAN 1.5;
— SSTC NRS (Ukraine), TRANSURANUS v1m1j17;
— VTT (Finland), FRAPCON 4.0 and FRAPTRAN 2.0;
— VNIINM, Bochvar Institute (Russia), RAPTA 5.2.

4.2.3.1.Results at the end of the base irradiation

For all participants, the calculated burnup was close to the average measured discharge burnup of the fuel rod (Fig. 85). The predicted pellet to cladding gap at the end of the irradiation was more scattered (Fig. 86). As a general trend, low values of residual gap were expected at this burnup, but no experimental data was available. The diametral clad strain was scattered among various calculations (Fig. 87). On the other hand, a reasonable agreement was achieved for the clad elongation (Fig. 88). The calculated corrosion layer (Fig. 89) was in good agreement with the experimental data (of 5 µm) for most of the participants.

Some participants provided results for the radial distribution of fission gas inventory before the transient (Fig. 90). A significant discrepancy between the calculated and measured values was evident.

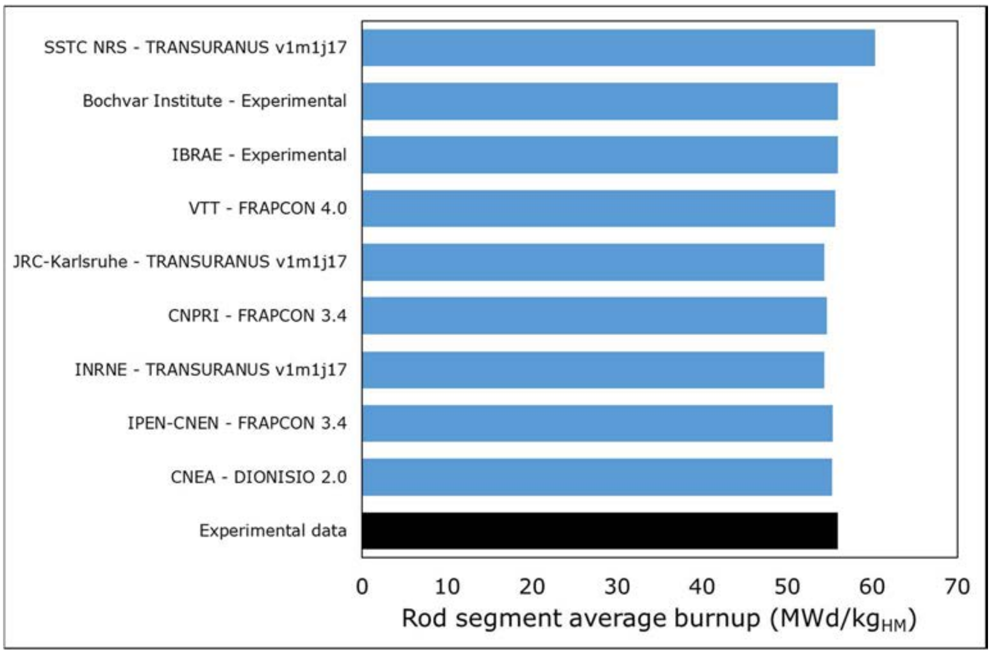

FIG. 85. Comparison of the rod segment average burnup for the base irradiation of the IFA-650.11 test.

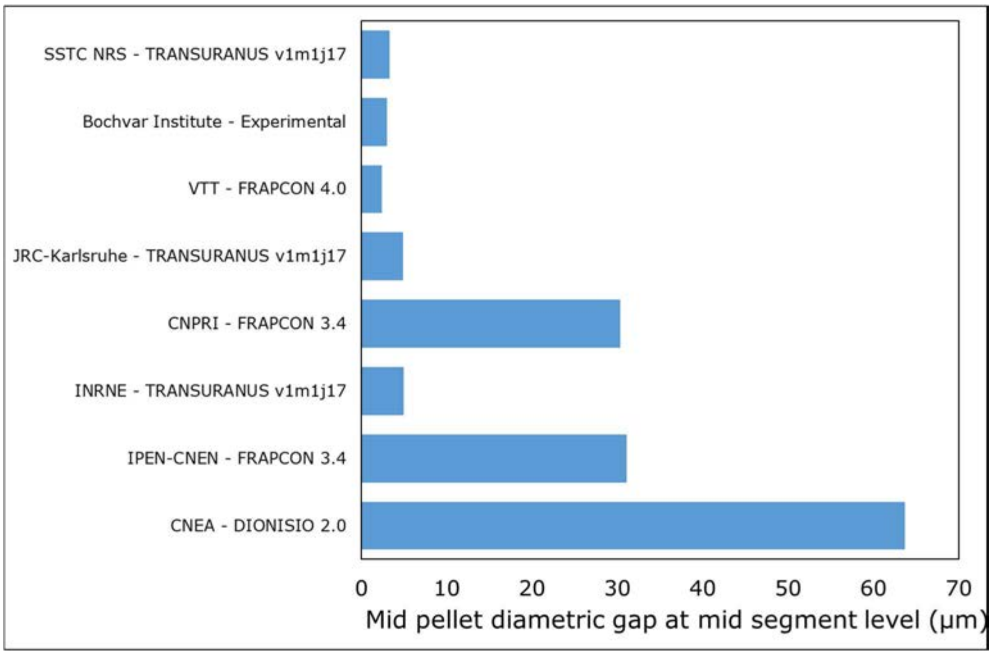

FIG. 86. Comparison of the diametral gap at the mid pellet at the end of the base irradiation of the IFA-650.11 test.

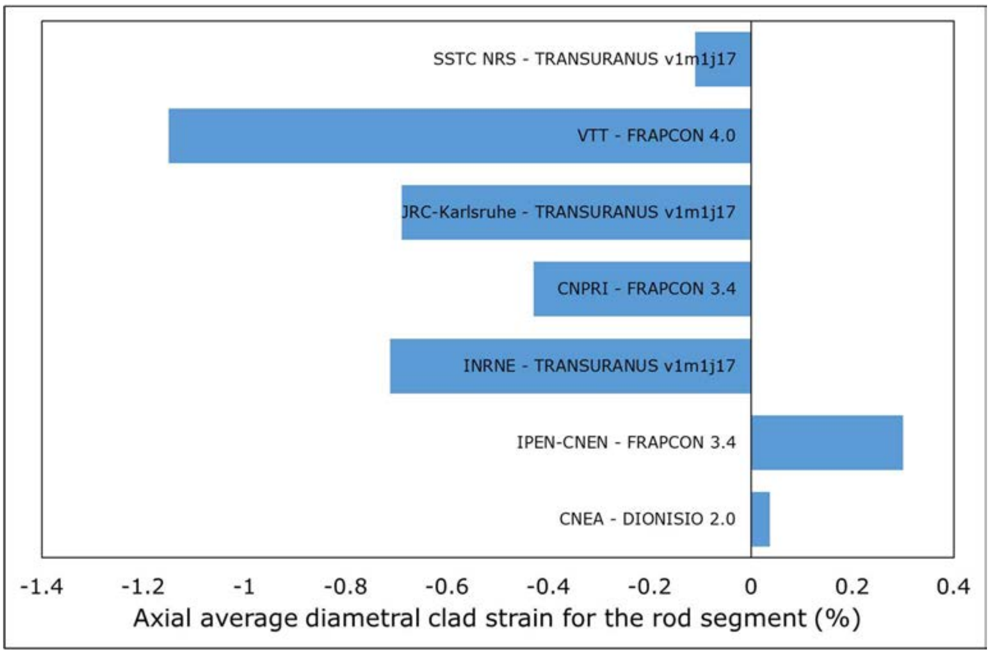

FIG. 87. Comparison of the axial average diametral clad strain at the end of the base irradiation of the IFA-650.11 test.

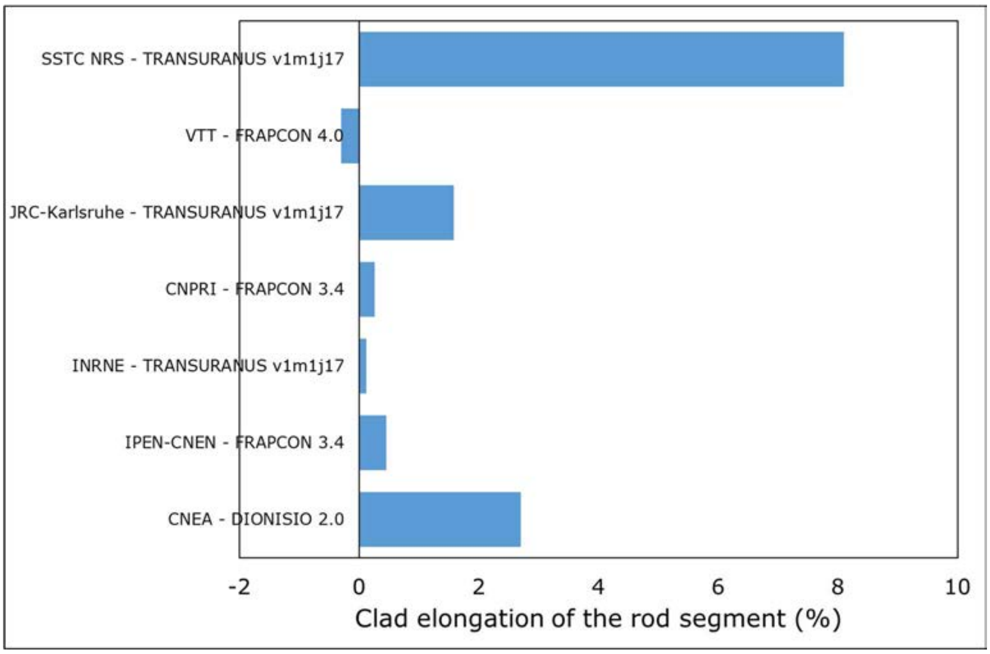

FIG. 88. Comparison of the clad elongation at the end of the base irradiation of the IFA-650.11 test.

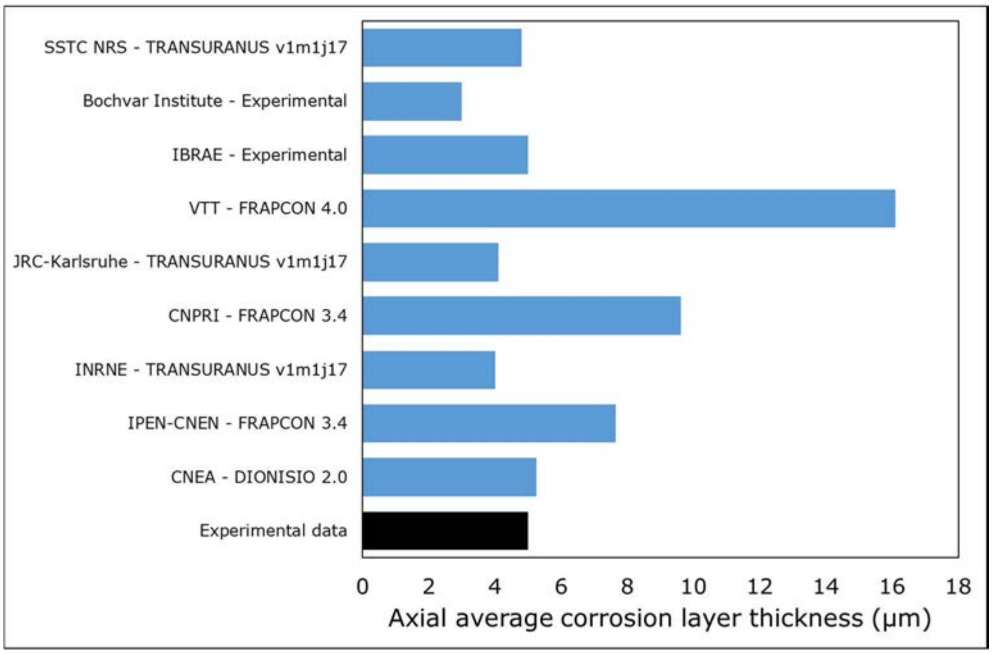

FIG. 89. Comparison of the axial average corrosion layer thickness at the end of the base irradiation of the IFA-650.11 test.

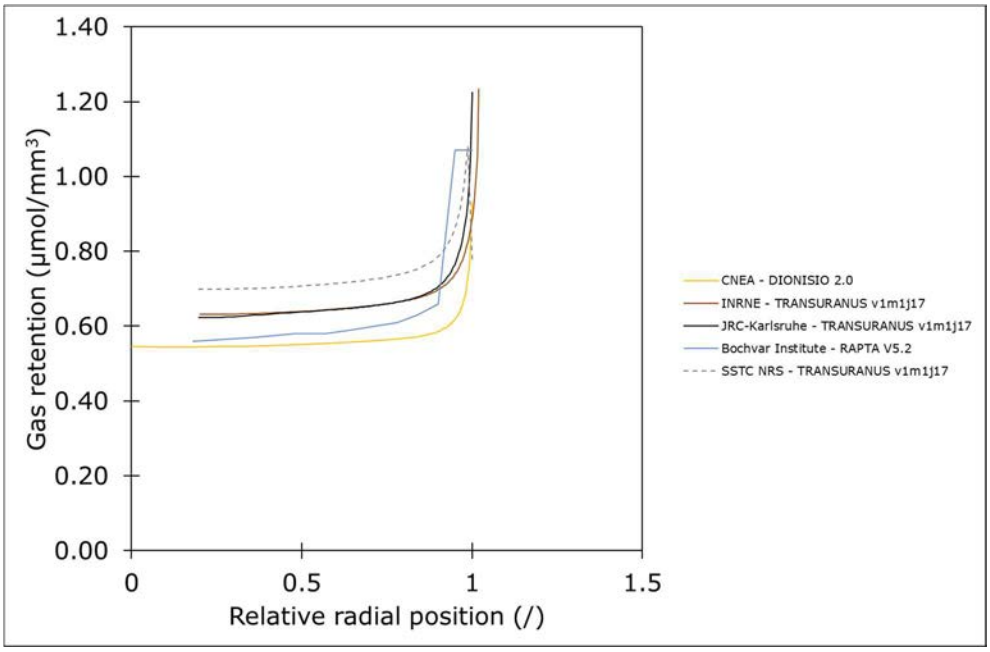

FIG. 90. Comparison of gas retention at the end of the base irradiation for the IFA-650.11 test.

4.2.3.2.Results during the LOCA transient

For the following Figs, time reference was set at the beginning of the transient. A comparison of the calculated plenum temperature is indicated in Fig. 91. A clustering in two group of results was emerged. The difference was probably caused by the specific modelling assumptions selected by the participants for the calculation of the plenum temperature (the clustering did not depend on the code used for the simulation).

A comparison of the calculated total fission gas release is indicated in Fig. 92. The scattering among the predicted values was significant, as the kinetic evolution of the fission gas release along the transient were deviated significant. The number of participants able to calculate this quantity was limited. This observation indicated the importance of further model development for the prediction of fission gas behaviour during the transients.

A comparison of the calculated internal pressure is indicated in Fig. 93. Instead of the ballooning phase (pressure decrease before burst), several participants predict an increase in the pressure prior to the burst. As described by CIEMAT, a specific algorithm was used by FRAPTRAN to evaluate the inner pressure in the plenum. The qualitative agreement among the participants was reasonable.

A comparison of the cladding outer temperature (at the position of the burst) is indicated in Fig. 94. Results was reasonably close to each other, with a similar time evolution. The predicted cladding temperature would depend on the boundary conditions adopted by the participants.

A comparison of the cladding elongation is indicated in Fig. 95. The scattering of results among various participants was significant. This could be ascribed to the material properties of the cladding used in different codes, since the thermal boundary conditions are similar among the partners.

A comparison of the cladding radial displacement (at the position of the burst) is indicated in Fig. 96. Similar considerations and comments as for the elongation could be made.

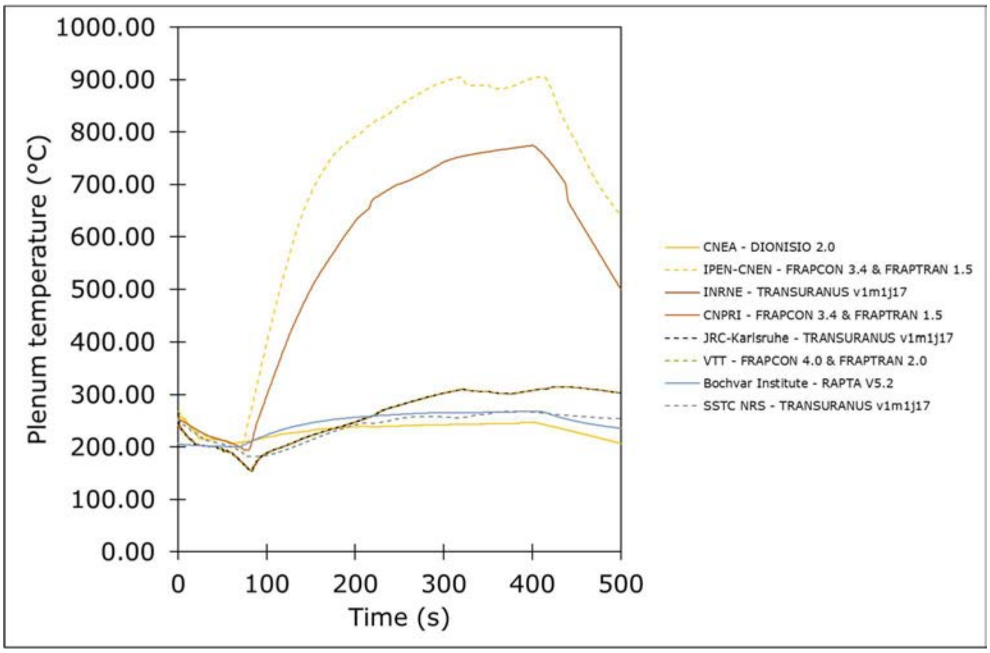

FIG. 91. Comparison of the plenum temperature during the LOCA transient of the IFA-650.11 test.

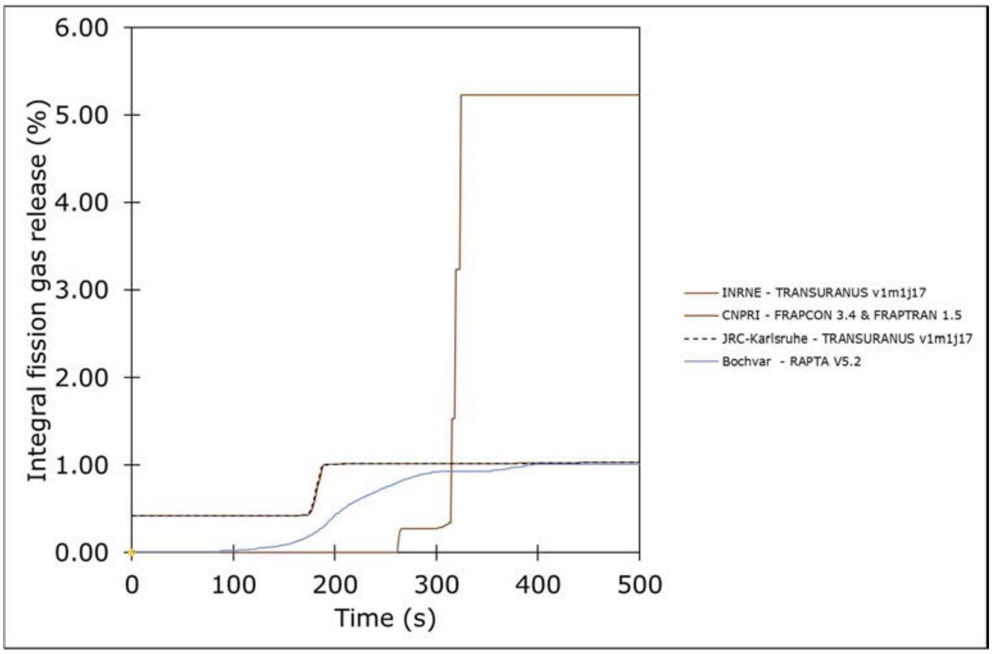

FIG. 92. Comparison of the total fission gas release during the LOCA transient of the IFA-650.11 test.

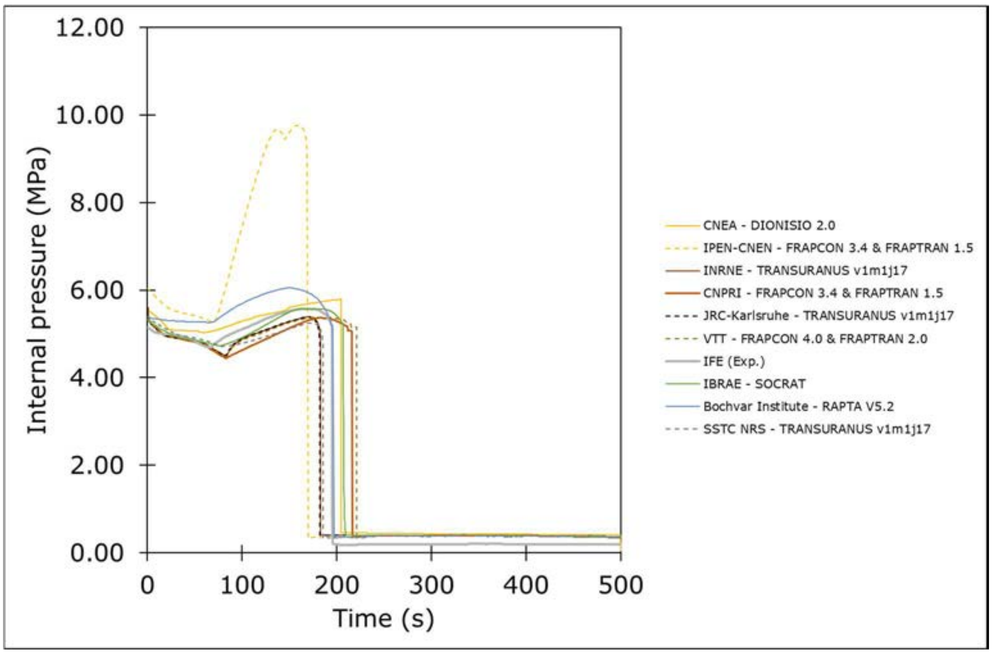

FIG. 93. Comparison of the internal pressure during the LOCA transient of the IFA-650.11 test.

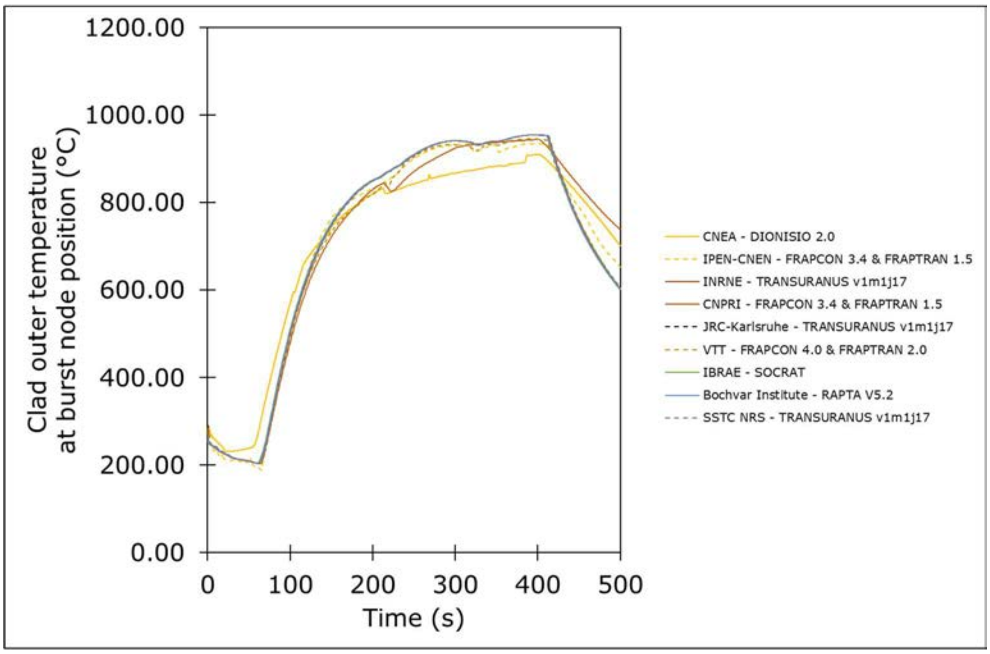

FIG. 94. Comparison of the clad outer temperature at burst position during the LOCA transient of the IFA-650.11 test.

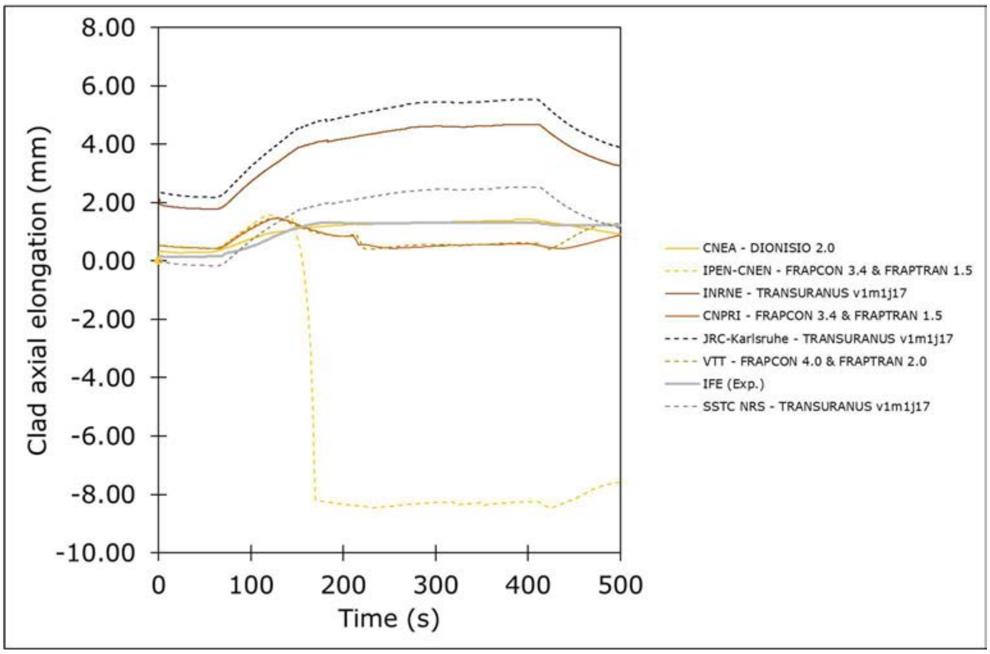

FIG. 95. Comparison of the clad axial elongation during the LOCA transient of the IFA-650.11 test.

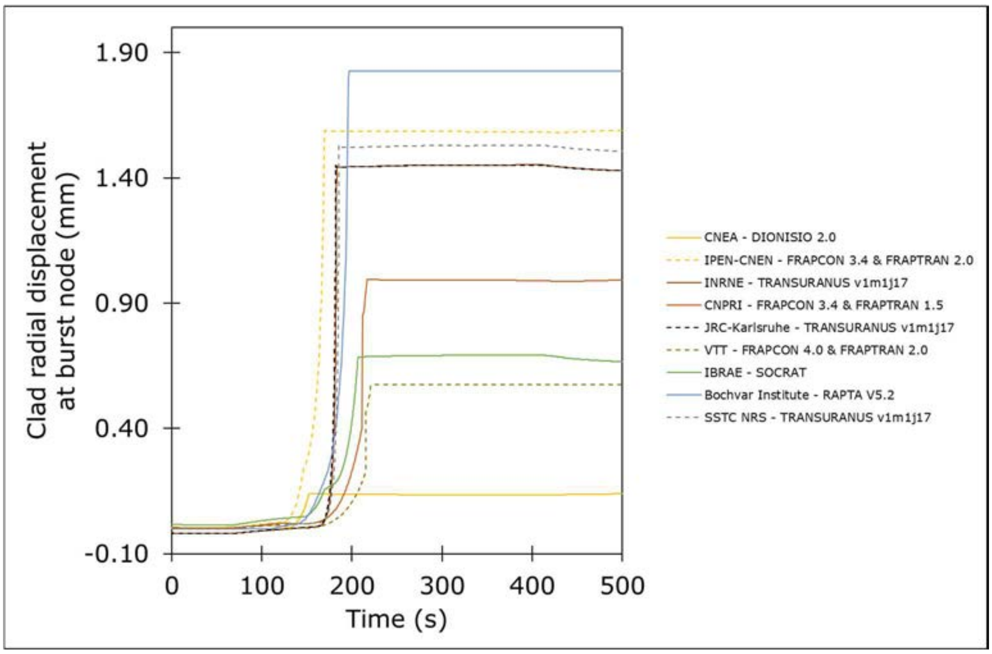

FIG. 96. Comparison of the clad radial displacement at burst position during the LOCA transient of the IFA-650.11 test.

4.2.3.3.Results at the end of the LOCA transient

The scatter in the predicted failure times among the different participant was less significant than in the other IFA-650 tests (see Fig. 97).

The axial profile of the cladding diameter (and in general indicating the position of the burst) and the diametral gap are shown Figs 98 and 101, respectively. The scattering of the calculated deformation was related to the burst criteria used in various codes. The experimental data (i.e. maximum strain or stress criteria) were quite scattered that led to different results.

The cladding oxide thickness calculated by the participants was also scattered (Fig. 99), despite the cladding temperature used as an input for the code was similar for all participants. The same level of scattering was observed for the equivalent cladding reacted (as illustrated in Fig. 100). Potentially different oxidation models were existed for different participants.

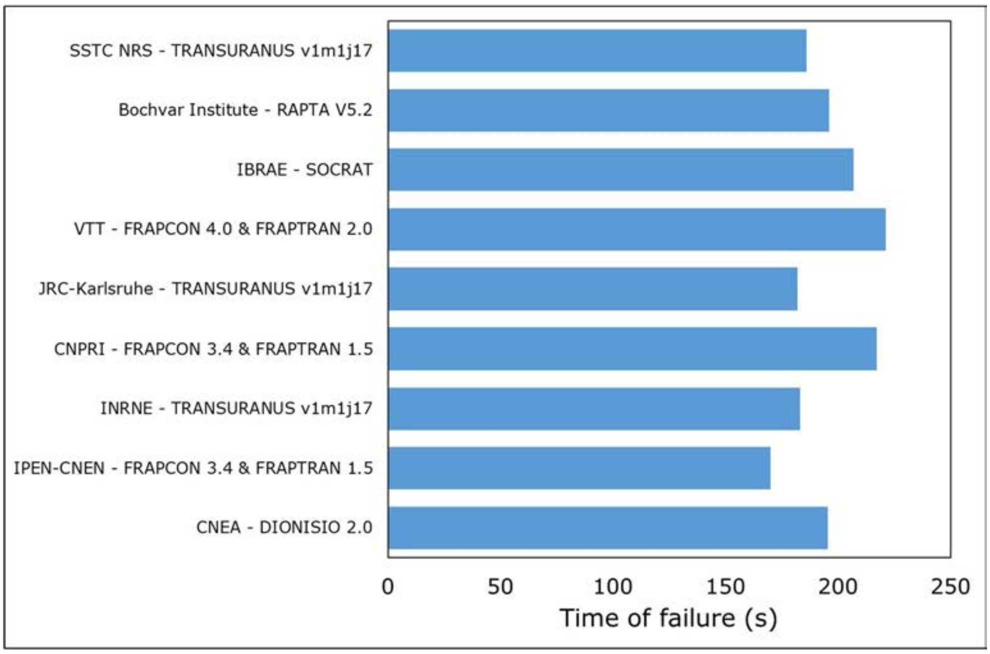

FIG. 97. Comparison of the time of failure of the IFA-650.11 test.

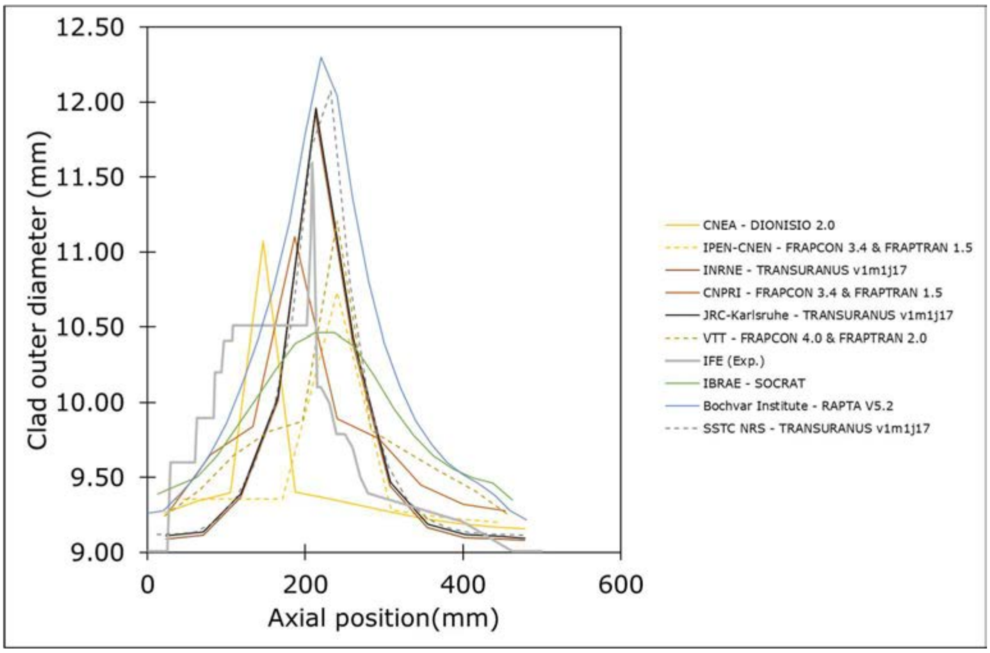

FIG. 98. Comparison of the cladding outer diameter after the IFA-650.11 test.

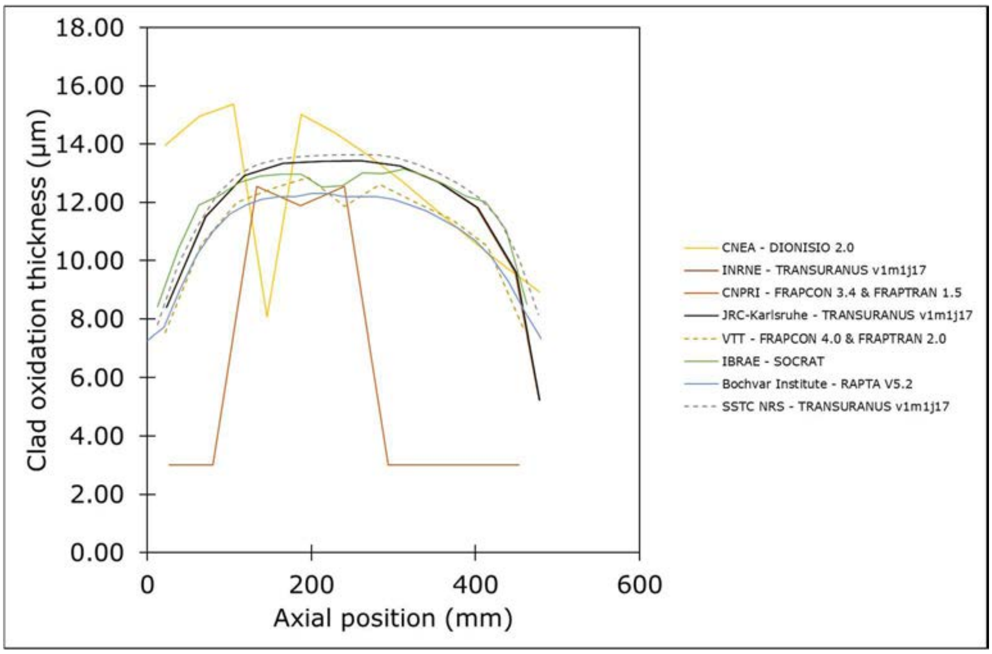

FIG. 99. Comparison of the cladding oxidation thickness after the IFA-650.11 test.

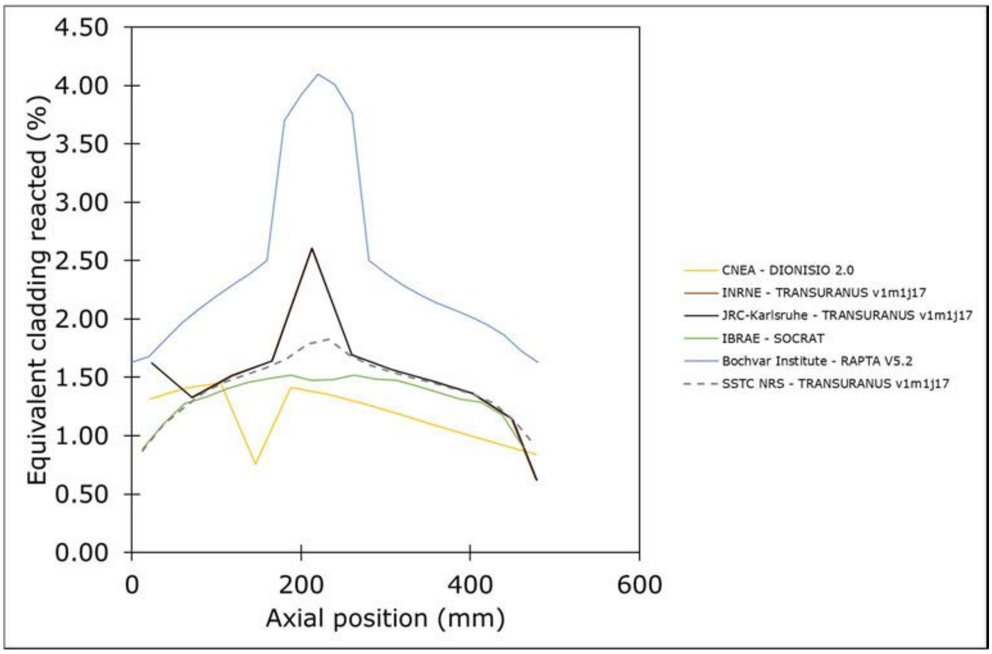

FIG. 100. Comparison of the equivalent cladding reacted after the IFA-650.11 test.

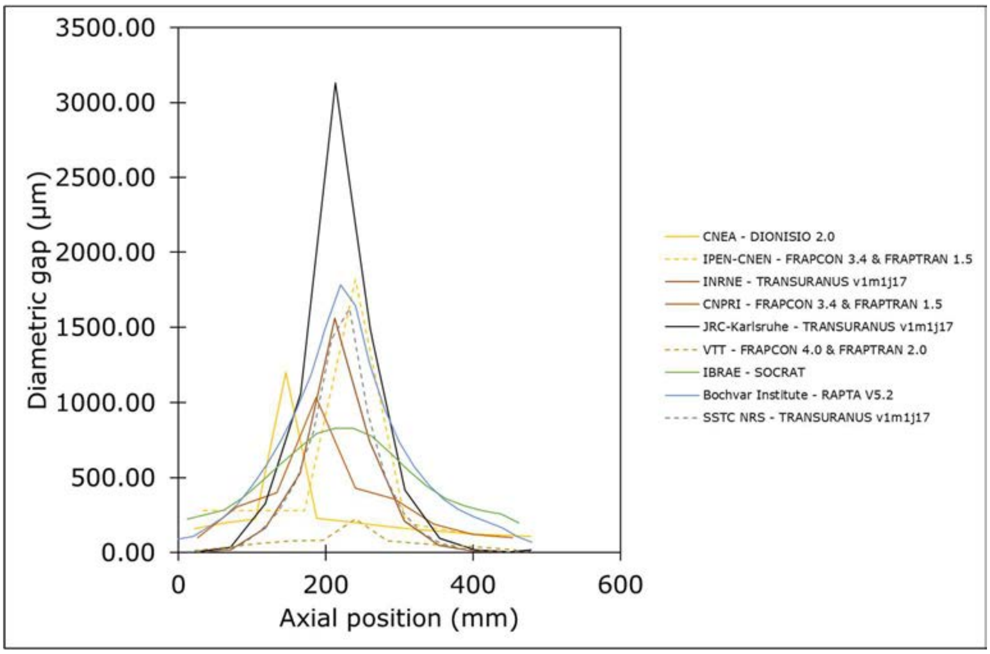

FIG. 101. Comparison of the diametral gap after the IFA-650.11 test.

4.3. STUDSVIK LOCA TEST (NRC-192)

Seven organizations from seven different countries provided results for this Studsvik 192 test:

— CNEA (Argentina), DIONISIO 2.0 code;
— CEA (France), ALCYONE V1.4 code;
— VTT (Finland), FRAPCON 4.0 & FRAPTRAN 2.0 codes;
— CIEMAT (Spain), FRAPCON 3.5 & FRAPTRAN 1.5 codes;
— SST-CNRS (Ukraine), TRANSURANUS v1m1j17 code ;
— MTA-EK (Hungary), FRAPTRAN 1.4 code;
— SSM/ Quantumtech (Sweden), FRAPCON 3.5 & FRAPTRAN-QT-1.5 codes.

4.3.1. Results at the end of the base irradiation

Most of the participants used the base irradiation conditions (power history) provided by US NRC to simulate the initial state of the rod before the transient.

MTA-EK did not calculate the behaviour of the rod after the base irradiation, but rather the end-of-life measured data was used as the initial state of the rod before the LOCA test.

The calculated burnup of the rod was close to the average measured discharge burnup of the fuel rod (Fig. 102). The residual pellet to cladding gap was scattered depending on the code and user (Fig. 103). Even if there was no experimental data for the gap after base irradiation, a value of a few microns seemed more reasonable than a wide gap because of fuel swelling and cladding creep at high burnup. Some participants had overpredicted this quantity.

The calculated diametral clad strain reported by participants was very different depending on the code used (Fig. 104). The calculated values, although, remain small. Experimentally, the diameter was slightly increased during the base irradiation (0.13%). Most codes provided a reasonable cladding elongation for the rod irradiated up to 70 GWd/tM (Fig. 105).

The corrosion layer calculated (Fig. 106) was between 10 and 40 µm, which was in a good agreement with the experimental data (between 25 and 30µm).

Only 3 participants calculated the radial distribution of fission gas inventory before the transient (Fig. 107). This quantity could be compared to EPMA or SIMS measurement, but the experimental data were not provided. Calculation showed that fission gas release during the base irradiation occurred in the center part of the rod, as expected.

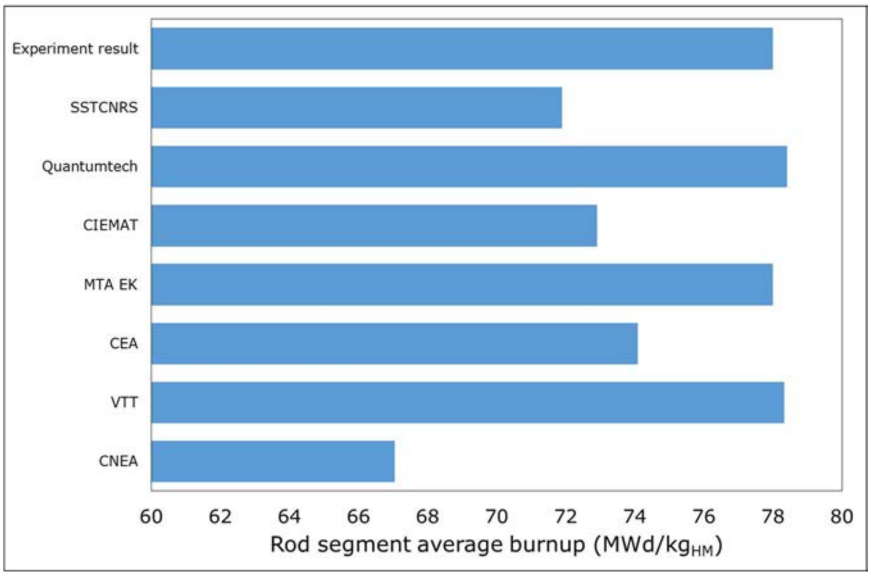

FIG. 102. Calculated average burn-up of the Studsvik 192 test rod segment.

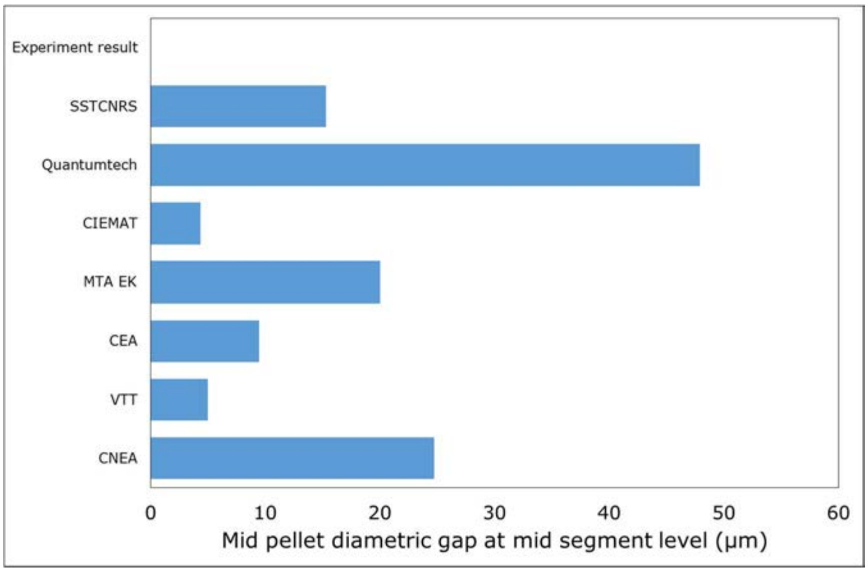

FIG. 103. Calculated gap at mid segment of the Studsvik 192 test rod segment before test.

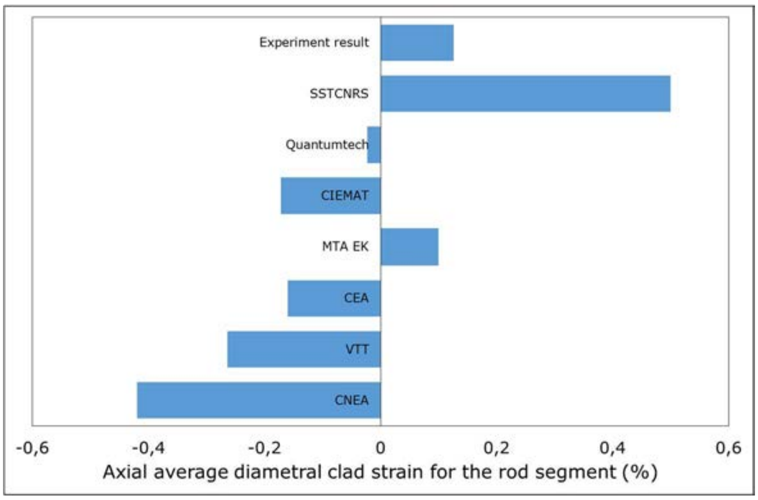

FIG. 104. Calculated average clad strain of the Studsvik 192 test rod segment before test.

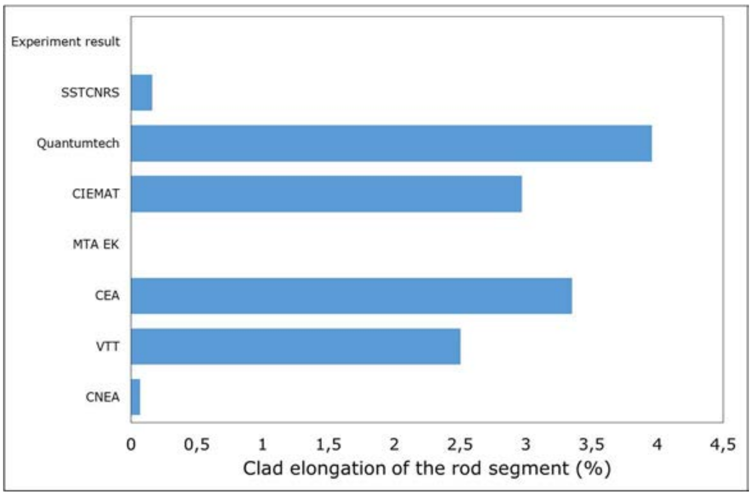

FIG. 105. Calculated cladding elongation of the Studsvik 192 test rod segment before test.

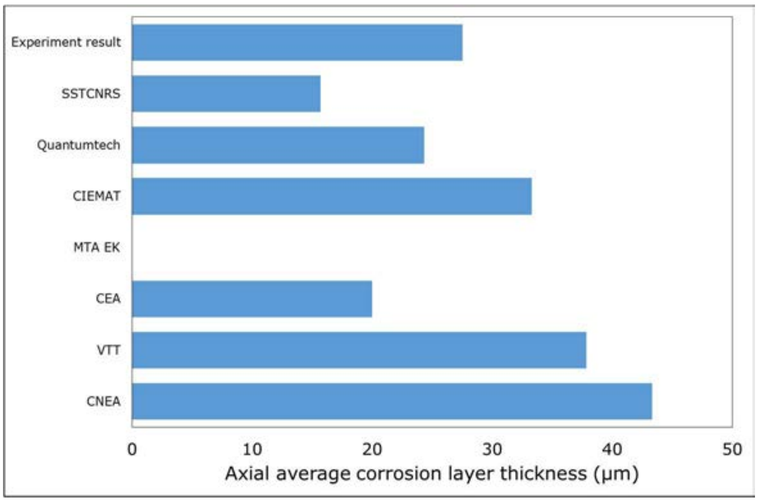

FIG. 106. Calculated average corrosion layer thickness of the Studsvik 192 test rod segment before test.

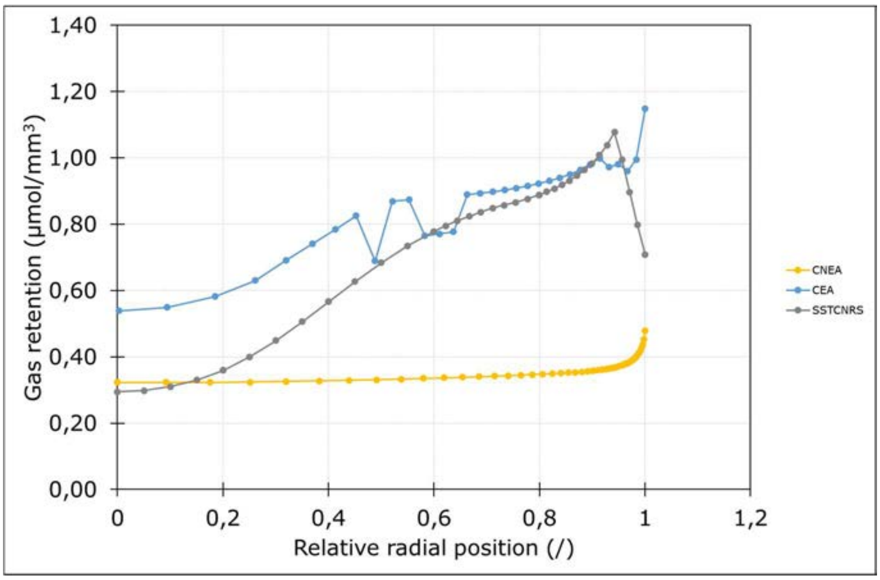

FIG. 107. Calculated fission gas inventory of the Studsvik 192 test rod segment before test at mid segment.

4.3.2. Results during the LOCA test

For the following Figs, time reference was set at the beginning of heat up (the transient).

Inner rod pressure evolution (Figs 108 and 109) indicated that all participants overestimated the burst time between 10 and 30 s. The pressure evolution during the test showed a ballooning phase (pressure decrease before burst). The modelling of plenum temperature was left to the participants, as the experiment was complex and not all temperatures were measured. Most participants considered a quasi-constant temperature in the plenum, except CEA (Fig. 110). Even CEA considered a high temperature in the plenum, it did not result in an over-estimation of the pressure in the rod.

Participants used the cladding temperature data provided by US-NRC in the data sheet to model the outer cladding temperature profile. All data calculated at the burst node were consistent (Fig. 111).

According to the participants, the calculated cladding axial and radial displacements during the test could be very different (Figs 112 and 113). Results were mainly obtained from the cladding creep behaviour law used in the code, and all codes had a different one. Some participants used a higher creep rate (mainly FRAPTRAN code users) than others (TRANSURANUS, DIONISIO, ALCYONE) as illustrated in these Figs. The effect of boundary conditions (cladding temperature profile) was negligible as all participants practically used the same assumptions.

Only CEA could calculate fission gas release during the test (Fig. 114). The main mechanism modelled in the ALCYONE code was gas release by intergranular fragmentation. This fragmentation could occur after the cladding burst (ALCYONE). In some codes (FRAPTRAN-QT), fuel fragmentation and relocation were calculated but extra fission gas release was not introduced. The evolutions of the corresponding models were detailed in the participants' reports.

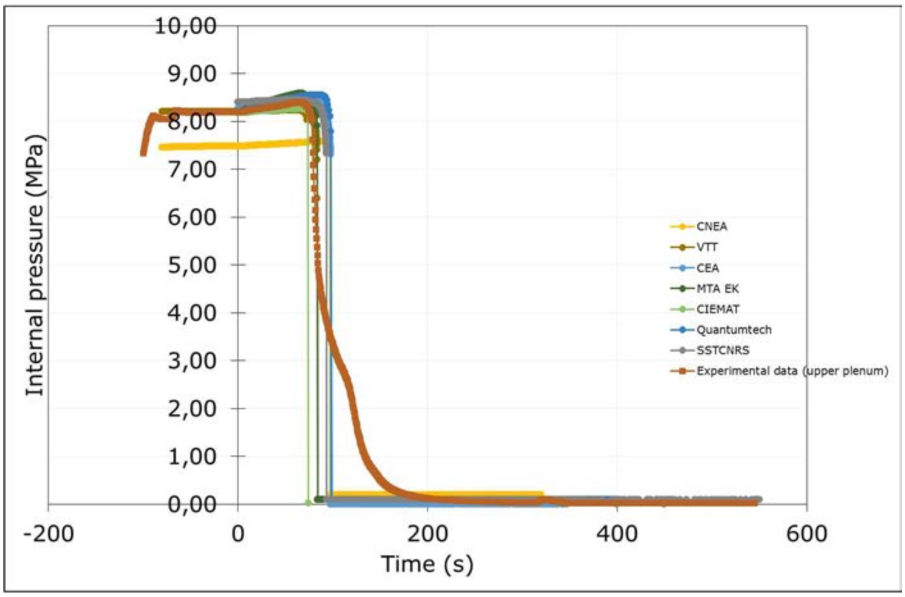

FIG. 108. Rod inner pressure calculated during test (Studsvik 192 LOCA test).

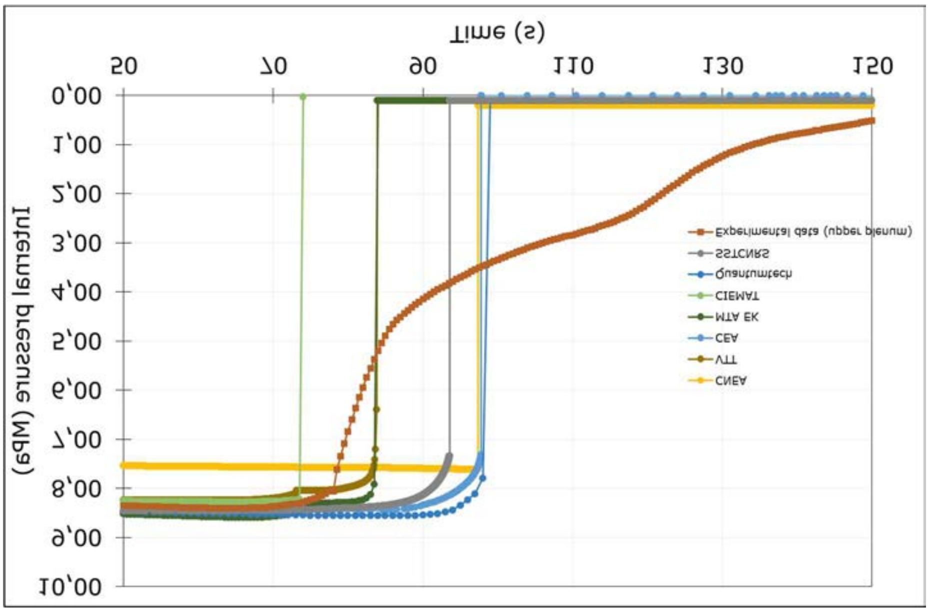

FIG. 109. Rod inner pressure calculated around the burst (Studsvik 192 LOCA test).

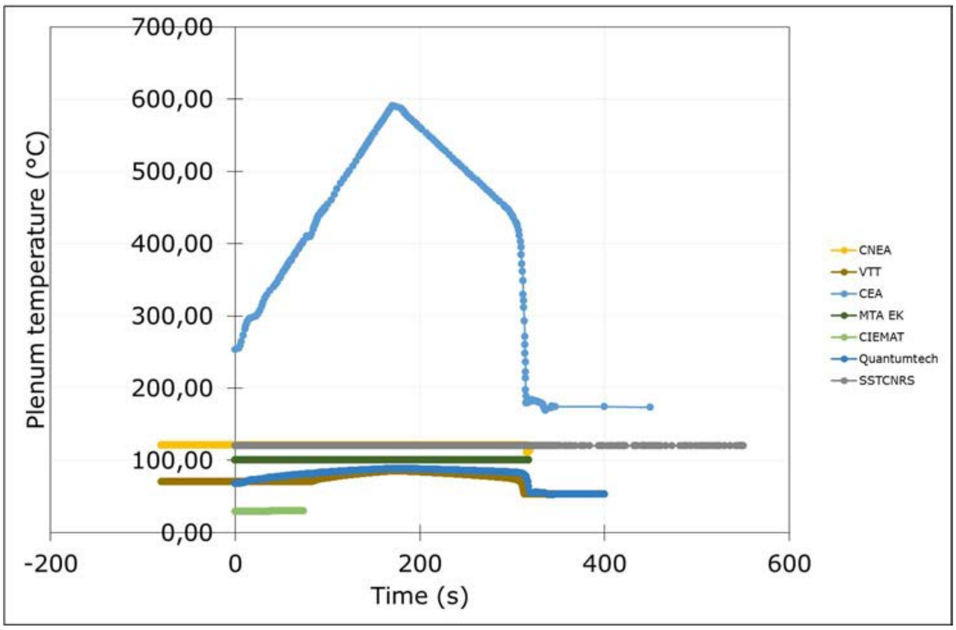

FIG. 110. Plenum temperature calculated during test (Studsvik 192 LOCA test).

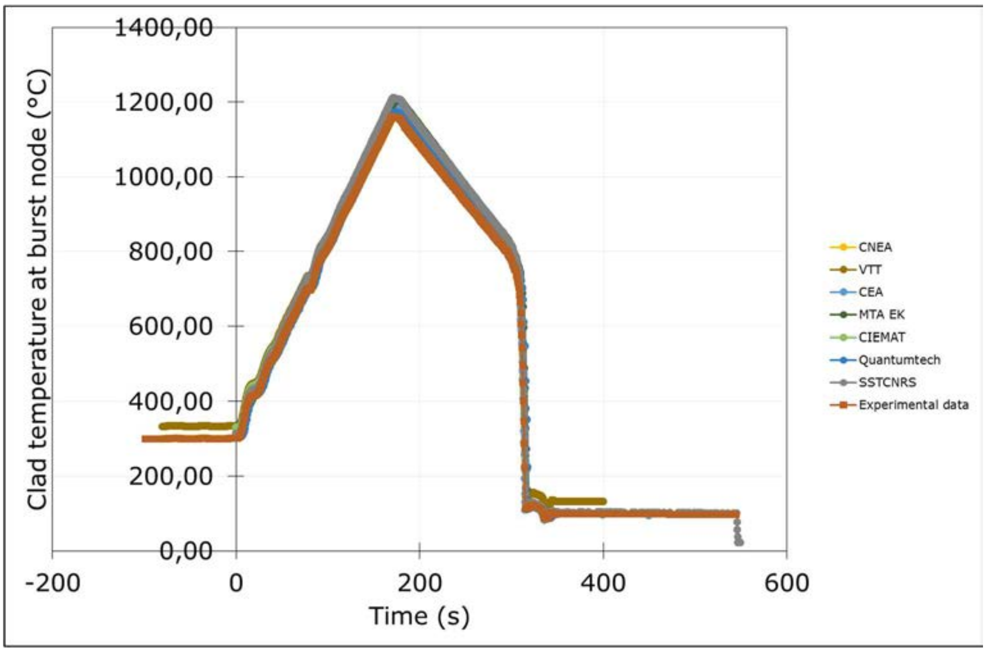

FIG. 111. Clad temperature at burst node calculated during test (Studsvik 192 LOCA test).

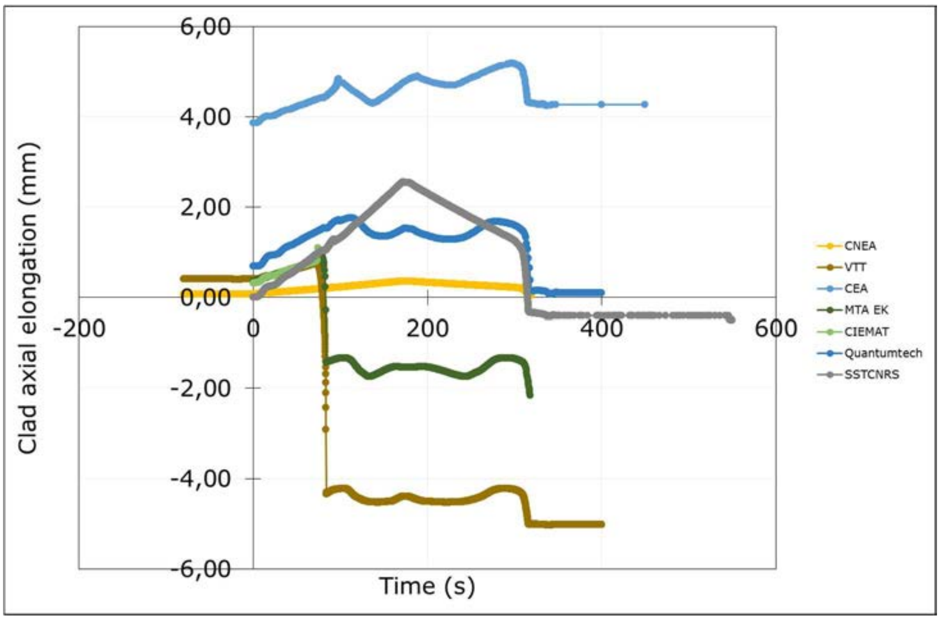

FIG. 112. Cladding axial elongation calculated during test (Studsvik 192 LOCA test).

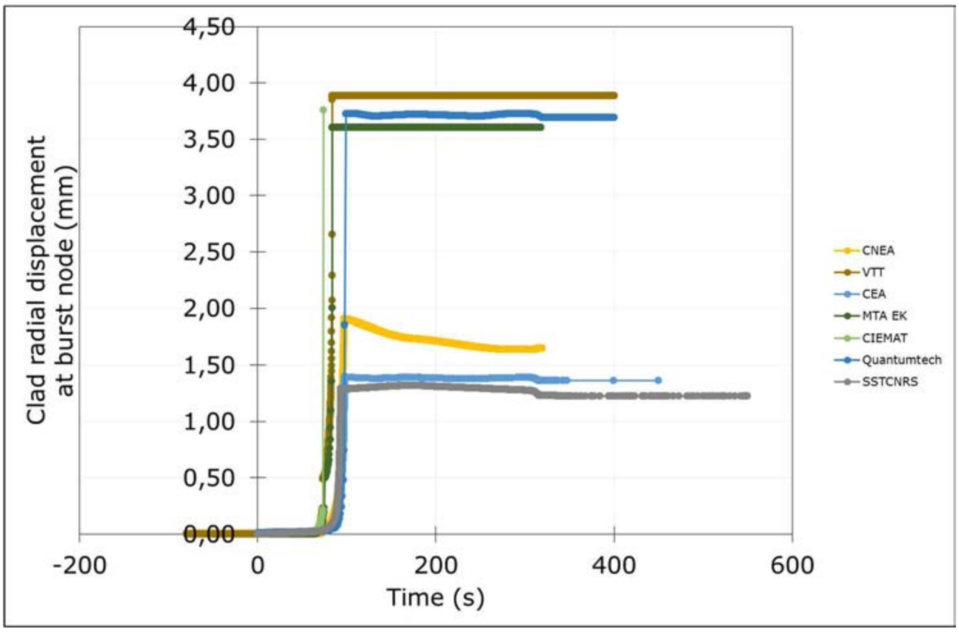

FIG. 113. Cladding radial displacement at burst node calculated during test (Studsvik 192 LOCA test).

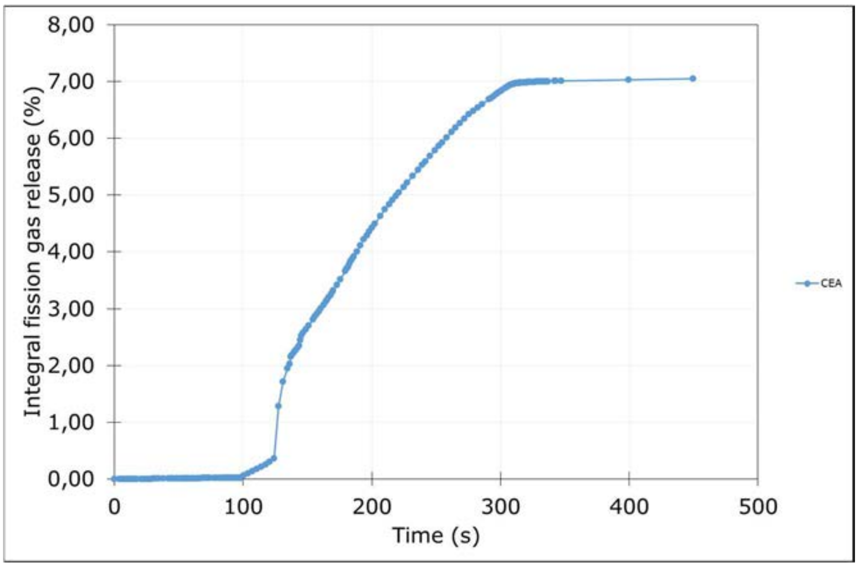

FIG. 114. Calculated fission gas release during test (Studsvik 192 LOCA test).

4.3.3. Results at the end of the LOCA test

All participants slightly over-estimated the time of failure of the rod segment (Fig. 115) between 10 and 25 s, except CIEMAT with FRAPTRAN code.

Practically all participants located the burst node at mid-length of the rod segment (Fig. 116), whereas the experimental burst node was a bit further down the length. Two explanations for the experimental result: either there was an axial gradient of temperature that made the experimental burst node further down, or a localized overpressure in the rod due to local fragmentation (and so fission gas release) before the burst.

As per other tests, the scattering of the calculated maximum cladding deformation was related to the difference in burst criteria (i.e. the maximum strain or stress criteria) used in various codes. As the experimental data available to build this criterion were very much scattered, different approaches would lead to different results.

The cladding oxide thickness calculated by the participants was also scattered (Fig. 117), despite the cladding input temperature was approximately the same for all participants. The deviation was even more for participants who used FRAPTRAN. The same observation could be made for the equivalent cladding reacted (Fig. 118) and the hydrogen content in the cladding. Different oxidation models might have been used for the participants.

For all the participants, the calculated maximum pellet-cladding gap was observed at mid-length (Fig. 119).

Two participants provided an assessment of fuel fragmentation volume fraction along the rod segment (Fig. 120). SSM/ QuantumTech's used the fragmentation and relocation model implemented in FRAPTRAN, whereas MTA-EK's used the HBS volume fraction in the pellet before the test. It was assumed that only the rim structure could be fragmented during this test. Although a model for intergranular fragmentation was implemented in CEA's code ALCYONE, this model was considered for calculating gas release than fuel fragmentation.

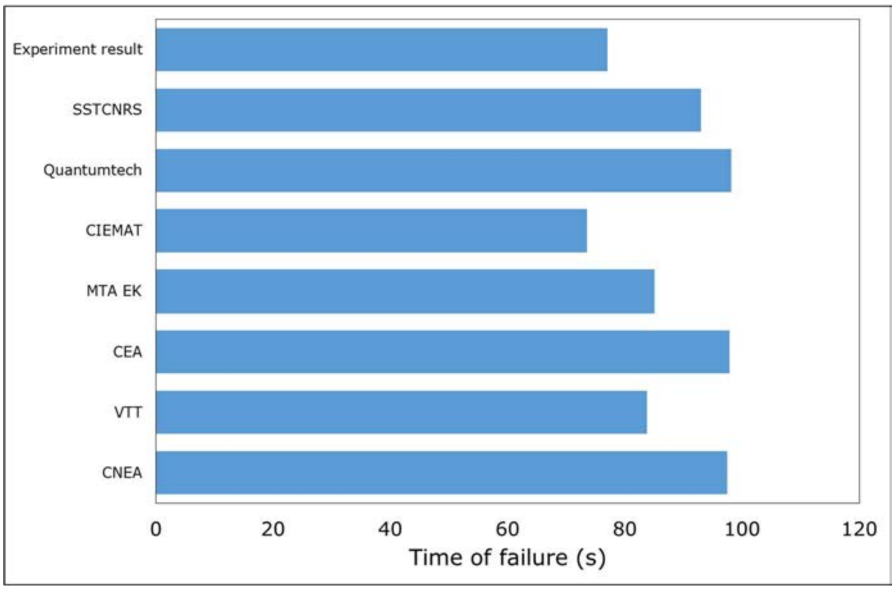

FIG. 115. Calculated time-of-failure (Studsvik 192 LOCA test).

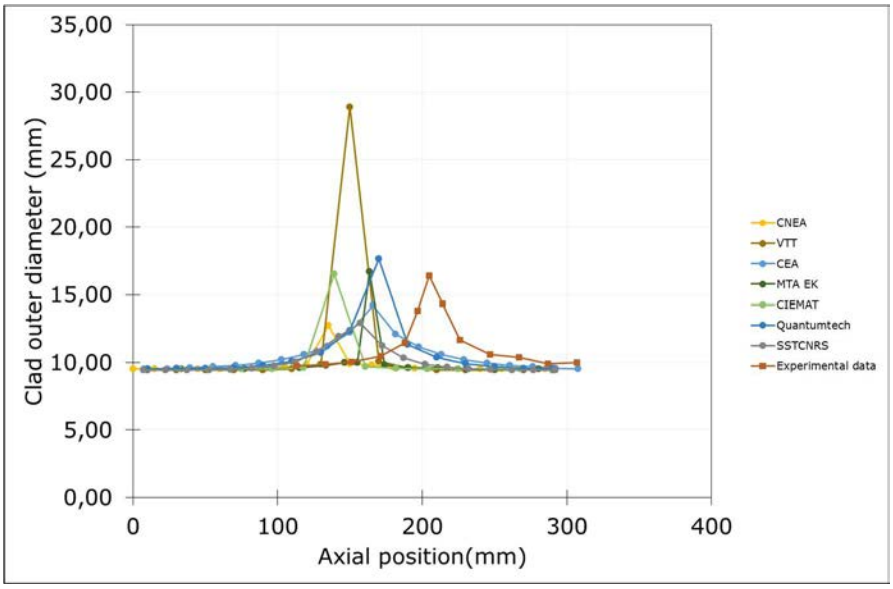

FIG. 116. Cladding outer diameter calculated at end-of-test (Studsvik 192 LOCA test).

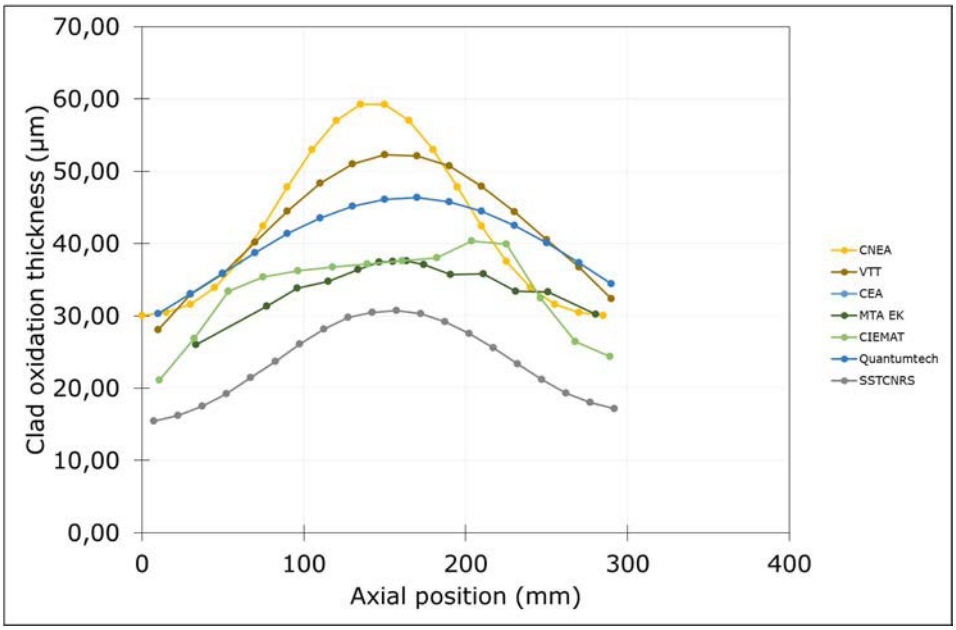

FIG. 117. Cladding oxidation thickness calculated at end-of-test (Studsvik 192 LOCA test).

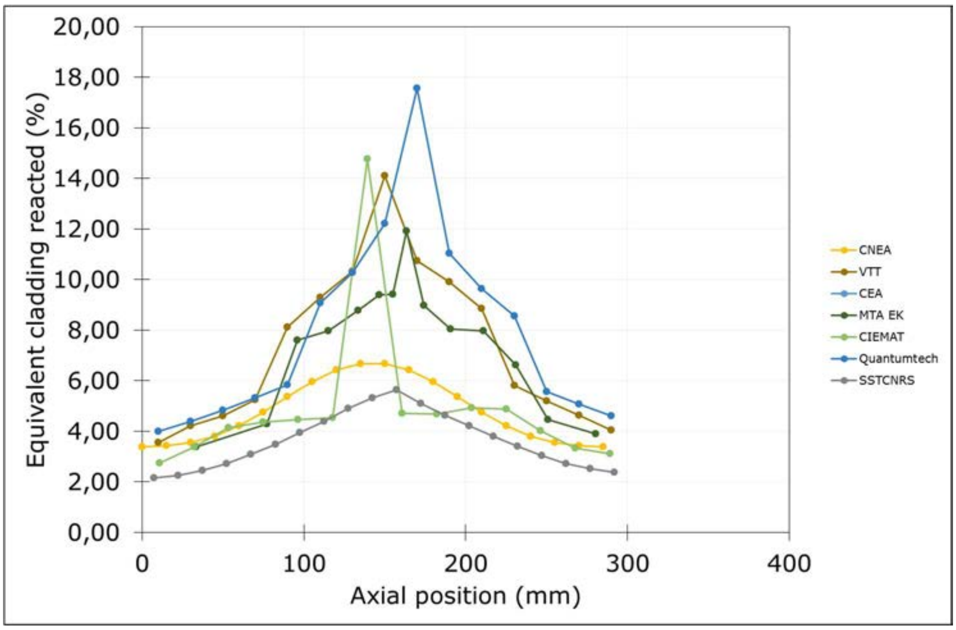

FIG. 118. Equivalent cladding reacted calculated at end-of-test (Studsvik 192 LOCA test).

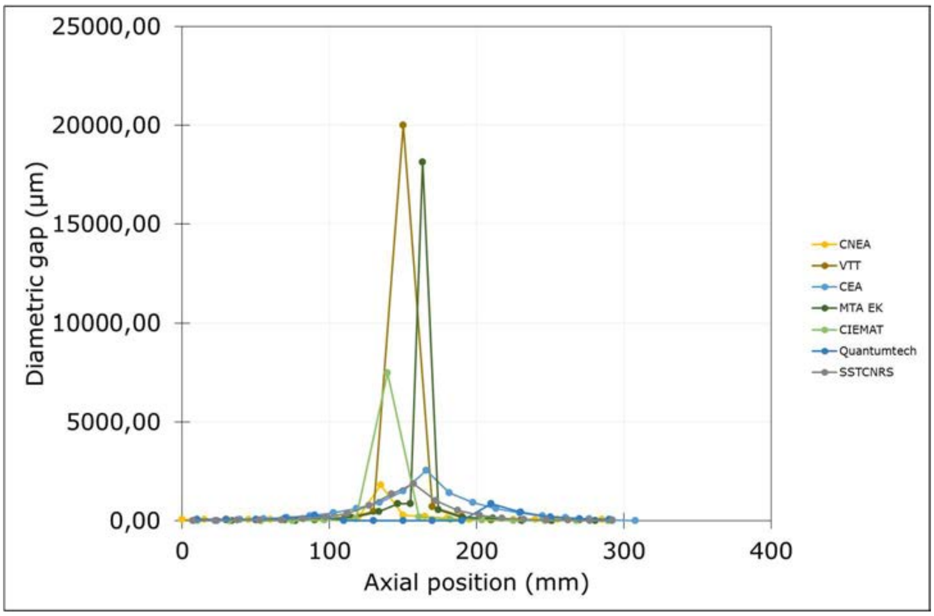

FIG. 119. Calculated pellet-cladding gap at end-of-test (Studsvik 192 LOCA test).

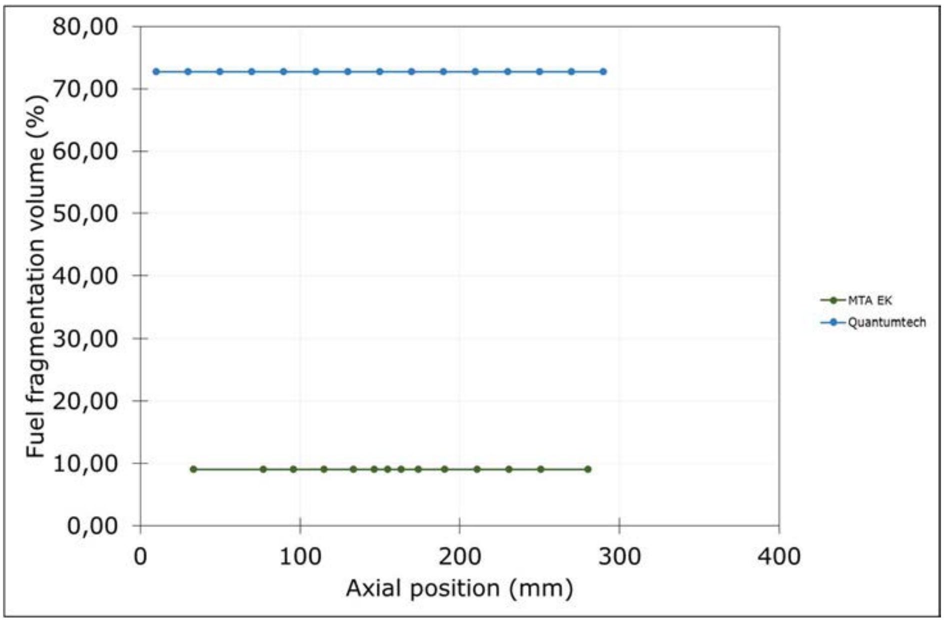

FIG. 120. Fraction of fragmented fuel (Studsvik 192 LOCA test).

4.4. QUENCH-LOCA L1

Four organizations provided results for this test case:

— CNEA (Argentina), DIONISIO 2.0 code;
— INL (USA), BISON 1.4 code;
— JRC (European Commission), TRANSURANUS v1m2j17 code ;
— GRS (Germany), ATHLET-CD 3.1A code.

Although participants had simulated different rods from the out-of-pile bundle test provided by KIT, it was agreed that results from different codes would only be compared with the experimental data from rod# 4 reported in this section.

The results provided by INL and GRS were shifted (corrected) since they applied a different time for the start of their simulations. Their results were started at the onset of the temperature increase at around 100.6 s, corresponding to the increase of the electrical power that lead to the LOCA event. Hence the time-dependent curves were shifted by 100.6 s (and accordingly the predicted time for burst).

4.4.1. Results during the QUENCH-LOCA test

The results obtained from different codes were compared with experimental data provided by KIT. Member States decided to compare the calculated internal gas pressure (MPa) and the cladding outer temperature (ºC) at the burst location, as a function of time (s) for rod # 4. Results are illustrated in Figs 121 to 123.

The internal gas pressure evolution (see Fig. 121) indicated that, apart from the DIONISIO prediction, the codes closely followed the on-line measured pressure values prior to burst. BISON and TRANSURANUS used the measured data as input values for their simulations, rather than using the code calculated values, as if it was a sealed rod in a reactor. ATHLET-CD also used an initial internal pressure and calculated the pressure evolution. ATHLET-CD code, as a system code, used groups of rods during the simulation. Rod# 4 was an object representing the rods# 2, 4, 6, 8 that had the same thermal hydraulic and mechanical behaviour within the system code.

Results around the burst time for rod# 4 is indicated in Fig. 122. The difference between code predictions and the measured data stemmed from the fact that simulation tools simply considered an instantaneous drop in rod pressure upon burst and stopped the calculation (BISON). The measured value revealed that the pressure drop was not instantaneous.

Given that many thermocouple readings were available in the KIT bundle test, most participants used the measured values as the boundary conditions for the benchmark exercise that focused on the fuel rod behaviour. DIONISIO and ATHLET-CD relied on their own thermal hydraulic models for estimating the temperature profile along the cladding during the test. ATHLET-CD predicted the same temperature behaviour as the measured values, but the peak temperature at 350 s was lower than the experiment (see Fig. 123).

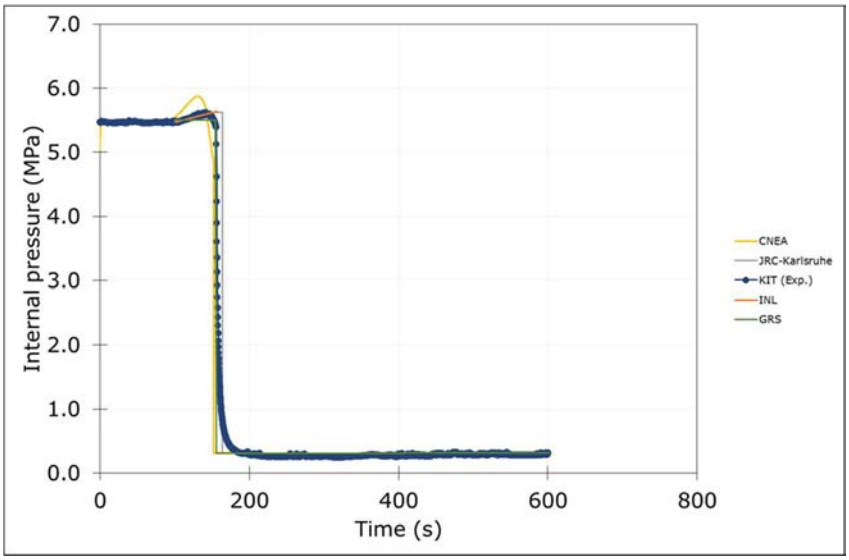

FIG. 121. Comparison of the rod internal pressure (MPa) versus time (s) in rod 4 of the QUENCH-LOCA L1 experiment at KIT, with predicted values obtained from DIONISIO, TRANSURANUS, BISON and ATHLET-CD.

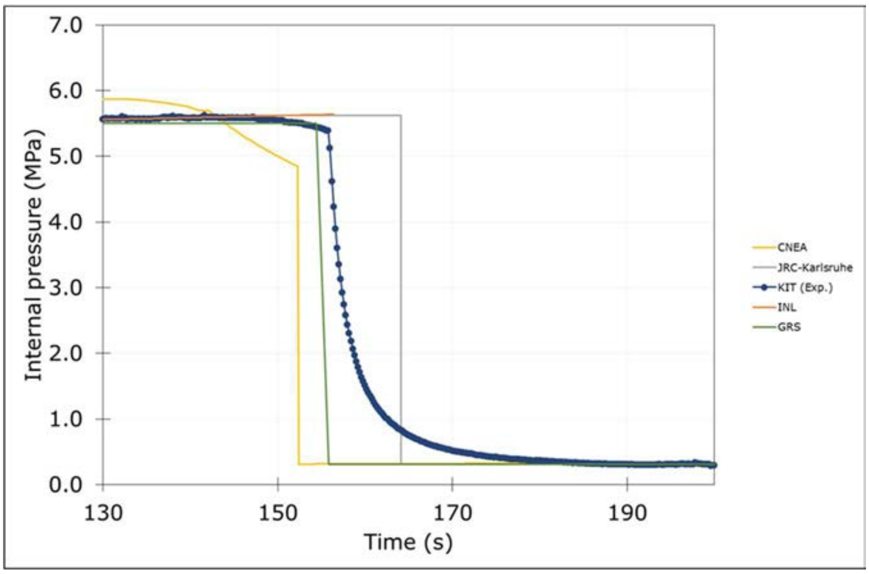

FIG. 122. Comparison of the rod internal pressure (MPa) versus time (s) around the burst location in rod 4 of the QUENCH-LOCA L1 experiment at KIT, with predicted values obtained from DIONISIO, TRANSURANUS, BISON and ATHLET-CD.

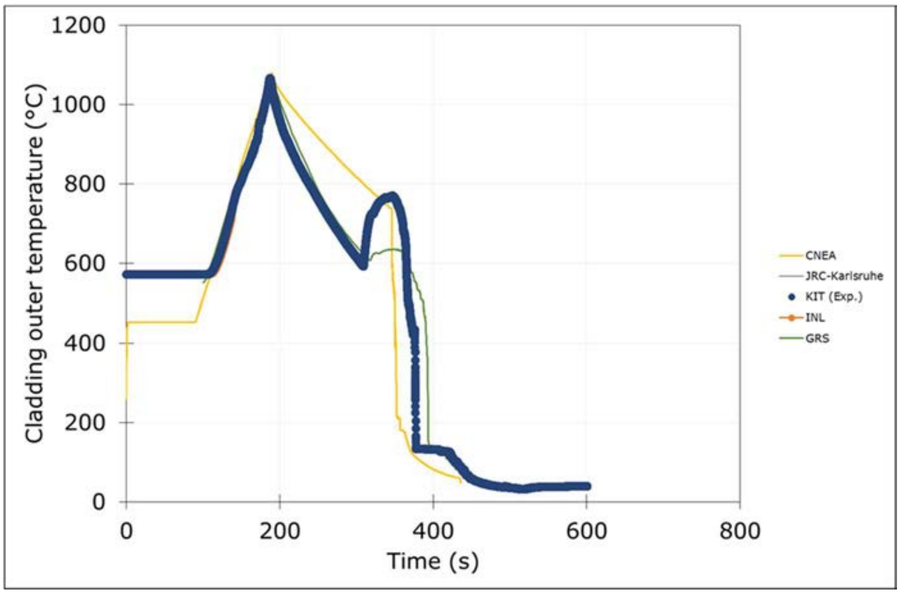

FIG. 123. Comparison of the cladding outer temperature (ºC) at the axial position of the burst versus time (s) in rod 4 of the QUENCH-LOCA L1 experiment at KIT, with predicted values obtained from DIONISIO, TRANSURANUS, BISON and ATHLET-CD.

4.4.2. Results after the QUENCH-LOCA test

At the end of the LOCA test, participants were asked to compare their simulated values for:

— The cladding outer diameter (mm), the cladding oxidation thickness (microns), the equivalent cladding reacted (%) and the hydrogen content (ppm), as a function of the axial position (mm), are illustrated from Figs 124 and 127.

— Failure time (s), burst pressure (MPa), average cladding hoop stress (MPa) at the burst location, axial location (mm) of the burst, clad outer temperature (ºC) at the burst location, clad average hoop strain (%) at the burst location are illustrated from Figs 128 to 133.

The axial profiles of the cladding diameters after the test (see Fig. 124) indicated some scattering, although the overall agreement was reasonable for all predictions. The position of the burst opening was in relatively good agreement, considering the dissimilarities in the boundary conditions as outlined above, along with the differences in the axial discretization that was also visible in the plot. The peak position obtained with BISON agreed with the ballooning of the cladding at 916 mm (without burst); whereas the peak position predicted by TRANSURANUS lied between this value and a maximum ballooning of 982 mm (with burst). The burst position should normally occur at the highest temperature. However hot spot could accommodate rod bending and the contact location between the pellets and the cladding could then be changed. This phenomenon is stochastic and could not be modelled easily. The scattering of the calculated maximum deformation was also related to the difference in burst criteria (such as maximum strain or stress criteria) and the predicted cladding temperature (as indicated in Fig. 123) used in various codes.

The measured tangential strain from PIE included the opening after burst, whereas the computer codes did not account for this opening. After subtracting this opening, the maximum strain values would be 11–15 % smaller for all rods. It was evident that the BISON code underpredicted the tangential strain, whereas all other codes overpredicted the maximum strain after burst. However, the deviation between the predicted and measured maximum strain values was within the experimental uncertainty.

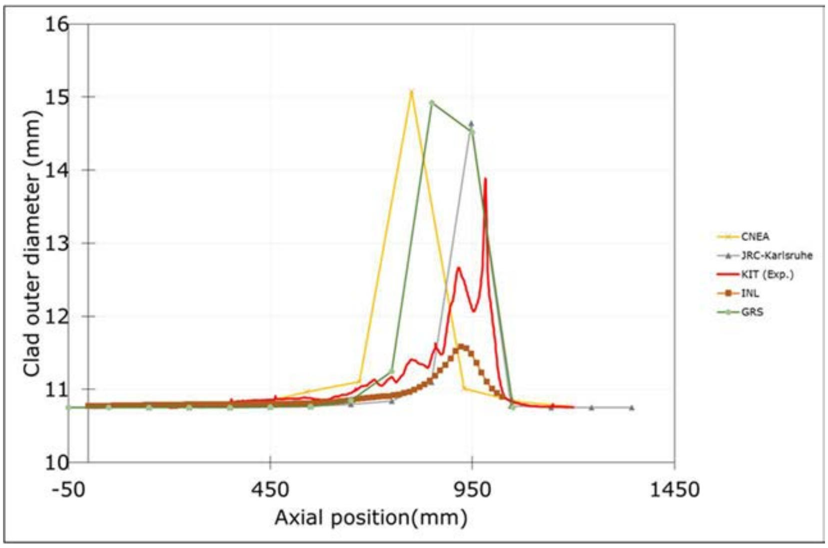

FIG. 124. Cladding outer diameter calculated at the end-of-test for rod 4 (QUENCH-LOCA L1 test).

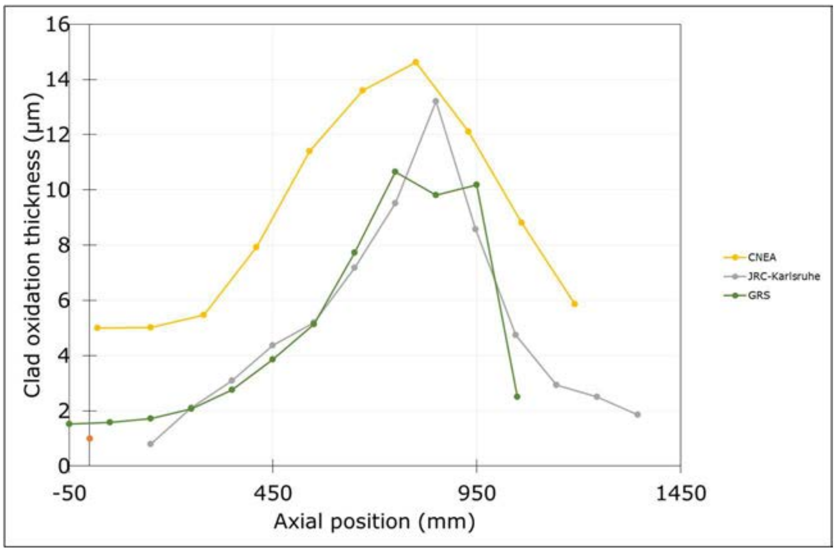

FIG. 125. Cladding oxide thickness calculated at the end-of-test for rod 4 (QUENCH-LOCA L1 test).

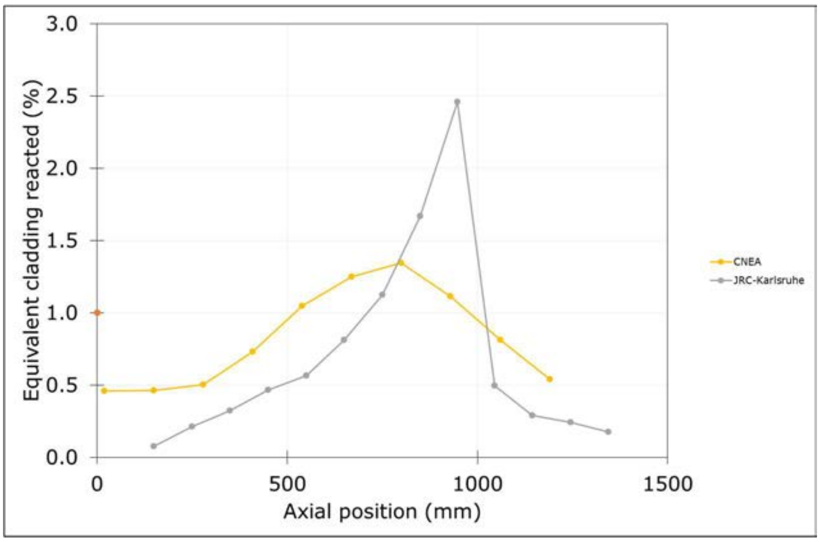

FIG. 126. Equivalent cladding reacted calculated at the end-of-test for rod 4 (QUENCH-LOCA L1 test).

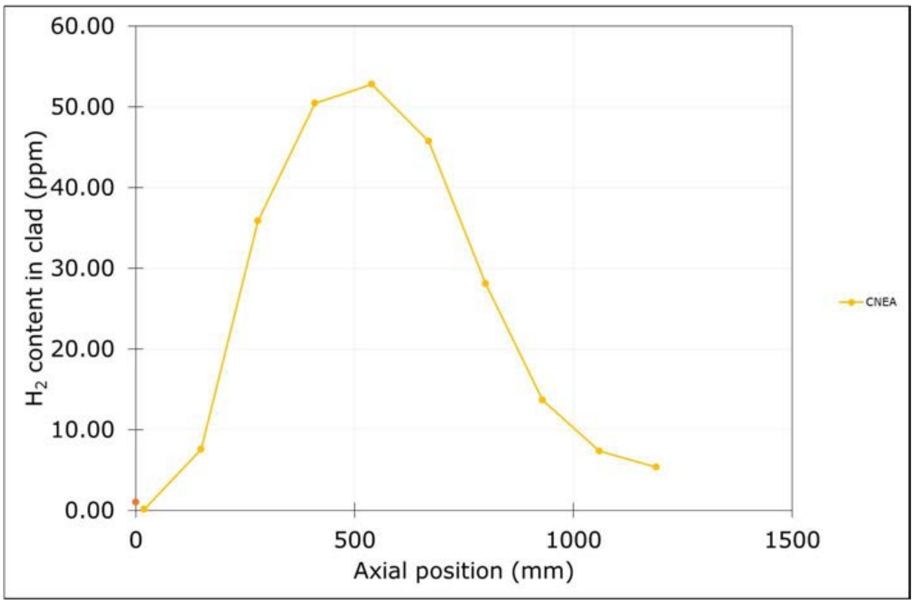

FIG. 127. Hydrogen content in cladding at the end-of-test for rod 4 (QUENCH-LOCA L1 test).

The cladding oxidation thicknesses along the rod after the LOCA experiment calculated by the participants are reported in Fig. 125, while the experimental values are reported in Section 2.4. Taking into account that the values obtained with the codes for the oxidized layer thickness are only for the ZrO_2 layer thickness, whereas the experimental values represent a sum of the thickness of ZrO_2 and α–Zr(O), and the large experimental scatter, it is fair to conclude that the values obtained with the codes are close to the measured values of ZrO_2.

The predicted code values are also scattered, despite the cladding temperature used as input of the code is close for all participants, being probably very sensible to this parameter. The same observation can be made about the equivalent cladding reacted depicted in Fig. 126. It is very likely that specific differences in the parametrization of the models exist for the different participants. Finally, it should be pointed out that only predictions for the hydrogen content in the cladding at the end of the test were provided by the DIONISIO code and depicted in Fig. 127 for the sake completeness.

Rod failure times are reported in Fig. 128. The calculated values were scattered as compare to the experimental burst time, but the several factors should be considered:

— There was a spread on the axial temperature profiles, as indicated in Section 2.4 above;
— There was a radial temperature gradient in the bundle;
— The observed bending of the fuel rods (related to azimuthal temperature variations) was not simulated by the codes;
— The observed clad ballooning was not symmetric.

The TRANSURANUS code indicated the largest over-predicted burst time for this rod. To assess the effect of some known uncertainties, a few additional calculations were carried out. For instance, the impact of a ±10% spread on the cladding temperature was analyzed. The effect of this coolant temperature variation on the burst time was consistent with the spread of the burst time observed. Hence the coolant temperature would have an impact on the burst time. This was consistent with the conclusions from the uncertainty analysis reported in Section 5. One could conclude that the measured and calculated burst times were in reasonable agreement. The difference between the predicted and the experimental values was not significant, when considering the experimental uncertainties and the azimuthal temperature that could not be typically captured by the 1.5D fuel performance codes.

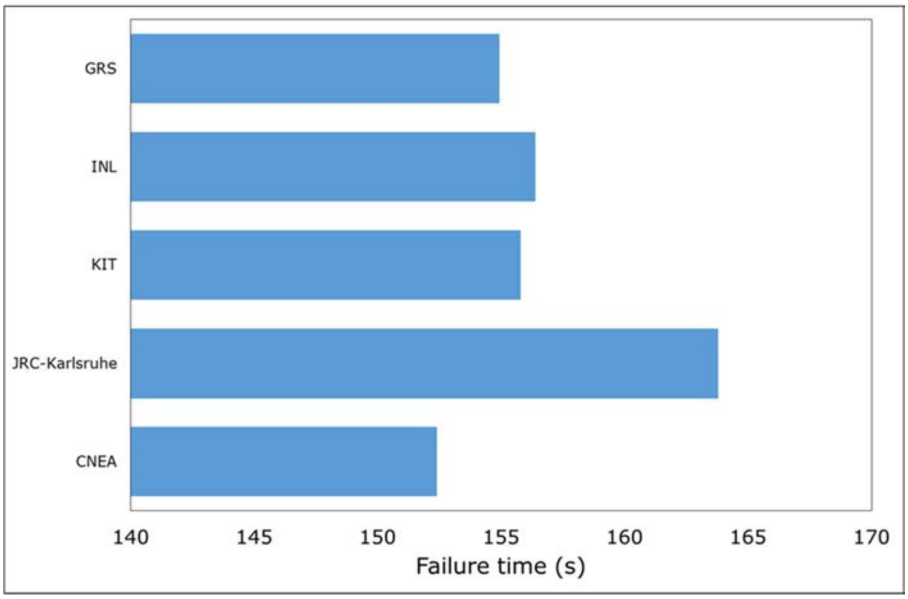

FIG. 128. Failure time (s) of rod 4 in QUENCH-LOCA L1 test at KIT.

The predicted burst pressures were compared with the experimental value, as summarized in Fig. 129. Except for the DIONISIO code that underpredicted the measured burst pressure, the other codes tend to be overpredicted. However, BISON and TRANSURANUS imposed a rod internal pressure based on the measured values that could explain the degree of overprediction. DIONISIO and ATHLET-CD codes used the calculated coolant temperatures. Nevertheless, the cladding temperature at the time-of-failure in DIONISIO was quite close to the measured value as show in Fig. 132 below. DIONISIO used FEM to discretize the half-pellet of each sector and an average value on stress to calculate the burst criteria (rather than the maximum value in a single element). This was done to avoid abnormal (extreme) values, but could underestimate the value on burst or the maximum stress.

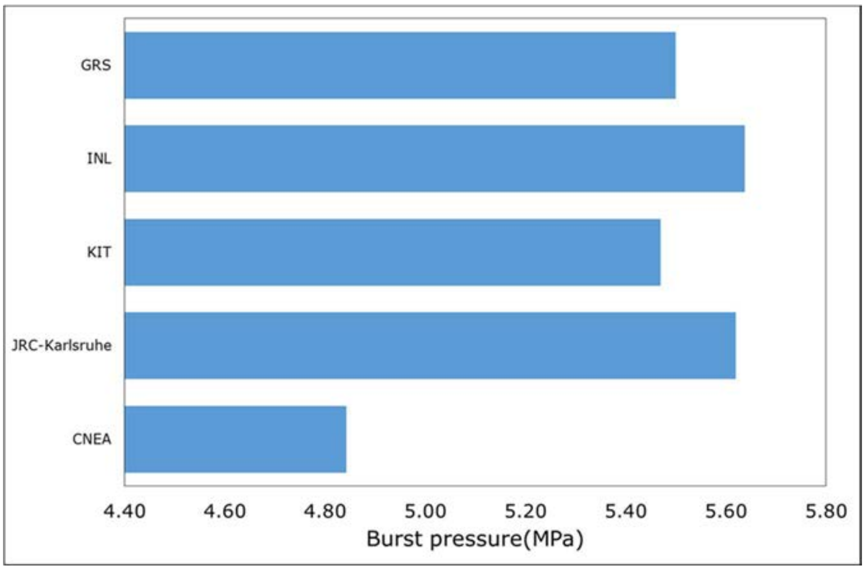

FIG. 129. Burst pressure (MPa) at failure in rod 4 in QUENCH-LOCA L1 test at KIT.

Fig. 130 indicated the average cladding hoop stress at burst elevation. The values obtained from TRANSURANUS and ATHLET-CD were almost two time those from DIONISIO and BISON codes. This could reflect on the experimental uncertainty on the burst stress, which was usually reported as a function of temperature in a logarithmic scale.

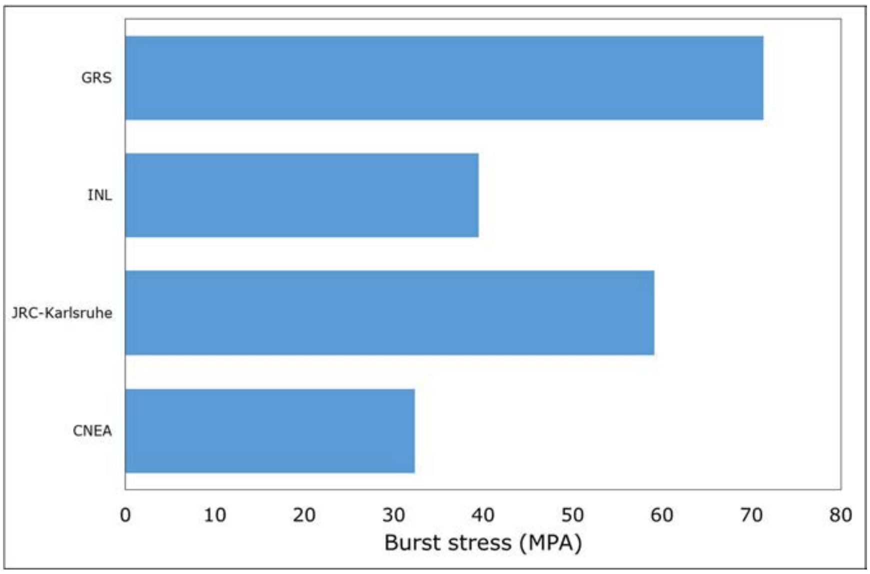

FIG. 130. Average cladding hoop stress (MPa) at burst elevation in rod 4 (QUENCH-LOCA L1 test) at KIT.

The predicted burst elevations are indicated in Fig. 131. Although the results were consistent with the axial plots for the outer diameter, results would also depend on the axial discretisation used in different simulations. The low value obtained by DIONISIO code was most likely affected by the axial distribution of the coolant temperature which was calculated, whereas the other codes simply applied the measured temperatures (as the boundary condition) during the test. This is consistent with the lower axial elevation of the burst position revealed in Fig. 131.

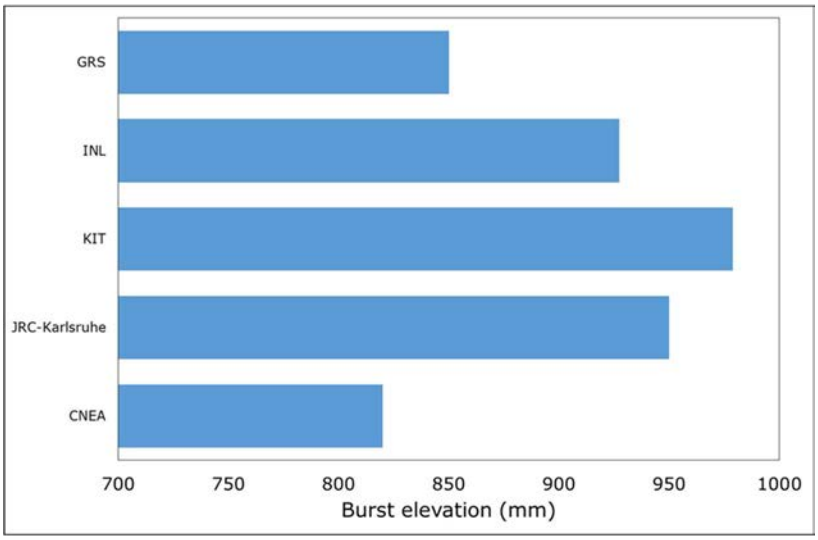

FIG. 131. Axial position of the centre of the burst (mm) of rod 4 in QUENCH-LOCA L1 test at KIT.

The clad temperatures at burst are indicated in Fig. 132, which are consistent with the trends as shown in Fig. 123. TRANSURANUS code predicted a low temperature, as the imposed clad temperature was decreased with an overpredicted burst time. The opposite was true for the BISON code. The ATHLET-CD code on the other hand indicated a lower temperature because of the lower burst elevation at 850 mm. The temperature predicted by ATHLET-CD at 950 mm, representing the measured burst elevation, was approximately 30 K higher than at 850 mm, which was comparable to the experimental value.

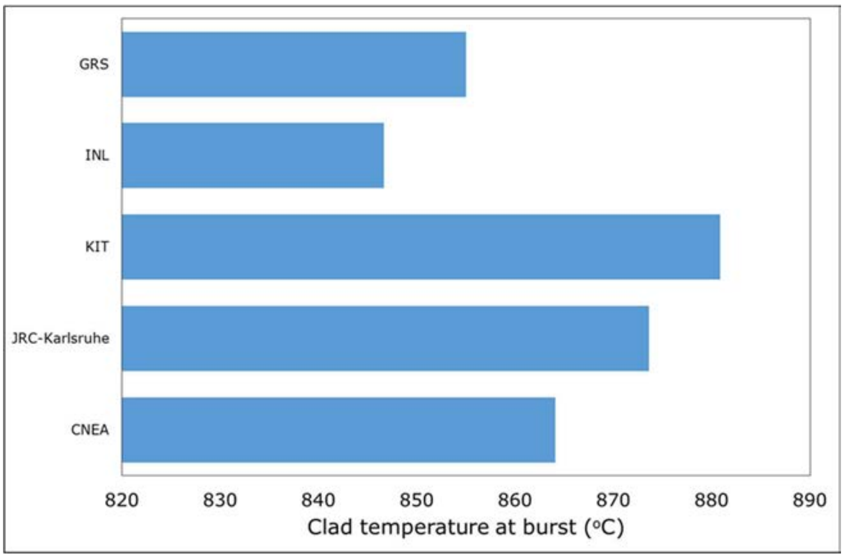

FIG. 132. Clad outer temperature (^oC) at burst elevation of rod 4 in QUENCH-LOCA L1 test at KIT.

The predicted maximum tangential strains after the tests, compared with the measured value, are as indicated in Fig. 133. The overall picture was consistent with those results illustrated in Fig. 124, i.e. the BISON code underpredicted while the other codes overpredicted the maximum deformation. One should note that the experimental value included the burst opening size. The measured strain would be reduced by about 11–14%, if the burst opening size was not included.

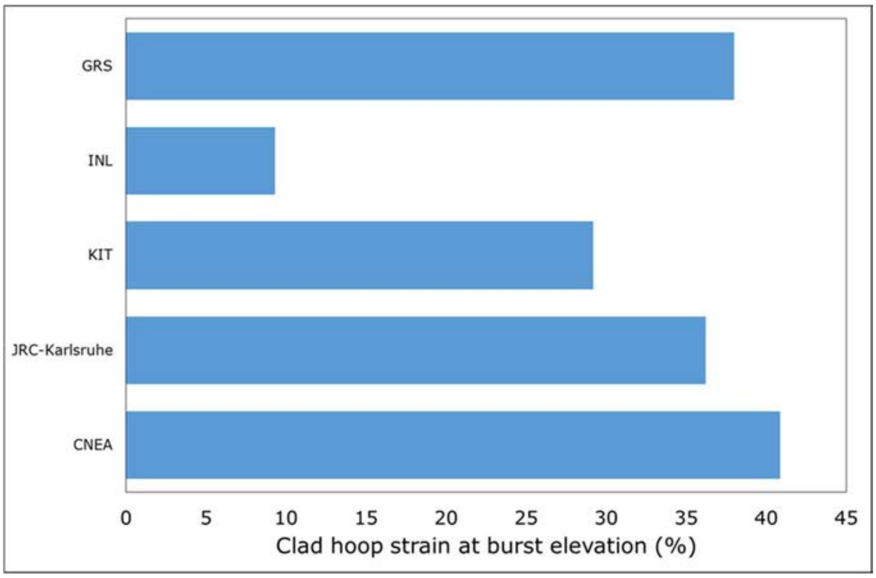

FIG. 133. Clad average hoop engineering strain (%) at burst elevation of rod 4 in QUENCH LOCA L1 test at KIT.

4.5. CORA-15

Two organizations provided results for this case:

— GRS (Germany), ATHLET-CD code;
— IBRAE (Russia), SOCRAT code.

For both codes, the rod bundle was simulated by four concentric rings according to Table 10, an inner ring (ROD1) containing the central unheated rod, a second ring containing four heated rods (ROD2), a third ring containing six unheated rods and two absorber rods (ROD3) and an outer ring with twelve heated rods (ROD4).

TABLE 10. CORA-15 ROD GROUPS FOR MODELLING

Rod group in code	Number of rod in the CORA-15 test bundle
Rod 1	Central unheated rod (4.4)
Rod 2	Inner heated rods (3.3), (3.5), (5.5), (5.3)
Rod 3	Unheated rods (4.2), (2.2), (2.4), (2.6), (6.6), (6.4);
	Absorber rods (4.6), (6.2) in ATHLET-CD
Rod 4	Outer heated rods (1.1), (1.3), (1.5), (1.7), (3.7), (5.7), (7.7), (7.5), (7.3), (7.1), (5.1), (3.1)

The reference time (0 s) was established for the beginning of the experiment. The reference bundle elevation (0 mm) corresponded to the bottom of the heated length in the rod simulator.

4.5.1. Cladding burst parameters for the CORA-15 bundle

Table 11 shows results of both codes concerning the burst parameters. Experimental average values of the burst time for corresponding rod groups are included.

TABLE 11. BURST DATA CALCULATED BY ATHLET CD (GRS), SOCRAT (IBRAE) *(in comparison with experimental results)*

Description	Rod 1	Rod 2	Rod 3	Rod 4	Source
Time of burst (s)	3595	3571	3612	3570	GRS
	3619	3559	3626	3593	IBRAE
	3601	3559[e] 3548-3564[f]	3609[e] 3565-3645[f]	3580[e] 3494-3618[f]	Experiment
Internal rod pressure[a] (MPa)	6.90	6.92	6.68	6.81	GRS
	6.15	5.85	6.0	5.85	IBRAE
	6.15	5.44 (rod 3.3)	5.73 (rod 6.6)	5.84 (rod 7.7)	Experiment
Axial elevation (mm)[b]	750	750	750	750	GRS
	783	717	783	750	IBRAE
			—[g]		Experiment
Cladding outer temperature[c] (°C)	767	762	766	754	GRS
	842	827	847	847	IBRAE
	Between 650 and 850 (estimated)				Experiment
Maximum hoop strain[a] (%)	43.64	40.97	40.55	38.87	GRS
	36	36	36	38	IBRAE
			—[h]		Experiment
Average hoop stress[a] (Mpa)	133.3	82.2	82.2	79.6	GRS
			—[h]		Experiment

[a] At predicted burst time.
[b] Of middle of clad burst opening.
[c] At the middle of the burst at predicted burst time.
[d] Azimuthal average hoop stress (Mpa) σ_b in cladding at predicted burst time.
[e] Mean.
[f] Time span.
[g] —: Not available because of the bundle melting.
[h] —: Not available.

The corresponding comparison diagrams together with experimental data are presented in Fig. 134.

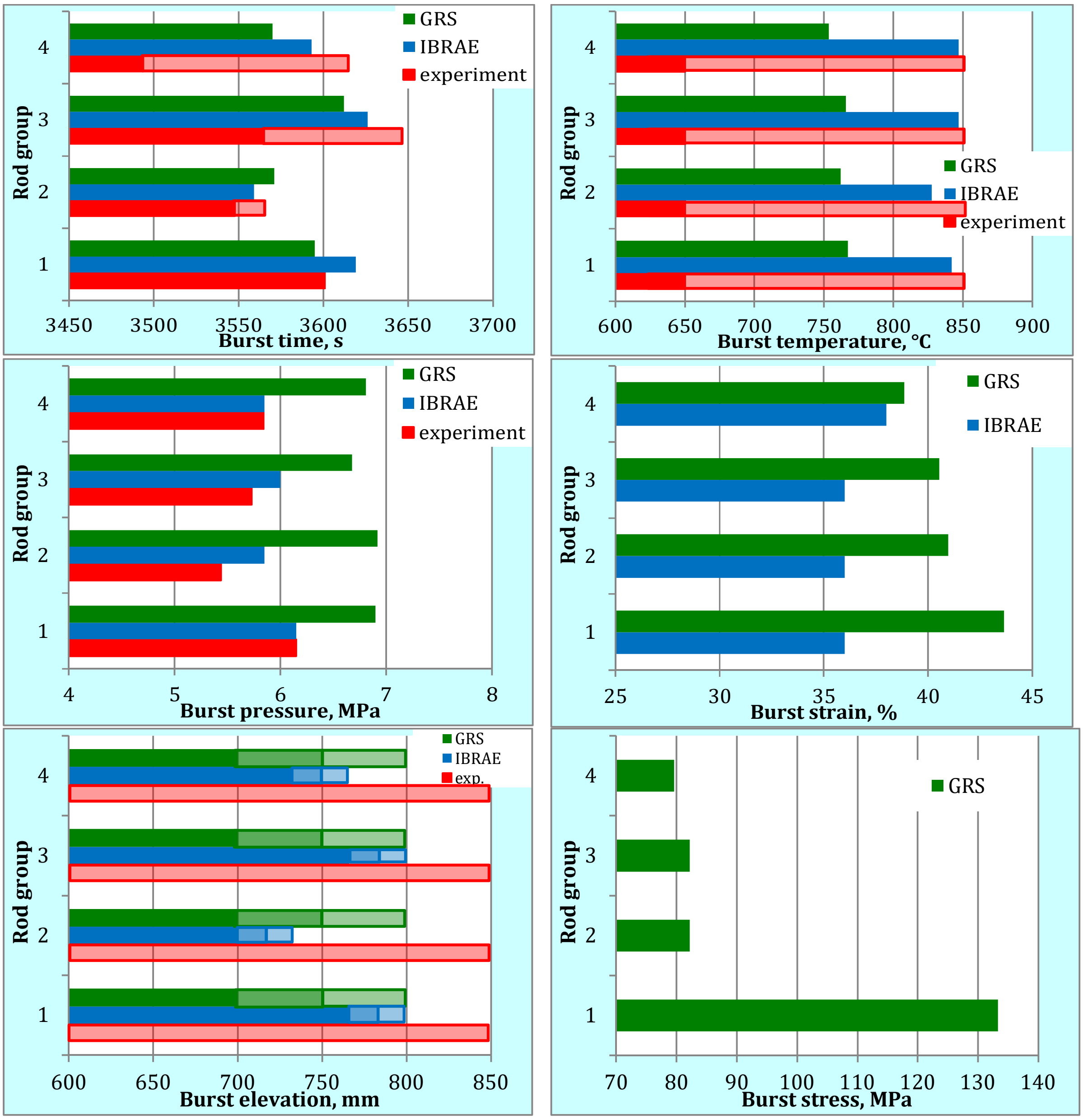

FIG. 134. Burst parameters. Transparent bars show uncertainty ranges. Transparent red corresponds to the measurement uncertainties, transparent green and blue - predictions with the axial node size of 100 mm (GRS) and 33 mm (IBRAE), respectively.

Measured data that characterized the cladding burst were the burst time and the burst pressure derived from the pressure evolutions. The burst elevations were not available because of the bundle melting in the expected ballooning zone. The burst time depended mainly on the temperature distribution within the cross-section since the initial inner pressure was small. The test exhibited a large burst time span of 150 s (from 3494 to 3644 s). This indicated a large cladding temperature difference in the burst cross-sections that could be estimated as 150 K based on the measured burst time span and the heat up rate (1 K/s). The temperature differences could be resulted from the heat losses (outer heated claddings were colder than inner ones), presence of unheated rods and absorbers as well as from a local temperature non-uniformity. Table 11 indicated the following burst sequence in the test: heated inner claddings (rod 2) – outer heated claddings (rod 4) – unheated central cladding (rod 1) – inner unheated cladding (rod 3). The burst time span was calculated within the experimental scattering of ATHLET as well as SOCRAT. Burst pressure was captured by both codes with a tendency of slight overestimated (the measured burst pressure values, provided for the groups 2–4 in Fig. 134, were derived from the pressure evolutions of individual rods as indicated in the Table 11, not averaged over the groups).

The burst elevation could be estimated assuming that the ballooning and rupture occurred at the hottest elevation. Fig. 135 displays vertical temperature profiles at the beginning (3500 s), the middle (3600 s) and the end (3650 s) of the burst time span derived from the available TC readings. This facilitated the estimation of the hottest zone location between 250 mm and 850 mm at the beginning, and between 600 and 850 mm at the middle and the end of burst time span. The hottest zone was calculated at around an elevation of 750 mm. Considering the node sizes, the axial elevations of the clad burst openings in all rods predicted both by ATHLET and SOCRAT were located between 700 and 800 mm (Fig. 134).

The burst temperatures of the unheated cladding were estimated to rise from 650 to 800 °C during the burst time span. The heated rods were estimated to be 50 K hotter than the unheated ones based on the difference of 50 s between the mean values of the burst times. So, the estimated temperature range for both the heated and unheated rods would be approximately 650 to 850 C.

Maximum hoop strain achieved at the opening of the burst was calculated by both codes as $\varepsilon_b = 100 \cdot (D_{act} - D_0)/D_0$, where $D_{act} = (D_{ext} + D_{in})/2$ was the mean diameter of cladding, D_{ext} and D_{in} were external and internal cladding diameters at the opening at the burst time, and D_0 was the initial mean cladding diameter. Both codes used a simple failure criterion based on the maximum strain.

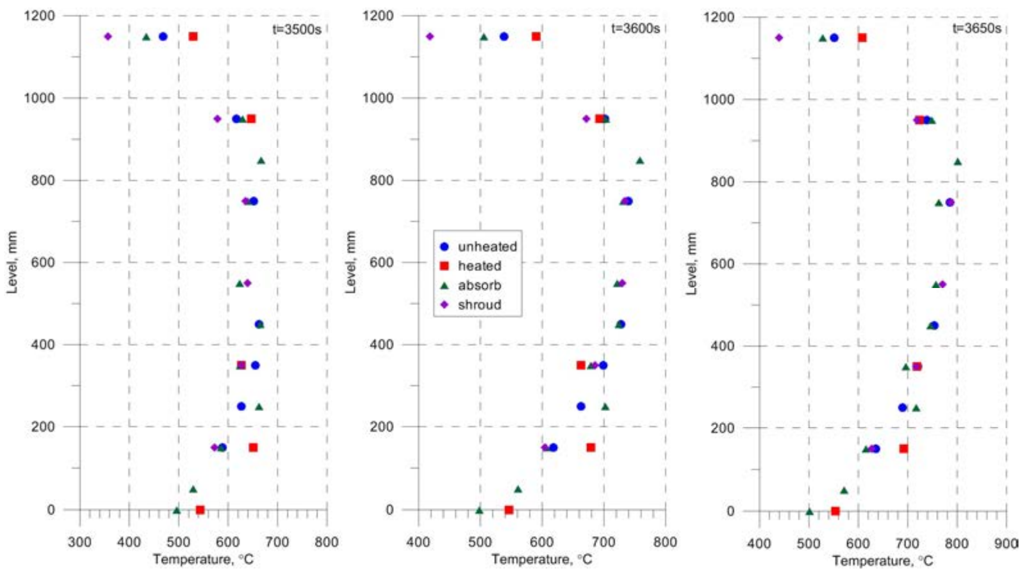

FIG. 135. Vertical temperature distribution at the burst time span.

4.5.2. Time dependences and axial dependences of LOCA events for central rod 4.4 of the CORA-15 bundle

ATHLET and SOCRAT gave reasonable temperature predictions (see Figs 136 and 137). However, there were discrepancies in the pressure modelling: higher burst pressure for ATHLET (GRS) than for SOCRAT (IBRAE) (Fig. 137).

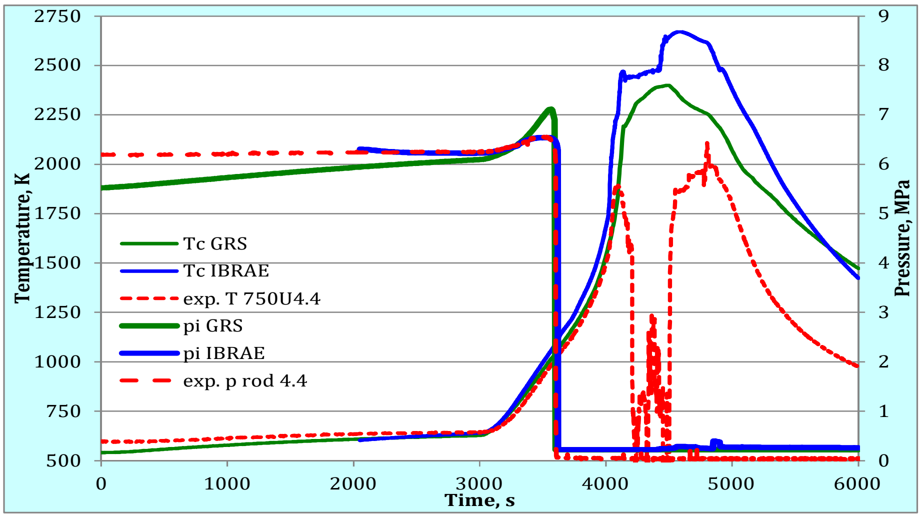

FIG. 136. Comparison of temperature (Tc) and internal pressure (pi) histories during the test (at an elevation of 750 mm).

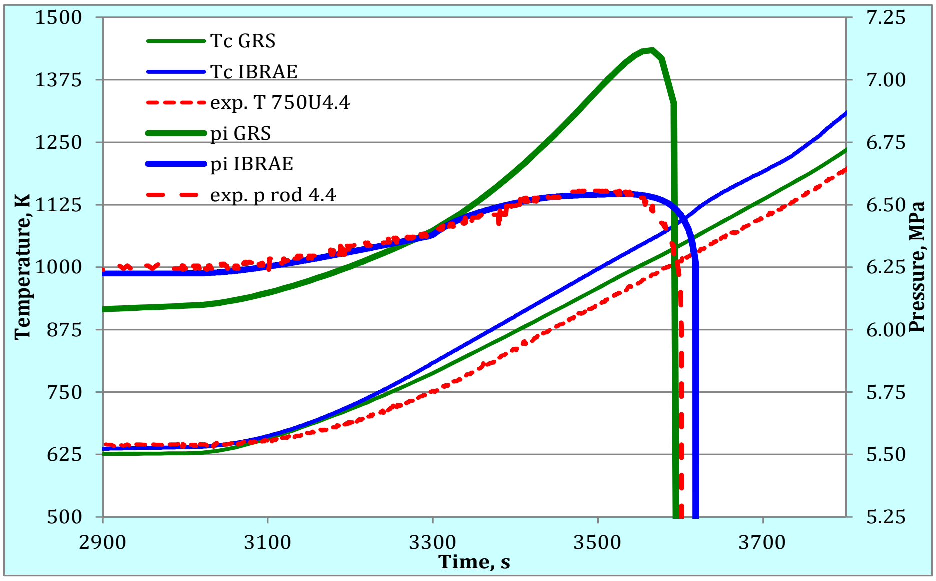

FIG. 137. Comparison of temperature (Tc) and internal pressure (pi) histories during the LOCA transient (at an elevation of 750 mm).

There was a remarkable coincidence in the location and extent of the ballooning zone predicted by both codes as indicated in Fig. 138, though ATHLET revealed a stronger ballooning in comparison with SOCRAT. The reason of a sharp decrease of the residual metal thickness between 450 and 950 mm was the thinning of the cladding due to ballooning. The influence of the oxide layer was minimal at the time of the burst due to low oxide thickness (Fig. 139). SOCRAT indicated more oxidation (in narrower region) due to higher burst temperatures.

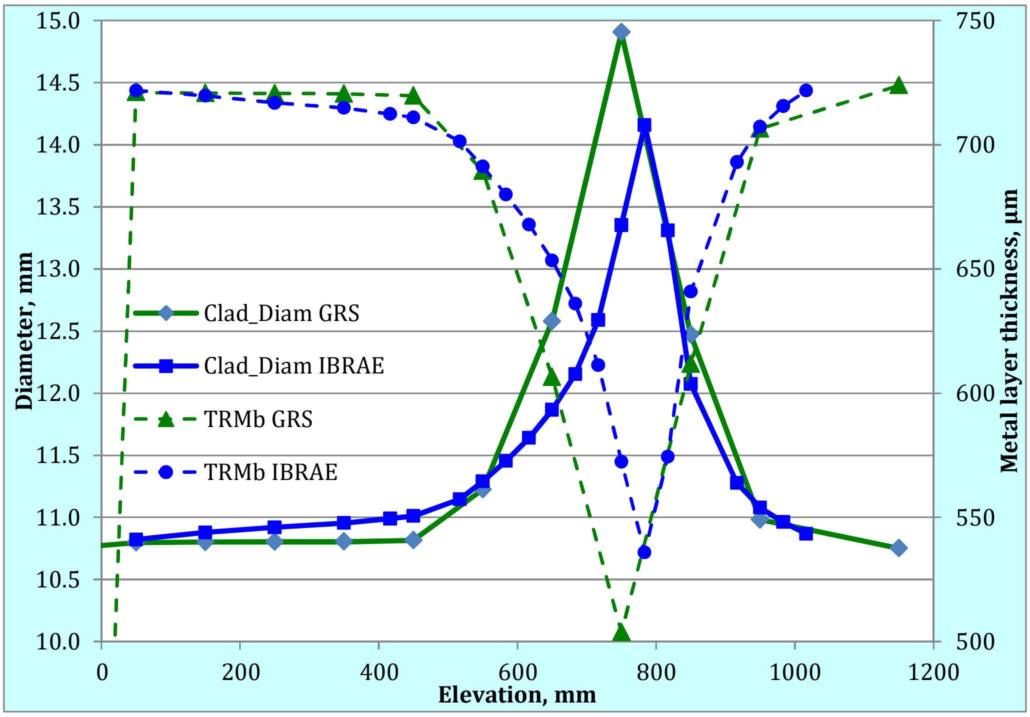

FIG. 138. Axial distributions of cladding external diameter and residual metal at burst time.

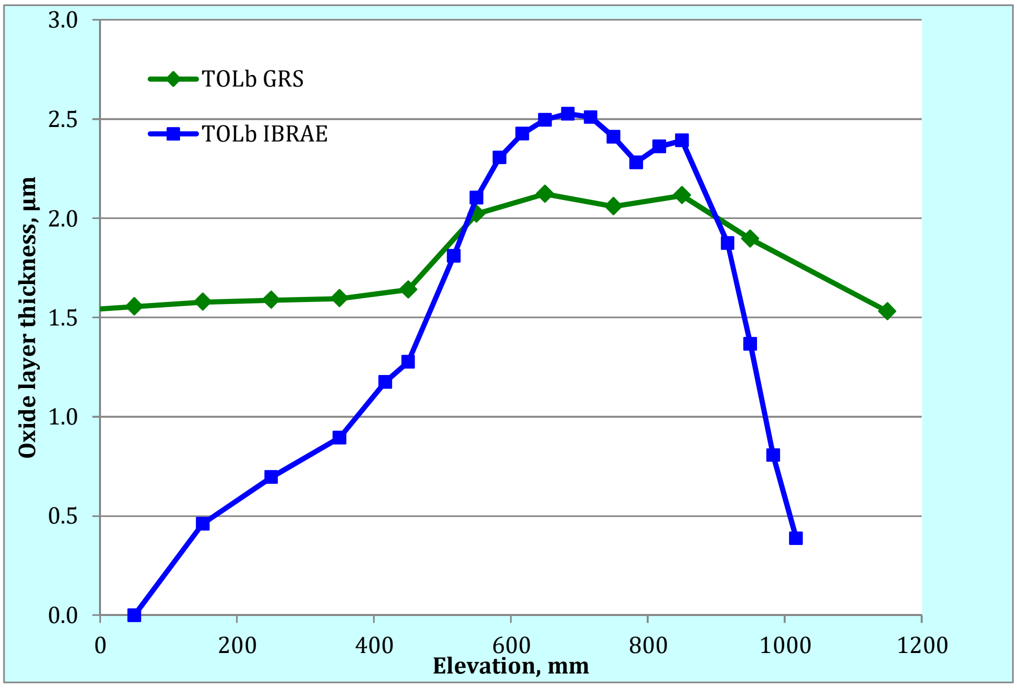

FIG. 139. Axial distributions of oxide layer ZrO_2 at the outer cladding surface.

4.5.3. Post-test outer oxide layer thickness of the CORA-15 claddings

The thickness of ZrO_2 films at different elevations for different element groups is indicated in Fig. 140. Debris from ZrO_2 relocated with the melt or any information about oxidized part of the melt were not provided.

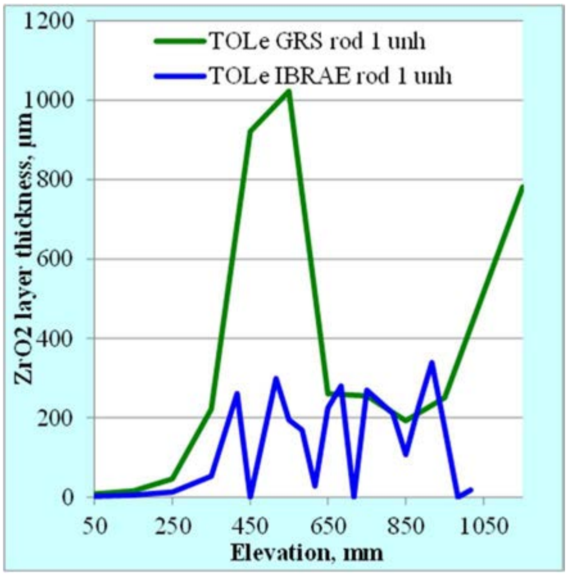

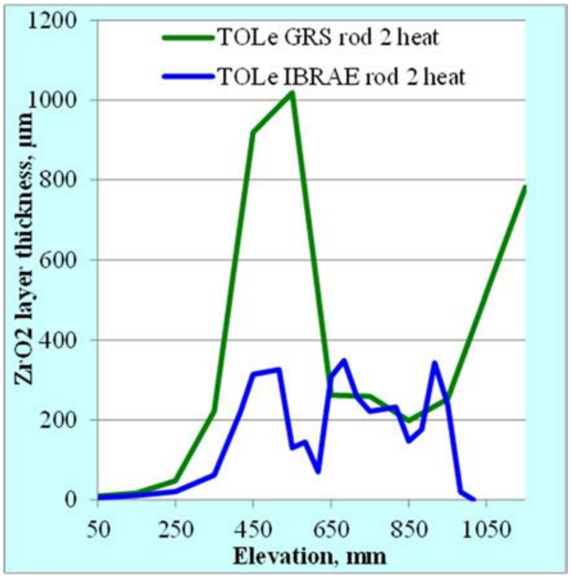

Unheated Control Rod Group 1 Heated Rod Group 2

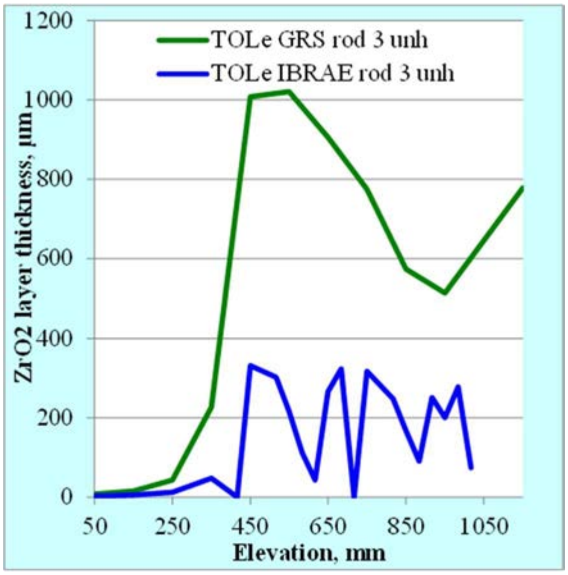

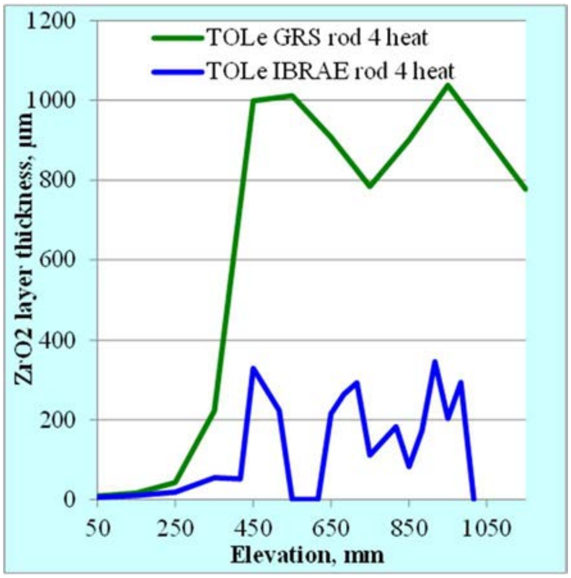

Unheated Rod Group 3 Heated Rod Group 4

FIG. 140. Results on calculated final axial distribution of oxide layer thickness at the end of the test.

Concerning the GRS data, it should be mentioned that for the central unheated rod 1 and inner heated rod group 2, the cladding metal between 650–950 mm was completely relocated to lower elevations during the time interval from 4190–4250 s. Thereafter, the thickness of residual metal at those elevations was calculated to be zero. Oxide layer at elevation 950 mm was 251 µm, afterwards it was kept constant. This was the reason why it was less than the corresponding thickness at elevation 1150 mm, where the oxidation continues with the cooling phase.

The IBRAE data showed axial variation of residual ZrO_2 thickness connected with the modelling of the start of the melt formation and its relocation through breaches of claddings. The degradation of ZrO_2 cladding were governed by set of different phenomena: ballooning and burst, dissolution of oxides by molten Zr, and loss of cladding integrity due to transformation into debris.

4.5.4. Post-test blockage of the CORA-15 bundle

The bundle blockage is defined as a reduction of the area of the original fluid channel by an increase in material area A_m:

$$B = 100\% \cdot (A_m - A_{m,initial})/A_c\ ,$$

where the area of the initial fluid channel $A_c = A_s - A_{m,initial} = A_s - 23A_{rod} - 2A_{abs}$ = 0.00673 – 0.00209 – 0.0003 = 0.00434 m² with area inside the shroud A_s = 0.00673 m². Please note that the cross-sectional areas for one of those 23 fuel rods $A_{rod} = 90.87$ mm² and one of 2 absorber rods $A_{abs} = 150$ mm².

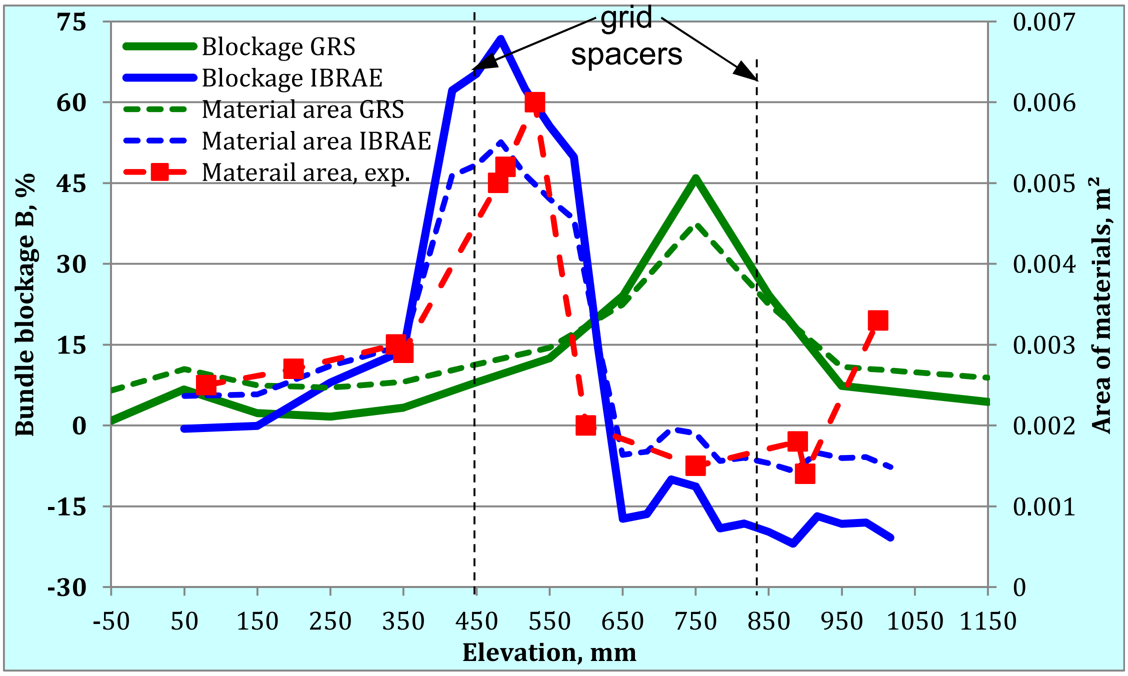

FIG. 141. Results on material distribution (A_m) and bundle blockage B at the end of the test.

As indicated in Fig. 141, IBRAE calculation predicted the relocation of molten materials from upper elevations to the middle grid spacer (about 500 mm). For GRS, the lack of modelling melt retention by spacer grids leads to an overestimation of the temperatures at elevations below the spacer grid at 450 mm. To artificially simulate this retention effect, a very low relocation velocity for the metallic (Zr) melt was used, which shifted the axial profile of the blockage to higher elevations.

4.5.5. Hydrogen release during the CORA-15 test

Comparison of the hydrogen flowrate and total mass calculated at the outlet of the test section, with data measured by two mass spectrometers located in the gas lines, were presented in Figs 142 and 143. Both codes predicted the total hydrogen mass at the end of the test sampling line, within the measurement uncertainties illustrated.

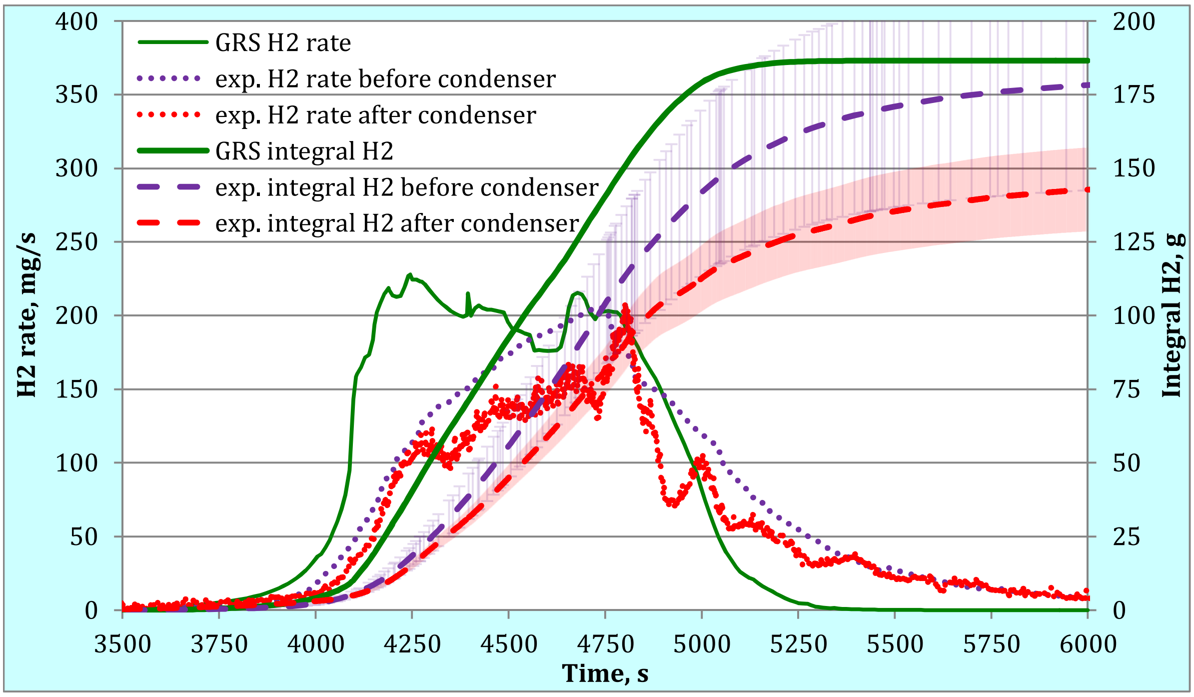

FIG. 142. Comparison of GRS calculation results with experimental data of two mass spectrometers.

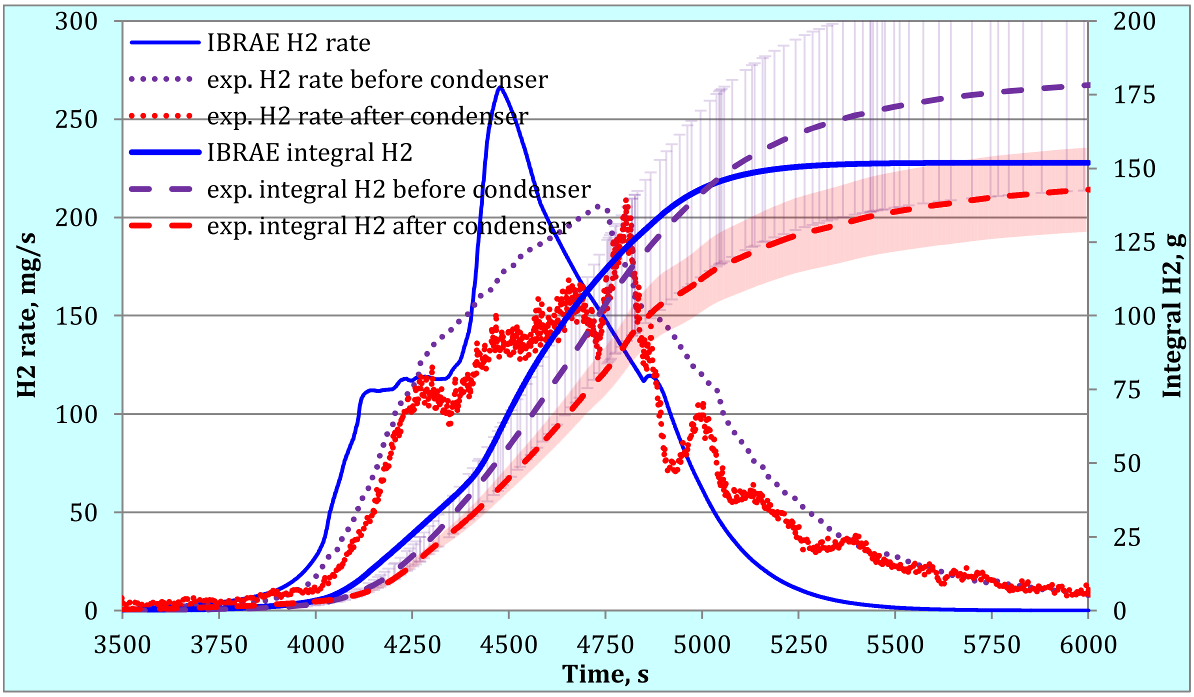

FIG. 143. Comparison of IBRAE calculation results with experimental data of two mass spectrometers.

A correction of hydrogen evolution should be performed, considering the peculiarities of the gas lines with the spectrometer (effects of transport delay, dilution, mixing and so on). For instance, as indicated in Fig. 144, the measured hydrogen curves after the condenser in the other test (CORA-W2) were corrected to reproduce the hydrogen curves at the outlet of the test section. This correction facilitated a direct comparison between the measured and calculated values.

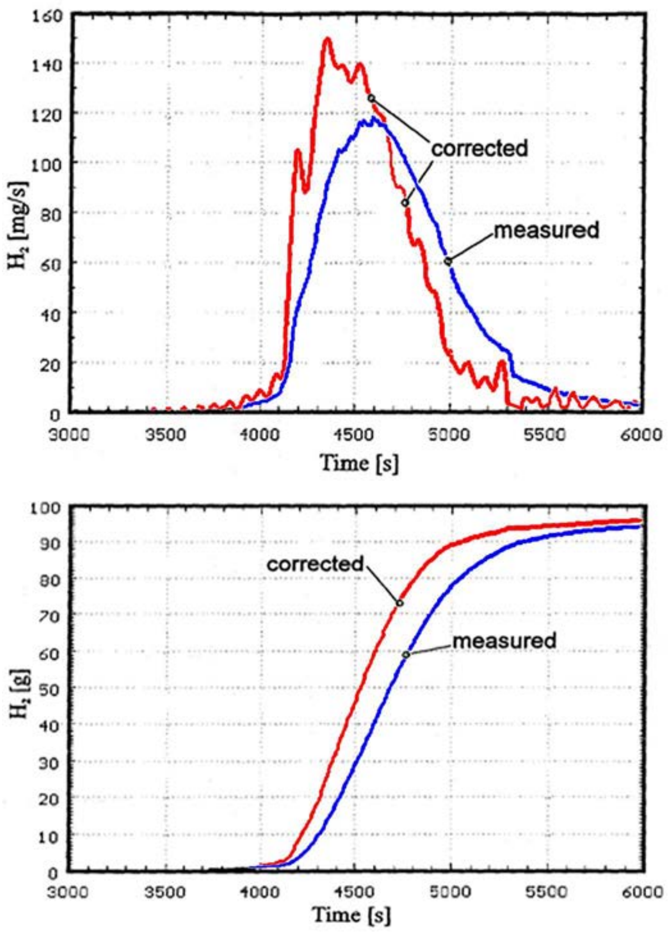

FIG. 144. Effect of measurement - hydrogen production measured by spectrometer and corrected to a test section outlet in CORA-W2 test [98].

5. UNCERTAINTY AND SENSITIVITY ANALYSIS FOR IFA-650.10

5.1. INTRODUCTION

As part of the FUMAC project, an uncertainty and sensitivity analysis (UASA) was performed on the modelling of the Halden LOCA test IFA-650.10 (PWR rod, without significant axial relocation) with different fuel rod codes.

The objective was to verify the key physical phenomena (such as clad and fuel temperatures, rod internal pressure, clad elongation, and clad outside diameter) which were well bound by the measured data. As an optional activity for some participants, sensitivity analysis for these phenomena was also completed through global sensitivity analysis (GSA).

This chapter describes the fuel codes and the statistical uncertainty and sensitivity analysis tools; the specifications for the uncertainty and sensitivity analysis tools; and the comparison and discussion of the uncertainty and sensitivity analysis results provided by the participants.

5.2. PARTICIPANTS AND USED CODES

As shown in Table 12, seven participants performed the uncertainty analysis, and six participants performed the sensitivity analysis.

TABLE 12. PARTICIPANTS OF UNCERTAINTY AND SENSITIVITY ANALYSIS

Participant	Code	UA/SA Tool	UA	SA
CNEA	DIONISIO-2.0	DAKOTA	Y	Y
CEA	ALCYONE-1D	URANIE	Y	Y
CIAE	FTPAC	DAKOTA	Y	Y
CIEMAT	FRAPTRAN-1.5	DAKOTA	Y	Y
IPEN	FRAPTRAN	Excel	Y	Y
Tractebel	FRAPTRAN-TE-1.5	DAKOTA	Y	Y
JRC	TRANSURANUS	Built-in (M-C)	Y	

Five different fuel rod codes (DIONISIO, ALCYONE, FTPAC, FRAPTRAN, TRANSURANUS) and four different statistical uncertainty and sensitivity analysis tools (DAKOTA, URANIE, Excel, and built-in Monte Carlo function) were used. The analyses were performed according to the specifications (see Annex I).

Results submitted by the participants were analyzed and compared with the available experimental data in this chapter. A detailed discussion of the results from each participant could be found in their respective reports, as compiled in the Annex II.

5.3. SPECIFICATIONS

5.3.1. Methodology

The following uncertainty analysis approach was adopted amd a common list of input uncertainty parameters was defined, covering:

- Fuel manufacturing data;
- Operating and test conditions;
- Material properties and models;
- The uncertainties on the output parameters of interest were quantified using the input uncertainty propagation method through Monte-Carlo simulations [99].

The non-parametric order statistics [100] was a well established and shared methodology in the nuclear community [101–102], and hence the methodology was recommended for this activity. Methodologies for sampling and for the uncertainty and sensitivity analysis [99–109] are described in Section 2 of Annex I.

If a participant does not have his own tool, a statistical UASA analysis tool (DAKOTA [110]) may be used, which may be obtained freely from ANL.

The participant, however, has the freedom to use other alternative method or tool to perform the UASA, or to perform only the uncertainty analysis.

A common list of output parameters was defined for this CRP, the results were provided for comparison.

5.3.2. Definition of input uncertainty parameters

The input uncertainty parameters to be considered are defined in Table 13 for Halden LOCA test IFA-650.10 [111]. For simplicity, a normal distribution was assumed for all input uncertainty parameters. Note also that the uncertainty on the model input parameters is defined as a multiplier (the mean value of 1.00 is thus the calculated best estimate value), the uncertainty on the measured or calculated temperature (cladding, coolant or plenum) is defined as an adder (the mean value of T is thus the measured or calculated best estimate value).

TABLE 13. LIST OF INPUT UNCERTAINTY PARAMETERS FOR IFA-650.10

Input Uncertainty Parameters	Distribution				
	Mean	Standard Deviation	Type	Lower bound	Upper bound
Cladding outside diameter (mm)	9.50	0.01	Normal	9.48	9.52
Cladding inside diameter (mm)	8.36	0.01	Normal	8.34	8.38
Pellet outside diameter	8.2	0.01	Normal	8.18	8.22
Fuel theoretical density (kg/m3 at 20°C)	10457	50	Normal	10357	10557
U^{235} enrichment (%)	4.487	0.05	Normal	4.387	4.587
Filling gas pressure (MPa)	4.0	0.05	Normal	3.9	4.1
Relative power during base irradiation	1	0.01	Normal	0.98	1.02
Relative power during test	1	0.025	Normal	0.95	1.05
Test rod power profile	1	0.01	Normal	0.98	1.02
Cladding temperature (°C)	T (Measured)	10	-	T-20	T+20
Coolant temperature (°C)	T (Calculated)	5	-	T-10	T+10
Clad-to-coolant heat transfer coefficient multiplier (same Coef. applied for all flow regimes)	1.00 (Calculated)	0.125	Normal	0.75	1.25
Fuel thermal conductivity model multiplier	1.00	5%	Normal	0.90	1.10
Clad thermal conductivity model multiplier	1.00	5%	Normal	0.90	1.10
Fuel thermal expansion model multiplier	1.00	5%	Normal	0.90	1.10
Clad thermal expansion model multiplier	1.00	5%	Normal	0.90	1.10
Fuel densification model multiplier	1.00	5%	Normal	0.90	1.10
Fuel solid swelling model multiplier	1.00	5%	Normal	0.90	1.10

Input Uncertainty Parameters	Distribution				
	Mean	Standard Deviation	Type	Lower bound	Upper bound
Fuel gaseous swelling model multiplier	1.00	5%	Normal	0.90	1.10
Clad Yield stress multiplier	1.00	5%	Normal	0.90	1.10
Fuel heat capacity multiplier	1.00	1.5%	Normal	0.97	1.03
Cladding heat capacity multiplier	1.00	1.5%	Normal	0.97	1.03
Cladding elastic modulus multiplier	1.00	5%	Normal	0.90	1.10
Cladding corrosion model multiplier during steady-state operation	1.00	12.5%	Normal	0.75	1.25
Cladding hydrogen pickup fraction multiplier during steady-state operation	1.00	15%	Normal	0.7	1.30
Cladding oxidation model multiplier at high temperature	1.00	15%	Normal	0.7	1.30
Thermal conductivity multiplier of the oxide layer	1.00	10%	Normal	0.80	1.20
Fission gas release (or gas diffusion coefficient) multiplier	1.00	25%	Normal	0.50	1.50
Gap gas conductivity multiplier	1.00	12.5%	Normal	0.75	1.25
Fuel/cladding emissivity multiplier	1.00	5%	Normal	0.90	1.10
Fuel radial relocation multiplier	1.00	10%	Normal	0.80	1.20
Fuel fragment packing fraction multiplier (if applicable)	1.00	10%	Normal	0.80	1.20
Cladding strain threshold multiplier for fuel mobility (if applicable)	1.00	10%	Normal	0.80	1.20
Cladding Meyer hardness multiplier	1.00	5%	Normal	0.90	1.10
Cladding annealing multiplier	1.00	5%	Normal	0.90	1.10
Cladding burst criteria multiplier	1.00	10%	Normal	0.80	1.20
Cladding burst strain criteria multiplier	1.00	10%	Normal	0.80	1.20
Plenum gas temperature (°C)	T (measured or calculated)	5	-	T-10	T+10

5.3.3. Modelling assumptions

Due to complexity to simulate the thermal hydraulic behaviours and the differences that may appear from various assumptions and/or models, it was recommended to use the thermal hydraulic boundary conditions calculated from SOCRAT [112], namely:

- Coolant temperatures;
- Clad to coolant heat transfer coefficients (HTCs).

The clad to coolant heat transfer coefficients should be determined from the total heat flux (radiative and convective), namely HTC = Q_{tot} / (T_{clad} –T_{cool}), for each axial node. This will allow the fuel rod code to calculate the cladding temperatures T_{clad}.

Alternatively, the measured or calculated cladding temperatures could be imposed directly as the boundary conditions.

The rodlet plenum temperature (T_{plenum}) should be taken from the measurement, or from any appropriate empirical plenum gas temperature model.

A steady state of 100 s should be simulated before the beginning of blowdown. The transient calculation should stop at 600 s (after the scram at 517 s).

The recommended maximum time step is 0.1 s during the steady-state and 0.001 s during the transient and 0.0002 s during the burst period, but short time steps can be used for stability of calculations.

5.3.4. Output parameters

For the uncertainty analysis, each participant is requested to provide lower and upper bounds (LB, UB) associated with all the time trend of output parameters listed in Table 14 (the recommended frequency is 10 s). In addition, the results of the calculation with the nominal value of the input parameters, also called reference calculation (REF) should be provided.

For the sensitivity analysis, the partial rank correlation coefficients (PRCC, or Spearman's RCC if PRCC is not available) of the above output parameter vs. each of the input uncertainty, at the times defined in Table 15, and the maximal value for each correspondence parameter should be provided.

TABLE 14. LIST OF OUTPUT PARAMETERS TO BE PROVIDED

Parameter	Unit	Description
Fuel rod internal pressure (RIP)	MPa	Fuel rod internal pressure
Fuel centreline temperature (TFC)	°C	Temperature of fuel centreline at peak power/burst node
Fuel surface temperature (TFO)	°C	Fuel surface temperature at peak power/burst node
Cladding inside surface temperature (TCI)	°C	Cladding inside surface temperature at peak power/burst node
Cladding outside surface temperature (TCO)	°C	Cladding outside surface temperature at peak power/burst node
Cladding outside surface oxide layer thickness (TOL)	mm	Cladding outside surface oxide layer thickness at peak power/burst node
Equivalent cladding reacted (ECR)	%	Equivalent cladding reacted at peak power/burst node
Cladding outside diameter (DCO)	mm	Cladding outside diameter at peak power/burst node
Cladding effective stress (CES)	MPa	Cladding effective stress at peak power/burst node
Cladding elongation (ECT)	mm	Clad total axial elongation
Fuel elongation (EFT)	mm	Fuel column total axial elongation (expansion)

TABLE 15. LIST OF DIFFERENT TIMES FOR SENSITIVITY ANALYSIS OUTPUT

Time/ parameters	t1	t2	t3	t4	t5
Definition	End of natural circulation	Beginning of blowdown	End of cooldown	Burst	End of calculation
Value	100.0 s	110 s	170 s	350 s	600 s

5.4. COMPARISON OF UNCERTAINTY ANALYSIS RESULTS

The calculation results of the 200 successful runs were collected. The 5th and 196th ranks were chosen to estimate the upper/lower (95%/5%) uncertainty bounds (LB, UB) of the output parameter of interest, according to the order statistics (except that JRC used directly Monte Carlo method to obtain the upper/lower (95%/5%) uncertainty bounds (LB, UB)). The results of the reference case (REF) were also provided.

The uncertainty of the following main output parameters were compared and discussed in this report:

- Rod internal pressure (RIP);
- Cladding outer surface temperature (TCO) at burst node;
- Fuel outer surface temperature (TFO) at burst node;
- Cladding total elongation (ECT);
- Cladding outside diameter (DCO) at burst node.

Comparison of the experimental data within the reference and upper bound values, for each of the main output parameters, allowed an assessment of the adequacy of the model and the conservatism of the upper bound value.

Comparison of the uncertainty bands, obtained by different participants for each of the main output parameters with measurements, allowed to quantify the *accuracy* of the model.

Comparison of the position of the reference case within the uncertainty bands, by different participants for each of the main out parameters, allowed detection of *bias* (if any) in the model.

Finally, comparison of the differences between the maximum UB values and minimum LB values (the global uncertainty width) and the maximum REF values and minimum REF values (the global reference dispersion) allowed identification of the proportion of the model difference in the global uncertainty width, as well as the position of the experimental data.

5.4.1. Rod internal pressure (RIP)

The calculated reference rod internal pressure is indicated in Fig. 145. Reasonably agreements with the experimental data were obtained. With the exception for Tractebel and JRC, all participants predicted an early burst. CEA's results after the burst were discarded since they are not physical. The results between CIEMAT, IPEN and Tractebel were different, although the same FRAPTRAN code, with different versions, options, and assumptions (clad and plenum gas temperatures) were used.

The calculated upper bound for rod internal pressure is indicated in Fig. 146, which does not bound the experimental data, except for Tractebel (trend and burst time) and JRC (burst time). This was not surprising as only Tractebel and JRC predicted well for the burst time (see Fig. 145).

The calculated uncertainty band for rod internal pressure is indicated in Fig. 147. The uncertainty bounds were between 0.25–0.45 MPa (about 4%) close to the burst time, except for those lower values predicted by JRC and IPEN.

Fig. 148 indicated the position of the reference within the uncertainty band for rod internal pressure. The reference values were closer to the lower bound before the burst (R = (REF – LB)/(UB – LB) < 0.5), and closer to the upper bound at the burst (R > 0.5).

Interesting observation could be made from Fig. 149. The experimental data were bounded by both the minimum and maximum reference values (reference dispersion) and the minimum and maximum uncertainty values (uncertainty width). This indicated that there was no bias in the rod internal pressure model, whose uncertainty band could be quantified by the statistical approach.

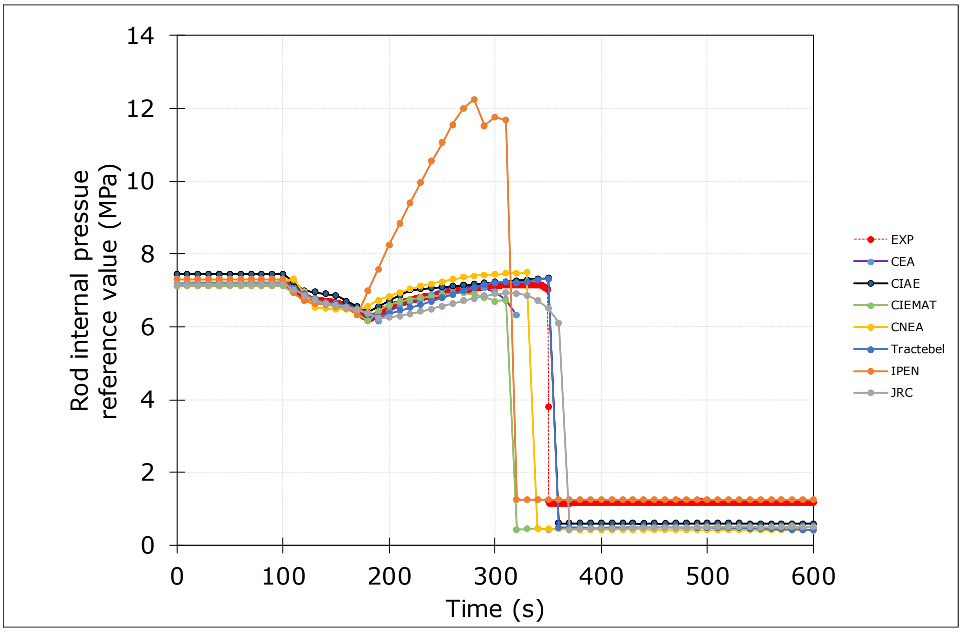

FIG. 145. IFA-650.10: Reference values for the rod internal pressure.

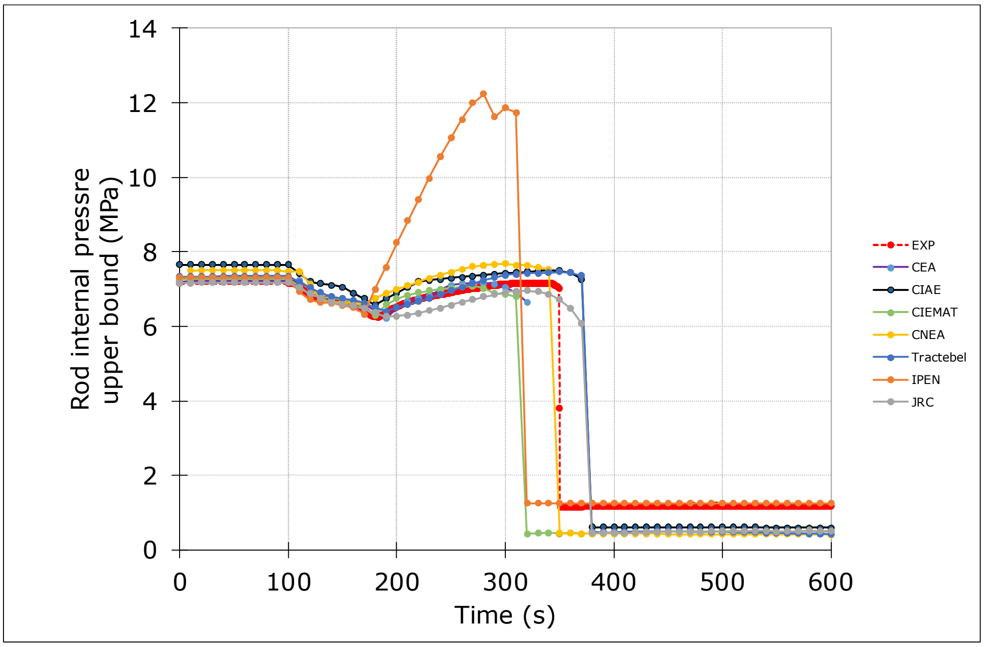

FIG. 146. IFA-650.10: Upper bounds for the rod internal pressure.

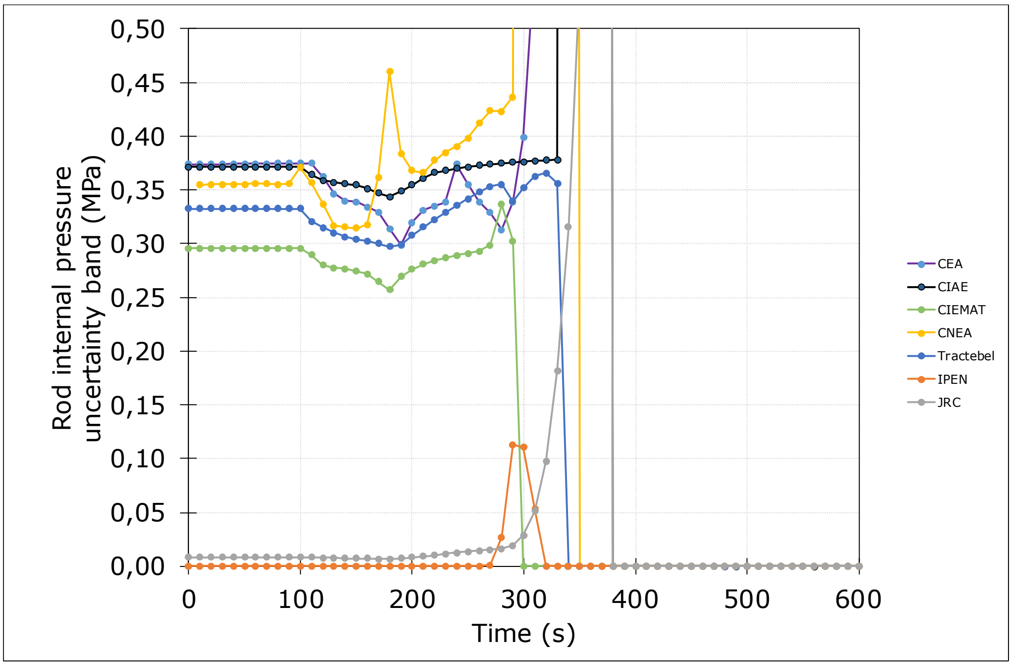

FIG. 147. IFA-650.10: Uncertainty bands for the rod internal pressure.

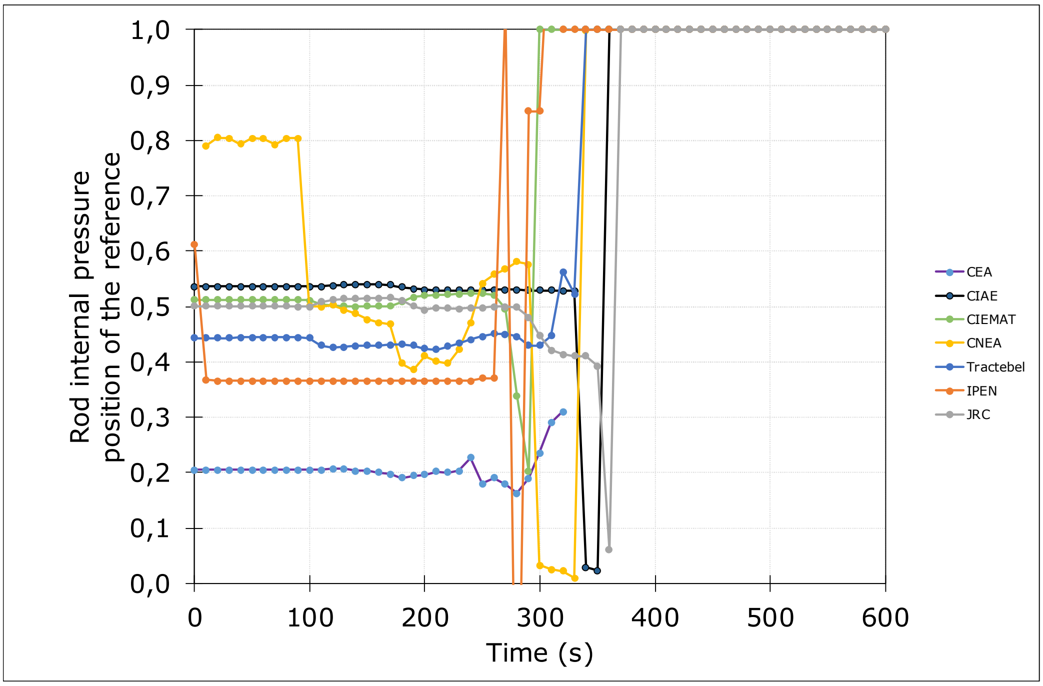

FIG. 148. IFA-650.10: Position of the reference values within the uncertainty band for the rod internal pressure.

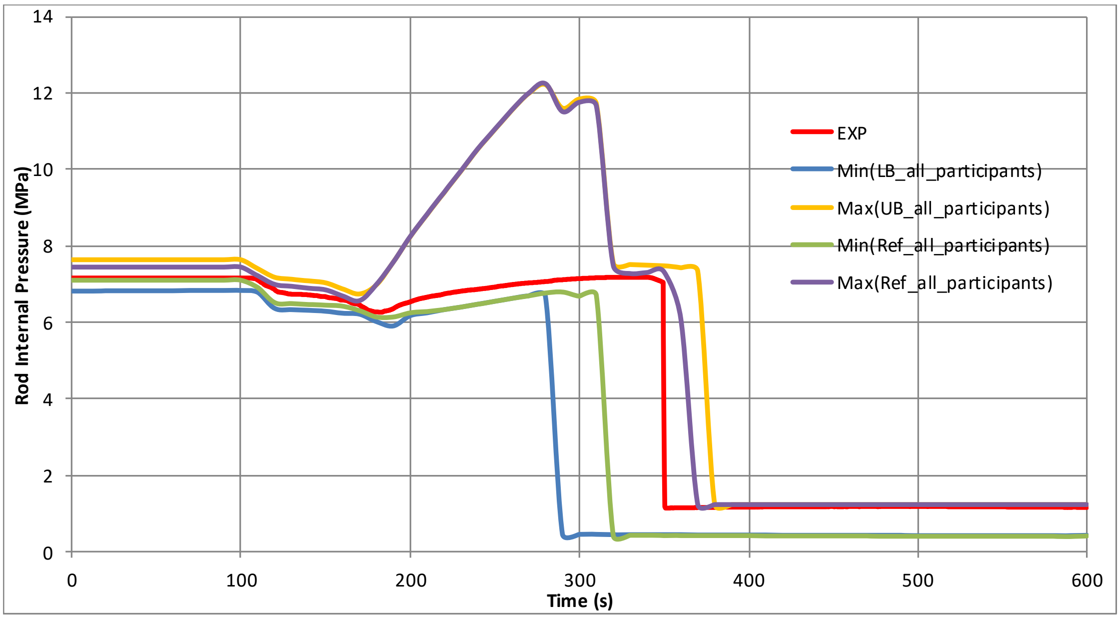

FIG. 149. IFA-650.10: The global reference dispersion and uncertainty width of all participants for the rod internal pressure.

5.4.2. Clad outer surface temperature (TCO)

The calculated reference clad outer surface temperature is indicated in Fig. 150, which is slightly higher than the experimental data. Instead of using the SOCRAT calculated coolant temperature, heat transfer coefficient and the associated uncertainties, as requested in the Specifications, IPEN used the measured clad temperature directly.

The location of the calculated cladding surface temperature at burst node was not precisely the one that was measured, hence the results could be slightly different and more refined nodalization and measurements were recommended. Results obtained from CIEMAT, IPEN and Tractebel were different, although the same FRAPTRAN code, but with different versions, options and assumptions, was used.

The calculated upper bound clad outer surface temperature is indicated in Fig. 151, which does bound the experimental data. Note again that IPEN used the measured clad temperature directly, instead of using the SOCRAT calculated coolant temperature and heat transfer coefficient and the associated uncertainties as requested in the Specifications.

The calculated uncertainty band for clad outer surface temperature is indicated in Fig. 152. The uncertainty bounds were between 0–80°C, which was about 10% of the reference value. In general, the uncertainty bands were higher after burst.

The position of the reference within the uncertainty band for clad outer surface temperature is indicated in Fig. 153. The reference values were closer to the middle of the uncertainty band (R = (REF – LB)/(UB – LB) = 0.5), except for CIEMAT (which was closer to upper band after burst) and IPEN (from which the uncertainty band was not considered).

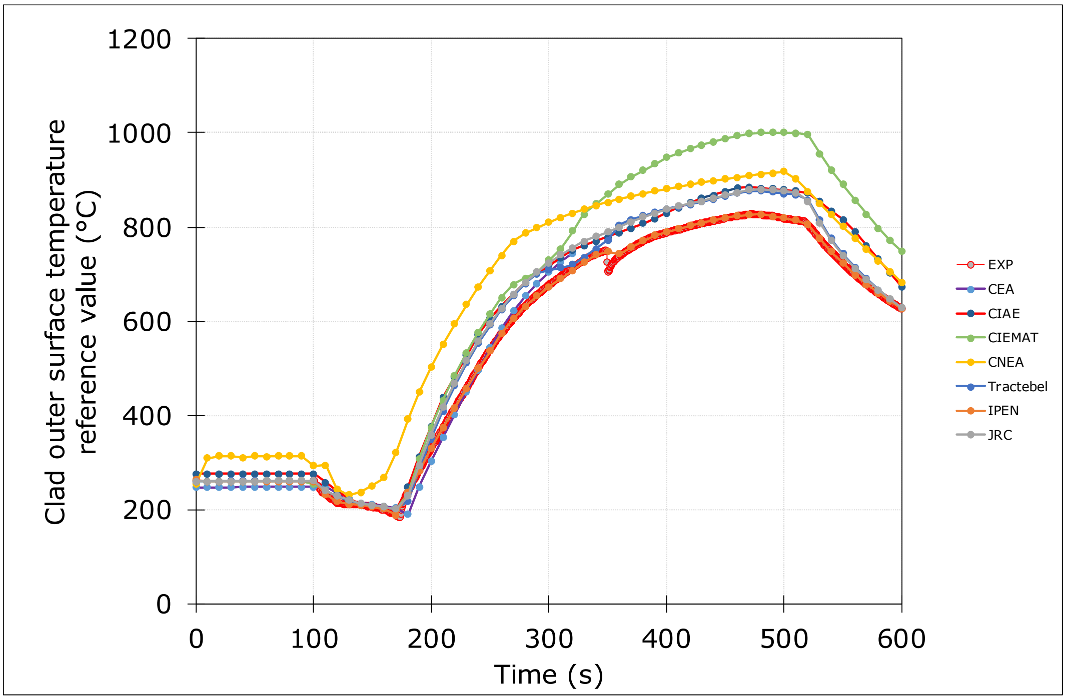

FIG. 150. IFA-650.10: Reference values for clad outer surface temperature.

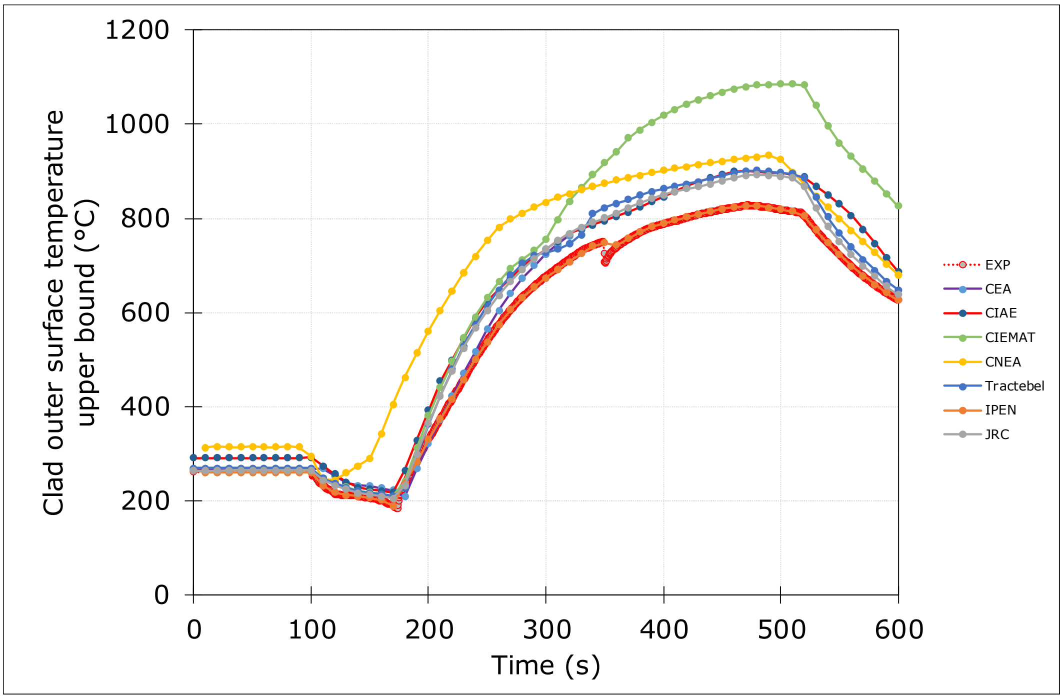

FIG. 151. IFA-650.10: Upper bounds for clad outer surface temperature.

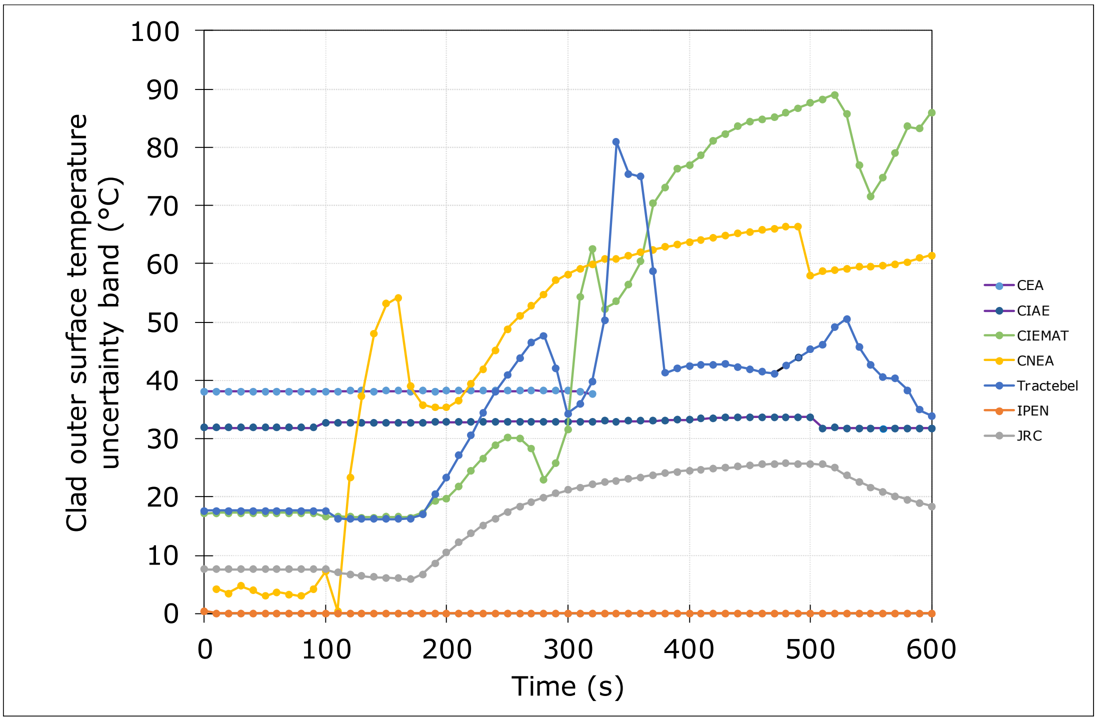

FIG. 152. IFA-650.10: Uncertainty bands for clad outer surface temperature.

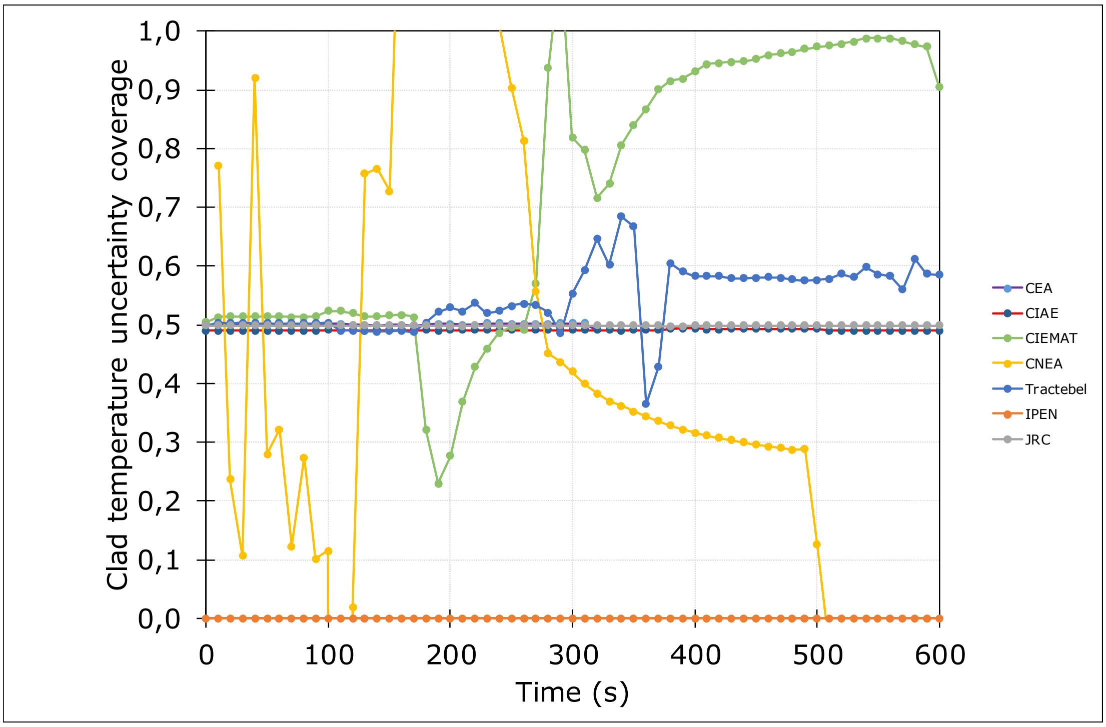

FIG. 153. IFA-650.10: Position of the reference within the uncertainty band for clad outer surface temperature.

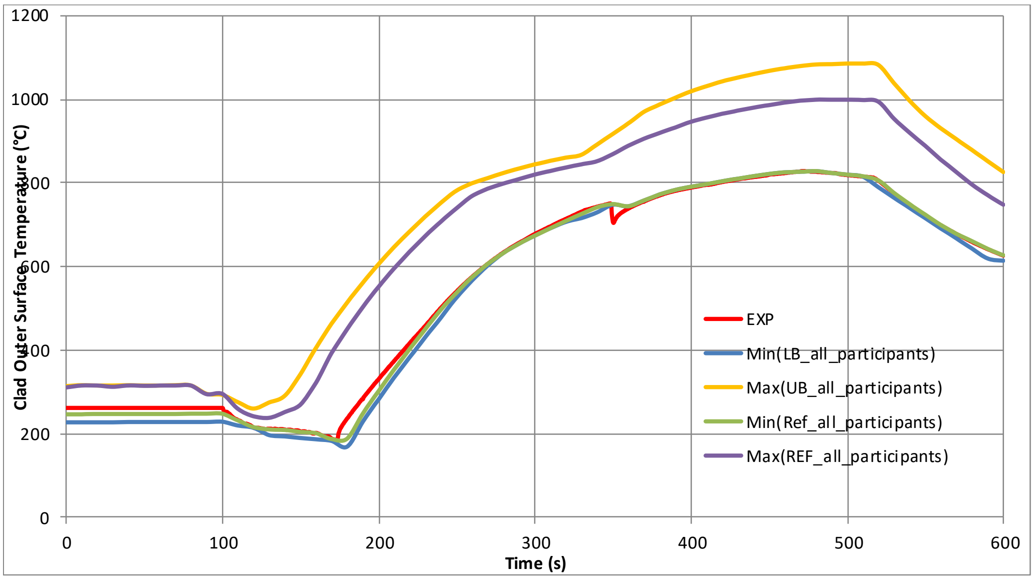

FIG. 154. IFA-650.10: The global reference dispersion and uncertainty width of all participants for clad outer surface temperature.

The experimental data are bounded by both the maximum reference and the UB values, as indicated in Fig. 154. Both the minimum reference and LB values were close to the experimental data, this indicated that a significant bias in the thermal hydraulic boundary conditions could exist.

5.4.3. Fuel outer surface temperature (TFO)

The calculated reference fuel outer surface temperature is indicated in Fig. 155. No experimental data was available for comparison. However, all but the CNEA results were consistent with the clad outer surface temperature (Fig. 150). As noted previously, the difference of results was obtained between CIEMAT, IPEN and Tractebel, using the same FRAPTRAN code but with different versions, options and assumptions.

The calculated upper bound, uncertainty band, and the position of the reference values for fuel outer surface temperature are indicated from Figs 156 to 158. The uncertainty band (Fig. 157) was greater than that for the clad outer surface temperature (Fig. 152), due to the involvement of modelling uncertainties (such as clad/fuel thermal conductivity, gap conductance, etc.). The reference values were closer to the middle of the uncertainty band (R = (R = (REF – LB)/(UB – LB) = 0.5), except for CIEMAT (which is closer to upper band after burst) and IPEN (which uncertainty band was not considered).

The reference dispersion and uncertainty width presented by all participants were quite close, as indicated in Fig. 159. The difference between the reference values was dominant in the uncertainty width.

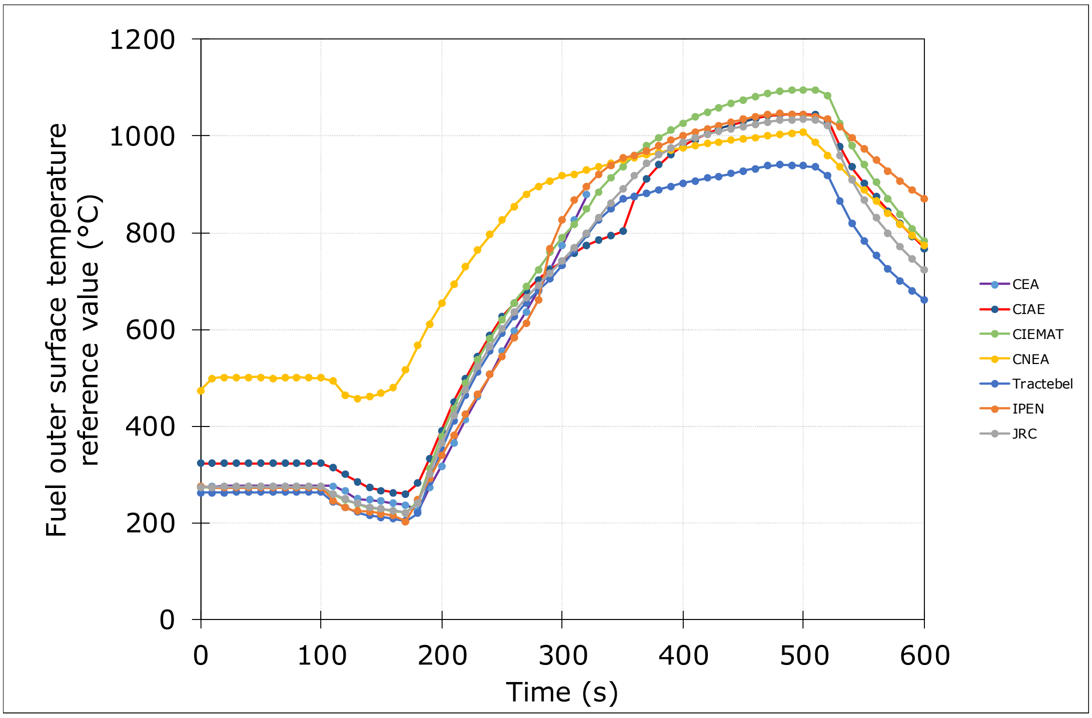

FIG. 155. IFA-650.10: Reference values for fuel outer surface temperature.

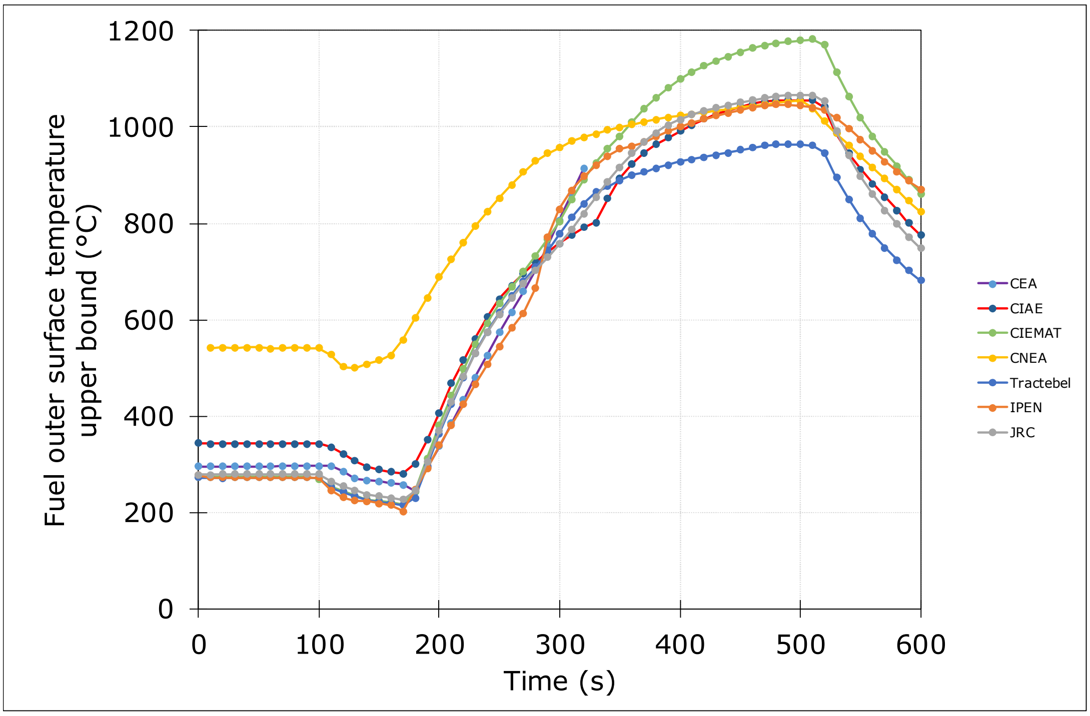

FIG. 156. IFA-650.10: Upper bound for fuel outer surface temperature.

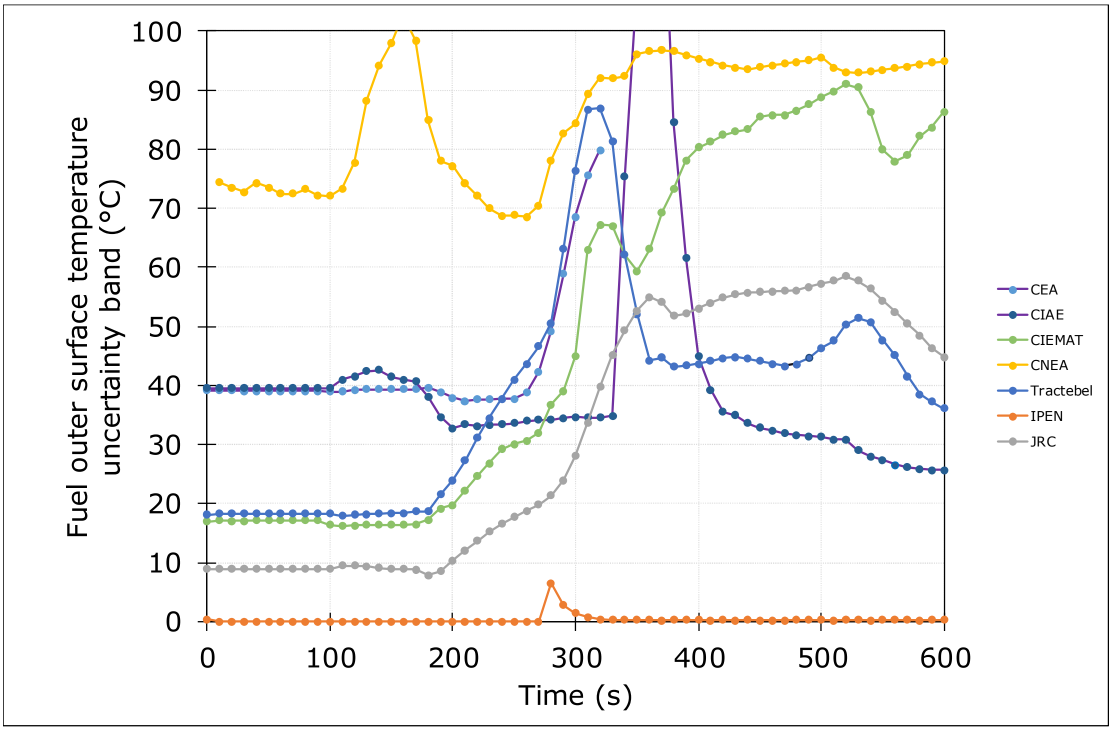

FIG. 157. IFA-650.10: Uncertainty bands for fuel outer surface temperature.

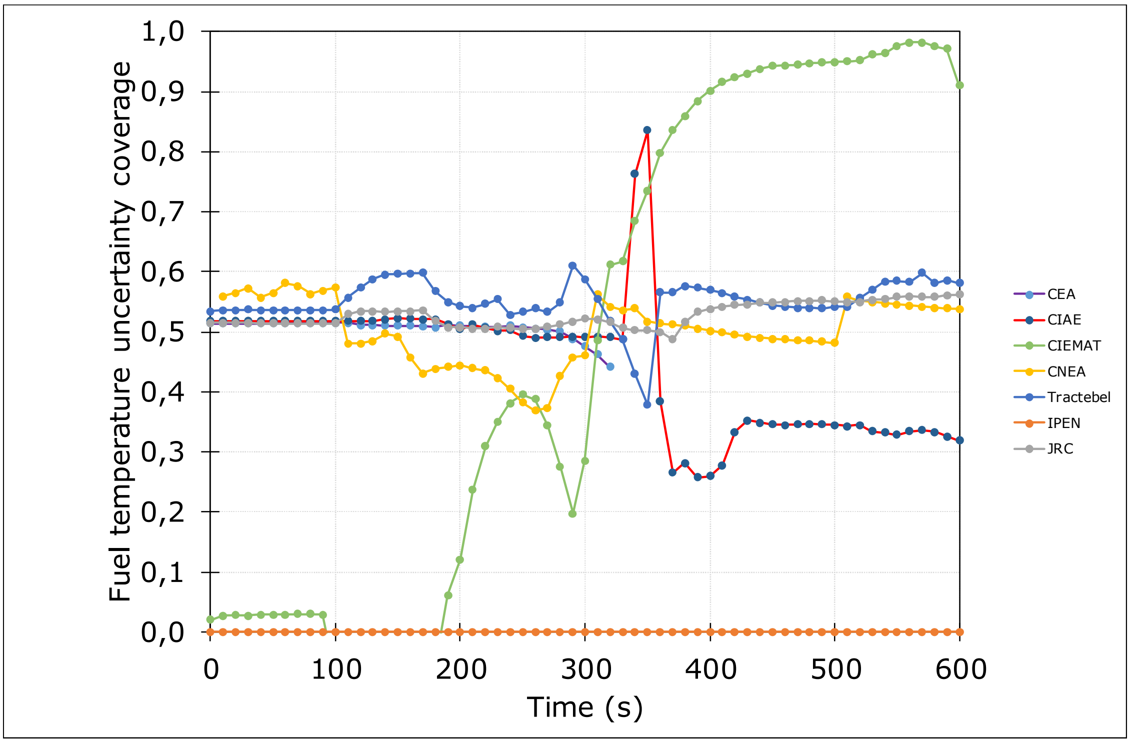

FIG. 158. IFA-650.10: The position of the reference within the uncertainty band for fuel outer surface temperature.

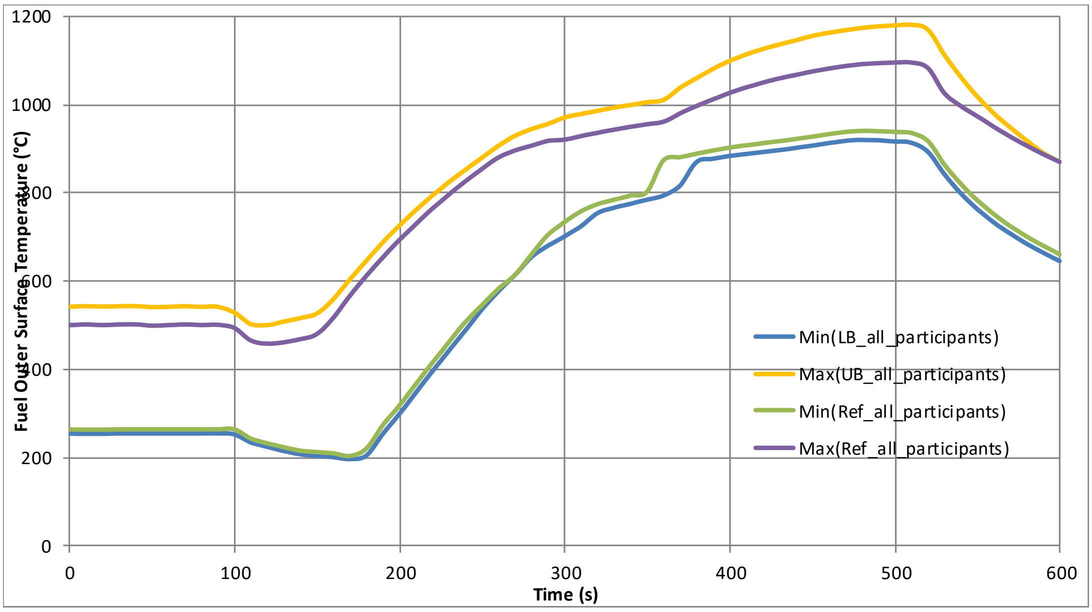

FIG. 159. IFA-650.10: The global reference dispersion and uncertainty width of all participants for fuel outer surface temperature.

5.4.4. Clad elongation (ECT)

The calculated reference clad elongation in comparison with the experimental data is indicated in Fig. 160. Despite the different in initial states, the heatup period before burst were generally well predicted by all participants. However, FRAPTRAN predicted a reduction after burst. The difference between CIEMAT, Tractebel and IPEN was noted again, when difference versions of the FRAPTRAN code were used.

The calculated upper bound clad elongation is indicated in Fig. 161, which does bound the experimental data except for the much lower results after burst predicted by the FRAPTRAN (CIEMAT, IPEN and Tractebel). The large initial uncertainty could be due to the different in starting points between the calculations and the experiment. A correction could probably be applied but it would depend on several input uncertainty parameters.

The calculated uncertainty band for clad elongation is indicated in Fig. 162. The uncertainty bounds were generally small, except for the large bands after burst with FRAPTRAN. With FRAPTRAN code, with BALON2 model being activated, FRACAS-1 was not able to correctly predict the behaviour of the cladding elongation after the burst. FEA model should be able to do a better job but was not used in this case. The uncertainty band followed the same trend as the reference case. This implied that the mechanical deformation model was not sufficiently good and should be improved. Those improvements could be made directly to the code (such as calibration, input data, meshing etc.) or the modification of the models (such as improved ballooning model or use of FEA).

The position of the reference was within the uncertainty band for clad elongation as shown in Fig. 163. The reference values were closer to the middle of the uncertainty band (R = (REF – LB)/(UB – LB) = 0.5).

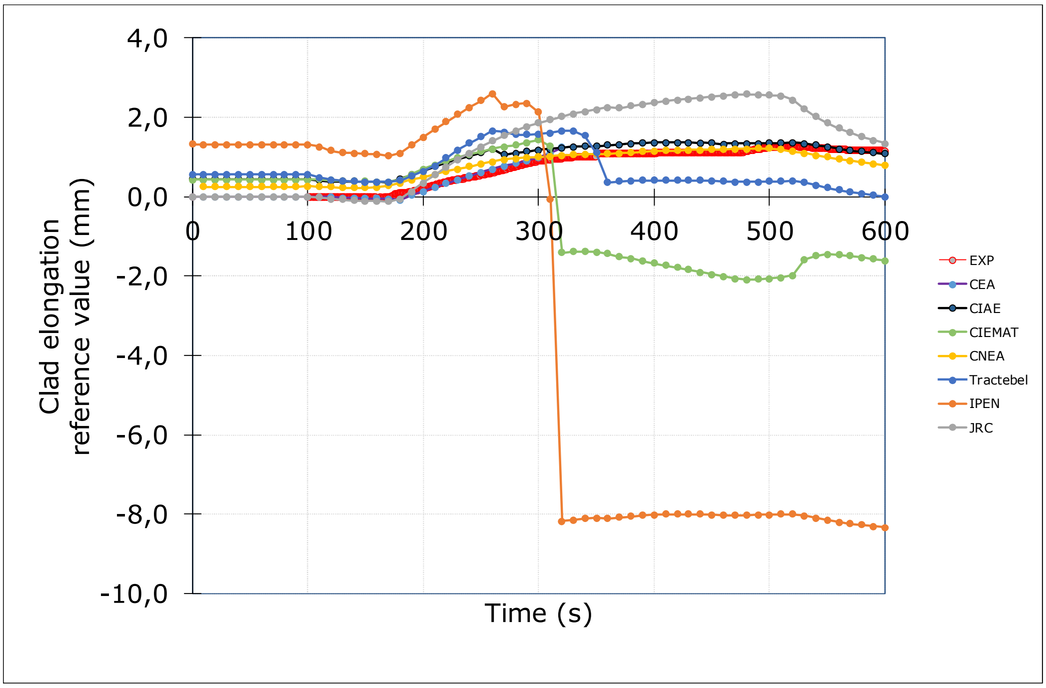

FIG. 160. IFA-650.10: Reference values for clad elongation.

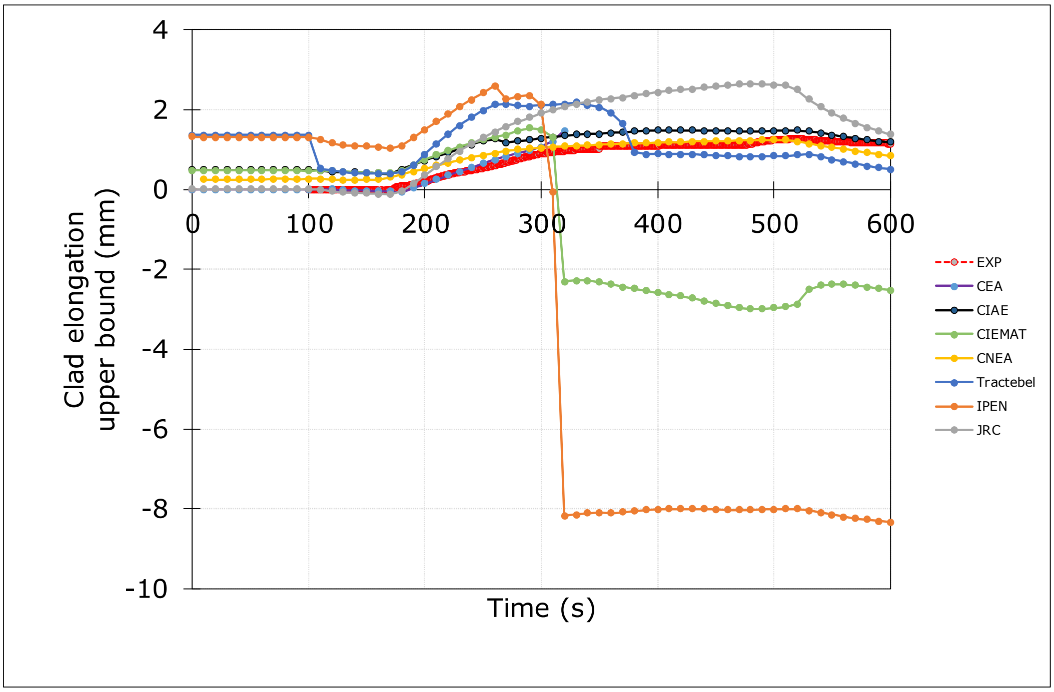

FIG. 161. IFA-650.10: Upper bounds for clad elongation.

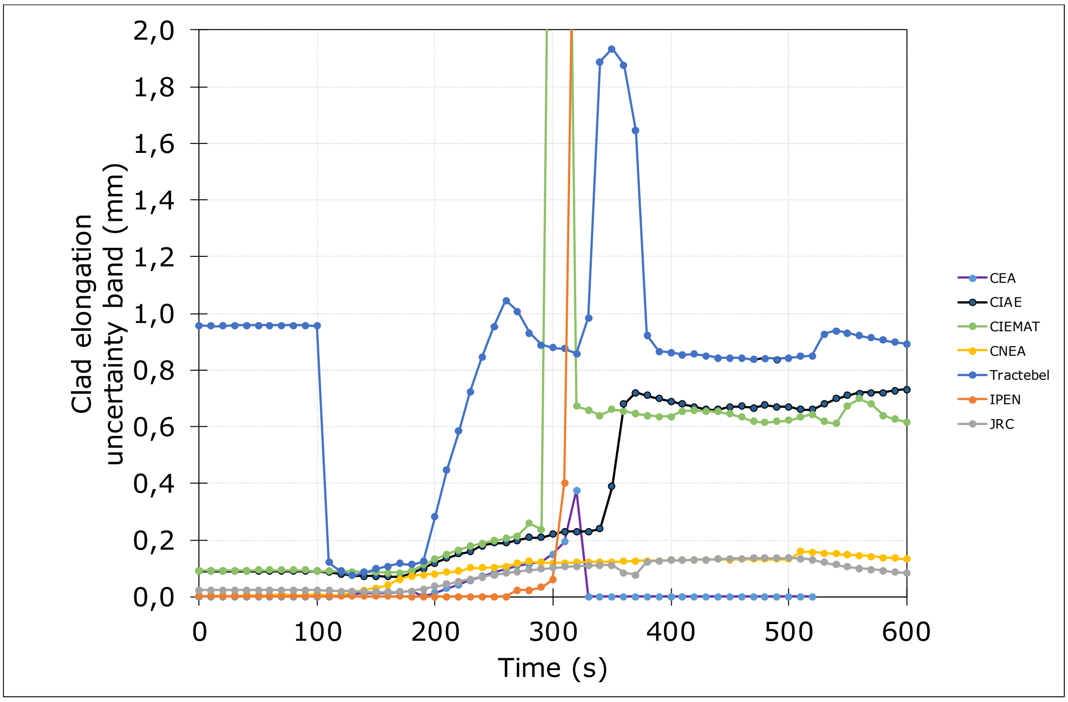

FIG. 162. IFA-650.10: Uncertainty bands for clad elongation.

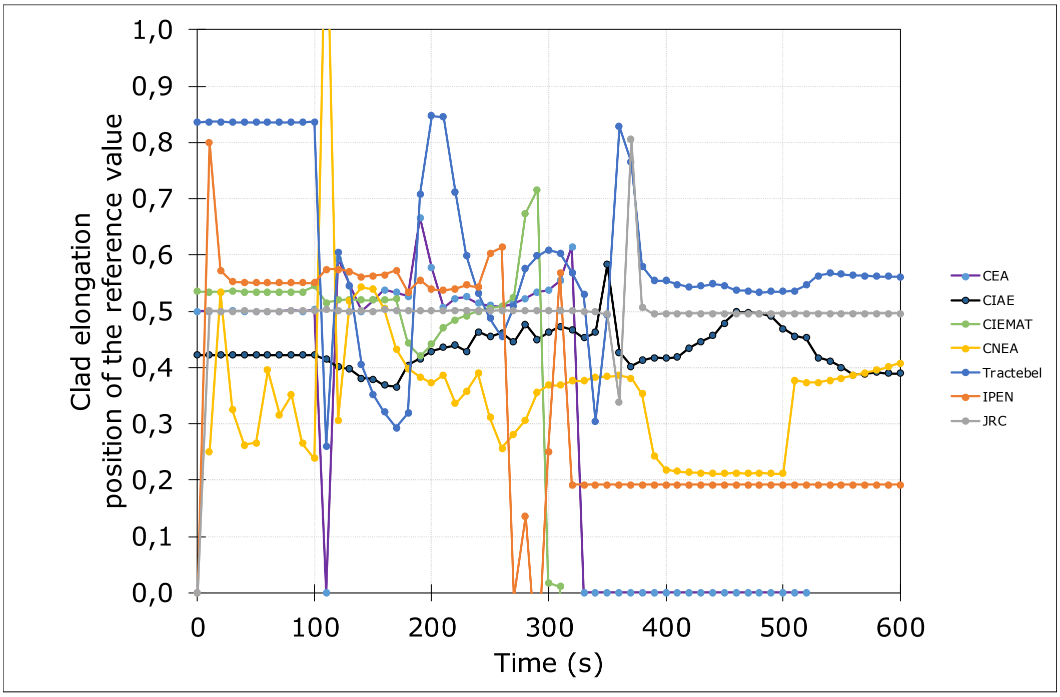

FIG. 163. Position of the reference within the uncertainty band for clad elongation.

Fig. 164 indicated the reference dispersion and uncertainty width for all participants were quite large. The difference between the reference values dominated the global uncertainty width.

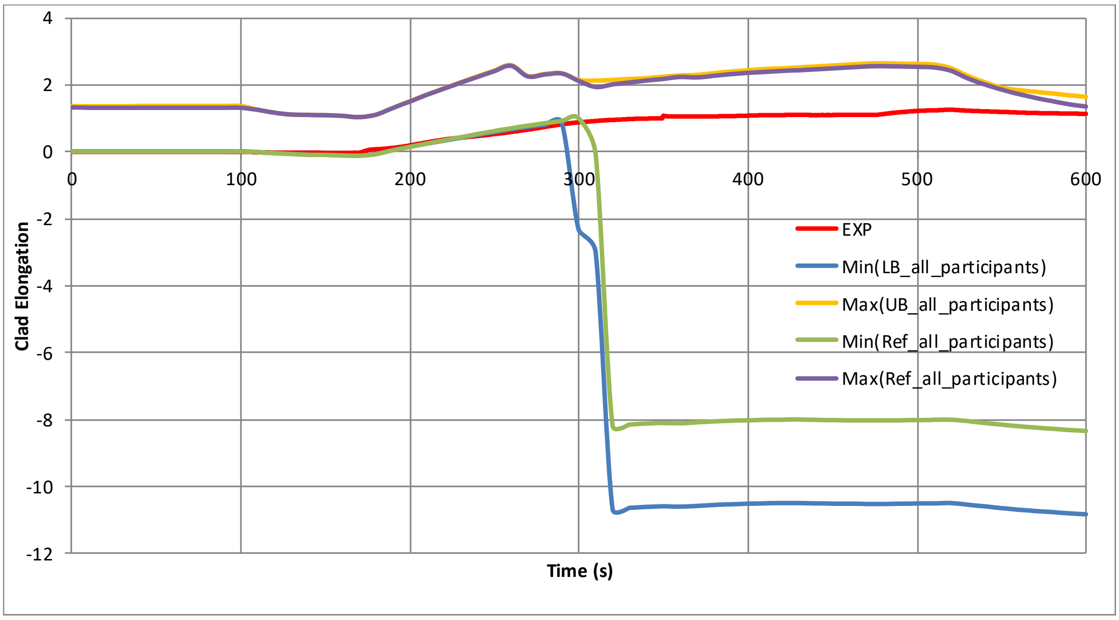

FIG. 164. IFA-650.10: Global reference dispersion and uncertainty width of all participants for clad elongation.

5.4.5. Clad outside diameter (COD) at burst node

Except for IPEN, the calculated reference clad outside diameter is indicated in Fig. 165. CEA and CNEA results after burst were discarded. However, the difference between CIEMAT (highest in COD) and Tractebel (lowest in COD), both using the FRAPTRAN code but with different versions and options, was noted again.

The calculated upper bound clad outside diameter is indicated in Fig. 166. Participant results bounded the experimental data, except for the Tactebel results that could be improved by using the FEA model.

The calculated uncertainty band for clad outside diameter is indicated in Fig. 167. The uncertainty bounds were between 0–3.5 mm (up to 40%).

The position of the reference within the uncertainty band for clad outside diameter is indicated in Fig. 168. The reference values are closer to the middle of the uncertainty band (R = (REF – LB)/(UB – LB) = 0.5) before the burst.

It is interesting to note that the reference dispersion and uncertainty width of all participants were quite large, as indicated in Fig. 169. The differences between the reference values of all participants dominated the global uncertainty width. The minimum LB and REF values were quite close, indicating that the model contained a significant bias and was not adequate for uncertainty analysis. This was due to the use of FRACAS-1 model in the FRAPTRAN code used by Tractebel, which could be improved by using the FEA model.

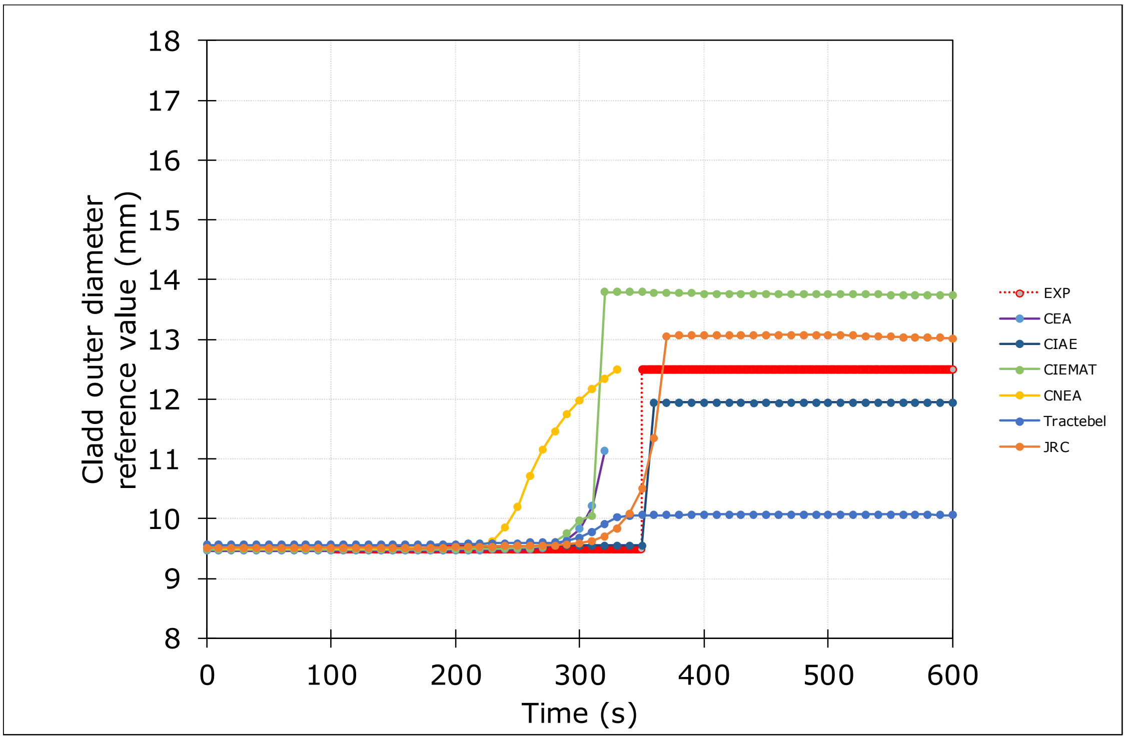

FIG. 165. IFA-650.10: Reference values for clad outside diameter.

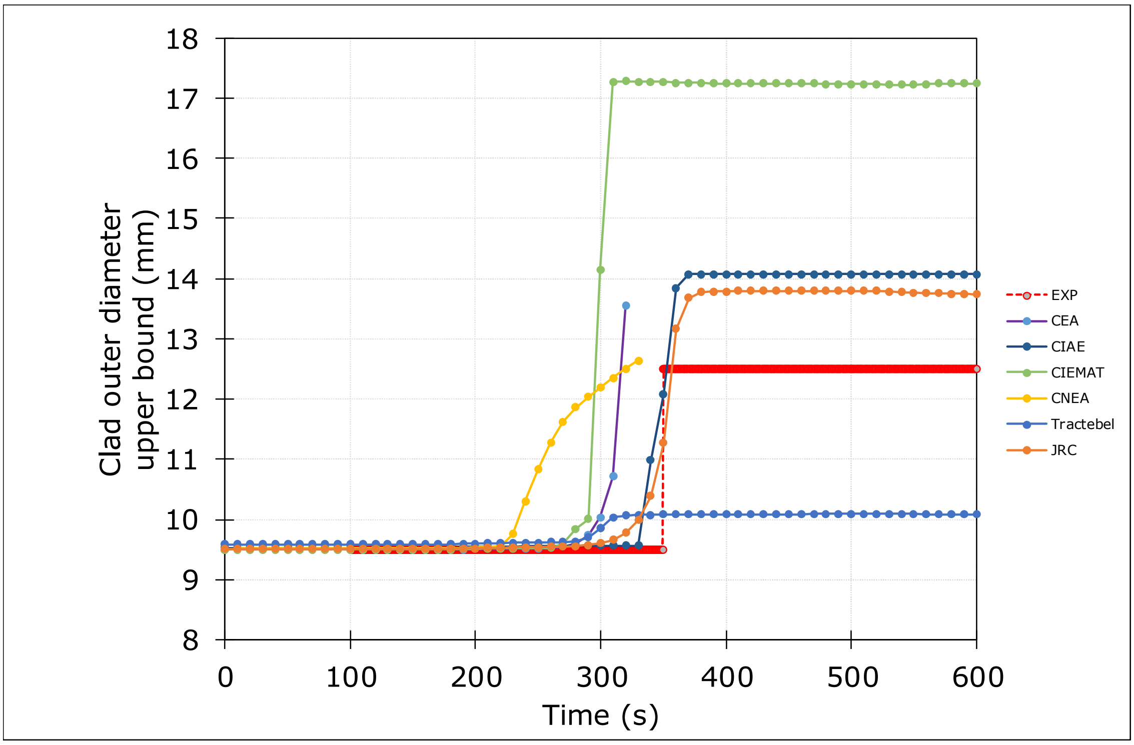

FIG. 166. IFA-650.10: Upper bounds for clad outside diameter.

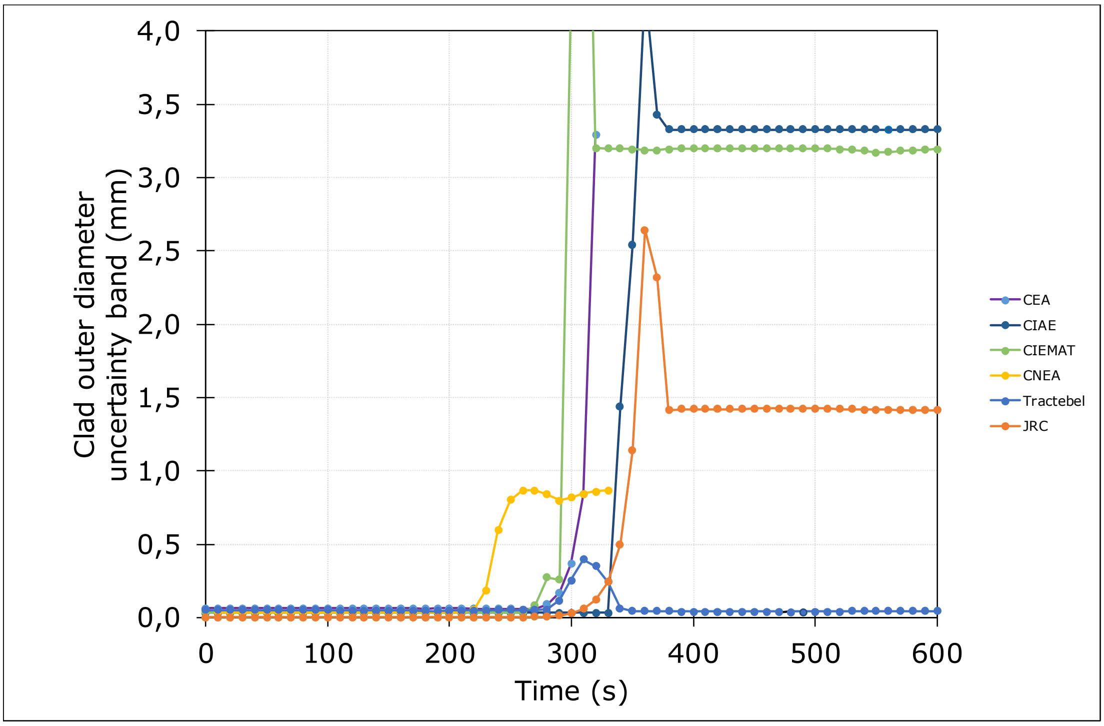

FIG. 167. IFA-650.10: Uncertainty bands for clad outside diameter.

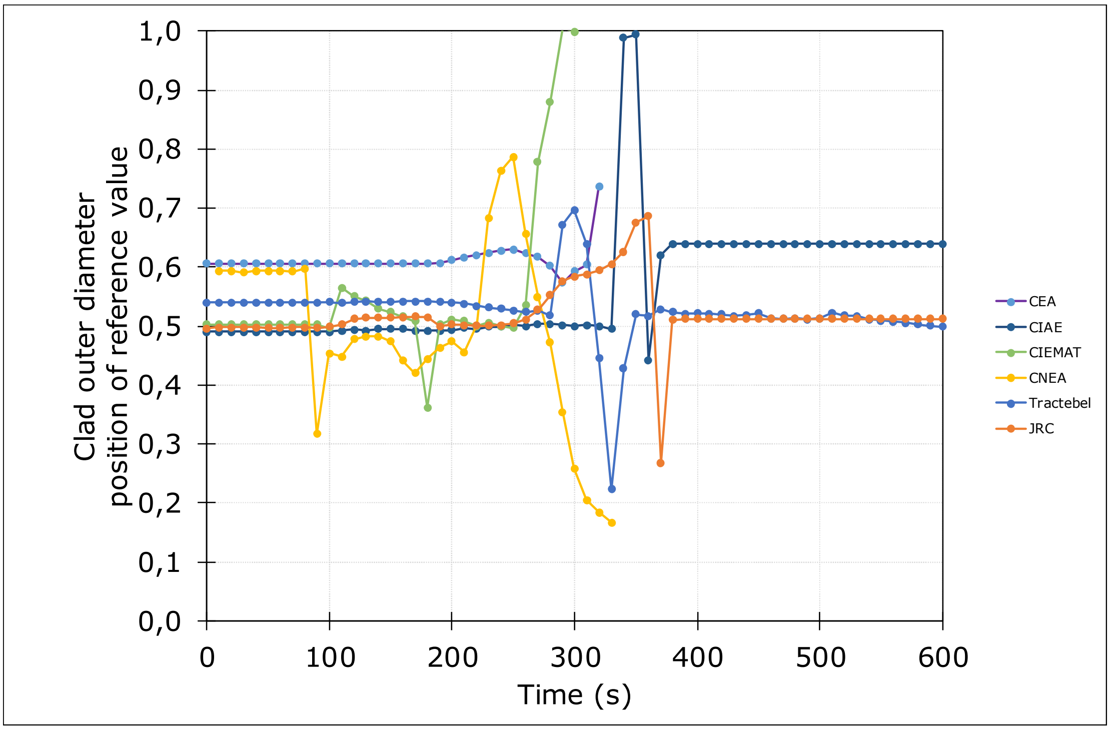

FIG. 168. IFA-650.10: Position of the reference within the uncertainty band for clad outside diameter.

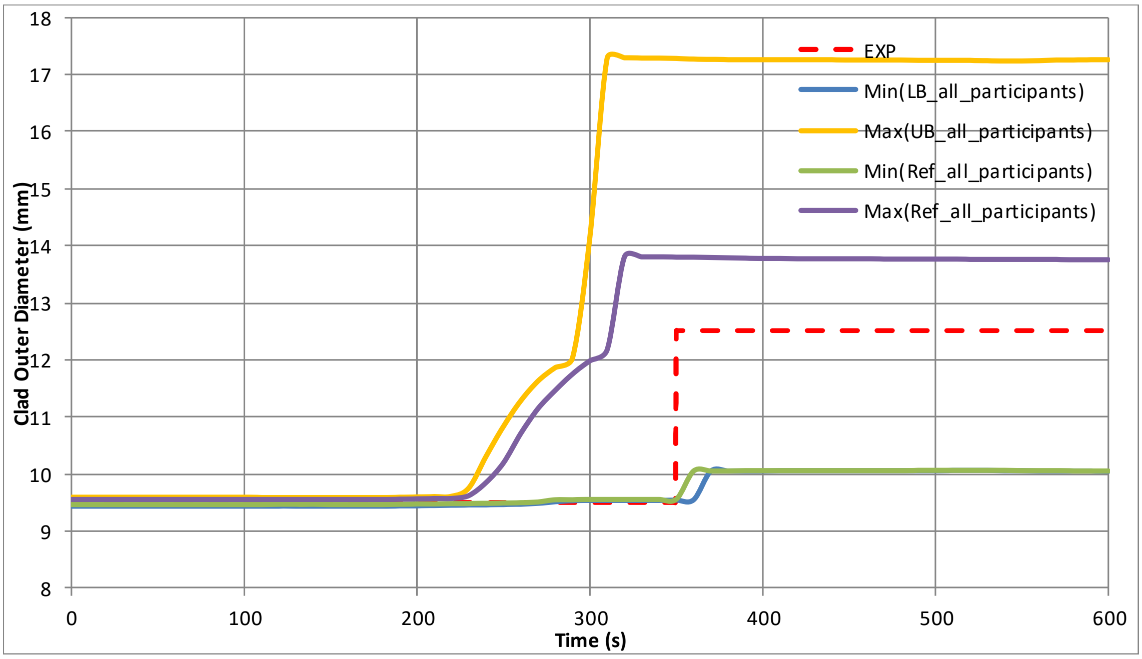

FIG. 169. IFA-650.10: Global reference dispersion and uncertainty width of all participants Clad outside diameter.

5.5. COMPARISON OF SENSITIVITY ANALYSIS RESULTS

The global sensitivity analysis (GSA) is a powerful tool to identify the most influential input uncertainty parameters on each output parameter of interest. They can be identified by using various sensitivity indices like correlation coefficients and well-defined significance thresholds. Specific guidance and interpretation of the significance depends on the number of samples, number of variables, and analysis tolerance.

In the current work, the Partial Rank Correlation Coefficients (PRCCs) were used and arbitrary significance threshold of 0.5 were chosen for identification of the high influence of the input uncertainty parameters on the output parameter (i.e., PRCC > 0.5). Lower values imply low (PRCC < 0.25) or medium influence (0.25 ≤ PRCC ≤ 0.5).

An example of calculating PRCCs by Tractebel, using FRAPTRAN-TE-1.5 and DAKOTA, is shown in Table 16. The PRCC for each output parameter of interest as a function of all the input parameters change during the transient was summarized. The values shown in this table were the maximum during the transient. The red cells were those of high influence, with at least one instant (of PRCC > 0.5), during the transient.

Comparison of the PRCCs by different participants for each of the main output parameters facilitated the identification of a common list of high influential input parameters or phenomena. A common list of high influential input parameters for each output is summarized in Fig. 171, based on the PRCCs at their maximum absolute values of all participants. The red cells with ‘1’ implied that a high influence parameter being identified by at least 1 participant.

Input uncertainty parameter	RIP	TFC	TFO	TCI	TCO	TOL	ECR	DCO	CES	ECT	EFT
Cladding outside diameter (mm)	18%	9%	12%	13%	12%	11%	83%	19%	83%	17%	8%
Cladding inside diameter (mm)	70%	63%	64%	50%	50%	6%	82%	81%	90%	79%	50%
Pellet outside diameter	65%	56%	60%	40%	40%	7%	17%	83%	77%	79%	43%
Fuel theoretical density (kg/m3 at 20 °C)	10%	39%	36%	38%	38%	9%	9%	13%	10%	15%	21%
U^{235} enrichment (%)	10%	10%	12%	12%	12%	9%	8%	11%	12%	11%	14%
Filling gas pressure (MPa)	98%	15%	30%	28%	28%	8%	17%	35%	92%	26%	11%
Relative power during base irradiation	10%	8%	9%	9%	9%	6%	10%	7%	8%	10%	9%
Relative power during test	53%	94%	93%	94%	94%	52%	54%	80%	33%	39%	84%
Test rod power profile	10%	25%	7%	8%	7%	11%	8%	85%	9%	10%	6%
Cladding temperature (°C)											
Coolant temperature (°C)	39%	95%	96%	100%	100%	58%	60%	73%	27%	87%	90%
Clad-to-Coolant heat transfer coefficient	85%	100%	98%	99%	99%	90%	91%	96%	64%	77%	94%
Fuel thermal conductivity model	16%	80%	26%	29%	29%	14%	15%	10%	7%	44%	42%
Clad thermal conductivity model	11%	9%	8%	44%	8%	9%	8%	7%	5%	9%	4%
Fuel thermal expansion model	18%	19%	17%	13%	13%	8%	17%	51%	43%	61%	99%
Clad thermal expansion model	11%	11%	12%	14%	15%	7%	6%	96%	19%	97%	9%
Fuel densification model	24%	36%	38%	18%	18%	7%	10%	61%	51%	54%	35%
Fuel solid swelling model	25%	40%	41%	24%	24%	11%	16%	62%	55%	60%	31%
Fuel gaseous swelling model	39%	38%	38%	24%	24%	10%	11%	65%	56%	61%	30%
Clad Yield stress	44%	25%	59%	67%	66%	15%	37%	77%	36%	55%	21%
Fuel heat capacity	20%	69%	67%	69%	69%	14%	13%	31%	16%	17%	48%
Cladding heat capacity	6%	15%	19%	20%	20%	7%	9%	7%	6%	9%	14%
Cladding elastic modulus	10%	9%	9%	11%	11%	9%	7%	13%	17%	10%	13%
Cladding corrosion model during steady-state operation	10%	11%	29%	22%	22%	100%	100%	21%	57%	15%	11%
Cladding hydrogen pickup fraction during steady-state operation	11%	10%	10%	7%	7%	11%	6%	10%	6%	11%	11%
Cladding oxidation model at high temperature	13%	7%	7%	18%	18%	83%	84%	10%	11%	11%	4%
Thermal conductivity of the oxide layer	6%	5%	5%	10%	10%	8%	8%	7%	7%	6%	6%
Fission gas release (or gas diffusion coefficient)	8%	5%	7%	6%	10%	9%	9%	9%	13%	9%	2%
Gap gas conductivity	17%	59%	91%	48%	47%	15%	17%	47%	14%	19%	44%
Fuel/cladding emissivity	8%	7%	19%	13%	13%	9%	7%	17%	11%	10%	10%
Fuel radial relocation	10%	6%	8%	17%	15%	8%	8%	6%	7%	7%	8%
Fuel fragment packing fraction (if applicable)	14%	7%	7%	10%	10%	12%	12%	8%	6%	12%	11%
Cladding strain threshold for fuel mobility (if applicable)	12%	4%	5%	15%	15%	15%	13%	8%	10%	15%	8%
Cladding Meyer hardness	8%	11%	11%	16%	16%	9%	9%	13%	12%	7%	4%
Cladding annealing	65%	51%	79%	82%	82%	28%	56%	90%	47%	63%	35%
Cladding burst criteria	9%	4%	9%	5%	5%	7%	5%	14%	9%	10%	6%
Cladding burst strain criteria	6%	10%	9%	10%	9%	5%	12%	10%	11%	6%	5%
Plenum gas temperature (°C)	95%	5%	16%	23%	23%	9%	13%	21%	86%	15%	12%

FIG. 170. High Influential input uncertainty parameters based on PRCC at their maximum for each output from Tractebel, as an example is illustrated.

Input uncertainty parameter	RIP	TFC	TFO	TCI	TCO	TOL	ECR	DCO	CES	ECT	EFT
Cladding outside diameter (mm)	0	0	0	1	0	0	1	1	1	0	0
Cladding inside diameter (mm)	1	1	1	1	0	0	1	1	1	1	1
Pellet outside diameter	1	1	1	1	0	0	0	1	1	1	1
Fuel theoretical density (kg/m3 at 20 °C)	0	0	0	0	0	0	0	0	0	0	0
U^{235} enrichment (%)	0	0	0	0	0	0	0	0	0	0	0
Filling gas pressure (MPa)	1	0	0	0	0	0	0	1	1	1	0
Relative power during base irradiation	0	0	0	0	0	0	0	0	0	0	0
Relative power during test	1	1	1	1	1	1	1	1	0	0	1
Test rod power profile	0	0	0	0	0	0	0	1	0	0	0
Cladding temperature (°C)	1	1	1	1	1	1	0	1	1	1	1
Coolant temperature (°C)	1	1	1	1	1	1	1	1	0	1	1
Clad-to-Coolant heat transfer coefficient	1	1	1	1	1	1	1	1	1	1	1
Fuel thermal conductivity model	1	1	0	0	0	0	0	1	0	0	1
Clad thermal conductivity model	0	0	0	1	0	0	0	0	0	0	0
Fuel thermal expansion model	1	1	1	0	0	0	0	1	1	1	1
Clad thermal expansion model	1	1	1	0	0	0	0	1	1	1	1
Fuel densification model	0	0	0	0	0	0	0	1	1	1	0
Fuel solid swelling model	0	0	0	0	0	0	0	1	1	1	0
Fuel gaseous swelling model	0	0	0	0	0	0	0	1	1	1	0
Clad Yield stress	0	0	1	1	1	0	0	1	1	1	0
Fuel heat capacity	0	1	1	1	1	0	0	0	0	0	0
Cladding heat capacity	0	0	0	0	0	0	0	0	0	0	0
Cladding elastic modulus	0	0	0	0	0	0	0	1	0	1	0
Cladding corrosion model during steady-state operation	0	0	0	0	0	1	1	0	1	0	0
Cladding hydrogen pickup fraction during steady-state operation	0	0	0	0	0	0	0	0	0	0	0
Cladding oxidation model at high temperature	0	0	0	0	0	1	1	0	0	0	0
Thermal conductivity of the oxide layer	0	0	0	0	0	0	0	0	0	0	0
Fission gas release (or gas diffusion coefficient)	0	0	0	0	0	0	0	0	0	0	0
Gap gas conductivity	1	1	1	1	0	0	0	0	1	0	1
Fuel/cladding emissivity	0	0	0	0	0	0	0	0	0	0	0
Fuel radial relocation	0	0	0	0	0	0	0	0	0	0	0
Fuel fragment packing fraction (if applicable)	0	0	0	0	0	0	0	0	0	0	0
Cladding strain threshold for fuel mobility (if applicable)	0	0	0	0	0	0	0	0	0	0	0
Cladding Meyer hardness	0	0	0	0	0	0	0	0	0	0	0
Cladding annealing	1	1	1	1	1	0	1	1	0	1	0
Cladding burst criteria	0	0	0	0	0	0	0	0	0	0	0
Cladding burst strain criteria	0	0	0	0	0	0	0	0	0	0	0
Plenum gas temperature (°C)	1	0	0	0	0	0	0	1	1	0	0

FIG. 171. Common list of high influential input uncertainty parameters based on PRCC at their maximum for each output.

Input uncertainty parameter	Fuel Thermal +RIP	Clad thermal +ECR	Fuel/Clad Mechanical	Overall
Cladding outside diameter (mm)	0	1	1	1
Cladding inside diameter (mm)	1	1	1	1
Pellet outside diameter	1	1	1	1
Fuel theoretical density (kg/m3 at 20 °C)	0	0	0	0
U^{235} enrichment (%)	0	0	0	0
Filling gas pressure (MPa)	1	0	1	1
Relative power during base irradiation	0	0	0	0
Relative power during test	1	1	1	1
Test rod power profile	0	0	1	1
Cladding temperature (°C)	1	1	1	1
Coolant temperature (°C)	1	1	1	1
Clad-to-Coolant heat transfer coefficient	1	1	1	1
Fuel thermal conductivity model	1	0	1	1
Clad thermal conductivity model	0	1	0	1
Fuel thermal expansion model	1	0	1	1
Clad thermal expansion model	1	0	1	1
Fuel densification model	0	0	1	1
Fuel solid swelling model	0	0	1	1
Fuel gaseous swelling model	0	0	1	1
Clad Yield stress	1	1	1	1
Fuel heat capacity	1	1	0	1
Cladding heat capacity	0	0	0	0
Cladding elastic modulus	0	0	1	1
Cladding corrosion model during steady-state operation	0	1	1	1
Cladding hydrogen pickup fraction during steady-state operation	0	0	0	0
Cladding oxidation model at high temperature	0	1	0	1
Thermal conductivity of the oxide layer	0	0	0	0
Fission gas release (or gas diffusion coefficient)	0	0	0	0
Gap gas conductivity	1	1	1	1
Fuel/cladding emissivity	0	0	0	0
Fuel radial relocation	0	0	0	0
Fuel fragment packing fraction (if applicable)	0	0	0	0
Cladding strain threshold for fuel mobility (if applicable)	0	0	0	0
Cladding Meyer hardness	0	0	0	0
Cladding annealing	1	1	1	1
Cladding burst criteria	0	0	0	0
Cladding burst strain criteria	0	0	0	0
Plenum gas temperature (°C)	1	0	1	1

FIG. 172. Common list of high influential input uncertainty parameters for each fuel modelling aspect.

Based on the current sensitivity study results, a common list of high influential input uncertainty parameters could be identified for each aspect of the fuel rod code, as shown in Fig. 172. Again, the red cells with '1' implied that a high influence parameter being identified by at least 1 participant.

In summary, the following input uncertainty parameters were of high influence on the overall fuel code models, including fuel and cladding thermal and mechanical modelling:

— Fuel rod geometries: clad outside/inside diameter, fuel pellet diameter;
— Test conditions: filling gas pressure, power and clad-to-coolant heat transfer (coolant temperature and clad-to-coolant heat transfer coefficients, or clad temperature) during the test. The axial power profile was also important for mechanical modelling;
— Material properties and models related to fuel-to-clad heat transfer: fuel thermal conductivity and heat capacity; gap conductivity; fuel thermal expansion, densification and swelling; cladding thermal expansion, yield stress, annealing; cladding steady-state corrosion and high-temperature oxidation;
— Plenum gas temperature.

On the contrary, the following input uncertainty parameters appeared to have only low or medium influence:

— Fuel manufacturing data (Fuel density, Enrichment);
— Operation conditions: Relative power during base irradiation;
— Material properties: models related to clad heat capacity, Meyer hardness, burst strain criteria or burst stress and strain criteria, fuel radial relocation, fuel/cladding emissivity, fission gas release. The axial relocation related parameters (fuel fragmentation fraction, strain threshold for fuel mobility) had no influence as the axial relocation model is not used.

The non-significance of some input uncertainty parameters was surprising. For example, in FRAPTRAN (without the axial relocation model), the ballooning and burst were predicted by the BALON2 model which calculated the extent and shape of the localized large cladding deformation (ballooning) that occurred between the time that the cladding effective strain exceeds the instability strain and the time of cladding rupture. The BALON2 model predicted failure (burst) in the ballooning node when the cladding true hoop stress exceeded an empirical limit that was a function of cladding temperature, or when the predicted cladding permanent hoop strain exceeds the strain limit that was a function of cladding temperature. It was expected that there should be at least an impact of the 'cladding burst stress criteria' or 'cladding burst strain criteria'.

One should not forget the limitations of using the correlation coefficients. Indeed, the impact of a single input uncertainty parameter on a specific output parameter could be non-linear and non-monotonic and thus not captured by the correlation coefficients like PRCC. Another explanation would be that those parameters affect only the burst time, but not the other parameters. This would make their effect harder to notice.

5.6. CONCLUSIONS

An uncertainty and sensitivity analysis was performed on the simulation of the Halden LOCA test IFA-650.10, according to detailed Specifications. Seven participants submitted their uncertainty analysis results, and six participants submitted their sensitivity analysis results. The provided results were compared and discussed, in comparison with the available experimental data.

The comparison of the uncertainty analysis showed that the uncertainty bands were acceptable for the fuel and clad thermal behaviour (RIP, TCO and TFO), but quite large for the clad mechanical behaviour prediction (ECT and DCO). The mechanical models for the clad deformation still required improvement, at least for certain fuel rod codes (i.e., FRAPTRAN).

The comparison of the sensitivity analysis results helped to identify a common list of high influential input uncertainty parameters for each output parameter, and for each aspect (fuel and clad thermal and mechanical modelling) and phenomena within the fuel rod codes.

It should be noted that a significant user-effect existed, as illustrated by the differences in the three results using FRAPTRAN.

5.7. SUMMARY AND RECOMMENDATIONS

Within the FUMAC project, the following achievements were made:

- Verified experimental data set on fuel characteristics in accident conditions, supporting codes development and validation for potential extension of the IFPE database;
- Better predictive capabilities of fuel performance codes: improved models, material properties and numerical algorithms for the simulation of nuclear fuel under DBA and DEC, with consideration of uncertainties;
- Extended collaboration between some Member State organizations (examples: INL-POLIMI-JRC collaboration agreement; IFE-IBRAE collaboration and joint presentation at the Enlarged Halden Programme Group Meeting, 2017) beyond the FUMAC project timeframe.

Many participants acknowledged the IAEA for organizing this CRP, which provided an ideal platform to compare their code results with others and especially with experimental data, to which they otherwise would not have access.

All experimental data revealed a relatively large spread of the measured burst strains, which was determined by the local conditions of temperature and pressure, and by the heterogeneities and composition or micro-structural variations in the materials under investigations. An uncertainty analysis of the experimental data was therefore recommended, including those data that were used for the development and validation of the codes applied.

It has been reiterated that this CRP triggered new collaborations, led to the development and improvement of common models, for those that have been used by a larger user group (e.g. FRAPTRAN, TRANSURANUS). It has also enabled to point out differences in the interpretation of some experiments and therefore in the use of the codes, the so-called user effects.

The active participation of organizations that provided the experimental data has also been very instrumental in clarifying various questions raised during the project.

The following recommendations were made:

- More analysis and cases for VVER fuel would be needed, especially in view of recent advanced fuel developments;
- A general interest has been expressed to consider a similar analysis for advanced fuels and cladding materials, including some of the so-called accident tolerant fuels;
- For a successful CRP that involves so many cases and participants, the duration of the project meetings may be extended, enabling for instance to analyze better model details and code changes as well as their comparison with more detailed experimental data;
- Deeper analysis of failure criteria with advanced tools, and uncertainty analysis on experimental data would be beneficial;
- Need more quantitative information about fuel fragmentation.

Participants also recommended that the future CRP should focus on fuel modelling with more practical applications to support the sustainability of nuclear technology, diversification of fuel supply, and innovation in fuel technology development.

REFERENCES

[1] MISFELDT, I., “The D-COM Blind Problem on Fission Gas Release: Experimental Description and Results, Summary report,” in OECD-NEA-CSNI/IAEA Specialists' Meeting on Water Reactor Fuel Safety and Fission Product Release in Off-Normal and Accident Conditions, IAEA-IWGFPT/16, p. 411, Roskilde, Denmark, 16–20 May 1983.

[2] KILLEEN, J., TURNBULL, J. A., SARTORI, E., “Fuel Modelling at Extended Burnup: IAEA Coordinated Research Project FUMEX-II”, Proceedings of International LWR Fuel Performance Meeting, American Nuclear Society, San Francisco, California, USA, 30 September–3 October, 2007.

[3] INTERNATIONAL ATOMIC ENERGY AGENCY, “Fuel Modelling at Extended Burnup (FUMEX-II)”, IAEA TECDOC-1687, IAEA, Vienna, Austria, 2012.

[4] INTERNATIONAL ATOMIC ENERGY AGENCY, “Improvement of computer codes used for fuel behaviour simulation (FUMEX-III)”. IAEA-TECDOC-1697, IAEA, Vienna, Austria, 2013.

[5] HÓZER, Z., GYŐRI, C., HORVÁTH, M., NAGY, I., MARÓTI, L., MATUS, L., WINDBERG, P., FRECSKA J.,” Ballooning Experiments with VVER Cladding”, Nuclear Technology 152(3), 273, 2005.

[6] PEREZ-FERÓ, E., GYŐRI, C., MATUS, L., VASÁROS, L., HÓZER, Z., WINDBERG, P.,MARÓTI, L., HORVÁTH, M., NAGY, I., CSORDÁS, A.P, NOVOTNY T., “Experimental database of E110 claddings exposed to accident conditions”, J. Nucl. Mater., 397, 48, 2010.

[7] FLANAGAN, M., et al., Post-test examination results from integral, high-burnup, fueled LOCA tests at Studsvik Nuclear Laboratory, Report NUREG-2160, U.S. Nuclear Regulatory Commission, Washington, DC, USA, 2013.

[8] HELIN, M. and J. FLYGARE, NRC LOCA tests at Studsvik: Design and construction of test train device and tests with unirradiated cladding material, Report STUDSVIK/N-11/130, Studsvik Nuclear AB, Studsvik, Sweden, 2013.

[9] FLANAGAN, M. and P. ASKELJUNG. Observations of fuel fragmentation, mobility and re-lease in integral high-burnup, fueled LOCA tests. OECD Halden Reactor Project LOCA Workshop, May 29–30, 2012, Lyon, France: OECD Halden Reactor Project, Halden, Norway, 2012.

[10] ZWICKY, H.-U., Re-fabrication of ramp rodlet Z-3 from Westinghouse father rod irradiated in North Anna. Report N-05/131 Rev. 1, Studsvik Nuclear AB, Nyköping, Sweden, 2006.

[11] ZWICKY, H.-U., Re-fabrication of ramp rodlet Z-4 from Westinghouse father rod irradiated in North Anna. Report N-05/133 Rev. 1, Studsvik Nuclear AB, Nyköping, Sweden, 2006.

[12] RAYNAUD, P.A.C., NRC Studsvik LOCA test 192, 2014, MS Excel data file contributed to the IAEA CRP FUMAC on December 8, 2014, U.S. Nuclear Regulatory Commission, Washington, DC, USA, 2014.

[13] JERNKVIST, L.O., Computational assessment of LOCA simulation tests on high burnup fuel rods in Halden and Studsvik. Report SSM 2017:12, Swedish Radiation Safety Authority, Stockholm, Sweden, 2017.

[14] ERBACHER, F. J., H. J. NEITZEL, AND K. WIEHR. Effects of thermohydraulics on clad ballooning, flow blockage and coolability in a LOCA. NO. IWGFPT--16. 1983.

[15] STUCKERT, J., GROßE, M., RÖSSGER, C., KLIMENKOV, M., STEINBRÜCK, M., WALTER, M. QUENCH-LOCA program at KIT on secondary hydriding and results of the commissioning bundle test QUENCH-L0. Nucl. Eng. Des. 255 (2013) 185–201.
[16] VESHCHUNOV, M.S., SHESTAK. V.E., Modelling of Zr alloy burst cladding internal oxidation and secondary hydriding under LOCA conditions. J. Nucl. Mater., 461 (2015) 129–142.
[17] NUREG/CR-7023, Vol. 1, Revision 1: "FRAPTRAN 1.5: A Computer Code for the Transient Analysis of Oxide Fuel Rods", USNRC, May 2014.
[18] NUREG/CR-7023, Vol. 2, Revision 1: "FRAPTRAN 1.5: Integral assessment", USNRC, May 2014.
[19] JERNKVIST, L. O., MASSIH A. R., and ALVESTAV A., Axial relocation of fragmented and pulverized fuel and its effects on fuel rod heat load during LOCAs, Top Fuel 2015, paper A0059, 2015.
[20] GOVERS K., VERWERFT M., "Simulation of ballooning & relocation in the Halden LOCA tests with FRAPTRAN", EHPG meeting, 2014.
[21] JERNKVIST, L. O., MASSIH, A. R., ALVESTAV, A., "Computational assessment of axial fuel relocation in Halden IFA-650 LOCA tests. In Proceedings of Enlarged Halden Program Group Meeting, Sandefjord, Norway, OECD Halden Reactor Project, May 8–13, 2016.
[22] JERNKVIST L. O., and MASSIH, A. R., "Models for axial relocation of fragmented and pulverized fuel pellets in distending fuel rods and its effects on fuel rod heat load," SSM research report 2015:37, Swedish Radiation Safety Authority (SSM), Stockholm, Sweden, September 2015.
[23] JERNKVIST, L. O., "Observed and corrected errors in source code and algorithms of FRAPTRAN-1.5," Report TR15-002V2, Quantum Technologies AB, March 2016.
[24] ZHANG, J., "Code modification requirements specifications (CMRS) for extension and adaptation of FRAPTRAN-1.5 for LOCA fuel behaviour modelling," Internal report FUELROD/4DO/0437004/000/00, Tractebel, February 2016.
[25] JERNKVIST, L. O., "The FRAPTRAN-TE-1.5 computer program", Report TR16-001, Quantum Technologies AB, March 2016.
[26] LASSMANN, K., URANUS -- A computer programme for the thermal and mechanical analysis of the fuel rods in a nuclear reactor, Nucl. Eng. Des. 45 (1978) 325.
[27] LASSMANN, K., TRANSURANUS: a fuel rod analysis code ready for use, J. Nucl. Mater. 188 (1992) 295.
[28] LASSMANN, K., RONCHI, C., SMALL, G. J., The development of fuel performance models at the European institute for transuranium elements, J. Nucl. Mater. 166 (1989) 112.
[29] LASSMANN, K., O'CARROL, C., DE LAAR, J.V., WALKER, C. T., The radial distribution of plutonium in high burnup UO2 fuels, J. Nucl. Mater. 208 (1994) 223.
[30] LASSMANN, K., WALKER, C. T., DE LAAR, J.V., LINDSTRÖM, F., Modelling the high burnup UO2 structure in LWR fuel, J. Nucl. Mater. 226 (1995) 1.
[31] LASSMANN, K., DE LAAR, J.V., "The Transient TRANSURANUS version", Proceedings of IAEA RER/4/019, Licensing Fuel and Fuel Modelling Codes for WWER Reactors, Seminar " Implementation of the WWER version of the TRANSURANUS code and its application to safety criteria", Sofia, Bulgaria, 7–11 December 1998.

[32] UFFELEN, V.P, GYORI, Cs., SCHUBERT, A., DE LAAR, J.V., HOZER, Z., SPYKMAN, G., Extending the application range of a fuel performance code from normal operating to design basis accident conditions, J. Nucl. Mater. 383 (2008) 137.
[33] GYORI, Cs., HÓZER, Z., LASSMANN, K., SCHUBERT, A., DE LAAR, J.V., HATALA, B., CVAN, M., "Extension of Transuranus code applicability with Niobium containing cladding models (EXTRA) ", Final Report, EVOL-EXTRA-D5 / FIKS-CT2001-00173, 2004.
[34] SPYKMAN, G., MÄRTENS, D., BOUR, D., KOCK, P., LASSMANN, K., SCHUBERT, A., DE LAAR, J.V., "Implementation of a Cladding Failure Model for a Loss of Coolant Accident (LOCA)-Analysis in Transuranus", Proceedings of Enlarged Halden Programme Group Meeting on High Burn-up Fuel Performance, Safety and Reliability, Sandefjord, Norway, 9–14 May 2004.
[35] DI MARCELLO, V., SCHUBERT, A., DE LAAR, J.V., VAN UFFELEN, P., The TRANSURANUS mechanical model for large strain analysis, Nucl. Eng. Des. 276 (2014) 19.
[36] PASTORE, G., Luzzi, L., Di Marcello, V.,VAN UFFELEN, Physics-based modelling of fission gas swelling and release in UO2 applied to integral fuel rod analysis, Nucl. Eng. Des. 256 (2013) 75.
[37] DI MARCELLO, V., RONDINELLO, V., SCHUBERT, A., DE LAAR, J.V., VAN UFFELEN, P., Modelling actinide redistribution in mixed oxide fuel for sodium fast reactors, Progress in Nuclear Energy 72 (2014) 83.
[38] DI MARCELLO, V., SCHUBERT, A., DE LAAR, J.V., VAN UFFELEN, P., Extension of the TRANSURANUS plutonium redistribution model for fast reactor performance analysis, Nucl. Eng. Des. 248 (2012) 149.
[39] LASSMANN, K., HOHLEFELD, F., The revised URGAP model to describe the gap conductance between fuel and cladding, Nucl. Eng. Des. 103 (1987) 215.
[40] SCHUBERT, A., VAN UFFELEN, P., DE LAAR, J.V., Walker, C. T., HAECK, W., Extension of the TRANSURANUS burn-up model, J. Nucl. Mater. 376 (2008) 1
[41] MARELLE, V. et al., Thermo-mechanical modelling of PWR fuel with ALCYONE. in proceedings of Top Fuel 2011, Chengdu, China, 2011.
[42] MARELLE, V. et al., New developments in ALCYONE 2.0 fuel performance code. in proceedings of Top Fuel Boise Idaho USA, 2016.
[43] STRUZIK, C. et al., Validation of fuel performance CEA code ALCYONE, scheme 1D, on extensive data base. in proceedings of Top Fuel 2012, Manchester, United Kingdom, 2012.
[44] SERCOMBE, J. et al., Stress concentration during pellet cladding interaction: Comparison of closed-form solutions with 2D (r,theta) finite element simulations. Nucl. Eng. Des. 260, 175, 2013.
[45] MICHEL, B. et al., 3D fuel cracking modelling in pellet cladding mechanical interaction. Engineering Fracture Mechanics 75, 3581, 2008.
[46] MARELLE, V., Validation of PLEIADES/ALCYONE 2.0 fuel performance code. WRFPM2017, Jeju Island Corea, 2017.
[47] JOMARD, G. et al., CARACAS: an industrial model for the description of fission gas behaviour in LWR-UO2 fuel. in Proceedings WRFPM 2014, Sendaï (Japan), 2014.
[48] NOIROT, L. et al., MARGARET: A comprehensive code for the description of fission gas behaviour. Nuclear Enginering and design 241, 2011.

[49] WILLIAMSON, R.L., HALES, J.D., NOVASCONE, S. R., TONKS, M.R., GASTON, D.R., PERMANN, C.J., ANDRS, D., MARTINEAU. R.C., Multidimensional multiphysics simulation of nuclear fuel behaviour. J. Nucl. Mater. 423, 149, 2012.

[50] GASTON, D., NEWMAN, C., HANSEN, G., LEBRUN-GRANDIÉ, D., MOOSE: A parallel computational framework for coupled systems of nonlinear equations, Nucl. Eng. Des., 239, 1768, 2009.

[51] RASHID, M.M., Incremental kinematics for finite element applications, International Journal of Numerical Methods and Engineering 36, 3937, 1993.

[52] HALES, J.D., WILLIAMSON, R.L., NOVASCONE, S.R., PASTORE, G., SPENCER, B.W., STAFFORD, D.S., GAMBLE, K.A., PEREZ, D.M., GARDNER, R.J., LIU, W., BISON theory manual: The equations behind nuclear fuel analysis. Technical Report INL/EXT-13-29930, Rev.1. Idaho National Laboratory, 2014.

[53] PASTORE, G., SWILER, L.P., HALES, J.D., NOVASCONE, S.R., PEREZ, D.M., SPENCER, B.W., LUZZI, L., VAN UFFELEN, P., WILLIAMSON R.L., . Uncertainty and sensitivity analysis of fission gas behaviour in engineering-scale fuel modelling. J. Nucl. Mater. 465, 398, 2015.

[54] WILLIAMSON R.L., GAMBLE, K.A., PEREZ, D.M., NOVASCONE, S.R., PASTORE, G., GARDNER, R.J., HALES, J.D., LIU, W., MAI, A., Validating the BISON fuel performance code to integral LWR experiments. Nucl. Eng. Des. 301, 232, 2016.

[55] Assessment of BISON: A Nuclear Fuel Performance Analysis Code. BISON Release 1.3, Technical Report INL/MIS-13-30314 Rev. 3, Idaho National Laboratory, 2016.

[56] PASTORE, G., NOVASCONE, S.R., WILLIAMSON R.L., HALES, J.D., SPENCER, B.W., STAFFORD, D.S., Modelling of fuel behaviour during loss-of-coolant accidents using the BISON code. In: Proc. of the LWR Fuel Performance Meeting, Zurich, Switzerland, September 13–17, 2015.

[57] PASTORE, G., WILLIAMSON R.L., NOVASCONE, S.R., SPENCER, B.W., HALES, J.D., Modelling of LOCA tests with the BISON fuel performance code. In: Enlarged Halden Programme Group Meeting, Fornebu, Norway, May 8-13, 2016.

[58] WILLIAMSON R.L., FOLSOM, C.P., PASTORE, G., VEEARAGHAVAN, S., Reactivity insertion accident (RIA) capability status in the BISON fuel performance code. Technical Report CASL-X-2016-1104-000, Consortium for Advanced Simulation of LWRs, July 2016.

[59] PASTORE, G., FOLSOM, C.P., WILLIAMSON R.L., HALES, J.D., LUZZI, L., PIZZOCRI, D., BARANI T., Modelling fission gas behaviour with the BISON fuel performance code. In Enlarged Halden Programme Group Meeting, Lillehammer, Norway, September 24-29, 2017.

[60] HALES, J.D., WILLIAMSON R.L., NOVASCONE, S.R., PEREZ, D.M., SPENCER, B.W., PASTORE, BG., Multidimensional Multiphysics Simulation of TRISO Particle Fuel, J. Nucl. Mater. 443, 531, 2013.

[61] PASTORE, G., PIZZOCRI, D., NOVASCONE, S.R., PEREZ, D.M., SPENCER, B.W., WILLIAMSON R.L., VAN UFFELEN, P., LUZZI, L., Modelling of transient fission gas behaviour in oxide fuel and application to the BISON code. In Enlarged Halden Programme Group Meeting, Røros, Norway, September 7–12, 2014.

[62] BARANI, T., BRUSCHI, E., PIZZOCRI, D., PASTORE, G., VAN UFFELEN, P., WILLIAMSON R.L., LUZZI, L., Analysis of transient fission gas behaviour in oxide fuel using BISON and TRANSURANUS, J. Nucl. Mater. 486, 96, 2017.

[63] SOBA, A., DENIS, A., DIONISIO 2.0: New version of the code for simulating a whole nuclear fuel rod under extended irradiation, Nucl. Eng. and Des. 292, 213, 2015.
[64] SOBA, A., DENIS, A., ROMERO, L., VILLARINO, E., SARDELLA, F., A high burn-up model developed for the DIONISIO code, J. Nucl. Mater., 433(1), 160, 2013.
[65] SOBA, A., LEMES, M., DENIS, A., An empirical formulation to describe the evolution of the high burnup structure, J. Nucl. Mater., 456, 174, 2015.
[66] SOBA, A., LEMES, M., GONZÁLEZ, M.E., DENIS, A., ROMERO, L., Simulation of the behaviour of nuclear fuel under high burnup conditions, Ann. Nucl. Energy. 70, 147, 2014.
[67] LEMES, M., SOBA, A., DAVERIO, H., DENIS, A., Inclusion of models to describe severe accident conditions in the fuel simulation code DIONISIO, Nucl. Eng. and Des. 315, 1, 2017.
[68] GEELHOOD, K.J., LUSCHER, W.G., CUTA, J.M., FRAPTRAN-1.5: A Computer Code for the Transient Analysis of Oxide Fuel Rods. U.S. Nuclear Regulatory Commission, 2014.
[69] WILLIAMSON R.L., PASTORE G., NOVASCONE. S.R., et al. Modelling of LOCA Tests with the BISON Fuel Performance Code. Idaho National Laboratory, Idaho Falls, United States, 2016.
[70] ROSINGER H.E., NEITZEL H.J., ERBACHER F.J., Development of a Burst Criterion for Zircaloy Fuel Cladding under LOCA Conditions. In Proc. IAEA Specialist Meeting on Fuel Element Performance Computer Modelling, Blackpool, UK, pp. 21–35. 1980.
[71] GEELHOOD, K.J., LUSCHER, W.G., FRAPTRAN-1.5: Integral Assessment. U.S. Nuclear Regulatory Commission, 2014.
[72] RAPTA-5.2 software tool. ROSTECHNADZOR (Federal Environmental, Industrial and Nuclear Supervision Service), SEC NRS (Scientific and Engineering Centre of Nuclear and Radiation Safety), Certificate of Computer Code № 399 of 14.07.2016.
[73] FEDOTOV, P., Analytical functions used for description of the plastic deformation process in zirconium alloys VVER type fuel rod cladding under designed accident conditions. Proceedings of the Fifth International Conference. VVER Fuel Performance, Modelling and Experimental Support. 29 September – 3 October 2003, Albena, Bulgaria. p. 417–429.
[74] FEDOTOV P., NECHAEVA O., SALATOV A., LOSHMANOV L., Universal model of zirconium alloys plastic deformation under VVER design basis accident (DBA) conditions. 6-th International Conference on VVER Fuel Performance, Modelling and Experimental Support. 19-23 September 2005, Bulgaria.
[75] FEDOTOV, P.V., GONCHAROV, A.A., KUMACHEV, A.V., MEDVEDEV, A.V., NECHAEVA, O.A., NOVIKOV, V.V., ONUFRIEV, A.V.,SALATOV, A.V., MOLCHANOV, V.L., PIMENOV, YU.V., ALEKSEEV, A.V., KISELEVA, I.V., SHULIMOV, V.N., FEDIK, I.I., NALIVAEV, V.I., PARSHIN, N.YA., KONSTANTINOV. V.S., Estimation of Water-Water Energy Reactor Fuel Rod Failure in Design Basis Accidents, Proceeding of 2005 Water Reactor Fuel Performance Meeting, Kyoto, Japan, 2-6 October 2005, p.p. 835–847.
[76] VESHCHUNOV, M.S., BOLDYREV, A. V., OZRIN, V.D., SHESTAK, V.E., TARASOV, V.I., A new mechanistic code SFPR for modelling of single fuel rod performance under various regimes of LWR operation, Nucl. Eng. Des. 241, 2822–2830 (2011).

[77] VESHCHUNOV, M.S., OZRIN, V.D., SHESTAK, V.E., TARASOV, V.I., DUBOURG, R., NICAISE, G., Development of the mechanistic code MFPR for modelling fission products release from irradiated UO2 fuel. Nucl. Eng. Des. 236, 179–200 (2006).
[78] VESHCHUNOV, M.S., DUBOURG, R., OZRIN, V.D., SHESTAK, V.E., TARASOV, V.I., Mechanistic modelling of Urania fuel evolution and fission product migration during irradiation and heating. J. Nucl. Mater. 362, 327 (2007).
[79] HOFMANN, P., NOACK, V., VESHCHUNOV, M.S., BERDYSHEV, A.V., BOLDYREV, A.V., MATWEEV, L.V., PALAGIN, A.V., SHESTAK, V.E., Physico-Chemical Behaviour of Zircaloy Fuel Rod Cladding Tubes During LWR Severe Accident Reflood, Report FZKA 5846, Karlsruhe, Germany (1997).
[80] HOFMANN, P., MIASSOEDOV, A., STEINBOCK, L., STEINBRUECK, M., BERDYSHEV, A.V., BOLDYREV, A.V., PALAGIN, A.V., SHESTAK, V.E., VESHCHUNOV, M.S., Quench Behaviour of Zircaloy Fuel Rod Cladding Tubes. Small-Scale Experiments and Modelling of the Quench Phenomena. Report FZKA 6208, INV-COBE (98)-D018, Karlsruhe, Germany (1999).
[81] VESHCHUNOV M.S., SHESTAK, V.E., Model for Melt Blockage (Slug) Relocation and Physico-Chemical Interactions during Core Degradation under Severe Accident Conditions. Nucl. Eng. Des. 238 (2008) 3500–3507
[82] KIM H.C., et al., Development of fully coupled MARS-KS/FRAPTRAN code system for simulation of fuel behaviour during LOCA, Transactions of the Korea Nuclear Society Autumn meeting, Gyeongju, Korea, October 26, 2017.
[83] GEELHOOD, K.J., LUSCHER, W.G., BEYER, C.E., CUTA, J.M., FRAPTRAN 1.4: A Computer Code for the Transient Analysis of Oxide Fuel Rods, NUREG/CR-7023, Vol.1, 2011.
[84] MARS Code manual, Volume I: Code Structure, System Models, Solution Methods, KAERI/TR-2812, 2004.
[85] GEELHOOD, K.J., LUSCHER, W.G., BEYER, C.E., CUTA, J.M., FRAPTRAN 1.4: A Computer Code for the Transient Analysis of Oxide Fuel Rods, NUREG/CR-7023, Vol. 1, PNNL-19400, 2011.
[86] HÄMÄLÄINEN, A., STENGÅRD, J.-O., MIETTINEN, J., KYRKI-RAJAMÄKI, R., Coupled Code FRAPTRAN - GENFLO for Analysing Fuel Behaviour During PWR and BWR Transients and Accidents. Proceeding of: Technical Committee meeting, 10 September 2001, Halden, Norway, IAEA-TECDOC-1320, 2001.
[87] MIETTINEN, J., HÄMÄLÄINEN, A., 2002. GENFLO - A General Thermal Hydraulic Solution for Accident Simulation. VTT Research Notes 2163, ISBN 951-38-6083-3, ISSN 1455-0865. www.vtt.fi/inf/pdf/tiedotteet/2002/T2163.pdf (visited 5 May 2017).
[88] ORGANISATION FOR ECONOMIC CO-OPERATION AND DEVELOPMENT, NUCLEAR ENERGY AGENCY, Benchmark Calculations on Halden IFA-650 LOCA Test Results, NEA/CSNI/R6, 2010.
[89] MIETTINEN, J., Thermohydraulic Model SMABRE for Light Water Reactor Simulations. Thesis for the degree of Licentiate of Technology, Helsinki University of Technology, 2000.
[90] ARKOMA, A., IKONEN, T., Sensitivity analysis of local uncertainties in large break loss-of-coolant accident (LB-LOCA) thermo-mechanical simulations. Nucl. Eng. Des., 305, 293, 2016.

[91] ARKOMA, A., HÄNNINEN, M., RANTAMÄKI, K., KURKI, J., and HÄMÄLÄINEN, A., Statistical analysis of fuel failures in large break loss-of-coolant accident (LBLOCA) in EPR type nuclear power plant. Nucl. Eng. Des., 285, 1, 2015.
[92] AUSTREGESILO, H., BALS, C. AND TRAMBAUER, K., 2007. Post-Test Calculation and Uncertainty Analysis of the Experiment Quench-07 with the System Code ATHLET-CD. Nucl. Eng. Des., 237(15–17), PP.1693-1703.
[93] BOLSHOV, L.A., DOLGANOV, K.S., KISELEV, A.E. STRIZHOV, V.F., 2019. Results of SOCRAT code development, validation and applications for NPP safety assessment under severe accidents. Nucl. Eng. Des., 341, pp.326–345.
[94] DI MARCELLO, V., SCHUBERT, A., DE LAAR, J.V., VAN UFFELEN, P., The TRANSURANUS mechanical model for large strain analysis. Nucl. Eng. Des. 276, 19, 2014.
[95] ERBACHER, F. J., NEITZEL, H. J., ROSINGER, H., SCHMIDT, H., WIEHR, K., Burst criterion of Zircaloy fuel claddings in a loss-of-coolant accident. In Zirconium in the Nuclear Industry, Fifth Conference, ASTM STP 754, D.G. Franklin Ed., pages 271. American Society for Testing and Materials, 1982.
[96] ERBACHER, F.J., NEITZEL, H.J., WIEHR, K., Technical Report 4781, Kernforschungszentrum Karlsruhe (KfK), Germany, 1990.
[97] LAVOIL, A., LOCA Testing at Halden; The Tenth Experiment IFA-650.10. Technical Report HWR-974, OECD Halden Reactor Project, 2010.
[98] HAGEN, S., HOFMANN, P., NOACK, V., SCHANZ G., et al. "Behaviour of VVER-1000 Fuel Element with Boron Carbide/Steel Absorber Tested under Severe Fuel Damage Conditions in the CORA Facility. Results of Experiment CORA-W2". KfK 5363, 1994.
[99] GENTLE, E., "Monte-Carlo Methods," Encyclopaedia of Statistics, 5, pp. 612-617, John Wiley and Sons, New-York, 1985.
[100] CONOVER, W., Practical non-parametric statistic, Wiley, New York, 1999.
[101] GLAESER, H., "GRS Method for Uncertainty and Sensitivity Evaluation of Code Results and Applications," Science and Technology of Nuclear Installations, Volume 2008, Article ID 798901, 2008.
[102] ZHANG, J., SEGURADO J., SCHNEIDESCH, C., "Towards an Industrial Application of Statistical Uncertainty Analysis Methods to Multi-physic Modelling and Safety Analyses," Proc. OECD/CSNI Workshop on Best Estimate Methods and Uncertainty Evaluations, Barcelona, Spain, 16–18 November 2011.
[103] WILKS, S.S., Determination of sample sizes for setting tolerance limits, Ann. Math. Stat. 12, 91, 1941.
[104] GUBA, A., MAKAI, M., PAL L., "Statistical aspects of best estimate method-I"; Reliability Engineering and System Safety, 80, 217, 2003.
[105] DE CRÉCY, A., et al., "The BEMUSE Programme: Results of the First Part Concerning the LOFT L2-5 Test," Proceedings of 14th International Conference on Nuclear Engineering, Miami, Florida, USA, 17 July, 2006.
[106] GLAESER, H., "BEMUSE Phase VI Report, Status report on the area, classification of the methods, conclusions and recommendations," OECD/NEA/CSNI/R (2011) 4, March 2011.
[107] MCKAY, M. D., "Sensitivity and uncertainty analysis using a statistical sample of input values," Ch. 4, "Uncertainty Analysis", Ronen, Y. Editor, CRC Press, Florida, USA, 1988.

[108] HELTON, J.C., JOHNSON, J.D., SALLABERRY, C.J., STORLIE, C.B., “Survey of sampling-based methods for uncertainty and sensitivity analysis,” Reliability Engineering and System Safety, 91,10, 2006.
[109] IOOSS B., LEMAITRE, P., “A review on global sensitivity analysis methods,” in Uncertainty management in Simulation-Optimization of Complex Systems: Algorithms and Applications (C. Meloni and G. Dellino, Eds), Springer, 2015, http://www.springer.com/business.
[110] ADAMS, B., et al., "DAKOTA, A Multilevel Parallel Object-Oriented Framework for Design Optimization, Parameter Estimation, Uncertainty Quantification, and Sensitivity Analysis: Version 5.1 User's Manual", Sandia Technical Report SAND2010-2183, Updated Version 5.3, December 2013. (http://www.cs.sandia.gov/dakota).
[111] LAVOIL, A., “LOCA Testing at Halden, the Tenth Experiment IFA-650.10”, HWR-974, OECD Halden Reactor Project, December 2010.
[112] KISELEV, A., “Short Information on the Results Of IFA-650.9, IFA-650.10 and IFA-650.11 Calculations with Socrat Code”, Technical Note, Version 3, IBRAE RAN, December 2016.

ANNEX I:

SPECIFICATIONS FOR UNCERTAINTY ANALYSIS ON MODELLING OF THE HALDEN LOCA TEST IFA-650.10

I–1. INTRODUCTION

During the 2nd RCM of the FUMAC project, it was agreed to perform an uncertainty and sensitivity analysis (UASA) based on one chosen IFA-650 test using simplified T/H boundary conditions (i.e., coolant temperature and heat transfer coefficients calculated by SOCRAT, or the measured or calculated cladding temperatures).

The objective is to verify if the quantified uncertainties on the predicted key physical parameters (cladding temperature, plenum gas temperature, plenum gas pressure, burst time, strain, elongation, equivalent cladding reacted, hydriding, etc.) well bound the measured data during the test, and as an optional activity for the interested participants, to identify the important input parameters through global sensitivity analysis (GSA).

Considering the complexity of IFA-650.9 (very high burnup, completed T/H conditions, need axial relocation model), it was proposed to choose either IFA-650.10 (for PWR) or IFA-650.11 (for VVER) with moderate burnup and without significant axial relocation, as the case for the UASA.

The following approach was proposed:

— Using input uncertainty propagation method, based on non-parametric order statistics;
— Sample number is chosen to 200;
— A common list of input uncertainty parameters will be agreed, covering fuel manufacturing data, properties and models, operating and test conditions;
— A common list of output uncertainties will be agreed;
— If the participant has no own tool, a statistical UASA analysis tool (DAKOTA) may be used, which may be obtained freely from SNL.

The participant, however, has the freedom to use other alternative method or tool to perform the UASA, or perform only the uncertainty analysis.

— This report gives:
— A short description of the proposed uncertainty and sensitivity analysis methodology (§2);
— A specification of the test case IFA-650.10 (§3) (which can be adapted to IFA650.11);
— A list of input uncertainties to be considered for IFA650.10 (§4) (can be adapted to IFA650.11);
— A list of output uncertainties to be provided (§5);
— A process and schedule (§6).

This specification follows the same approach as for the OECD RIA benchmark Phase II.

I–2. METHODOLOGY

I–2.1. Uncertainty analysis: input uncertainty propagation method

Among all the available uncertainty analysis methods, the probabilistic input uncertainty propagation method is so-far the most widely used in the nuclear safety analysis [I–1].

In this method, the fuel codes are treated as 'black boxes', and the input uncertainties are propagated to the simulation model output uncertainties via the code calculations with sampled input data from the known distributions [I–2].

The method consists in the following steps (Fig. I–1):

(a) Specification of the problem: All relevant code outputs and corresponding uncertain parameters for the codes, plant modelling schemes, and plant operating conditions are identified;

(b) Uncertainty modelling: the uncertainty of each uncertain parameter is quantified by a probability density function (pdf) based on engineering judgment and experience feedback from code applications to separate and integral effect tests and to full plants simulation. If dependencies between uncertain parameters are known and judged to be potentially important, they are quantified by correlation coefficients;

(c) Uncertainty propagation through the computer code: the propagation is performed using Monte-Carlo simulations [I–3]. In Monte-Carlo simulation, the computer code is run repeatedly, each time using different values for each of the uncertain parameters. These values are drawn from the probability distributions and dependencies chosen in the previous step. In this way, one value for each uncertain parameter is sampled simultaneously in each repetition of the simulation. The results of a Monte-Carlo simulation lead to a sample of the same size for each output quantity;

(d) Statistical uncertainty analysis of the results: with sufficient large number of Monte-Carlo simulations, the output sample can be used to get any typical statistics of the code response such as mean or variance, the upper or lower bounds, and to determine the cumulative distribution function (CDF). The CDF allows to derive the percentiles of the distribution (if X is a random variable and F_X its CDF, the α-percentile, $\alpha \in [0;1]$, is the deterministic value $X\alpha$ such that $F_X(X\alpha) = P(X \leq X\alpha) = \alpha$.

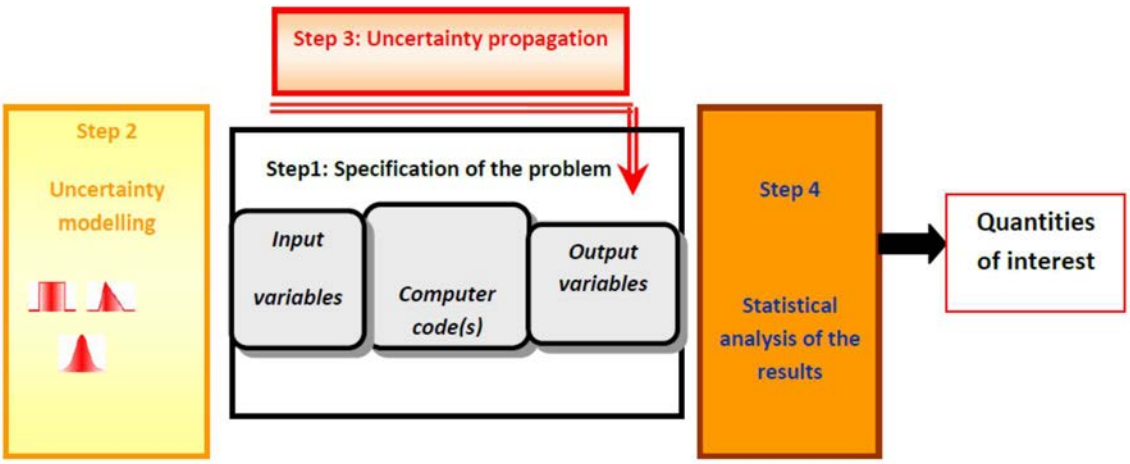

FIG. I–1. The four steps of an input uncertainty propagation method.

A simple way to get information on percentiles is to use order statistics [I–4], which is a well-established and shared methodology in the nuclear community and hence is recommended for this activity [I–5] [I–6] [I–7].

The principle of order statistics is to derive results from the ranked values of a sample. If $(X^1, \dots, X^N)$ denotes a sample of any random variable, X, and $(X^1, \dots, X^N)$ the corresponding ranked one, order statistics first provides an estimation of the percentile of interest since the α -percentile can be estimated by $X^{(\alpha,N)}$. Moreover, it turns out that the CDF of $X^{(k)}$, $F_X\left(X^{(k)}\right)$, follows the Beta law $\beta(k, N-k+1)$, which does not depend on the distribution of X. This key result allows quantifying the probability that any ranked value is smaller than any percentile by the following formula:

$$P\left(X^{(k)} \leq X\alpha\right) = F_{\beta(k,N-k+1)}(\alpha) \tag{I1}$$

where $F_{\beta(k,N-k+1)}$ denotes the CDF of the Beta law $\beta(k, N-k+1)$.

Equation (I1) can then be used to derive:

1) Lower and upper bounds of a percentile of interest, given the sample size N and the confidence level β that controls the probability that $X^{(k)} \leq X\alpha$. It requires to solve the equation $F_{\beta(k,N-k+1)}(\alpha) = \beta$;

2) The minimal sample size (and therefore the minimal number of computer runs) to obtain a lower or upper bound of a given percentile with a given confidence level. It leads to the so-called Wilk's formula [I–4]:

$$N = \ln(1-\beta)/\ln\alpha \tag{I2}$$

and Guba's estimate in Case of multiple output parameters in [I–5].

Order statistics are widely used since nothing should be known about the distribution of the random variable except that it is assumed continuous. Moreover, this method is very simple to implement, which makes it extremely interesting for licensing applications to nuclear safety analyses.

Due to its simplicity, robustness and transparency, this method will be used in this benchmark. The highly recommended sample size is set to 200 (i.e. 200 code runs will be performed). Strong justifications should be given if a lower number of code runs is performed. The sample is constructed according to the selected pdfs coming from the uncertainty modelling step and assuming independence between input parameters following a Simple Random Sampling (SRS) as recommended for the use of order statistics in BEMUSE [I–6] [I–7].
Moreover, we focus on the estimation of a lower, resp. upper, bound of the 5%, resp. 95%, percentiles α at confidence level β higher than 95%. For $N = 200$, $\beta = 0.95$ and $\alpha = 0.05$ or 0.95, Equation (I1) leads to:

$$P\left(X^{(5)} \leq X_{5\%}\right) > 0.95,$$

$$P\left(X^{(196)} \leq X_{95\%}\right) > 0.95$$

the lower, resp. upper, bound is defined in this benchmark by $X^{(5)}$, resp. $X^{(196)}$.

For a proper use of order statistics, all code runs should be successfully terminated. If not, it is therefore recommended to correct the failed code runs. As noticed during the BEMUSE project [I–7], some failures can come from a too large time step and the run can be continued after time step reduction. If there is no possible correction, a careful checking of the output evolution is be performed in the failed runs to keep the results before the failures occur and use the previous methodology to analyse them. When the number of failures is relatively low, a conservative treatment can also be considered by assuming that the n failed runs produced the n most adverse values of the output of interest.
Participants are requested to clearly describe in their contribution their approach to handle this topic.

I–2.2. Sensitivity analysis: Global sensitivity analysis method

Besides the uncertainty analysis, and as an optional activity for the interested participants, a complementary study may be performed to get qualitative insights on the most influential input parameters.

This work can be done based on a global sensitivity analysis using the 200 code runs previously obtained. This is usually done together with the statistical uncertainty analysis, using the same tool.

More precisely, if Y denotes the response of interest and $\{X_i\}_{i=1,\ldots,p}$ the set of p uncertain input parameters (also called regressors), it will require to compute the following classical correlation coefficients:

Linear (or Pearson's) simple correlation coefficients (SCC): for each i,

$$\rho_i = \frac{C_{ov}(Y,X_i)}{\sigma_X \sigma_Y} \tag{I3}$$

where σ_X and σ_Y are the empirical standard deviations of X and Y.

They correspond to the p correlation coefficients between the response and the p regressors. They measure the degree of linear dependence between the response and the p regressors taken separately.

A better measure of linear relation between the response and one of the p regressors is the so-called partial correlation coefficient (PCC), in which the correlation between the two variables under consideration is calculated and corrected for the linear contribution of the remaining variables. Indeed, since this correction removes linear trends associated with other variables, the PCC would lead to higher number than the Pearson's simple correlation coefficient.

Spearman's rank correlation coefficient (RCC): same definition as SCC but replacing input and output values by their respective ranks. Working with ranks allows one to extend the previous underlying linear regression model to a monotonic non-linear one. In the presence of nonlinear but monotonic relationships between the response and each of the p regressors, use of the ranks can substantially improve the resolution of sensitivity analysis results [I–8].

The partial rank correlation coefficient (PRCC) provides an improved measure of the monotonic relation between the response and one of the p regressors by removing trends associated with other variables. Again, the PRCC would lead to higher number than the Spearman's rank correlation coefficient.

Based on this information (Pearson's SCC or Spearman's RCC, PCC or PRCC), the most influential uncertain input parameters can be identified.

Note that the above correlation coefficients estimate the linear connection (SCC) or the monotonic one (RCC) between the input and the target output parameters. Moreover, no interaction between input parameters is considered [I–9].

As the fuel rod codes are all complex models, and there are certain interactions between input parameters, these coefficients can only be considered as qualitative and relative index is used for screening the non-important input parameters.

Other sensitivity measures, such as the Sobol's indexes, could be obtained by using the variance-based decomposition method [I–10]. The Sobol's indexes provide quantitatively the contribution of the uncertainty of each input parameter to the target output parameter uncertainty. However, the variance-based decomposition method requires much more calculations efforts, therefore is not recommended for the current benchmark.

I–2.3. The tool

The participant can choose the tool that is available for him to perform the proposed UASA.

The DAKOTA (Design Analysis Kit for Optimization and Terascale Applications) code has been developed by the Sandia National Laboratory [I–11]. It can be freely downloaded from the website http://www.cs.sandia.gov/dakota.

As shown in Fig. I–2, DAKOTA provides a flexible, extensible interface between simulation codes and iterative analysis methods, via DAKOTA input files and executables.

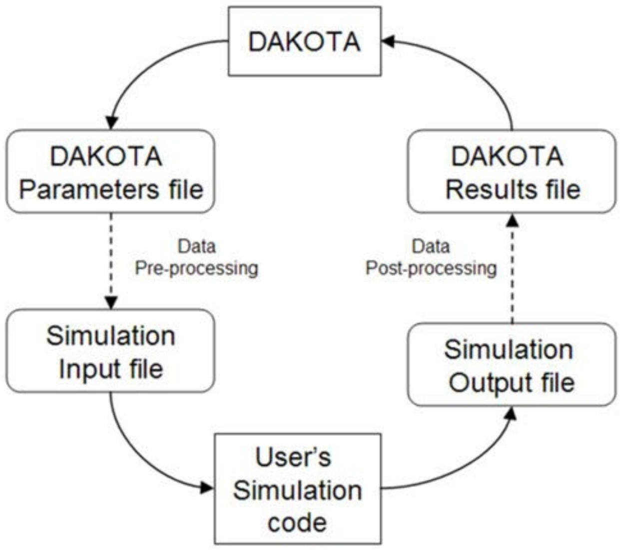

FIG. I–2. DAKOTA uncertainty analysis process.

Among others, DAKOTA contains algorithms for uncertainty quantification (UQ) with sampling (Monte-Carlo or Latin Hypercube), epistemic uncertainty methods (Second order probability or Dempster-Shafer theory of evidence), and sensitivity analysis. These capabilities may be used on their own or as components within advanced strategies.

For the applications presented in this activity, the input uncertainty parameters range and distributions, as well as the uncertainty analysis method and number of samples are defined in the DAKOTA Input File.

Based on the sampled or assigned input uncertainty parameters in the DAKOTA Parameter File, various scripts can be developed to create the code input files, to execute the simulation jobs, and to collect the code calculation output data into the DAKOTA Results File. The DAKOTA Executable will then perform the requested statistical uncertainty and sensitivity analysis, and provide the information in the DAKOTA Output Files.

I–3. SPECIFICATION OF THE CASE

I–3.1. Test IFA-650.10

The objective of the Halden LOCA tests IFA-650 is to study fuel behaviours such as fuel fragmentation and relocation, cladding ballooning, burst (rupture) and oxidation during typical LOCA transient for PWR, BWR and VVER high burnup fuels.

In the IFA-650 LOCA tests, a single fuel rodlet is in a high-pressure flask connected to the heavy water loop 13 of the Halden reactor. The fuel power is controlled by reactor power. Nuclear power generation in the fuel rod is used to simulate decay heat, whereas the electrical heater surrounding the rod is simulating the heat from surrounding rods.

As shown in Fig. 3 (Section 2.2), the rig and rod instrumentations consisted of three cladding thermocouples at the bottom (TCC1) and upper (TCC2 & 3) part of the rod, three heater thermocouples at different axial elevations (TCH1 at bottom, TCH2 at mid and TCH3 at top), a cladding extensometer (EC2) and a rod pressure sensor (PF1), rig coolant thermocouples (two at rig inlet, TI, and two at outlet, TO), three axially distributed vanadium neutron detectors (ND) to measure axial power distribution and two fast response cobalt NDs to monitor rapid flux and power changes.

The detailed description of IFA-650.10 can be found in Section 2.2. The test segment was cut from a standard PWR fuel rod test which had been irradiated in the PWR Gravelines 5 (900 MWe EDF, France) during five cycles from August 1988 to August 1995 to a burn-up of 61 MWd/kgU (average cycle powers 195, 230, 215, 185 and 150 W/cm). The length of the fuel stack was ~ 440 mm and no end pellets were inserted.

The rod was filled with a gas mixture of 95 % argon and 5 % helium at 40 bars. Argon was chosen to simulate the fission gases, whereas a small amount of helium is required for the leak test of the rod. The rod plenum volume (free gas volume) was made relatively large to maintain stable pressure conditions until cladding burst. The total free gas volume of ~16–17 cm^3 was thus practically all located in the plenum, outside the heated region.

The test was conducted in May 2010. The evolution of the main test results is illustrated in Figs 20 and 21 (Section 2.2).

The initial loop pressure was ~70 bar and the counter pressure in the blowdown tank was ~2 bar. Shortly before the test start, the outer loop was by-passed, and after ~3 minutes with natural circulation in the rig, the LOCA was initiated by opening the valves leading to the shielded blowdown tank.

The target peak cladding temperature was 850 °C. Cladding failure occurred ~249 s after blowdown at ~755 °C (TCC1) as evidenced by pressure, cladding temperature measurements as well as the gamma monitor on the blowdown line to the dump tank.

Spraying was started 12 s after the burst to ensure that the fission products are transported out of the loop. The test was terminated by a reactor scram 417 s after the blowdown initiation. At the end of the test, the rig was filled with helium for dry storage.
Slight clad ballooning and burst were detected and verified by the gamma scanning performed at Halden. No fuel relocation was seen during the test, which was subsequently confirmed by the gamma scanning.

I–3.2. Modelling

The total length of the test fuel rod should be modelled by at least 17 radial nodes and 7 axial nodes.

The initial conditions of the test fuel rod can be modelled by a steady state simulation of the base in-reactor irradiations. In both steady state and transient fuel rod input models, most of the data were set according to the specifications of IFA-650 tests or the code manual recommended values. The refabricated rodlet input model should be validated by comparing with available measured data. The refabricated rodlet initialization file should be the output of steady-state input model which contains gas data from the initial rod and subsequent Fission Gas Release (FGR) history data. The number of moles of new gas mixture and the relative amount of each gas species in the refabricated rodlet should be adapted to match the calculated and measured initial rod internal pressure.

The provided measured data during tests include (see Fig. 20 and 21):

— Three measured cladding temperatures at the bottom (TCC1) and upper (TCC2 & 3);
— Measured rod internal pressure (PF1);
— Measured plenum temperature (T_{plenum});
— Three measured heater temperatures at different axial elevations (TCH1 at bottom, TCH2 at mid and TCH3 at top);
— Rig coolant temperatures (two at rig inlet, TIA, and two at outlet, TOA);
— Rig pressure and flowrate,;rod power (Co) and axial power distribution (V);
— Heater power (LHR heater).

Ideally, if one knows the transient evolution of coolant pressure, inlet temperature and flow rate in the channel between the rod and the heater, on can use the built-in (if any) fuel rod code heat transfer models to calculate the coolant temperatures, heat transfer coefficients, and cladding temperatures.

However, since most fuel rod codes do not simulate in detail the rig and the different phases of the test, and due to complexity to simulate the thermal hydraulic behaviours and the differences that may appear from various assumptions and/or models, it is recommended to use the thermal hydraulic boundary conditions calculated from SOCRAT [I–13], namely:

— Coolant temperatures;
— Clad to coolant heat transfer coefficients (HTCs).

The clad to coolant heat transfer coefficients should be determined from the total heat flux (radiative + convective), namely HTC = Q_{tot} / (T_{clad} – T_{cool}), for each axial node.

Alternatively, the measured or calculated cladding temperatures can be imposed directly as the boundary conditions.

The rodlet plenum temperature (T_{plenum}) should be taken from the measurement, or from any appropriate empirical plenum gas temperature model.

For the transient calculation, the rod axial power profile as shown in Fig. I–3 should be used.

The default 'best estimate' properties and models in the participant's fuel rod code should be selected, namely the:

— Fuel thermal conductivity, thermal expansion, specific heat models;
— Cladding thermal conductivity, thermal expansion, specific heat models;
— Fuel initial radial deformation and relocation due to densification, solid swelling and gas swelling;
— Cladding initial radial deformation;
— Rigid pellet and cladding deformation models (finite difference model) for fuel rod mechanical response;
— Default clad failure model;
— Fission gas release mode;
— Gap conductance model due to gap gas conductivity, fuel/cladding emissivity and cladding hardness;

— Cathcart-Pawel (C-P) model for high temperature oxidation;
— Non-protective initial oxide layer option.

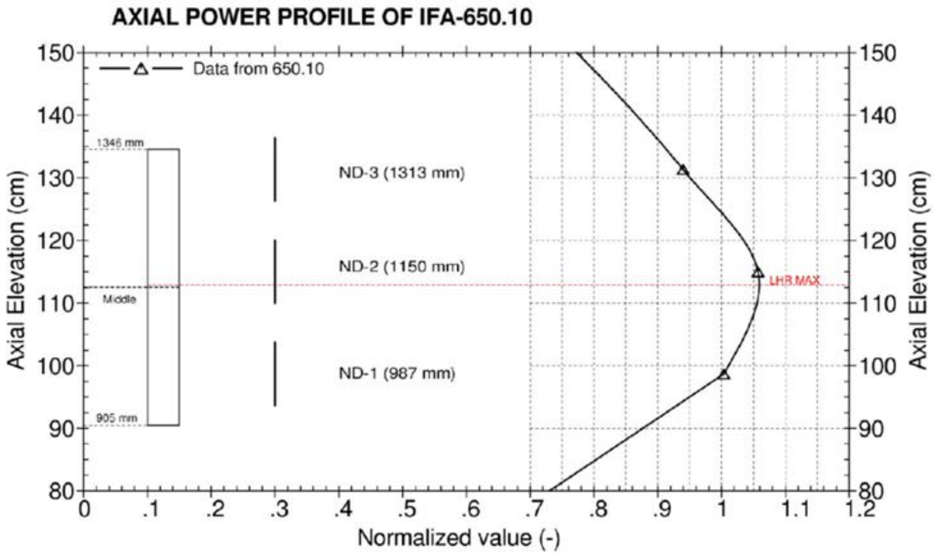

FIG. I–3. Axial power profile at the start of the test of IFA-650.10 [I–12].

If axial fuel relocation is available and used, the fitting parameters for the cladding burst strain, annealing rate, Yield stress, packing fraction, pellet-cladding gap width threshold for fuel fragment axial mobility should be set at their default values.

A steady state of 100 s should be simulated before the beginning of blowdown. The calculation should stop at 600 s (after the scram at 517 s).

The maximum time step during the transient should be chosen appropriately to capture the transient behaviours (e.g., < 0.1 s during the heat up phase).

I–4. DEFINITION OF INPUT UNCERTAINTIES

I–4.1. Identification of uncertainty parameters

From the preliminary calculation results [I–14] and based on engineering judgements, the following uncertainty parameters are identified. They may not be all relevant to the Halden LOCA tests but are included to determine the important parameters through the sensitivity analysis.

The participant can consider only the parameters applicable or relevant to his own code.

I–4.2. Uncertainties in fuel rod design/manufacturing data

The following relevant uncertainty parameters can be considered:

— Cladding outside/inside diameter;
— Fuel pellet outside diameter;
— ^{235}U enrichment;
— Fuel theoretical density;
— Rod gas-gap fill pressure.

I–4.3. Uncertainties in fuel rod operation and test boundary conditions

The uncertainty parameters in the initial states of the fuel rod are mainly related to the uncertainties in the base irradiation operating conditions. As the base irradiation operating conditions will be explicitly simulated, the uncertainties in the initial states of the fuel rod will be propagated from steady state fuel rod code (e.g., FRAPCON) to transient fuel rod code (e.g., FRAPTRAN):

- Cladding corrosion model (initial state);
- Cladding hydrogen pickup model (initial state).

The following relevant uncertainty parameters are considered on the test boundary conditions:

- Rod average power;
- Rod power profile;
- Decay heat model.

If the T/H boundary conditions as calculated by SOCRAT are used, the following uncertainties should be considered (if applicable):

- Coolant temperature;
- Clad to coolant heat transfer coefficient.

If the calculated or measured cladding temperatures are used as the boundary conditions, the measurement and/or the calculation uncertainties should be considered.

- Clad temperatures: measured or from SOCRAT calculations (if applicable).

I–4.4. Uncertainties in physical properties and key models

If applicable, the following relevant uncertainty parameters are considered (the final list depends on the selected code and the participant's choice):

- Fuel thermal conductivity;
- Cladding thermal conductivity;
- Fuel thermal expansion coefficient;
- Cladding thermal expansion coefficient;
- Fuel specific heat capacity;
- Cladding specific heat capacity;
- Fuel densification model;
- Fuel solid swelling model;
- Fuel gaseous swelling model;
- Fission gas release (or gas diffusion coefficient);
- Gap gas conductivity;
- Fuel/cladding emissivity;
- Fuel radial relocation;
- Cladding Meyer hardness;
- Cladding annealing;
- Cladding ballooning model;
- Cladding mechanical deformation;
- Cladding burst stress criteria;

- Cladding yield stress;
- Fuel axial relocation (fuel fragment packing fraction and cladding strain threshold for fuel mobility, if applicable);
- Cladding oxidation model at high temperature;
- Thermal conductivity of the oxide layer;
- Cladding burst strain criteria;
- Plenum gas temperature (empirical correlation from measured data or SOCRAT calculations);
- Cladding elastic modulus.

I–4.5. Definition of INPUT uncertain parameters

Table 13 provides the recommended input parameters (if applicable) as well as the information related to their uncertainties. For each of them, it includes a mean value, a standard deviation and a type of distribution.

To avoid unphysical numerical values, a range of variation (lower and upper bounds) is also provided. The sampling will be performed (i.e., truncated) between the upper and lower bounds. This information is then used to define a probability distribution for uncertainty modelling.

For the current benchmark application, a normal distribution has been assigned for simplicity to all the considered input parameters. Where applicable, the standard deviation has been taken as the half of the maximum of the absolute value of the difference between their nominal value and their upper or lower bound. In addition, the participants could perform sensitivity studies by using other distributions, such as uniform or histogram. These results could be reported at the RCM or the final report.

Depending on the code selected, it might be difficult to modify some recommended input parameters. In this case, the parameters can be discarded but this information must be clearly mentioned in participants’ contributions.

I–5. OUTPUT SPECIFICATION

I–5.1. Uncertainty analysis output

Each participant will give lower and upper bounds (LB, UB) for the output parameters listed in Table 14. A frequency of 10 s was recommended as the trending time. In addition, the results of the calculation with the nominal value of the input parameters, also called reference calculation (REF) will be provided.

I–5.2. Sensitivity analysis output

A list of times required for sensitivity analysis is proposed in Table 15. One formatted Excel file was also expected for providing the sensitivity analysis results.

Based on this information, the most influential uncertain input parameters with respect to the Fuel Thermal Behaviour (fuel pellet centreline and surface temperature), Clad Thermal Behaviour (cladding surface temperatures and oxidation layer thickness), and Mechanical Behaviour (Cladding diameter, effective stress) could be identified and given in the last columns of Table 13.

It is up to the participants to define the thresholds for measuring the importance (H, M or L), based on the sensitivity analysis results and his own experience. The following empirical thresholds could be used to indicate the relative importance (as recommended in the DAKOTA user's guide and some previous studies):

- H (High): absolute value of correlation coefficients ≥ 0.5;
- M (Medium): 0.5 > absolute value of correlation coefficients > 0.25;
- L (Low): absolute value of correlation coefficients ≤ 0.25.

Appropriate common thresholds for measuring the importance can be defined at a later stage.

I–5.3. Proposed Process and Schedule As per agreements

- Step 1 (J. Zhang): Proposal for a draft specification, and send to all participants for review/comments (by end-of-December 2016);
- Step 2 (all participants): Send comments/suggestions to J. Zhang (end-of-January 2017);
- Step 3 (J. Zhang): Send final Specification with a common list of input uncertainty parameters ranges and distributions and output (in Excel file) to all participants (end-of-June, 2017);
- Step 4 (all participants): Perform the uncertainty analysis according to the Specifications and send the results to IAEA (end-of-September 2017);
- Step 5 (IAEA and the Consulting team): Synthesis and compare uncertainty analysis results (end-of-October 2017);
- Step 6 (all participants): Prepare presentations, compare results and present conclusions (3rd RCM, November 13-17, 2017);
- Step 7 (IAEA and the Consulting team): Prepare final report (Consulting meeting, 2018).

REFERENCES TO THE ANNEX I

[I–1] GLAESER, H., "GRS Method for Uncertainty and Sensitivity Evaluation of Code Results and Applications, Science and Technology of Nuclear Installations, Volume 2008, Article ID 798901, 2008.

[I–2] ZHANG, J., SEGURADO J., SCHNEIDESCH, C., "Towards an Industrial Application of Statistical Uncertainty Analysis Methods to Multi-physical Modelling and Safety Analyses," Proc. OECD/CSNI Workshop on Best Estimate Methods and Uncertainty Evaluations, Barcelona, Spain, 16–18 November 2011.

[I–3] GENTLE, E., "Monte-Carlo Methods," Encyclopaedia of Statistics, 5, pp. 612–617, John Wiley and Sons, New-York, 1985.

[I–4] CONOVER, W., Practical non-parametric statistic, Wiley, New York, 1999.

[I–5] GUBA, A., MAKAI, M., PAL L., Statistical aspects of best estimate method-I; Reliability Engineering and System Safety 80, 217–232, 2003.

[I–6] DE CRÉCY, A., et al., "The BEMUSE Programme: Results of the First Part Concerning the LOFT L2-5 Test," Proceedings of 14th International Conference on Nuclear Engineering, Miami, Florida, USA, 17–20 July, 2006.

[I–7] GLAESER, H., "BEMUSE Phase VI Report, Status report on the area, classification of the methods, conclusions and recommendations," OECD/NEA/CSNI/R(2011)4, March 2011.

[I–8] MCKAY, M.D., "Sensitivity and uncertainty analysis using a statistical sample of input values," Ch. 4, Uncertainty Analysis, Ronen, Y. Editor, CRC Press, Florida, USA, 1988.

[I–9] HELTON, J.C., JOHNSON, J.D., SALLABERRY, C.J., STORLIE, C.B., "Survey of sampling-based methods for uncertainty and sensitivity analysis," Reliability Engineering and System Safety, 91(10), 10/2006.

[I–10] IOOSS B., LEMAITRE, P., "A review on global sensitivity analysis methods," in Uncertainty management in Simulation-Optimization of Complex Systems: Algorithms and Applications (C. Meloni and G. Dellino, Eds), Springer, 2015, http://www.springer.com/business.

[I–11] ADAMS, B., et al., "DAKOTA, A Multilevel Parallel Object-Oriented Framework for Design Optimization, Parameter Estimation, Uncertainty Quantification, and Sensitivity Analysis: Version 5.1 User's Manual", Sandia Technical Report SAND2010-2183, Updated Version 5.3, December 2013, http://www.cs.sandia.gov/dakota.

[I–12] LAVOIL, A., "LOCA Testing at Halden, the Tenth Experiment IFA-650.10", HWR-974, OECD Halden Reactor Project, December 2010.

[I–13] KISELEV, A., "Short Information on the Results of IFA-650.9, IFA-650.10 and IFA-650.11 Calculations with SOCRAT code", Technical Note, version 3, IBRAE RAN, December 2016.

[I–14] ZHANG, J., UMIDOVA, Z., DETHIOUX, A., "Simulation of fuel behaviours under LOCA and RIA using FRAPTRAN and uncertainty analysis with DAKOTA", in "Modelling of Water Cooled Fuel Including Design Basis and Severe Accidents, Proceedings of a Technical Meeting Held in Chengdu, China, 28 October – 1 November 2013", IAEA-TECDOC-CD-1775, 2015.

LIST OF PARTICIPANTS

Zhang, J.	Tractebel Engineering S.A., Avenue Ariane 7, 1200 Brussels, BE, Belgium Email: jinzhao.zhang@tractebel.engie.com
Abe, A.	Instituto de Pesquisas Energéticas e Nucleares (IPEN-CNEN/SP), Avenida prodessor Lineu Prestes, 2242, 05508-000 São Paulo, Brazil Email: ayabe@ipen.br
Boneva, S.	Institute for Nuclear Research and Nuclear Energy (INRNE), Bulgarian Academy of Science, 72 Tzarigradsko Chausee Blvd. 1784 Sofia, Bulgaria. Email: boneva@inme.bas.bg
Ji, S.	China Institute of Atomic Energy, ZinZhen P.O. BOX: 275, Beijing 102413, FangShan District, China Email: songtaoji@139.com
Ren, Q.	China Nuclear Power Technology Research Institute, Yitian Road, Jiangsu Building, 13/F, Block A, 518026, Shenzhen City, China E-mail: renqisen@cgnpc.com.cn
Van Uffelen, P.	European Commission, Materials Research Department Institute for Transuranium Elements, Postfach 2340, 76125 Karlsruhe, Germany Email: paul.van-uffelen@ec.europa.eu
Stuckert, J.	Karlsruhe Institute of Technology, Hermann-von-Helmholtz-Platz 1, 76344 Eggenstein Leopoldshafen, Germany Email: juri.stuckert@kit.edu
Tulkki, V.	VTT Technical Research Centre of Finland, P.O. BOX 1000, Vuorimiehentie 3, Otaniemi, 02044 Espoo, Finland Email: ville.tulkki@vtt.fi
Boulore, A.	Centre CEA de Saclay (Essonne) Gif-sur-Yvette 91191, France Email: antoine.boulore@cea.fr
Kulacsy, K.	Hungarian Academy of Sciences, Centre of Energy Research, Konkoly Thege út 29-33, P.O. Box 49. 1121 Budapest, Hungary Email: katalin.kulacsy@energia.mta.hu

Luzzi, L.
Politecnico di Milano,
Dipartimento di Energia,
Via Lambruschini 4 (Building 25),
20156 Milano, Italy
Email: lelio.luzzi@polimi.it

Fujioka, K.
Nuclear Regulatory Authority (NRA),
1-9-9 Roppongi,
106-8450 Minato-ku,
Tokyo, Japan
Email: kazuharu_fujioka@nsr.go.jp

Koo, Y.H.
Korean Atomic Energy Research Institute (KAERI),
111 Daedeok-daero 989 beon-gil, Yuseong-gu,
305353 Daejeon,
Republic of Korea
Email: yhkoo@kaeri.re.kr

Wiesenack, W.
OECD Halden Reactor Project; Institute for Energy Technology
P.O. BOX 173, Os Alle 5,
N1751 Halden, Norway
Email: wolfgang.wiesenack@hrp.no

Fedotov, P.
Joint Stock Company (JSC), A.A. Bochvar High-Technology Research Institute of Inorganic Materials,
P.O. BOX. 369, JSC "VNIINM", 5-a Rogova str.,
Moscow, Russian Federation
Email: fpvpetr@rambler.ru

Kiselev, A.
Nuclear Safety Institute of Russian Academy of Sciences (IBRAE),
Bolshaya Tulskaya str. 52, 115191,
Moscow, Russian Federation
E-mail: ksv@ibrae.ac.ru

Herranz, L.
Centro de Investigaciones Energeticas, Medioambientales y Tecnologicas (CIEMAT),
Avenida Complutense 40,
28040 Madrid, Spain
Email: luisen2013@gmail.com

Jernkvist, L.
Quantum Technologies AB,
Uppsala Science Park,
SE-75183 Uppsala, Sweden
Email: loje@quantumtech.se

Cherednichenko, O.
Energorisk Ltd.,
T. Strokacha 7,
P.O. Box. 141, 031448 Kiev,
Ukraine
Email: cherezo@bigmir.net

Ieremenko, M.
State Scientific and Technical Center for Nuclear and Radiation Safety (SSTC NRS),
Stusa Vasilya Vul, 35/37,
03142 Kyiv, Ukraine
Email: ml_eremenko@sstc.com.ua

Williamson, R.	Battelle Energy Alliance LLC, Idaho National Laboratory (INL) 2525 N. Fremont Avenue, P.O. Box 1625, 83415-3840 Idaho Falls ID, United States of America. Email: Richard.williamson@inl.gov
Xu, P.	5801 Bluff Road Postal Code: 29601, Hopkins, South Carolina, USA E-mail: xup@westinghouse.com
Porter, I.	Nuclear Regulatory Commission (US-NRC), Washington 20555, District of Columbia, United States of America. Email: ian.porter@nrc.gov
Austregesilo, H.	Gesellschaft für Anlagen- und Reaktorsicherheit (GRS) GmbH Cooling Circuit Department, Reactor Safety Research Division, Forschungszentrum, Boltzmannstr. 1485748 Garching, Germany E-Mail: henrique.austregesilo@grs.de (Active observer)

CONTRIBUTORS TO DRAFTING AND REVIEW

Boulore, A.	CEA, France
Chan, P.	International Atomic Energy Agency
Pastore, G.	Batelle INL, USA
Pizzocri, D.	Politecnico di Milano, Italy
Rathod, V.	International Atomic Energy Agency
Stuckert, J.	KIT, Germany
Van Uffelen, P.	EC/JRC, Germany
Veshchunov, M.	International Atomic Energy Agency
Wiesenack, W.	IFE-HRP, Norway
Zhang, J.	TRACTEBEL, Belgium

IAEA
International Atomic Energy Agency

No. 26

ORDERING LOCALLY

IAEA priced publications may be purchased from the sources listed below or from major local booksellers.

Orders for unpriced publications should be made directly to the IAEA. The contact details are given at the end of this list.

NORTH AMERICA

Bernan / Rowman & Littlefield
15250 NBN Way, Blue Ridge Summit, PA 17214, USA
Telephone: +1 800 462 6420 • Fax: +1 800 338 4550
Email: orders@rowman.com • Web site: www.rowman.com/bernan

Renouf Publishing Co. Ltd
22-1010 Polytek Street, Ottawa, ON K1J 9J1, CANADA
Telephone: +1 613 745 2665 • Fax: +1 613 745 7660
Email: orders@renoufbooks.com • Web site: www.renoufbooks.com

REST OF WORLD

Please contact your preferred local supplier, or our lead distributor:

Eurospan Group
Gray's Inn House
127 Clerkenwell Road
London EC1R 5DB
United Kingdom

Trade orders and enquiries:
Telephone: +44 (0)176 760 4972 • Fax: +44 (0)176 760 1640
Email: eurospan@turpin-distribution.com

Individual orders:
www.eurospanbookstore.com/iaea

For further information:
Telephone: +44 (0)207 240 0856 • Fax: +44 (0)207 379 0609
Email: info@eurospangroup.com • Web site: www.eurospangroup.com

Orders for both priced and unpriced publications may be addressed directly to:

Marketing and Sales Unit
International Atomic Energy Agency
Vienna International Centre, PO Box 100, 1400 Vienna, Austria
Telephone: +43 1 2600 22529 or 22530 • Fax: +43 1 26007 22529
Email: sales.publications@iaea.org • Web site: www.iaea.org/publications

19-00921

International Atomic Energy Agency
Vienna
ISBN 978–92–0–163919–6
ISSN 1011–4289